Princeton University

Final Report

NASA RESEARCH PROGRAM

The Roles of Fluid Motion and Other Transport Phenomena in the Morphology of Materials

Contract NAG 3-447

July 1983 - October 1987

Prepared for
Lewis Research Center
Cleveland, Ohio
May 1988

D. A. Saville
Department of Chemical Engineering
Princeton University
Princeton, NJ 08544

TABLE OF CONTENTS

ABSTRACT

We investigated the influence of transport phenomena on the morphology of crystalline materials. Two problems were studied: one dealt with the effects of convection on the crystallization of pure materials, the other with the crystallization of proteins from solution. In the first study we were interested in how convection alters the stability of the growth process and the relation between undercooling and the growth speed. In the second, we sought to find out why protein crystals grow as slowly as they do and how crystal morphology depends on the growth rate and crystal size. In both studies the research focussed on developing fundamental data that is a prerequisite for any microgravity experiments.

In the study of dendrite morphology, a computation scheme was developed which simulates the evolution of a needle-shaped crystal in an undercooled melt in the presence of convective heat transfer. The algorithm provides a model of crystal growth which includes the physical processes currently thought to govern growth. The only approximations are those necessary to the numerical solution of the equations, i.e., representation of the solution at a finite number of "points" using a boundary integral method for tracking the interface. We did not resort to linearization nor did we assume quasi-static behavior of the temperature field. Thus, the evolution of the interface can be tracked in space and time to ascertain its form and stability. The algorithm was used to study the influence of convection and interfacial energy (the Gibbs-Thompson effect) on growth processes.

A new class of steady state shapes was found for growth in the presence of fluid motion. The relation between growth rate, undercooling, flow strength, and the other parameters was derived. The relation reduces to the well-known Ivantsov form when convection is absent. The stability of these shapes, as well as those found in the absence of convection, was investigated by following the non-linear evolution of the interface after it was perturbed. These interfaces were always unstable and the well-known tip-splitting instability appeared. Adding the effect of interface curvature on temperature (the Gibbs-Thompson effect) produced new interface configurations, which were almost paraboloidal. These shapes were always stable. These results are contrary to those found in connection with either the theory of marginal stability or microscopic solvability. The reasons for this are unknown. The algorithm is a solution of the full non-linear problem so some discrepancies are to be expected. However, the qualitative difference in behavior deserves further study and the numerical algorithm should be carefully checked. If the numerical algorithm is indeed error free, then currently accepted theories will need revision. One paper derived from this part of the study has been published in Physical Review A, others are in preparation.

The work on protein crystal growth was not carried as far as that on dendrite morphology due to the need to develop experimental apparatus. In the first part of this study the influence of fluid motion and other transport processes was investigated. Theoretical work disclosed that flow processes appear to be too weak to slow crystal growth or cause it to terminate. Criteria were developed to indicate when diffusion rates would begin to influence crystal growth. According to the criteria, none of the extant studies on growth kinetics could have been limited by transport rates. In each case, observations ceased before the crystals had grown large enough for diffusion to play a significant role.

With the results of the theoretical study in hand, we proceeded to develop apparatus to measure growth rates of single protein crystals. Apparatus was constructed to grow single crystals on a sting under carefully controlled conditions and record the growth process with a digital imaging system. We believe it is imperative to study growth processes quantitatively in systems where crystals are allowed to grow to the size (larger than 0.1mm) where mass transfer effects could be important. These studies should include measurements of structure designed to ascertain whether or not there are changes associated with the growth rate itself. At present, we are ready to proceed with the experimental study and have arranged to collaborate with a protein crystallographer in Princeton's Chemistry Department.

SUMMARY & CONCLUSIONS

DENDRITIC CRYSTAL GROWTH IN THE PRESENCE OF CONVECTION

Background

Extant theories of crystallization deal primarily with diffusion controlled growth. However, experimental work on the crystallization of a model compound[1] shows that natural convection has a strong influence at low undercoolings. This is particularly vexing since low undercoolings are of interest when one seeks to establish a correspondence between theory and experiment for dendritic growth. Low undercoolings promote slow growth and crystals with large tips, which make photographic studies easier. Accordingly, it has been suggested that experiments in a microgravity environment would enable one to test theories under relatively quiescent conditions. Current theories omit convective transport, however, and it is clear that a general understanding of the role of convection is necessary. Indeed, natural convection is always present in the terrestrial environment and it might be advantageous to add forced convection to alter the growth process. The presence of convective transport makes the theory much more complicated, especially when the flow is generated by buoyancy driven motions due to the inevitable coupling between the equation of motion and the temperature (or concentration) field. Nevertheless, a rigorous theory which includes convective transport would be extremely useful. A theory describing the effects of forced convection is a logical step towards developing a comprehensive understanding.

Summary Of Completed Work

We studied situations where forced convection is aligned with the crystal axis. The detailed results of that study are contained in a PhD thesis by P. J. Beaghton. A paper on our steady state model was published in Physical Review A (copies of the thesis and the paper are appended to this report) and papers dealing with the steady state model and our tracking scheme were given at meetings of the American Physical Society Division of Fluid Dynamics and The American Institute of Chemical Engineers. Other papers are in preparation.

Ivantsov's theory deals with the growth of needle-shaped crystals in a pure, subcooled melt but no allowance is made for the effects of interfacial energy on the melting point (the Gibbs-Thompson effect) or convective heat transfer. Nevertheless, this theory depicts many features of the growth process correctly, so it is the logical vantage point from which to consider other factors. Recently, the influence of interfacial energy ("surface tension") and anisotropy have been studied and a theory known as "microscopic solvability" developed [2-6].

To investigate the influence of convection, we first looked into the steady state growth of an axisymmetric crystal. Using the integral equation describing growth of an isothermal crystal in the presence of forced convection aligned with the crystal axis, we uncovered a new set of steady, self-similar solutions analogous to those of Ivantsov, viz., paraboloids of revolution. Here the flow is represented by an exact solution to the Navier-Stokes equations in the Oseen approximation; the convective terms in the energy equation are taken into account rigorously. A relation between the growth rate, undercooling, and strength of the imposed flow was derived. It reduces to the Ivantsov result in the absence of convection. We calculated the effects of the flow strength on the Peclet number-undercooling relation and, as expected, there is a strong effect. To establish the relation between growth rate, tip radius, undercooling, and flow strength, however, another expression is needed, just as was the case with the Ivantsov theory.

To develop the second relation needed to set the tip speed we could have reworked the microscopic solvability theory (assuming it is the correct approach) in a form which includes convection. We did not do this. First, it is not yet proven that microscopic solvability will explain the selection of tip speeds and sizes observed experimentally; more experimental results are needed with materials having different degrees of anisotropy. In addition, it is not obvious that flow alters events on the submicroscopic scale of the capillary length in a significant fashion. It may be that microscopic solvability is unaffected. This is certainly an important issue but some understanding of the global character of the problem should be obtained first. Thus, our efforts are directed towards developing a numerical scheme in which convective transport and non-linear effects are taken into account so as to enable us to track large scale interface motion.

A rather general numerical algorithm was developed to compute the motion of an axisymmetric crystal. (The algorithm is described in Beaghton's PhD thesis.) For example, with the algorithm we can start a needle shaped crystal in the steady state configuration determined by diffusion and convection, add surface tension and track the system as it moves to its new steady state shape. This solution gives the shape of the interface and the relation between the various parameters in the presence of flow and capillary effects. Then the interface can be perturbed and the stability of the new state ascertained. Perturbations can also be added arbitrarily during the evolution.

Our numerical algorithm mitigates, to a substantial degree, the prohibitively large cost and storage requirements of other PDE solvers when applied to this sort of problem. The technique is based on the transformation of the transient convective-diffusion equation and the equations of motion for the fluid and the interface into a boundary integral problem.

Accordingly, the major part of the computational effort is the evaluation of integrals. Traditional PDE integration schemes such as finite differences or finite elements would require discretization of an infinitely large domain and the subsequent calculation of internal values of the temperature that are increasingly less relevant as one moves away from the solid-melt boundary. Our method is superior to the aforementioned techniques since the internal points can be distributed in an optimal fashion and efficient schemes are available to evaluate integrals. We recalculate the perturbed flow and temperature fields as the system evolves. Interface shape is calculated explicitly at each time step and regridding avoided.

Thus far we have:

Established that the computation method is "stable" and "converges" as the size of the time step is reduced and the number of points on the interface increased. In several tests we set the system on steady state solutions derived from either the Ivantsov theory or our convective theory. The system was then allowed to evolve (in time) without adding any sort of perturbation. The robustness of the algorithm was apparent from fact that the system stayed on the original solution.

Investigated the stability of the Ivantsov solution (which makes no allowance for interfacial energy or convection). Since this configuration is known to be unstable to infinitesimal perturbations it hardly comes as a suprise to find it unstable to finite amplitude perturbations.

Investigated the stability of interface shapes present when there is forced convection but no surface tension. They were unstable and small, finite amplitude perturbations grew without bound in the situations studied. Figure 1 illustrates the results of calculations in the absence of surface tension. Note the presence of "tip splitting".

Tracked the evolution from the Ivantsov solution to a state where the Gibbs-Thompson (interfacial tension or energy) effect was present. We also added anisotropy, in part. At present our algorithm is restricted to axisymmetric shapes, which precludes exact computation of anisotropic phenomena. Therefore we simply added a term analogous to that used in 2-dimensional calculations, i.e., the surface tension was made to depend on the angle between the local normal to the interface and the crystal axis. In the calculations done thus far the effect of this sort of "anisotropy" was small.

Investigated the stability of steady state solutions representing the effects of convection and surface tension. In the cases studied thus far, the system was stable to finite amplitude perturbations.

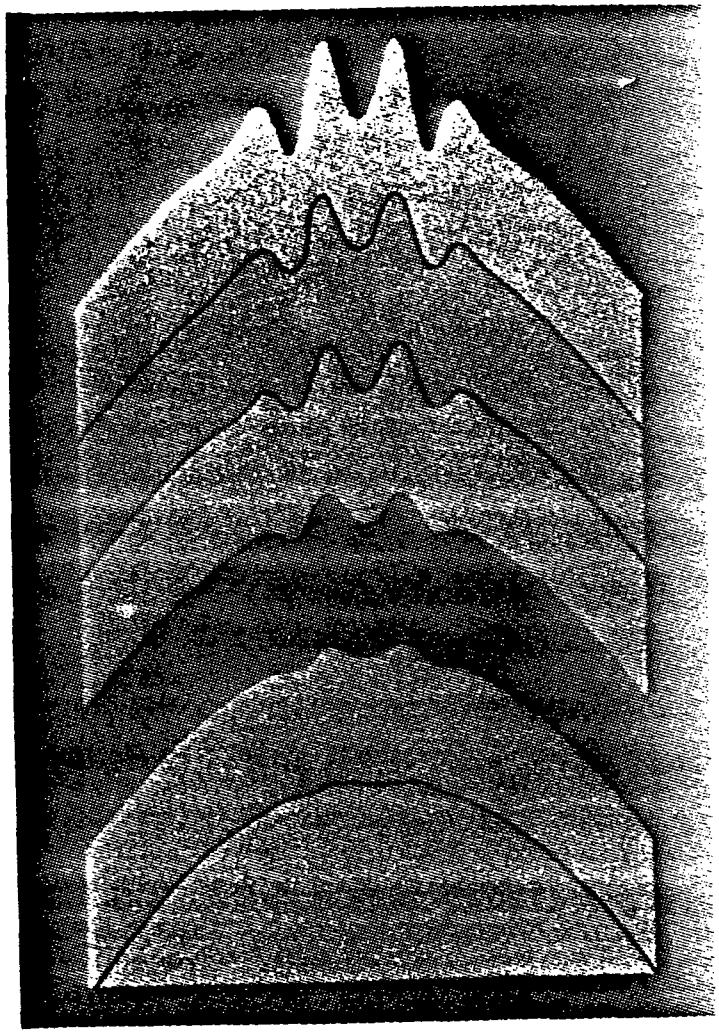

FIGURE 1 - A diagram showing evolution of a tip splitting instability on an axisymmetric crystal. Heat transfer is by diffusion and convection, surface tension is absent. The diagram was produced by the numerical algorithm that solves the time-dependent integral equation for the evolution of the crystal interface.

The Current State-Of-Affairs

We have constructed a new steady state theory which accounts for the effect of forced convection on dendritic growth. It shows that heat transfer by forced convection has a strong influence on quantitative aspects of dendritic growth but the qualitative features remain unchanged, i.e. the shape remains a paraboloid of revolution in the absence of the Gibbs-Thompson effect.

A new algorithm has been developed to track the non-linear evolution of a dendritic interface. The scheme accounts for effects of convection and surface tension with axisymmetric crystals. At present, we can study effects due to the strength of the external flow, the degree of supercooling, the amount of surface tension, and, in a somewhat ad hoc fashion, crystal anisotropy. However, only a relatively small number of situations have been investigated to date and we have not yet looked at regions very close to the tip of the dendrite in any detail. It should be possible to examine questions of "solvability" in a dynamic sense by computing the interface shape in more detail near the tip. Furthermore, the code can be expanded to cover non-axisymmetric growth by allowing for azimuthal variations in the shape of the interface and the velocity and temperature fields. This would allow us to account for anisotropy in a rigorous fashion.

PROTEIN CRYSTALLIZATION

Background

The crystallization of proteins is a key step in determining their molecular structure from x-ray crystallography, but the precise conditions under which a newly isolated protein will crystallize are unknown and must be found by trial and error over a wide range of pH, ionic strength, and protein concentration. Because proteins often form crystals which are too small or too disordered to diffract well, finding crystallization conditions is no guarantee that the resultant crystals will be suitable for x-ray analysis. It has been suggested that growth of suitable crystals is sometimes the limiting step in obtaining structural information[7]. Thus, if the reasons for such contrary behavior were known, it might be possible to optimize growth conditions to produce higher quality crystals for structure determination. Convection, in one form or another, has been observed to inhibit growth but results are still fragmentary [8]. If convection turns out to inhibit growth in general or alter crystals in other deleterious ways, then experiments in quiescent environments could lead to improved crystals. A microgravity environment, where convection and sedimentation are reduced compared to the terrestrial milieu, might provide a suitable venue.

An intensive study was begun by scientists at NASA and at several universities to see what advantages might accrue. The

overall effort is coordinated through Dr. Robert Snyder, Chief of the Biophysics Branch at MSFC. As the work unfolded, it was found that knowledge of the kinetics of protein crystallization is meager compared to that for inorganic crystals. For example, until recently there was no phase diagram for lysozyme, one of the most widely studied proteins, *or any other protein*. Hence a considerable part of the overall effort is devoted to very basic studies. Our study belongs to this class.

The work at Princeton was done by Mr. Marshall Grant, a PhD candidate. Because the field is moving rapidly, we kept in close contact with others working on the problem. An extensive presentation was made to NASA scientists and their collaborators on protein crystallization in March of 1987. The purpose of the meeting was to set out our plans to insure that we had a viable approach and would not duplicate work already in progress. The meeting was chaired by Dr. Snyder. Others in attendance were Dr. R. Naumann, Chief Scientist at the Space Science Laboratory, Dr. Charles Bugg, Director of the Center for Macromolecular Crystallography at the University of Alabama(Birmingham), Dr. Franz Rosenberger, Director of the Materials Research Center at the University of Alabama(Huntsville) and members of their research groups. Our plans were given strong endorsement. More recently (August of 1987), Dr. Marc Pusey of MSFC visited our laboratory to inspect the experimental set-up; Dr. Ray Salemme, a protein crystallographer at E. I. DuPont visited us in September to present a seminar and discuss our work.

The study of protein crystallization is difficult because protein molecules are extremely complex and there are strong intramolecular interactions in addition to interactions with solvent molecules and other proteins. It is often difficult to determine the state of a protein system because the physicochemical data (phase diagrams, activity coefficients, diffusion coefficients, state of aggregation, etc.) have either not been determined or have not been published. There are conflicts between data reported by different workers. For example, at pH 4, 20°C, and 50 mg/ml NaCl, the reported values for lysozyme solubility range from 1.7 mg/ml [9] to 4.3 mg/ml [10,11]. Pusey and Gernert [12] recently found that the solubilities of the orthorhombic and tetragonal forms are quite different, although differences between the molecular structures in the two forms are minor[13]. This lack of data makes it almost impossible to draw general conclusions regarding growth behavior and its relation to the quality of the resultant crystals. In the absence of verifiable relationships between system conditions and crystal properties, the protein crystallographer is forced to rely on intuition and repetition to obtain suitable crystals. Some proteins, moreover, have not yielded satisfactory crystals despite these efforts.

The small size and inherent disorder of protein crystals are two major concerns. A third, related, point is the question of conformation changes upon crystallization and their effect on protein crystal growth.

In the remaining part of this section we summarize results of an extensive survey made to clarify issues connected with the role of transport processes. Then we describe the apparatus constructed for our work.

Summary of Completed Work

Our initial effort focused on understanding why protein crystals grow slowly and terminate growth at relatively small sizes. Theoretical investigations were made of: (i) effects of fluid shear on protein binding; (ii) association of protein monomer in the bulk; (iii) salt gradients; (iv) contaminants; and (v) interface kinetics and mass transfer. The gist of our findings is described next; the full report is reproduced in the appendix.

Based on the experimental observation that crystals grown from stirred solutions tend to be smaller than those grown from quiescent solutions, crystallographers have recently sought to explain the small size of protein crystals in terms of various forms of convection. In particular, buoyancy-driven flows have attracted attention as a disruptive mechanism in protein crystal growth. We examined several scenarios wherein convective flows might interfere with the normal binding of protein molecules to the crystal surface and found that the fluid velocities which arise from density differences are too small to produce the proposed effects. Specifically, under "normal conditions" shear from natural convection appears insufficient: (i) to denature individual protein molecules or strip protein molecules from the crystal surface (the bond strength is too large to be affected by the relatively weak drag force); or (ii) to impose a preferred orientation on protein molecules at the surface (rotational diffusion quickly eliminates any bias due to shear).

Association of monomer may reduce concentrations significantly in the bulk and this would reduce growth rates but extant experimental techniques are not able to resolve the issue unambiguously. Salt gradients due to salt rejection at the crystal-fluid interface appear too weak to influence diffusion rates significantly. Contaminants which adsorb protein may reduce the protein concentration in the bulk significantly but experimental studies of contaminant effects are lacking.

As crystals grown in more-or-less quiescent environments get larger, the protein flux due to natural convection becomes much greater than the diffusive flux. At this point convective mass transfer effects may affect crystal growth. According to our calculations, previous work on protein crystal growth kinetics was done on crystals which were too small for convective effects to be significant insofar as mass transfer rates are concerned. Simply stated, it was shown that with the small crystals used in the quantitative studies, diffusion was so rapid that the interface concentration remained unchanged at the initial bulk

value throughout the growth period. Thus, the extant kinetic data do not indicate whether natural convection plays a role.

Nevertheless, experimental work by Pusey[8] shows an unambiguous effect of forced convection on the rate of growth of lysozyme crystals. We believe it is imperative to study growth processes quantitatively in systems where crystals are allowed to grow to the size (larger than 0.1mm) where mass transfer effects could be manifest. These studies should include measurements of structure designed to ascertain whether or not there are changes associated with the growth rate itself.

At this point we turned to the design and construction of apparatus to study the relation between growth rate, size and structure. The apparatus for this was purchased and assembled using funds from a Shell Foundation Institutional Grant to Princeton University.

Our intention is to examine the effect of crystal size on the growth and quality of a single crystal. Published experiments on the kinetics of protein crystal growth have been confined to crystals which are too small to exhibit significant size effects. The experimental procedure used to date (which involves introducing supersaturated protein solution into a sample cell, nucleating crystals on the sides of the container, and photographing the growing crystals) has severe limitations. First, only those crystals which are properly oriented with respect to the camera can be measured. Second, the crystals are often crowded so that the effects of neighboring crystals are significant and only average growth rates can be obtained. Finally, the surface of the sample cell probably alters the growth rate so that the behavior of an isolated crystal suspended in solution is still unknown.

We designed our experimental apparatus (Figures 2 and 3) to avoid the limitations listed above. Individual crystals are nucleated on a glass fiber "sting", which is then mounted on a microtranslator to provide "xyz" motion for positioning the crystal in the cell; a single rotator orients the crystal about the vertical axis. The sample cell is approximately 2 cm on a side to reduce wall effects. Once the crystal is in position, digitized images of the crystal can be captured at specific intervals using a video camera. This provides electronic, time sequenced images of the growing crystal. The capture time is 1/30 s and as many as six separate frames can be stored in the computer RAM and a video frame buffer. Writing each frame to disk can take about 10 seconds, but this does not present a serious limitation because most of our work will be in the size range where the time between images will be considerably longer than the disk access time. (This results from the combination of slow growth rates and relatively low magnification required to examine crystals larger than 100 microns in diameter.)

The Mitutoyo FS50 microscope and objectives are capable of magnifications between 2X and 100X with a minimum working

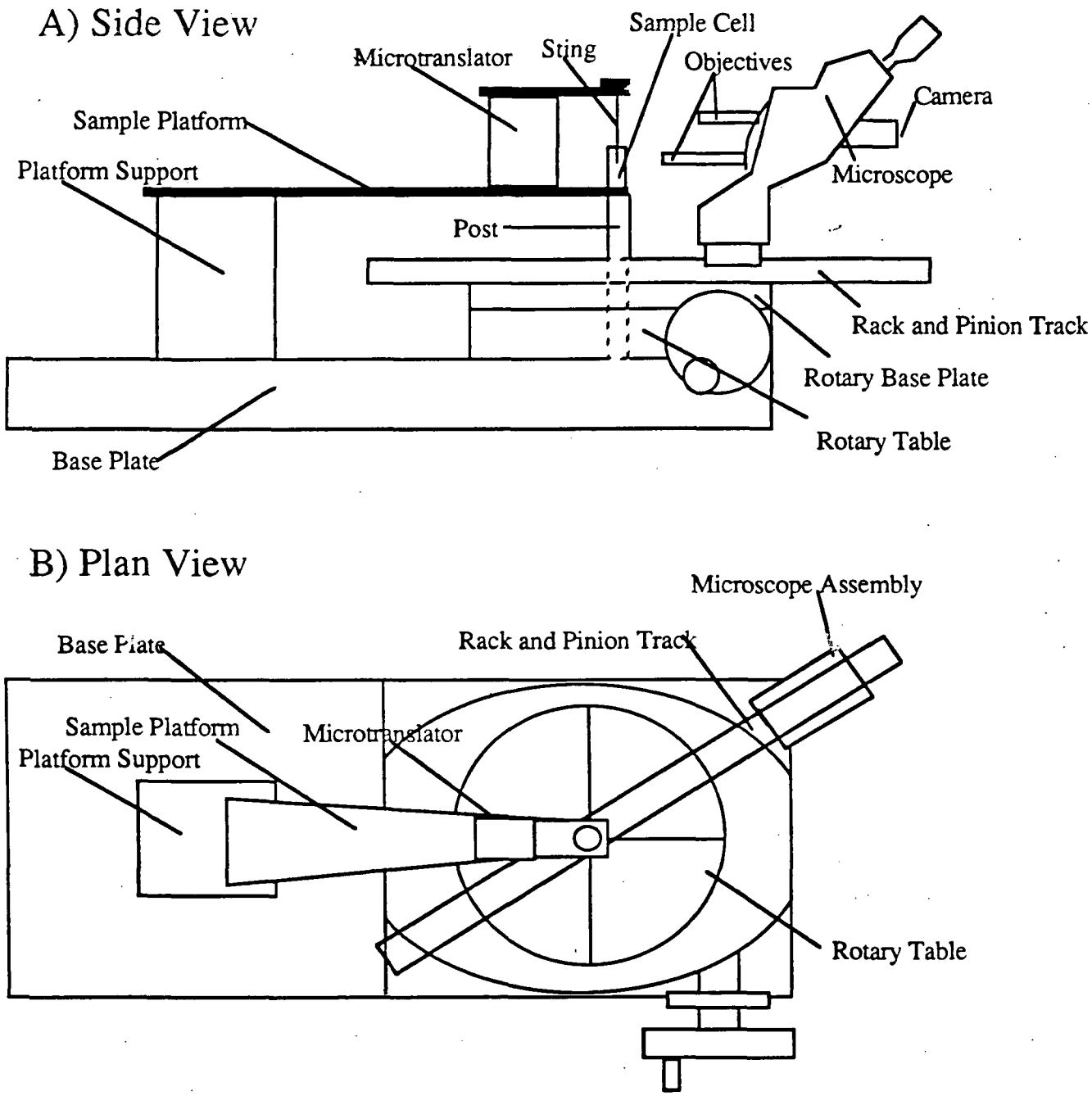

FIGURE 2 - Experimental apparatus for the protein crystal growth experiments.

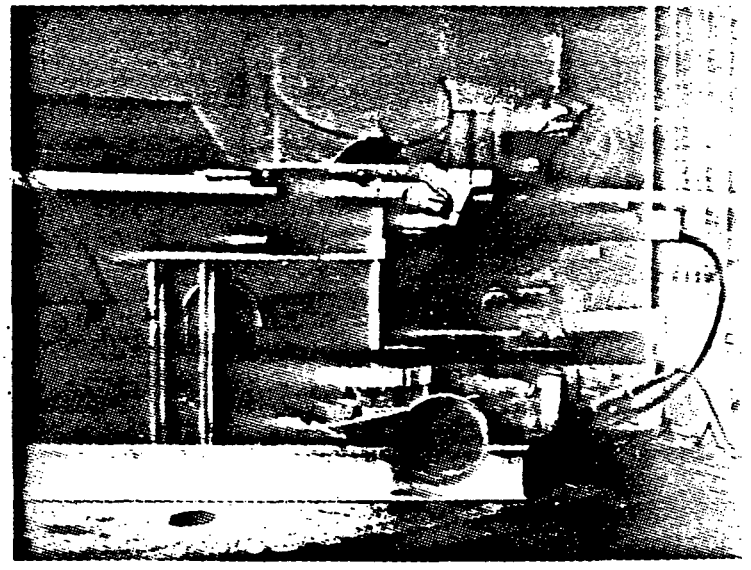

Growth Measurement Assembly

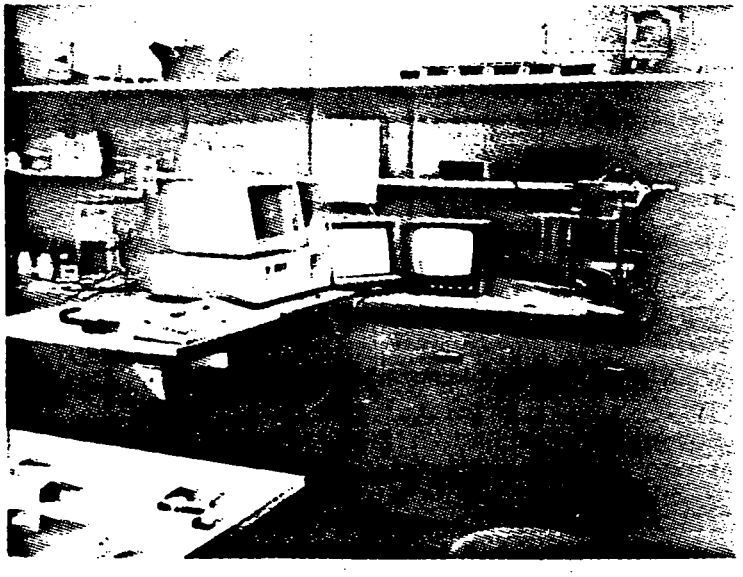

General Layout

FIGURE 3 - Photographs of the experimental equipment for protein crystal growth.

distance of 20.5mm. Thus, growth measurements of a crystal suspended in the chamber can be made without difficulty over the entire size range of interest. The microscope is mounted on a rack and pinion track to allow coarse focusing of the crystal image, while the microscope's focus adjustment will be used for fine focusing of the crystal image. A Hitachi KP-232 MOS camera sends the image to the video digitizing board (Matrox PIP-640) where it can be analyzed using an IBM PC-AT. An image of a 0.2mm lysozyme crystal which was digitized through a 5X objective is shown in Figure 4. Mounting the microscope track on a rotary table gives us the option of slowly rotating the microscope about the crystal so that measurements of different faces can be made in sequence. This feature is an improvement over the techniques of previous workers in that the growth of different faces of the same crystal can now be measured. The current design allows rotation through a minimum of 200 degrees of arc.

Temperature control utilizes a Lauda RMS-6 refrigerated circulator, which can control fluid temperature to within 0.01 degree K. The circulator pumps water through the sample cell as part of a cooling loop. (See Figure 5 for a schematic of the apparatus.) Reservoirs of protein/buffer solution and precipitant (salt)/buffer solution are immersed in the circulator's reservoir to maintain the temperature of the feed solutions. A peristaltic cassette pump supplies fresh solution to the growth cell in a once-through arrangement. Different concentrations of precipitant can be supplied by mixing salt solutions of different concentrations, while the total flow rate can be adjusted by changing the number of channels used to pump the solutions and by a flow control valve upstream of the growth cell.

The pH and ionic strength of the solution are monitored continuously using a computer interfaced to an Orion system which performs the actual measurement. At this time, there are no plans for active control of pH and ionic strength during the experiment.

The Current State-Of-Affairs

A careful study of the field shows that the protein crystals studied by previous experimenters were not large enough to exhibit mass transfer limitations, should they exist. Apparatus has been assembled which will allow us to study growth in a controlled environment and record and analyze crystal size using a video imaging system. With this apparatus single crystal growth rates can be measured over a range of crystal sizes.

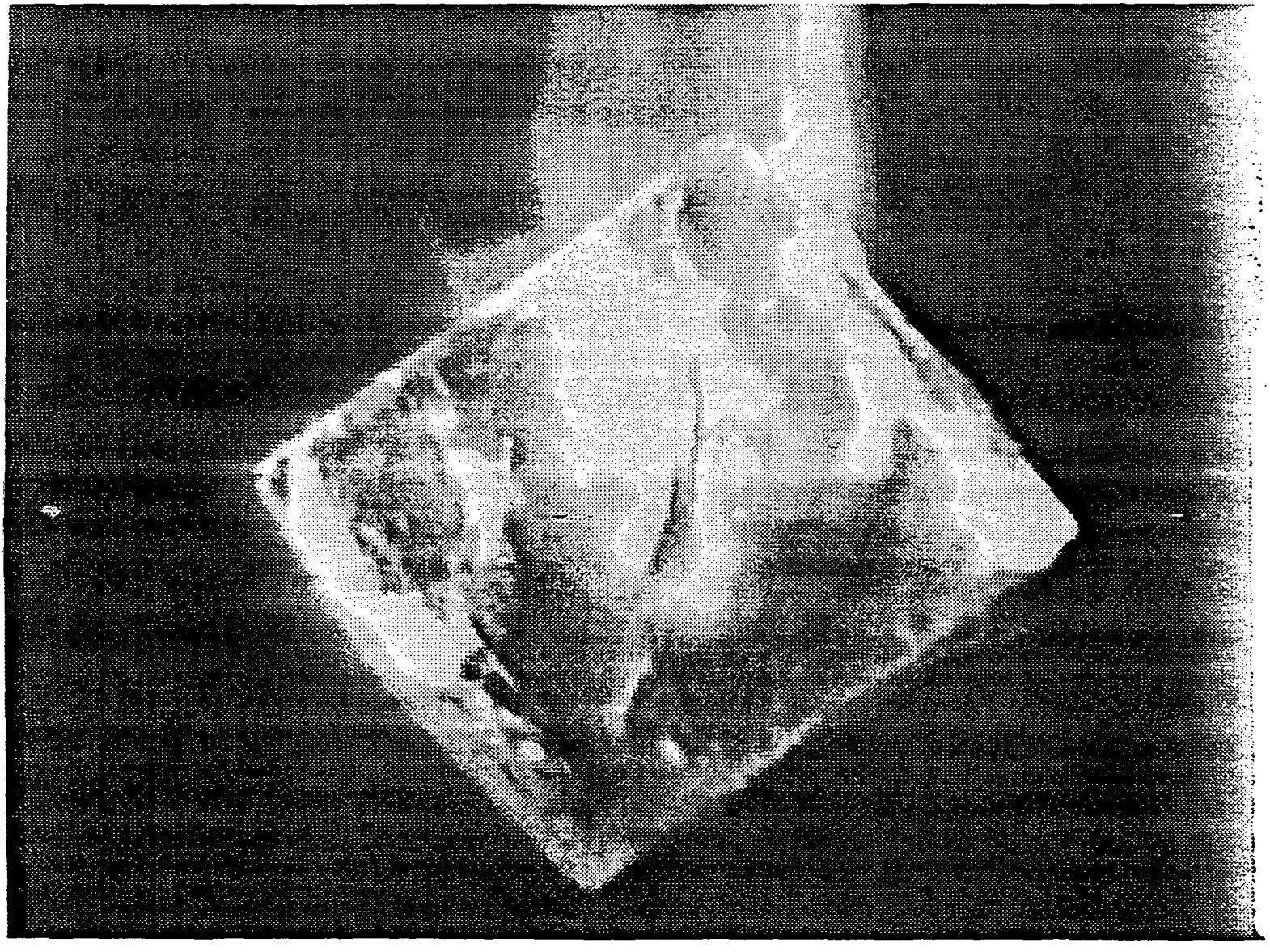

FIGURE 4 - A digitized image of a lysozyme crystal on the sting mounted in the apparatus shown in Figure 3.

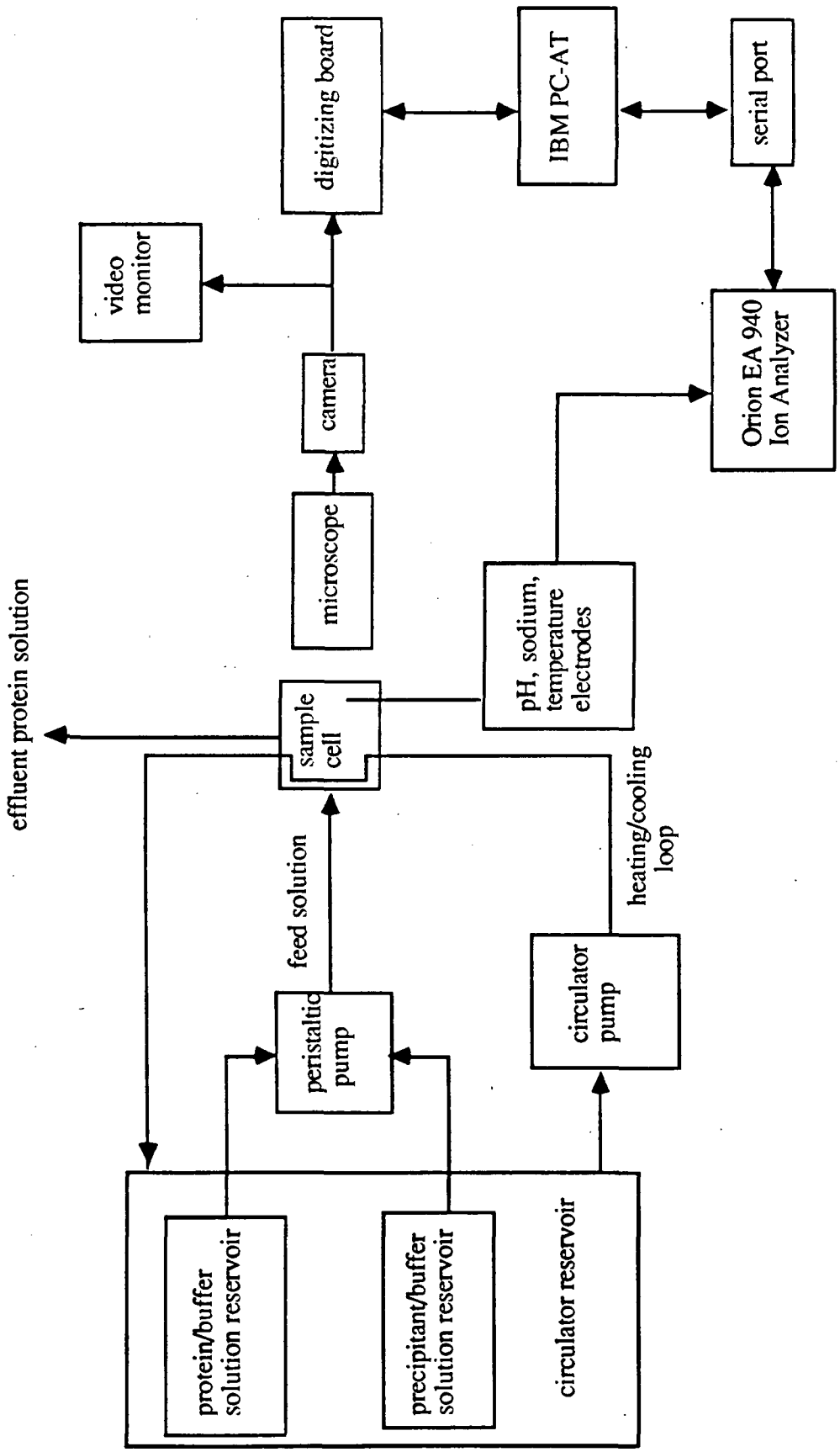

FIGURE 5 - A schematic of the experimental set-up for protein crystal growth.

RECOMMENDATIONS

CRYSTAL GROWTH IN THE PRESENCE OF CONVECTION

Recommendations for this portion of the work revolve around testing (and improving) the interface tracking algorithm. The work would provide a theoretical framework for evaluating experimental results on crystals grown in terrestrial or microgravity environments. This would lead to a computational algorithm which includes all the physics currently believed to influence crystal growth.

Specific topics for investigation are:

1. Exploration of the capabilities of the current algorithm.

   To date we have not covered a wide range of undercoolings, convective flow strengths, surface tension parameters, or other fluid properties. Thus, a general study of the program's capabilities is in order. In the process we would investigate the effect of flow on crystal shape and stability in some detail.

2. Expand the program so as to allow for fine scale resolution of the region near the dendrite tip.

   This is mainly a question of increased computer storage and execution time. First one should establish how much can be accomplished on the IBM 3081 mainframe and assess the advantages in moving to a supercomputer. The use of other systems would also be explored. Once this has been done we will be in a position to investigate "microscopic solvability" in the presence of convection.

3. Expand the algorithm to account for non-axisymmetric crystal shapes.

   Here again the limitation appears to be one of storage and execution time. We already do azimuthal integrations as part of the boundary integral technique so the extension should be relatively straightforward. This will allow us to include effects of crystal anisotropy on the surface tension.

PROTEIN CRYSTAL GROWTH

Here we present recommendations on how to determine relations between the quality of protein crystals, crystallization conditions, and protein properties. The experimental work would utilize apparatus described earlier. The program would establish certain fundamental aspects of protein crystal growth and forms an essential part of a broader effort aimed at assessing the advantages and disadvantages of growing protein crystals in a

microgravity environment.

Three related topics should be investigated. These are:

1. The Effect of Convective Mass Transfer on Protein Crystal Growth

   Crystal growth rates should be measured as a function of crystal size (which is equivalent to time) in order to determine if convection has an inhibitory effect on crystal growth. In some experiments the growth environment should be quiescent, in others forced convection will be present.

2. Studies on Crystal Disorder

   Crystals of different sizes should be examined using x-ray analysis to determine if there is a relation between crystal disorder and size. In particular, the evolution of crystal disorder should be studied to see if it can be related to growth conditions. Theoretical studies of crystal packing would indicate the effect of packing defects on solvation stabilization of the protein crystal.

3. Role of Conformation Change on Protein Crystal Growth

   The crystallization of a polypeptide, which is known to undergo large conformation changes upon crystallization, should be studied. The degree of similarity between the polypeptide's crystal growth behavior and that of a globular protein, which is not believed to undergo drastic conformation changes, would serve as an indication of the relative importance of molecular properties in determining crystal growth mechanisms.

REFERENCES

1. M. E.Glicksman and S. C. Huang Proc. 3rd European Symp. on Materials Science in Space, Grenoble, April 1979

2. J. S. Langer Phys. Rev. A 33, 435 (1986)

3. B. Caroli et. al. Phys. Rev. A 33, 442 (1986)

4. D. I. Merion Phys. Rev. A 33 2704 (1986)

5. D. A. Kessler et. al. Phys. Rev. A 33, 3352 (1986)

6. D. A. Kessler and H. Levine Phys. Rev. Lett. 57, 3069 (1986)

7. C. E. Bugg J. Crystal Growth 76, 535 (1976)

8. M. L. Pusey Personal Communication

9. M. L. Pusey and K. Gernert "A method for rapid liquid-solid phase solubility measurements" [submitted to J. Crystal Growth] (1987).

10. M. L.Pusey, R. S. Snyder and R. Naumann J. Biol. Chem. 261 6524 (1986).

11. Z. Kam, H. B. Shore and G. Feher J. Mol. Biol. 123 539 (1978).

12. G. Feher and Z. Kam Meth. Enzym. 114 77 (1985).

13. J. Berthot et. al. Proc. Roy. Soc. B217, 471 (1983).

14. Eisenberg, D. and A. D. McLachlan. Nature 319 199 (1986).

15. Sasaki, et. al Nature 257 751 (1975).

16. Karplus, M. and D. L. Weaver. Nature 260 404 (1976).

APPENDICES

BIBLIOGRAPHY OF THESES, PUBLICATIONS, AND PAPERS FROM NAG3-447

1. P. J. Beaghton Dendritic Growth in the Presence of Convection PhD Dissertation, Princeton University, January 1988 (145 pgs.)

2. D. A. Saville & P. J. Beaghton "Growth of needle-shaped crystals in the presence of convection" Phys. Rev. A 37 3423-3430 (1988).

3. M. L. Grant & D. A. Saville "Two Puzzling Aspects of Protein Crystal Growth" Interim report (28 pgs. + 6 figs.)

4. D. A. Saville & P. J. Beaghton "The effect of convection on the evolution of the dendritic crystal interface". Paper presented at the AIChE Annual Meeting, November 1987, New York.

5. D. A. Saville & P. J. Beaghton "The evolution of needle-shaped crystal interfaces in the presence of convection". Paper presented at the Annual Meeting of the Fluid Dynamics Division of the American Physical Society, November 1987, Eugene, Oregon.

DENDRITIC GROWTH
IN THE PRESENCE OF CONVECTION

by

Pantelis John Beaghton

A doctoral dissertation

submitted to the Department of Chemical Engineering, Princeton University,

in partial fulfillment of the requirement for the PhD degree.

January 1988

ACKNOWLEDGMENT

I would like to thank my advisor, Dudley A. Saville, for his guidance, advice, and patience during my years in Princeton. His enthusiasm has inspired my work, and his encouragement and support have helped me through the difficult moments.

I am appreciative of many fruitful and enjoyable discussions with Bill Russel and Roy Jackson. I am also grateful to Chris Floudas for the use of his computer facilities. Many thanks also to my friends, Mike, Kevin, Sanjib, Dimitri, Marshall and others, for the good times we shared. Finally, my love and warm thanks to Andrea, my best friend.

ABSTRACT

The motion of the freezing front between a dendritic crystal and a supercooled liquid is studied using an interface evolution equation derived from a boundary integral transformation of the transient convective-diffusion equation.

A new steady-state theory is introduced that incorporates the effects of convection in dendritic growth. It is shown that in the absence of capillary effects the shape of the crystal-melt interface is a paraboloid of revolution, similar to that found in situations where diffusion is the sole heat transfer mechanism. A relation between the supercooling, the product of the tip velocity and tip radius, and the strength of the flow is derived which reduces to the well-known Ivantsov theory in the absence of convection.

A non-linear interface-tracking algorithm is developed and used to study the temporal and spatial evolution of the dendritic interface. The important role of capillarity and convection on the interface dynamics is established and the response of the interface to finite amplitude disturbances is examined for the first time. Tip splitting is identified as the dominant destabilization mechanism in the limit of zero surface tension. Finite surface tension leads to interface stabilization, irrespective of the magnitude and structure of the external perturbations. Finally, convection significantly decreases the magnitude of the freezing velocity.

TABLE OF CONTENTS

CHAPTER 1: INTRODUCTION

The interrelation between non-equilibrium systems and complex growth forms was recognized long ago [1]. Over the past decade there has been renewed interest in the study of such systems and, in particular, processes of pattern formation in physical, chemical, and biological systems. Unfortunately, understanding phenomena as common as solidification or dendritic growth is hampered by the mathematical complexity of the problem and the subtle effects of microscopic mechanisms such as capillarity and interface attachment kinetics. Dendritic* growth, the formation of branched, tree-like structures, frequently appears in systems where an interface advances into a metastable phase such as a supercooled melt or a supersaturated solution. Often a needle-shaped tip propagates at a constant speed while sidearms appear continuously along the sides. The mathematical problem resembles the classical Stefan problem, where the diffusion equation for the temperature (or the solute concentration) must be solved with boundary conditions specified on the moving interface, the propagation velocity of which is determined by the heat (or solute) flux. On the other hand, important differences exist:

- The complex interface shape leads to mathematical problem that defies analytical solution.
- Natural convection due to thermal (or solutal) gradients destroys the mathematical simplicity of the diffusion equation necessitating a considerable increase in computational effort.

---

* from the Greek word $\delta\epsilon\nu\delta\rho o\nu$ (tree).

- The curved interface is not isothermal. Local deviations from the melting temperature of the crystal arise from the interaction between the interfacial energy and the local curvature of the solid-liquid interface (the Gibbs-Thomson relation). The capillary term leads to a singular perturbation problem which has only recently been identified [2-5].

Ivantsov's theory [6] is a cornerstone of our understanding of dendritic growth but deals only with situations where fluid motion and surface tension are absent. His theory describes a family of uniformly propagating "needle-crystals" in the form of isothermal paraboloids of revolution (or parabolas in two dimensions), characterized by the single relation between the dimensionless supercooling $\Delta = (T_M - T_\infty)c_p/L$ and the Péclet number $p = \rho V/2\alpha$. Here the tip radius is ρ, the tip velocity is V and α is the heat diffusivity of the melt. The difference between the melting temperature T_M and the bulk temperature T_∞ is scaled with the ratio of the latent heat of fusion, L, to the heat capacity, c_p.

The Ivantsov family of solutions is *degenerate:* for a given supercooling there exist an infinite number of paraboloidal solutions since only the product of the tip velocity and tip radius can be determined. In addition, linear stability analysis shows that the Ivantsov paraboloids are unstable to infinitesimal perturbations. The dominant destabilization mechanism is *tip splitting,* whereby the initially smooth tip splits into an increasing number of unstable fingers. This indeterminacy can be removed by introducing the effects of surface tension. According to the Gibbs-Thompson thermodynamic equation (derived in Appendix E), the (dimensionless) temperature of the solid-melt interface is given by $T_\Gamma = \Delta - (d_0/\rho)\mathcal{K}$, where $\mathcal{K}$ is the dimensionless local curvature and $d_0 = \gamma\, T_M c_p/L^2$ is a capillary length proportional

to the solid-liquid surface tension (see Appendix E). The first analysis of the effects of surface tension used the Ivantsov solution as a basic state and treated the capillary term in the Gibbs-Thompson boundary condition using a regular perturbation around the zero surface tension state [7]. For values of $\sigma \equiv d_0/(p\rho)$ greater than a critical value, σ^*, a continuous family of stable, modified Ivantsov dendrites was found.

The marginal stability hypothesis, developed by Langer and Müller-Krumbhaar [7], employs the linearized stability result along with *speculations* about the role of the non-linear effects. Every needle-shaped crystal displays sidebranches, i.e. dendritic growth, which is thought to be a result of non-linear processes. Tip splitting is supposed to be a phenomenon described by the linear theory whereas sidebranching is non-linear and therefore outside extant stability theories based on small amplitude (i.e. linearized) analyses. Accordingly, if we imagine a paraboloidal crystal growing into a supercooled melt, the operating point of the system (the tip radius and the tip speed that correspond to a given supercooling) would be set as follows. Suppose $\sigma > \sigma^*$, because either the tip is slender or the velocity small. Non-linear effects leading to sidebrances broaden the tip and σ decreases. If σ goes below σ^*, tip splitting occurs and forms more slender tips. This suggests that the natural operating point for the dendrite is determined by the marginally stable solution, $\sigma = \sigma^*$, which furnishes a second relation between ρ and V. Langer [8] acknowledges that the hypothesis is theoretically incomplete and a fully non-linear analysis is needed to test it.

Recent studies have focused on the subtle effects of surface tension on the mathematical structure of the problem. The curvature operator in the Gibbs-Thompson

equation contains higher order derivatives of the interface shape, multiplied by the very small coefficient (d_0/ρ). This leads to a singular perturbation problem with respect to the dimensionless capillary length (or the surface tension) and the interface shape cannot be represented as a regular perturbation about the Ivantsov steady-state. Since the capillary length d_0 is several orders of magnitude smaller than the tip radius ρ, the steady-state correction to the Ivantsov solution in the presence of surface tension is negligibly small. As a result, the marginal stability theory assumes that the smoothness of the Ivantsov solution is not affected by the inclusion of the capillary terms. However, a different approach is needed because the singular nature of the problem dictates the interface dynamics and the singular behavior is omitted from marginal stability. The recently developed *microscopic solvability* theory is implemented through numerical solution of the equations with the surface tension term taken into account rigorously near the tip.* The solution is joined onto the Ivantsov solution far from the tip, i.e., the surface tension correction to the shape is assumed to vanish as the crystal thickens (exponentially small corrections to the interface shape far from the tip are neglected). The microscopic solvability theory proposes the following:

a) For finite surface tension the steady-state correction to the Ivantsov solution is not smooth at the tip [2-5]. The numerical solution of an integral evolution equation shows that the resulting interface shapes have a sharp tip. However, cusp-like tips are not permitted by the diffusional kinetics that govern dendritic growth. In accordance to the microscopic solvability hypothesis, all admissible interface shapes should satisfy a mathematical solvability condition that requires a

* In contrast to the marginal stability analysis, the interface shape is *not* represented as a regular perturbation about the Ivantsov steady-state solution.

zero slope at the tip. The slope at the tip decays *exponentially* fast as surface tension approaches zero and the zero-slope-condition is only satisfied by the zero-surface-tension Ivantsov solution. This explains the failure of the regular perturbation analysis; the capillarity-induced correction is exponentially small and thus cannot be represented in terms of algebraic powers of the surface tension.

b) The microscopic solvability analysis also indicates that some finite degree of crystalline anisotropy produces dendrites with smooth tips [4,5]. The Gibbs-Thompson relation is modified to include the effects of surface tension anisotropy:

$$T_{\Gamma} = \Delta - (d_0/\rho)\,[1 - f(\theta_1, \theta_2)]\,\mathcal{K},$$

where θ_i represents the angle between the outward-pointing normal and the crystallographic axis i. The function $f(\theta)$, which in general depends on the geometric parameters of the crystal-melt interface, represents a measure of the surface tension anisotropy ($f = 0$ corresponds to isotropic surface tension). For sufficiently large amounts of anisotropy, there is always a discrete set of finite-surface-tension solutions that satisfy the microscopic solvability condition and thus have smooth tips [4,5].

c) Linear stability analysis shows that only the fastest growing dendrite is stable [9]. All the other members of the discrete set of allowed steady-states are unstable. As a consequence, the fastest growing mode represents the operating point of the dendrite.

The success of the microscopic solvability theory stems from its ability to determine a unique operating point for the dendrite. Nevertheless, a number of important fundamental issues are still unresolved:

- The sidebranch emission seems to be the result of the non-linear evolution of *finite* amplitude noise which cannot be incorporated in a linear stability analysis. Kessler and Levine argue that the tip instability in isotropic systems must be thought of as a non-linear instability [9]. They also state that sidebranching must be understood via a non-linear analysis of the amplification of finite noise as the disturbance moves away from the tip.
- In most of the theoretical work to date, the temperature (or solute concentration) field has been assumed to respond instantaneously to changes in the interface shape, which in turn implies that the diffusion equation can be solved in the "quasistatic" limit. This cannot be true for large supercoolings Δ where the diffusion length is comparable to the tip radius or the distance between sidebranches.
- There is as yet no evidence that the critical amount of anisotropic surface tension required to produce a unique, linearly stable, steady-state can be forced to remain constant as the interface evolves in time.
- Experiments in the low supercooling regime show that the sidebranch growth is orientation dependent and measured growth parameters such as the tip radius and the freezing velocity deviate from their pure diffusion predictions [10]. Existing dendritic growth models clearly cannot be used to study these important convective effects.

One of the reasons for the lack of a transient, convective-diffusion model of dendritic growth, aside from the computational difficulties to be described later, is the remarkable success of the quasistatic Ivanstsov theory. This simple theory remains,

despite its limitations, a valuable starting point since it accurately predicts the relationship between supercooling and Péclet number for a wide range of *moderate* to *large* supercoolings. Furthermore, the shape of a real dendritic tip region is unmistakably paraboloidal as in the Ivantsov theory. Sidebranches are encountered only after one moves five or ten tip radii away from the nose of the dendrite.

On the other hand, even under carefully controlled experimental conditions, thermal gradients in the melt generate buoyancy-driven flows which disturb the diffusion-dominated temperature profiles. Experiments by Glicksman and Huang [10] show how convection alters the morphology of the crystal and imposes an orientation dependence on the growth parameters. Figures 1 and 2 depict the tip velocity and the tip radius they measured with pure succinonitrile dendrites. The deviation from the pure diffusion predictions is clear at low supercoolings. Figure 3 shows the effect of convection on the morphology of the dendrite. The temperature field is severely distorted and an orientation-dependent elimination of sidebranches occurs. Although the purely diffusive Ivantsov theory can be applied to predict the experimentally measured Péclet number for supercoolings higher than 1°C (or, in dimensionless form, $\Delta > 0.05$), there is a strong deviation from the Ivantsov solution for smaller undercoolings (Fig. 4). Given these striking experimental results, it is worth considering how convection alters the theory. Convection has not been treated in theoretical work to date for several reasons*. The basic reason is the computational difficulty. The boundary integral formulation of the problem,

* McFadden and Corriell [11] recently extended the Ivantsov solution to include the effect of a flow field due to a density difference between the two phases. Their analysis, however, does not apply to motion driven by other forces and will not account for the orientation dependence of the experimentally grown crystals or explain the low supercooling deviation from the pure diffusion theory.

used almost exclusively in recent years, loses much of its simplicity when fluid flow is added since domain integrals are required to describe the effects of convection in the melt. In addition, the shape of the tip region remains paraboloidal, even for very small supercoolings, and this may have prompted investigators to neglect any heat transport mechanism that might destroy the paraboloidal symmetry of the pure diffusion case.

The primary objective of this work was to incorporate convection in a transient, three-dimensional dendritic growth model based on the convective heat diffusion equation without any *ad hoc* approximations. A new steady-state theory was developed that shows convection is compatible with the paraboloidal shape of the interface. This "convective" steady-state solution was then used as a starting point for a non-linear interface tracking algorithm. The numerical scheme solves an integral evolution equation for the interface shape and the Oseen hydrodynamic equation for the flow velocity simultaneously. Representative results indicate that capillarity and convection play important roles in the dynamics of dendritic growth.

This thesis is structurally divided in two major parts: a steady-state analysis of the convective effects is presented in Chapter 2 and a non-linear scheme tracking the interface evolution is presented in Chapter 3. The details of the mathematical derivations can be found in Appendices A-E.

In Chapter 2, a complement to Ivantsov's theory is presented to provide a basis for more detailed investigations where convection is present. In natural convection the temperature field is coupled to the equation of motion through the buoyancy term, which makes the problem all but intractable for most interface shapes unless one resorts to numerical methods to solve the partial differential equations. Thus,

a simpler flow, such as forced convection past a paraboloid of revolution, is used to express the salient effects of convection on the solidification front.

The velocity field used here is that for flow directed parallel to the axis of a paraboloidal crystal. An exact solution to the equations of motion in the Oseen approximation is used to represent the flow so that viscous and pressure forces are balanced with a small contribution from inertia. In Sec. 2.1 the integral equation that represents the interface shape is analyzed. Capillary effects are ignored, so the interface is isothermal. It is shown that uniformly-translating paraboloidal solidification fronts are admissible solutions. Then, an expression is given relating the supercooling to the Péclet number and the strength of the flow. The application of the steady-state analysis to the experimental system used by Glicksman and Huang [10] is discussed in Sec. 2.2.

In Chapter 3, a non-linear interface tracking scheme based on a boundary integral transformation of the transient convective-diffusion equation is introduced. With this algorithm all the unresolved issues can be addressed and the validity of "steady-state" results, such as the macroscopic solvability hypothesis, can be tested with a fully transient, non-linear calculation.

Boundary integral equations have received increased usage over the last few years*. These equations are very useful when evolution of a boundary is to be calculated, because, in contrast to treatments using partial differential equations, the solid-liquid interface discontinuity is embedded in the singular kernel of the integral equation and there is no need to divide the domain in two or more regions.

* Because of the range of problems, reports in the scientific literature are widely scattered. However, a useful treatise on boundary integral methods and their applicability to the solution of transport problems has been compiled by Brebbia *et al.* [12].

Recent steady-state models of dendritic growth make use of the integral equivalent of the diffusion equation to obtain the crystal-melt interface shape. The formulation presented here, although based on similar principles, actually represents a scheme for tracking the interface shape as it evolves in time and space. The presence of the convective term, which represents the effects of fluid flow in the melt, increases the dimensionality of the integral equation and requires special treatment. The problem must be solved numerically, and since the integral kernel is a non-linear function of the interface shape, Newton's iteration method is used to obtain the position of the interface at each time step.

The results presented in this thesis cover the moderate and high supercooling regimes and apply only to interface shapes that are single-valued functions of the radial coordinate. A summary of conclusions follows:

(i) The tip is unstable to *finite* amplitude perturbations if surface tension is absent, irrespective of flow strength. Given the results from the linearized theory without flow, this is not surprising. But it is important to know that the destabilization mechanism appears to be tip splitting. Noisy interface perturbations seem to invariably focus themselves on the tip region and incipient sidebranches are not seen.

(ii) Surface tension, however small, appears to stabilize the crystal interface for any flow strength. A steady-state is always reached, irrespective of the structure or the magnitude of the initial perturbation on the interface shape. The growth velocity of the dendrite decreases with increasing surface tension but the difference from the zero surface tension case is small. Convection is found

to significantly decrease the magnitude of the growth velocity but has no qualitative effect on the stability of the interface.

(iii) Anisotropy does not appear to have an important effect, qualitatively or quantitatively, on the dynamics of the interface. However, fully-three-dimensional (i.e., non-axisymmetric) perturbations will need to be tested before a complete understanding of the role of anisotropy can be gained.

(iv) The operating point of the dendrite is not established from the non-linear analysis presented here. However, the results of the analysis call into question all those obtained with the linearized theories now extant. Consider, first, the marginal stability hypothesis. Given the robust stability of shapes investigated here, it appears that the marginal stability hypothesis is wrong. The surface-tension adjusted shapes are found to be stable to finite amplitude perturbations. Thus, the central feature of marginal stability, a critical value of σ, simply does not exist when surface tension is considered in the context of finite amplitude effects. Second, microscopic solvability appears incomplete, at best. All the shapes investigated in this work are *stable* when finite amplitude effects were considered. Yet one feature of microscopic solvability is that only the fastest growing, smooth tip is stable. If this conclusion holds when finer resolution is considered at the tip, then the operating point selection mechanism is even more subtle than the microscopic solvability would suggest.

The outline of Chapter 3 is as follows. The formulation of the boundary integral equation for the interface shape is presented in Sec. 3.1.a. This evolution equation can be used to model growth under the most general conditions and is directly extendable to solute-transfer governed dendritic growth. An optimal set

of numerical discretization points, based on Gaussian quadrature formulae, is introduced in Sec. 3.1.b. and the boundary integral equation is transformed into a set of non-linear algebraic equations. The Oseen equation is also transformed in a boundary integral equation which is solved numerically for the velocity around the perturbed dendrite (the geometric complexity of the dendritic interface posed a challenging computational problem that was successfully handled by the integral formulation of the hydrodynamic equation). Sec. 3.2.a covers the numerical tests that show the excellent convergence characteristics of the numerical scheme. Representative results showing the profound effects of capillarity and convection are presented in Sec. 3.2.b. The role of anisotropy in the growth dynamics is discussed in Sec. 3.2.c. In addition, some ideas for future development are presented, including three-dimensional calculations to test the transient validity of the microscopic solvability hypothesis and a finer length scale for the tip region at low supercoolings.

The core of the mathematical derivations is presented in Appendices A through D. The appendices represent an integral part of this thesis and are grouped at the end of the manuscript for easy access. Appendix A contains the derivation of the integral evolution equation for the interface. The next two appendices highlight the difficulties associated with the numerical solution of integral equations. A series of variable transformations is employed and the integrals are finally transformed into finite sums. The temporal discretization of the boundary integrals is presented in Appendix B, while Appendix C describes their spatial discretization. The fluid velocity around the perturbed interface is calculated in Appendix D. The hydrodynamic equation is transformed to an integral equation which is solved numerically

using the boundary element method. The Gibbs-Thompson thermodynamic equation is derived in Appendix E. Figures and a listing of the FORTRAN code are presented in Appendices F and G. respectively.

REFERENCES

[1] D' Arcy Thompson, On Growth and Form (Cambridge University, Cambridge, 1917).

[2] J. S. Langer, Phys. Rev. A 33 (1986) 435.

[3] B. Caroli, C. Caroli, B. Roulet, and J. S. Langer, Phys. Rev. A 33 (1986) 442.

[4] D. I. Meiron, Phys. Rev. A 33 (1986) 2704.

[5] D. A. Kessler, J. Koplik, and H. Levine, Phys. Rev. A 33 (1986) 3352.

[6] G. P. Ivantsov, Dokl. Akad. Nauk SSSR 58 (1947) 567.

[7] J. S. Langer and H. Müller-Krumbhaar, Acta Metall. 26 (1978) 1697.

[8] J. S. Langer, Rev. Mod. Phys. 52 (1980) 1.

[9] D. A. Kessler and H. Levine, Phys. Rev. Lett. 57 (1986) 3069.

[10] M. E. Glicksman and S. C. Huang, Proc. 87th Natl. AIChE Meeting, Boston, August 1979; M. E. Glicksman and S. C. Huang, Proc. 3rd European Symp. on Material Sciences in Space, Grenoble, April 1979; S. C. Huang and M. E. Glicksman, Acta Metall. 29 (1981) 701.

[11] G. B. McFadden and S. R. Coriell, J. Crystal Growth 74 (1986) 507.

[12] C. A. Brebbia, J. C. F. Telles, and L. C. Wrobel, Eds., Boundary Element Techniques (Springer-Verlag, Berlin, 1984).

CHAPTER 2: STEADY-STATE THEORY

A new steady-state theory is introduced that incorporates the effects of convection in dendritic growth. It is shown that in the absence of capillary effects the shape of the crystal-melt interface is a paraboloid of revolution, similar to that found in situations where diffusion is the sole heat transfer mechanism. A relation between the supercooling, the product of the tip velocity and tip radius, and the strength of the flow is derived which reduces to the well-known Ivantsov theory in the absence of convection.

2.1. Development of the theory

Consider the steady uniform propagation of an isothermal solid-liquid interface with a constant freezing velocity $V\mathbf{i}_z$, as illustrated in Fig. 5. Densities of solid and liquid are assumed to be identical. In a frame of reference traveling with the front velocity V, the steady temperature field in the supercooled melt is governed by the convective-diffusion equation:*

$$\alpha\tilde{\nabla}^2\tilde{T} + V\frac{\partial\tilde{T}}{\partial\tilde{z}} = \tilde{\mathbf{v}}\cdot\tilde{\nabla}\tilde{T}, \tag{2.1}$$

where $\tilde{\mathbf{v}}$ is a steady flow field that satisfies the incompressible Navier-Stokes equations and the no-slip and mass conservation conditions on the solid-liquid interface. Since interface motion does not generate convection unless there is a density difference between the solid and liquid phase, $\tilde{\mathbf{v}} = 0$ in the absence of an externally imposed flow.

Capillary effects are neglected and the entire solid is assumed to be at its melting temperature T_M, while the bulk liquid phase is supercooled at T_∞. The

* The convective term $V\frac{\partial\tilde{T}}{\partial\tilde{z}}$ arises from the motion of the coordinate system.

heat conservation condition at the interface $\tilde{z} = \tilde{\zeta}(\tilde{x}, \tilde{y})$ reduces to

$$\frac{L}{c_p} V n_{\tilde{z}} = -\alpha \tilde{\nabla} \tilde{T} \cdot \hat{\mathbf{n}}, \tag{2.2}$$

where $\hat{\mathbf{n}}$ is the outward unit normal with $n_{\tilde{z}}$ as its $\tilde{z}$-component (in the zero-surface-tension limit, and in the absence of interior heat sources or sinks, the entire solid is isothermal).

Next, introduce a dimensionless temperature $T = (\tilde{T} - T_\infty)c_p/L$ and a dimensionless velocity $\mathbf{v} = \tilde{\mathbf{v}}/U_\infty$, and scale the lengths with $2\alpha/V$. In terms of dimensionless variables the equations are:

$$\nabla^2 T + 2\frac{\partial T}{\partial z} = 2\lambda\, \mathbf{v} \cdot \nabla T, \tag{2.3}$$

$$\nabla T \cdot \hat{\mathbf{n}}\big|_{z=\zeta(x,y)} = -2n_z\ , \tag{2.4}$$

$$T\big|_{z=\zeta(x,y)} = \Delta\ , \tag{2.5}$$

where $\lambda = U_\infty/V$; U_∞ represents the characteristic flow velocity. The interface $z = \zeta(x, y)$ and the solid are now at the temperature $\Delta \equiv (T_M - T_\infty)c_p/L$ (the dimensionless supercooling), whereas the dimensionless temperature goes to zero as $z \to \infty$.

The problem stated above can be cast in terms of integral equations. However, since the analysis is lengthy, it is presented in its entirety in Appendix A. Equation (A13) is a reformulation of the problem in terms of the integral evolution equation for the interface shape $\zeta(x, y)$:

$$\Delta = \int_{-\infty}^{\infty} dx' \int_{-\infty}^{\infty} dy'\, 2G_{ss}(\mathbf{x}_\Gamma, \mathbf{x}'_\Gamma) - \lambda \int_{-\infty}^{\infty} dx' \int_{-\infty}^{\infty} dy' \int_{\zeta(x',y')}^{\infty} dz'\, 2G_{ss}(\mathbf{x}_\Gamma, \mathbf{x}')\, \mathbf{v}(\mathbf{x}') \cdot \nabla T(\mathbf{x}')\ , \tag{2.6}$$

where $\mathbf{x} = (x, y, z)$ and $\mathbf{x}_\Gamma = (x, y, \zeta(x, y))$. $G_{ss}(\mathbf{x}, \mathbf{x}')$ denotes the Green's function corresponding to steady heat diffusion due to a point source at $\mathbf{x}$ in the reference frame moving with velocity V. In the pure diffusion problem $\lambda = 0$, so the temperature field is represented by an integral superposition of point heat sources along the solid-liquid interface ζ. The boundary temperature Δ can then be expressed in terms of two-dimensional integrals despite the three-dimensional structure of the temperature field. This reduction of the dimensionality of the problem makes the integral formulation very convenient when investigating interface motion if convection is absent.

The integral representation of the convective-diffusion equation involves integration over the entire fluid domain. (In the limit of pure diffusion, the second term on the right-hand-side of Eq. (2.6) vanishes). This increase in the dimensionality of the integral equation is due to the lack of appropriate Green's functions for partial differential equations with variable coefficients. Nevertheless, a scheme based on the integral formulation has many computational advantages over other methods even when there is flow in the melt.

The integral expression is now used to search for uniformly translating interface shapes in the presence of fluid flow. Experiments in the "convective" regime (low supercoolings) suggest that the tip region remains paraboloidal even when the characteristic flow velocity is much larger than the freezing velocity. Thus one needs to look for a class of temperature fields (and the corresponding flow fields) that satisfies the integral equation in cases where the interface is a paraboloid of revolution, viz.,

$$z = \zeta(x, y) = \frac{p}{2}\left(1 - \frac{x^2 + y^2}{p^2}\right) . \tag{2.7}$$

Here the Péclet number, p, can be viewed as the dimensionless radius of curvature at the tip of the paraboloid.

The search for interface shapes is patterned after Pelce and Pomeau [1], who used elementary variable transformations to show that the integral

$$\int_{-\infty}^{\infty} dx' \int_{-\infty}^{\infty} dy' \, 2G_{ss}(\mathbf{x}, \mathbf{x}')$$

is *independent* of $\mathbf{x} = (x, y, z)$ if both $\mathbf{x}$ and $\mathbf{x}'$ represent points on the same paraboloidal interface ζ, i.e. $\mathbf{x} = (x, y, \zeta(x, y))$ and $\mathbf{x}' = (x', y', \zeta(x', y'))$. Their result was used to demonstrate that the Ivantsov paraboloid is a solution of the pure diffusion equation and it can also be used to show that the integral

$$\int_{-\infty}^{\infty} dx' \int_{-\infty}^{\infty} dy' \, 2G_{ss}(\mathbf{x}, \mathbf{x}')$$

is independent of $\mathbf{x}$ when $\mathbf{x}$ and $\mathbf{x}'$ represent points on two different confocal paraboloids, such as those represented by Eq. (2.7) for two different Péclet numbers. Using Pelce and Pomeau's result, one can produce a class of temperature fields compatible with a paraboloidal interface shape. Since the left hand side of Eq. (2.6) is independent of the position vector $\mathbf{x}_\Gamma$, one must show that the right-hand-side can also be independent of $\mathbf{x}_\Gamma$ under certain assumptions about the nature of the temperature and flow fields. The first integral in the right-hand-side of Eq. (2.6) represents the contribution of diffusion and has already been shown by Pelce and Pomeau to be independent of the interface position vector $\mathbf{x}_\Gamma$ as long as $\mathbf{x}_\Gamma$ represents the same paraboloid as $\mathbf{x}'_\Gamma$. The second integral in Eq. (2.6), which comes from the convective term of the governing equation, must be shown to be independent of the position vector $\mathbf{x}_\Gamma$ as $\mathbf{x}_\Gamma$ traverses the paraboloidal interface ζ.

Let

$$I_c = \int_{-\infty}^{\infty} dx' \int_{-\infty}^{\infty} dy' \int_{\zeta(x',y')}^{\infty} dz'\, 2G_{ss}(\mathbf{x}_\Gamma, \mathbf{x}')\, \mathbf{v}(\mathbf{x}') \cdot \nabla T(\mathbf{x}')$$

be the convective contribution to the integral expression (2.6). Since paraboloidal shapes are under study it is convenient to introduce a paraboloidal coordinate system (diagrammed in Fig. 5):

$$\left\{ \begin{array}{l} w = \dfrac{z + \sqrt{x^2 + y^2 + z^2}}{p} \\ s = \dfrac{-z + \sqrt{x^2 + y^2 + z^2}}{p} \\ \varphi = \arctan \dfrac{y}{x} \end{array} \right\} .$$

In this new coordinate system, the interface defined by Eq. (2.7) is represented by the surface $w = 1$; $z \to \infty$ is equivalent to $w \to \infty$. Conversely, the surface $w = a$ represents a paraboloid confocal to $w = 1$ with a dimensionless tip radius $p' = ap$. The integral I_c becomes

$$I_c = \int_0^{2\pi} d\varphi' \int_0^{\infty} ds' \int_{w'=1}^{\infty} dw'\, p^3 \frac{s' + w'}{2} G_{ss}(\mathbf{x}_\Gamma, \mathbf{x}')\, \mathbf{v}(\mathbf{x}') \cdot \nabla T(\mathbf{x}') . \qquad (2.8)$$

If

$$p^3 \frac{s' + w'}{2} \mathbf{v}(\mathbf{x}') \cdot \nabla T(\mathbf{x}') \equiv \hat{A}(s', \varphi', w') \qquad (2.9)$$

were independent of s' and φ', (this will be shown to be true for a certain class of flows later) then Eq. (2.8) could be rewritten as

$$I_c = \int_{w'=1}^{\infty} dw' \frac{2}{p^2 w'} \hat{A}(w') \int_0^{2\pi} d\varphi' \int_0^{\infty} ds' \frac{p^2 w'}{2} G_{ss}(\mathbf{x}_\Gamma, \mathbf{x}') . \qquad (2.10)$$

Once this is done, the integrals with respect to s' and φ' can be rewritten in terms of x' and y' using the following coordinate system transformation

$$\int_0^{2\pi} d\varphi' \int_0^{\infty} ds' \frac{p^2 w'}{2} f(s', \varphi', w' = w') = \int_{-\infty}^{\infty} dx' \int_{-\infty}^{\infty} dy'\, g(x', y', z' = \zeta(x', y'))$$

where $w' = w'$ denotes that $f(s', \varphi', w')$ is calculated along a paraboloidal surface of constant w', and $g(s', \varphi', w')$ is the equivalent of $f(x', y', \zeta)$ in the paraboloidal coordinate system. Eq. (2.10) becomes

$$I_c = \int_{w'=1}^{\infty} dw' \, A(w') \int_{-\infty}^{\infty} dx' \int_{-\infty}^{\infty} dy' \, G_{ss}(\mathbf{x_\Gamma}, \mathbf{x}') \,, \tag{2.11}$$

where

$$A(w') = \frac{2}{p^2 w'} \hat{A}(w')$$

$$\mathbf{x}' = (s', \varphi', w') = \left(x', y', z' = \frac{pw'}{2} \left(1 - \frac{x'^2 + y'^2}{(pw')^2} \right) \right)$$

and

$$\mathbf{x_\Gamma} = (s, \varphi, w = 1) = \left(x, y, z = \frac{p}{2} \left(1 - \frac{x^2 + y^2}{p^2} \right) \right) .$$

For every value of w', $\mathbf{x}'$ and $\mathbf{x}$ represent two confocal paraboloids with a ratio of tip radii equal to w'. The extended result of Pelce and Pomeau therefore applies directly to the integrals over x' and y' in Eq. (2.11), i.e., for a given paraboloidal surface w' the integral does not depend on the position vector $\mathbf{x_\Gamma}$ as it moves along that surface. A final integration with respect to w' shows that the the convective integral in Eq. (2.6) is independent of the interface position vector $\mathbf{x_\Gamma}$ (which represents the paraboloidal surface ζ) as long as the quantity $A(s', \varphi', w')$ is a function of w' alone.

To identify a situation where $A(s', \varphi', w')$ is independent of s' and φ', consider the uniform propagation of a paraboloidal freezing front in the presence of a flow field with a far-field uniform velocity $-U_\infty \mathbf{i}_z$ in the direction of the axis of the

paraboloid, Fig. 5. The fluid velocity $\mathbf{v}$ satisfies the no-slip condition on the solid-liquid interface (note that in the moving reference frame, $\mathbf{v}$ does not include the uniform velocity $-V\mathbf{i}_z$ which is simply an artifact of the coordinate transformation.)

Uniform flow past paraboloids of revolution (or parabolas, in two dimensions) has been studied by a number of authors and Davis and Werle [2] showed that the solution to the Oseen equation

$$-\frac{2\lambda}{Pr}\frac{\partial \mathbf{v}}{\partial z} = -\nabla P + \nabla^2 \mathbf{v} \tag{2.12}$$

is a uniformly valid approximation* to solutions of the Navier-Stokes equations for small Reynolds numbers, $Re = \rho U_\infty/\nu = 2p\lambda/Pr$, where ν is the kinematic viscosity and $Pr \equiv \nu/\alpha$ is the Prandtl number. Wilkinson [3] derived an analytical expression for the Oseen flow velocity $\mathbf{v} = (v_w, v_s, v_\varphi)$ past a paraboloid in a uniform stream parallel to its axis. In paraboloidal coordinates the velocity is

$$v_w = \frac{1}{\sqrt{w+s}}\left[\frac{e^{-\Lambda} - e^{-\Lambda w}}{\Lambda\sqrt{w}E_1(\Lambda)} + \sqrt{w}\,\frac{E_1(\Lambda w) - E_1(\Lambda)}{E_1(\Lambda)}\right], \tag{2.13a}$$

$$v_s = -\frac{\sqrt{s}}{\sqrt{w+s}}\,\frac{E_1(\Lambda w) - E_1(\Lambda)}{E_1(\Lambda)}, \tag{2.13b}$$

$$v_\varphi = 0, \tag{2.13c}$$

where E_1 is the exponential integral of first order and $\Lambda = \lambda p/Pr$. On the surface $w = 1$ $(z = \zeta)$, $v_w = v_s = 0$, whereas for $w \to \infty$ $(z \to \infty)$, $v_w = -1$ and $v_s = 0$.

The introduction of paraboloidal coordinates yields

$$w\frac{\partial^2 T}{\partial w^2} + s\frac{\partial^2 T}{\partial s^2} + (1 + pw - \lambda p\sqrt{w(w+s)}v_w)\frac{\partial T}{\partial w} + (1 - ps - \lambda p\sqrt{s(w+s)}v_s)\frac{\partial T}{\partial s} = 0, \tag{2.14}$$

* This is true only for three-dimensional flows. In two dimensions the Oseen solution for flow past a parabola is not a uniformly valid approximation for low Reynolds numbers[12].

$$\left.\frac{\partial T}{\partial w}\right|_{w=1} = -p, \tag{2.15}$$

$$T\Big|_{w=1} = \Delta, \tag{2.16}$$

for axisymmetric temperature fields. Equation (2.14) can be rewritten as

$$w\frac{\partial^2 T}{\partial w^2} + s\frac{\partial^2 T}{\partial s^2} + (1+pw)\frac{\partial T}{\partial w} + (1-ps)\frac{\partial T}{\partial s} = \frac{p\lambda}{2}A(w,s), \tag{2.17}$$

where

$$A = 2\sqrt{(w'+s')}\left(\sqrt{w'}v_w\frac{\partial T}{\partial w'} + \sqrt{s'}v_s\frac{\partial T}{\partial s'} + \sqrt{\frac{(w'+s')}{4w's'}}v_\varphi\frac{\partial T}{\partial \varphi'}\right). \tag{2.18}$$

For a paraboloidal solidification front $A(w,s)$ and $T(w,s)$ must be independent of s. It is readily shown that $T = T(w)$ will satisfy Eqs. (2.15-2.17) with the velocity field represented by Eqs. (2.13), so here $A = A(w)$.

Now Eq. (2.17) can be integrated analytically to give the derivative of the temperature with respect to the normal coordinate w, i.e.,

$$\frac{\partial T}{\partial w} = -p\exp\left\{p(1-w)(1+\lambda) + \left[-1 + \frac{Pr\,e^{-\Lambda}}{E_1(\Lambda)}\right]\ln w + \frac{Pr}{E_1(\Lambda)}\left[-E_1(\Lambda) + E_1(\Lambda w) + E_2(\Lambda) - E_2(\Lambda w)\right]\right\}, \tag{2.19}$$

where E_1 and E_2 are the exponential integrals of first and second order, respectively. One more integration gives the surface temperature of the crystal, viz. Δ and the Péclet number p:

$$\Delta = -\int_{w=1}^{\infty} dw\,\frac{\partial T}{\partial w} = \int_{w=1}^{\infty} dw\,p\exp\left\{p(1-w)(1+\lambda) + \left[-1 + \frac{Pr\,e^{-\Lambda}}{E_1(\Lambda)}\right]\ln w + \frac{Pr}{E_1(\Lambda)}\left[-E_1(\Lambda) + E_1(\Lambda w) + E_2(\Lambda) - E_2(\Lambda w)\right]\right\}. \tag{2.20}$$

Recall that $\Lambda \equiv \lambda p/Pr$.

At this point a relation has been derived between the supercooling and Péclet number for a paraboloidal crystal formed by freezing of a supercooled melt in the presence of convection, viz.

$$\Delta = \Delta(p, \lambda, Pr). \tag{2.21}$$

Two new parameters are involved: a Prandtl number, ν/α, and the ratio of the velocity of the flow to the freezing velocity, λ. The relation is more complicated than that derived by Ivantsov for pure diffusion in that the convective velocity and the viscosity of the melt are involved. Furthermore, the parameter λ depends on the supercooling through V.

2.2. Discussion of results

The introduction of convective heat transfer into the equations governing dendritic growth has been shown to leave the paraboloidal shape intact when the flow structure has a certain form. This form derives from a solution to the viscous flow equations describing the interaction of a single axisymmetric dendrite with a uniform flow when the flow is slow i.e., in the Oseen approximation. This sort of convection leads to a new family of needle-crystals whose growth velocity is appropriately modified.

To illustrate the degree to which convection alters the relation between Péclet number and supercooling, some representative calculations using the properties of succinonitrile are presented in Fig. 6. As the figure indicates, forced convection increases the solidification rate substantially when the characteristic flow velocity is large compared to the solidification velocity. For example, at a dimensionless supercooling of 0.002, the Péclet number with a velocity ratio of 50 is almost twice the Ivantsov value. To emphasize that this is a very weak flow by ordinary standards we cite some results from experiments at low supercoolings.

At a dimensionless supercooling of 0.002, Glicksman and Huang [4] found the growth velocity to be roughly 0.8 microns per second and a velocity fifty times this is only 40 microns per second which, as the following scale analysis shows, can easily arise from buoyancy. The actual structure of the dendritic mass that generated flow in the experiments is not known but, as noted by Glicksman and Huang [4], it is larger than the radius of an individual tip. Accordingly, each dendritic arm is immersed in a flow field configured by the entire dendritic mass. If we assume

that the characteristic length scale for the crystal mass is l, then a representative velocity in a weak flow generated by natural convection is

$$U_\infty = C_1 \, \mathrm{Gr} \, \frac{\nu}{l}. \tag{2.22}$$

Here C_1 is a constant and ν is the kinematic viscosity. The Grashof number is

$$\mathrm{Gr} = \frac{g \beta \Delta L l^3}{c_p \nu^2}, \tag{2.23}$$

where g is the gravitational acceleration, β is the thermal expansivity of the melt, and $\Delta L / c_p$ is the supercooling. The velocity U_∞ is then proportional to the characteristic temperature difference and the square of the characteristic length:

$$U_\infty \approx \frac{g \beta L}{\nu \, c_p} \Delta l^2, \tag{2.24}$$

where the uncertainty of the constant C_1 has been absorbed by the "effective" convection length l. As a result, the absolute strength of the flow field decreases with decreasing supercooling. Using the properties of succinonitrile, we find

$$U_\infty = 740 \, \Delta l^2 \ cm/s$$

with l measured in centimeters. Accordingly a dendritic mass with a characteristic length of a little over half a millimeter would generate a 40 micron per second flow at an undercooling of 0.002. Nevertheless, the obvious differences between free and forced convection are enough to deter us from delving further into the experimental results until the detailed structure of free convection for this situation has been worked out.

It should be noted that our methodology differs from that of Glicksman and Huang [4], who used an alternative expression for the velocity U_∞, derived from a mass-transfer boundary-layer analysis:

$$U_\infty \approx \sqrt{\mathrm{Gr}}\frac{\nu}{l}.$$

Here the velocity is proportional to the square root of the Grashof number and can be written in terms of the length scale l:

$$U_\infty \approx \frac{g\beta L l^{\frac{1}{2}}}{c_p}\,\Delta^{\frac{1}{2}}.$$

This expression predicts unreasonably large velocities in the case of the the succinonitrile experiments (of the order of cm/s) and is clearly inappropriate for very low Grashof number flows.

The theory advanced here makes no allowance for the effects of surface tension which is known to have a profound effect on the details of dendritic growth. However, this theory provides the necessary starting point for the adaptation of more detailed theories to include convective effects which, according to the experimental results on succinonitrile, are quite important. The new "convective" steady-state solution represents the asymptotic form of the corresponding time-dependent solution at large distances from the tip. Furthermore, capillary effects are localized around the tip and thus the asymptotic solution is also valid for the general case of non-zero surface tension. As will be described in Chapter 3, the asymptotic solution facilitates the computation of the boundary integrals since the integrands reduce to their known asymptotic form far from the tip. In the next chapter, we present a non-linear scheme which tracks the evolution of the dendritic interface by solving the transient counterpart of Eq. (2.6) numerically.

REFERENCES

[1] P. Pelce and Y. Pomeau, Stud. Appl. Math. 74 (1986) 245.

[2] R. T. Davis and M. J. Werle, AIAA J. 10 (1972) 1224.

[3] J. Wilkinson, Quart. J. Mech. Applied Math. 8 (1955) 415.

[4] M. E. Glicksman and S. C. Huang, Proc. 87th Natl. AIChE Meeting, Boston, August 1979; M. E. Glicksman and S. C. Huang, Proc. 3rd European Symp. on Material Sciences in Space, Grenoble, April 1979; S. C. Huang and M. E. Glicksman, Acta Metall. 29 (1981) 701.

CHAPTER 3: INTERFACE TRACKING

A non-linear interface tracking algorithm, based on the boundary integral equation derived in Appendix A, is used to study the temporal and spatial evolution of the dendritic interface. The important role of capillarity and convection on the interface dynamics is established and the response of the interface to finite amplitude disturbances is examined for the first time.

3.1. FORMULATION AND NUMERICAL IMPLEMENTATION

3.1.a. Theoretical formulation

In this chapter we study the temporal and spatial departure of the freezing interface from the steady-state solutions described in the previous chapter. It is thus advantageous to solve the convective-diffusion equation in a reference frame moving with the velocity $V\mathbf{i}_z$ that corresponds to the underlying steady-state. With this coordinate transformation, steadily propagating fronts are replaced by *stationary* interfaces and the transient interface motion is studied separately.

We consider the evolution of a solid-liquid interface Γ solely controlled by the heat (solute) transport in the solid and liquid phases. The temperature (solute concentration) field $\tilde{T}$ obeys the transient convective-diffusion equation, written in a coordinate system that moves with a *constant* velocity $V\mathbf{i}_z$ parallel to the $z-$axis:

$$\frac{\partial \tilde{T}}{\partial \tilde{t}} + \tilde{\mathbf{v}} \cdot \nabla_{\mathbf{x}} \tilde{T} - \alpha \nabla^2_{\mathbf{x}} \tilde{T} - V \frac{\partial \tilde{T}}{\partial \tilde{z}} = 0, \tag{3.1}$$

where the $\tilde{\mathbf{x}}$ vector is represented by the triad $(\tilde{x}, \tilde{y}, \tilde{z})$=$(\tilde{\mathbf{r}}, \tilde{z})$ in cartesian coordinates and $(\tilde{r}, \varphi, \tilde{z})$ in polar cylindrical coordinates, $\alpha(\tilde{\mathbf{x}}, \tilde{t})$ is the local thermal diffusivity of the medium, and $\tilde{\mathbf{v}}(\tilde{\mathbf{x}}, \tilde{t})$ is the local velocity in the liquid phase.

According to the two-sided "symmetric" model, proposed by Langer [1], thermophysical properties of the two phases, such as the thermal diffusivity and the density, are equal (i.e., $\alpha_L = \alpha_S$ and $\rho_L = \rho_S$) and independent of temperature. Although this is not necessarily true for most materials, succinonitrile, a "plastic" organic crystal used extensively for dendritic growth experiments [2], possesses almost identical thermophysical constants in both liquid and solid phases. We adopt the two-sided model assumption throughout this chapter but have also derived a similar formulation for the one-sided model*. The motion of the interface is related to the rate at which the latent heat of solidification is removed away from the interface through the heat conservation condition at the interface. The latter relates the "jump" of the local temperature gradient to the normal component of the interface freezing velocity:

$$\hat{\mathbf{n}} \cdot \nabla_{\mathbf{x}} \tilde{T}_{(\text{liquid})} - \hat{\mathbf{n}} \cdot \nabla_{\mathbf{x}} \tilde{T}_{(\text{solid})} = -\frac{L}{c_p \alpha} \left[V + \frac{\partial \tilde{\zeta}}{\partial \tilde{t}} \right] \hat{\mathbf{n}} \cdot \mathbf{i}_z, \tag{3.2}$$

where the first term in the right-hand-side arises from the motion of the coordinate system and the second, time-varying, term represents the freezing velocity of the interface $\tilde{z} = \tilde{\zeta}(\tilde{\mathbf{r}}, \tilde{t})$ with respect to the moving frame of reference. Here L is the latent heat of fusion per unit volume and c_p is the specific heat (the symmetric model hypothesis implies that the specific heats of the two phases are identical).

The interface temperature is determined thermodynamically by the Gibbs-Thomson relation (see Appendix E)

$$\tilde{T}_\Gamma = T_M \left[1 - \frac{L}{c_p} d_0 [1 - \epsilon g(\theta_1, \theta_2)] \tilde{\mathcal{K}} \left\{ \tilde{\zeta}(\tilde{\mathbf{r}}, \tilde{t}) \right\} \right], \tag{3.3}$$

* The *one-sided* model, briefly discussed in Appendix A, assumes no heat flow in the solid (the "convective" steady-state solution, derived in Chapter 2, is compatible with both models since the solid is isothermal in the zero-surface-tension limit).

where T_M is the melting point, $d_0 = \gamma T_M c_p / L^2$ is the capillary length (proportional to the solid-liquid surface tension γ), ϵ represents a measure of the anisotropy of the surface tension [3,4], $g(\theta_1, \theta_2)$ is an order unity function of the crystal geometry, θ_i is the angle between the interface normal $\hat{\mathbf{n}}$ and the crystal axis i, and $\tilde{\mathcal{K}}$ is the local curvature of the interface, considered positive when the solid bulges into the liquid. The Gibbs-Thomson relation is derived under the assumption of local equilibrium (see Appendix E), but it serves as a good approximation under conditions encountered in dendritic growth.

Finally, the temperature field asymptotes to constant values as $\tilde{z} \to \pm\infty$:

$$\lim_{z \to \pm\infty} \tilde{T}(\mathbf{x}, t) = T_{\pm\infty}. \tag{3.4}$$

We now scale the lengths with $2\alpha/V$ and times with $4\alpha/V^2$. Eqs. (3.1-3.4) then become

$$\frac{\partial T}{\partial t} + 2\lambda\, \mathbf{v} \cdot \nabla_{\mathbf{x}} T - \nabla_{\mathbf{x}}^2 T - 2\frac{\partial T}{\partial z} = 0, \tag{3.5}$$

$$\hat{\mathbf{n}} \cdot \nabla_{\mathbf{x}} T_{(\text{liquid})} - \hat{\mathbf{n}} \cdot \nabla_{\mathbf{x}} T_{(\text{solid})} = -\left[2 + \dot{\zeta}(\mathbf{r}, t)\right] \hat{\mathbf{n}} \cdot \mathbf{i}_z, \tag{3.6}$$

$$T_\Gamma = \Delta - \nu \mathcal{K}\{\zeta(\mathbf{r}, t)\}, \tag{3.7}$$

$$\lim_{z \to \infty} T(\mathbf{x}, t) = 0 \text{ and } \lim_{z \to -\infty} T(\mathbf{x}, t) = \text{constant}, \tag{3.8}$$

where the temperature is now $T = (\tilde{T} - T_\infty) c_p / L$ and the velocity is $\mathbf{v} = \tilde{\mathbf{v}} / U_\infty$, $\lambda \equiv U_\infty / V$ is the ratio of the characteristic flow velocity scale U_∞ to the velocity V of the coordinate system, $\nu = d_0 [1 - \epsilon g(\theta_1, \theta_2)]\, V / 2\alpha$ is the (anisotropic) dimensionless capillary length function, $\Delta = (T_M - T_\infty) c_p / L$ is the dimensionless supercooling, $z = \zeta(\mathbf{r}, t)$ represents the interface Γ, and $\dot{\zeta}(\mathbf{r}, t) \hat{\mathbf{n}} \cdot \mathbf{i}_z = (\partial \zeta / \partial t) \hat{\mathbf{n}} \cdot \mathbf{i}_z$ is the normal component of the interface velocity *relative* to the moving reference frame.

In the melt, the velocity $\mathbf{v}$ obeys the Navier-Stokes equations for viscous, incompressible flow and satisfies the no-slip condition on the solid-liquid interface*. As mentioned in Chapter 2, the solidification of the interface alone does not generate fluid flow and in the absence of fluid flow the velocity $\mathbf{v}$ is identically zero everywhere in the domain *independently* of the coordinate system choice. In dimensionless form we have (the characteristic length, time, and velocity are $2\alpha/V$, $4\alpha/V^2$, and $U_\infty \equiv \lambda V$, respectively)

$$\frac{1}{Pr}\frac{\partial \mathbf{v}}{\partial t} + \frac{2\lambda}{Pr}\mathbf{v}\cdot\nabla_{\mathbf{x}}\mathbf{v} = -\nabla_{\mathbf{x}}P + \nabla_{\mathbf{x}}^2\mathbf{v}, \tag{3.9}$$

where Pr is the Prandtl number and $\mathbf{v} = 0$ on the interface Γ. For certain materials, including succinonitrile, the Prandtl number is sufficiently large and the temporal term in Eq. (3.9) can be neglected, implying that the velocity field responds instantaneously to changes in the interface shape. However, this is not true for metals, where the Prandtl number is quite small.

The coefficient of the second term in the left-hand-side of Eq. (3.9), which represents a measure of the inertial characteristics of the flow field, is also small, since the flow velocities that occur in dendritic solidification are generally small. Nevertheless, the inertial term becomes important at large distances away from the interface and must be included in order to obtain a uniformly valid representation of the flow field. As an alternative to solving the full non-linear Navier-Stokes equations, we use the linear approximation first suggested by Oseen [6]. In the Oseen approximation, the non-linear term $\mathbf{v}\cdot\nabla_{\mathbf{x}}\mathbf{v}$ is replaced by the linear term

* The assumption of equal densities implies that there is no flow through the interface due to volume change.

$(-\mathbf{i}_z \cdot \nabla_x \mathbf{v})$ utilizing the far-field velocity $(-\mathbf{i}_z)$. This linearized equation is a uniformly valid approximation of the Navier-Stokes equation in which the viscous and pressure forces are balanced with a small contribution of inertia. In Appendix D we present a boundary integral method for the calculation of the flow velocity $\mathbf{v}$, based on the methodology first applied by Youngren and Acrivos [7]. However, the complexity of the interface shape makes this problem computationally more difficult than the unidirectional streaming flows past smooth objects studied by Youngren and Acrivos.

The interface shape $z = \zeta(\mathbf{r}, t)$ appears only in the boundary conditions for the partial differential equations (3.5) and (3.9). As Eq. (3.6) suggests, it is not necessary to know the temperature at arbitrary positions around the solidifying front since only the temperature gradient normal to the interface is required to calculate the growth velocity. Consequently, if Eq. (3.5) and the corresponding boundary conditions could be transformed to give equations for the temperature gradient at the interface, then the solution of these equations would give all the information necessary from the point of view of solidification. Now it turns out that such equations can indeed be derived using Green's function techniques. In general, a non-local* integral equation is obtained which relates the normal derivative of the temperature field at the interface to the temperature field in the interior of the domain.

Before transforming the transient convective-diffusion Eq. (3.5) into an integral equation, it may be useful to explain the physical background of such equations. The

* A "non-local" equation for a particular point in space contains not only the local value of the field variable (or its derivatives) but also the value of the field variable (or its derivatives) in other points in the domain.

surface of discontinuity (in our case, the crystal-melt interface) acts as a distribution of "point sources" and "point dipoles." In the quasistatic case, and in the absence of sources or sinks in the domain, it can be shown that the surface source density equals the "jump" between the inner and outer normal gradient of the field (i.e., the temperature field) and the surface dipole density equals the "jump" between the outer and inner field value. In solidification, the temperature is continuous upon crossing the crystal-melt interface implying that no dipoles are needed and the interface can be represented solely in terms of point heat sources with a surface density determined by Eq. (3.6). Finally, it is possible to incorporate the time dependence of the heat diffusion equation into the integral equation. In this case, temporal integration introduces the effects of the interface history in addition to the non-local effects due to the spatial integration.

The transformation of a partial differential equation into an integral equation requires the use of the corresponding Green's function. This function represents the response of the field variable (i.e., the temperature) to an instantaneous point source*. The usefulness of the Green's function lies in the fact that it is a particular solution of the adjoint of the differential equation, and thus it already contains some of the characteristics of the desired solution.** A shortcoming of this approach is that there are no Green's functions, at least in a useful form, for differential equations with variable coefficients. A prime example is the convective-diffusion equation (3.5), where, due to the presence of the convective term $\mathbf{v} \cdot \nabla_{\mathbf{x}} T$, no Green's function is known for cases where the velocity varies with position.

---

* An instantaneous point source is represented by $\delta(\mathbf{x} - \mathbf{x}')\delta(t - t')$.

** Note that Eq. (A2), which is the adjoint of the heat diffusion equation, is defined in the *inverse* time space, represented by the time variable t'.

We now introduce the Green's function $G(\mathbf{x}, \mathbf{x}'; t - t')$ that represents the solution to the adjoint of the heat diffusion equation in a moving coordinate system and in an unbounded domain (see Appendix A), viz.,

$$G(\mathbf{x}, \mathbf{x}'; t - t') = \frac{H(t - t')}{[4\pi(t - t')]^{\frac{3}{2}}} \exp\left\{ - \frac{|\mathbf{r} - \mathbf{r}'|^2 + [z - z' + 2(t - t')]^2}{4(t - t')} \right\}, \quad (3.10)$$

where $H(t - t')$ is the Heaviside function and $G(\mathbf{x}, \mathbf{x}'; t - t') \equiv 0$ for $t < t'$. The fundamental solution $G(\mathbf{x}, \mathbf{x}'; t - t')$ represents the transient spatial response of the temperature field to a point source at $t = t'$ and $\mathbf{x} = \mathbf{x}'$ in the moving coordinate system. It is singular at ($\mathbf{x} = \mathbf{x}'$, $t = t'$), but continuous elsewhere.

The integral equation corresponding to Eq. (3.5), the transient convective-diffusion equation, is

$$\begin{aligned} T(\mathbf{x}, t) = & \int_{-\infty}^{t-} dt' \int d\mathbf{r}' \left[2 + \dot{\zeta}(\mathbf{r}', t') \right] G(\mathbf{x}, \mathbf{x}_\Gamma(t'); t - t') \\ & - 2\lambda \int_{-\infty}^{t-} dt' \int d\mathbf{r}' \int_{\zeta(\mathbf{r}', t')}^{\infty} dz' G(\mathbf{x}, \mathbf{x}'; t - t') \, \mathbf{v}(\mathbf{x}', t') \cdot \nabla_{\mathbf{x}'} T(\mathbf{x}', t'), \quad (3.11) \end{aligned}$$

according to the derivation given in Appendix A. The interface $\mathbf{x}_\Gamma$ is at $z = \zeta(\mathbf{r}, t)$ and $\int d\mathbf{r} = \int_0^\infty r \, dr \int_0^{2\pi} d\varphi$. It is worth noting that the first term in the right-hand-side of Eq. (3.11) represents a point source distribution along the interface with density equal to the discontinuous "jump" of the temperature gradient normal to the interface, which in turn is directly related to the interface velocity through the heat conservation condition Eq. (3.6). The second integral term, which acts as an effective volume distribution of sources, represents the effects of convection. Finally, the time integration stems from the transient nature of Eq. (3.5) and represents the history of the temperature field.

We now apply Eq. (3.11) to points on the interface $\mathbf{x} = \mathbf{x}_\Gamma \equiv (\mathbf{r}, z = \zeta(\mathbf{r},t))$ to yield

$$T(\mathbf{x}_\Gamma,t) = \Delta - \nu\mathcal{K}\{\zeta(\mathbf{r},t)\} = \int_{-\infty}^{t-} dt' \int d\mathbf{r}' \left[2 + \dot{\zeta}(\mathbf{r}',t')\right] G(\mathbf{x}_\Gamma(t), \mathbf{x}_\Gamma(t'); t-t')$$
$$-2\lambda \int_{-\infty}^{t-} dt' \int d\mathbf{r}' \int_{\zeta(\mathbf{r}',t')}^{\infty} dz' G(\mathbf{x}_\Gamma(t), \mathbf{x}'; t-t')\, \mathbf{v}(\mathbf{x}',t') \cdot \nabla_{\mathbf{x}'} T(\mathbf{x}',t'), \qquad (3.12)$$

where Eq. (3.7) has been substituted for the interface temperature $T(\mathbf{x}_\Gamma, t)$.

Equation (3.12) represents an integral evolution equation for the interface shape $\zeta(\mathbf{r},t)$, given the temperature field. Without flow ($\lambda = 0$), the "convective" integral in the right-hand-side vanishes and Eq. (3.12) can be solved to determine the only unknown, ζ. In the presence of flow, however, the convective integral represents the effect of a distribution of point sources in the fluid domain with (unknown) volume density $\mathbf{v}(\mathbf{x},t) \cdot \nabla_{\mathbf{x}} T(\mathbf{x},t)$. Thus we need to evaluate the temperature gradient and the flow velocity in the interior of the fluid domain (since $\mathbf{v} = 0$ in the solid.) Taking the gradient of Eq. (3.11) for $\mathbf{x} \neq \mathbf{x}_\Gamma$ gives

$$\nabla_{\mathbf{x}} T(\mathbf{x},t) = \int_{-\infty}^{t-} dt' \int d\mathbf{r}' \left[2 + \dot{\zeta}(\mathbf{r}',t')\right] \nabla_{\mathbf{x}} G(\mathbf{x}, \mathbf{x}_\Gamma(t'); t-t')$$
$$-2\lambda \int_{-\infty}^{t-} dt' \int d\mathbf{r}' \int_{\zeta(\mathbf{r}',t')}^{\infty} dz' \nabla_{\mathbf{x}} G(\mathbf{x}, \mathbf{x}'; t-t')\, \mathbf{v}(\mathbf{x}',t') \cdot \nabla_{\mathbf{x}'} T(\mathbf{x}',t'). \quad (3.13)$$

Eq. (3.13) can be directly used to evaluate interior values of the temperature gradient for a given interface shape $\zeta(\mathbf{r},t)$. The evaluation of the velocity field is discussed in the next section.

3.1.b. Numerical implementation

Now we apply the integral equation (3.12) and the auxilliary field equations (3.13) and (3.9) to study the temporal and spatial evolution of a crystal interface*.

* Our methodology actually applies to any advancing front that obeys similar equations.

As mentioned in the introduction, most investigations of dendritic growth involve numerical computations of the shapes of *steadily* advancing fronts and linear stability. Important "steady-state" theories, such as the microscopic solvability hypothesis, have not as yet been tested by a transient, non-linear, tracking scheme in which the position of the interface is updated continuously. In addition, the temporal derivative in Eq. (3.5) has been omitted from all previous work on the grounds that its effect is small at small supercoolings Δ. While this is true, the recent work on the microscopic solvability hypothesis has been carried out at moderate to high supercoolings, where the temperature field does not respond instantaneously to changes in the interface shape. The elimination of this "quasistatic" approximation changes the solution method significantly, since now the fully-transient integral equation is of the Volterra type in time. While the Fredholm type integral equation* that corresponds to the quasistatic case has been studied extensively and is suitable for an eigenmode stability analysis, the Volterra type equation is not amenable to such a stability analysis. Furthermore, the non-linearity of the integral kernel precludes the use of Laplace transforms that usually offer a useful but cumbersome alternative to the normal mode analysis. Finally, the incorporation of convection in the integral evolution equation increases its dimensionality and requires an iterative approach to be explained shortly. Convection has been neglected heretofore, although many investigators have noted that hydrodynamic effects are important in solidification and experiments have indicated the dramatic effects of convection in low supercoolings [2].

---

* An integral equation with *fixed* integration limits.

The next step is to develop a numerical procedure, based on Eq. (3.12), that corresponds to the solution of the full transient convective-diffusion Eq. (3.5). With this, shortcomings of other approaches are avoided and a reliable tool for the study of the non-linear evolution of crystal dendrites is set forth.

From $t' = -\infty$ to $t' = t_0$, the interface shape, the temperature field, and the flow field represent steady-state behavior denoted by the subscript $(_0)$. That implies that in the laboratory frame of reference the interface is a uniformly moving solidification front with a constant freezing velocity equal to that of the moving coordinate system and $\dot{\zeta}(\mathbf{r},t)$ is zero. By setting $t = t_0$ we can depict the steady-state propagation of the crystal-melt interface and examine the effects of convection on the existing steady-state theories. This aspect of our numerical work has been presented in Chapter 2. On the other hand, a perturbation in the interface velocity introduced at $t' = t_0$ causes deviations from the steady-state; the time integrals in Eqs. (3.12-3.13) can then be split in two integral parts. The integrals from $t' = -\infty$ to $t' = t_0$ represent the dependence of the current interface shape on the underlying steady-state, whereas the integrals from $t' = t_0$ to the current time represent the time history of the perturbed interface. Equations (3.12-3.13) now become

$$
\begin{aligned}
T(\mathbf{x}_\Gamma,t) = \Delta - \nu\mathcal{K}\{\zeta(\mathbf{r},t)\} = &\int_{-\infty}^{t_0} dt' \int d\mathbf{r}'\, 2\, G(\mathbf{x}_\Gamma(t),\mathbf{x}_{\Gamma_0}(t');t-t') \\
&+ \int_{t_0}^{t-} dt' \int d\mathbf{r}' \left[2+\dot{\zeta}(\mathbf{r}',t')\right] G(\mathbf{x}_\Gamma(t),\mathbf{x}_\Gamma(t');t-t') \qquad (3.14)\\
&- 2\lambda \int_{-\infty}^{t_0} dt' \int d\mathbf{r}' \int_{\zeta_0(\mathbf{r}')}^{\infty} dz' G(\mathbf{x}_\Gamma(t),\mathbf{x}';t-t')\ \mathbf{v}_0(\mathbf{x}')\cdot\nabla_{\mathbf{x}'}T_0(\mathbf{x}') \\
&- 2\lambda \int_{t_0}^{t-} dt' \int d\mathbf{r}' \int_{\zeta(\mathbf{r}',t')}^{\infty} dz' G(\mathbf{x}_\Gamma(t),\mathbf{x}';t-t')\ \mathbf{v}(\mathbf{x}',t')\cdot\nabla_{\mathbf{x}'}T(\mathbf{x}',t'),
\end{aligned}
$$

and

$$\nabla_{\mathbf{x}} T(\mathbf{x},t) = \int_{-\infty}^{t_0} dt' \int d\mathbf{r}'\, 2\, \nabla_{\mathbf{x}} G(\mathbf{x}, \mathbf{x}_{\Gamma_0}(t'); t-t')$$
$$+ \int_{t_0}^{t-} dt' \int d\mathbf{r}' \left[2 + \dot{\zeta}(\mathbf{r}',t')\right] \nabla_{\mathbf{x}} G(\mathbf{x}, \mathbf{x}_{\Gamma}(t'); t-t') \qquad (3.15)$$
$$- 2\lambda \int_{-\infty}^{t_0} dt' \int d\mathbf{r}' \int_{\zeta_0(\mathbf{r}')}^{\infty} dz' \nabla_{\mathbf{x}} G(\mathbf{x}, \mathbf{x}'; t-t')\, \mathbf{v}_0(\mathbf{x}') \cdot \nabla_{\mathbf{x}'} T_0(\mathbf{x}')$$
$$- 2\lambda \int_{t_0}^{t-} dt' \int d\mathbf{r}' \int_{\zeta(\mathbf{r}',t')}^{\infty} dz' \nabla_{\mathbf{x}} G(\mathbf{x}, \mathbf{x}'; t-t')\, \mathbf{v}(\mathbf{x}',t') \cdot \nabla_{\mathbf{x}'} T(\mathbf{x}',t'),$$

where $\mathbf{x}_{\Gamma_0}$ represents points on the steady-state interface shape $z = \zeta_0(\mathbf{r})$. Note that the interface velocity, $\dot{\zeta}(\mathbf{r},t)$, *relative* to the velocity of the advancing steady-state front is set to zero in the "steady-state" time interval $(-\infty, t_0)$. Also note that the Oseen approximation to the Navier-Stokes equation (3.9) (see Appendix D) is a "quasistatic" approximation and thus does not involve temporal integration. Nevertheless, it is implicitly time-dependent since the boundary shape changes continuously with time and, as shown in Appendix D, the flow velocity $\mathbf{v}(\mathbf{x},t)$ is recalculated at every time step.

At this point it is instructive to compare Eqs. (3.14-3.15) and their quasistatic, purely diffusive counterparts used in previous work [3,4,8,9].

- In the quasistatic approximation and in the absence of convection only the second integral in the right-hand-side of Eq. (3.14) survives out of the eight integrals appearing in Eqs. (3.14-3.15)*.
- In the steady-state models, the time integration is performed analytically over the entire time interval $(-\infty, t)$. In order to see why this is not possible in our case, consider the second integral in the right-hand-side of Eq. (3.14).

* With t_0 replaced by ∞.

In the steady-state case the interface shape $\mathbf{x}_\Gamma(t')$ does not change with time and is equal to the current interface shape $\mathbf{x}_\Gamma(t)$. This simplifies the analysis considerably, since the solution of a Volterra type equation is avoided. In the transient case, however, the interface shape is a continuous function of time and the Green's function G becomes a non-linear function of the *unknown* interface shape $\mathbf{x}_\Gamma(t')$. This precludes analytical integration and leads to a non-linear Volterra type integral equation and to the associated computational difficulties mentioned earlier in this chapter.

- In the absence of convection, Eq. (3.15) becomes obsolete since no interior values of the temperature field are required. This reduces the dimensionality of the problem and Eq. (3.14) becomes an *boundary* integral equation.

Having enumerated the differences between the steady-state and our "transient" problem, it becomes apparent that the latter is clearly harder, primarily because of three factors: non-linearity, transient nature, and convection. While the first two factors combined preclude the use of traditional stability methods and necessitate an interface tracking scheme, convection partially destroys the elegant features of the boundary integral approach. The convective term in the diffusion equation (3.5) is responsible for the domain integrals in Eqs. (3.14-3.15) that increase by one the dimensionality of the integral equations. In the numerical scheme that we present in this chapter we have coupled the essential features of the boundary integral method with a domain discretization that requires a minimal amount of interior points. We were thus able to avoid some of the problems with finite difference or finite element methods such as the complicated boundary geometry and the long computation times usually required for three-dimensional calculations. The

"differential" approach has not been successful because of the prohibitively large computer requirements for such a transient, three-dimensional convective-diffusion problem with a moving interface, since each point in the interior domain carries an equal weight. The success of our integral approach is based on the fact that the "influence" of the convective temperature field on the interface shape decays exponentially fast away from the interface and the corresponding domain integrals can be accurately calculated in the *vicinity* of the interface. Summarizing, our goal is to calculate iteratively the interface shape at time t using the evolution equation (3.14) that contains the time history and the non-local characteristics of the interface and using Eqs. (3.15) and (3.9) to update the temperature and velocity fields.

The temporal integration in the second and fourth integral terms in Eqs. (3.14-3.15) cannot be performed analytically since the interface shape, the temperature field, and the flow velocity $\mathbf{v}$ are all unknown functions of time. To calculate the temporal integrals numerically, the time domain $[t_0, t \equiv t_N)$ is split in N equal intervals. Over each such time interval, $[t_{n-1}, t_n)$, field variables, such as the interface shape, ζ, temperature, and velocity, are considered to be constant and equal to their respective value at the "nodal" point $\tilde{t} \in [t_{n-1}, t_n)$*. The actual location of the nodal point within each time interval depends on whether the integral belongs to Eq. (3.14) or Eq. (3.15). In the discretization of Eq. (3.14), where the objective is to use previously calculated values of all the field variables to calculate the new interface shape at time $t = t_N$, we place the nodal points $\tilde{t}_n$ at the *end* of each time interval. On the other hand, the calculation of the interior values of the temperature gradient and velocity is done iteratively and it requires the simultaneous knowledge

* The error associated with this approximation can be estimated from the mean value theorem.

of the interface shape. Here nodal points are placed at the beginning of each time interval and the requisite information for the calculation of the temperature field can be retrieved from prior time steps.

This temporal discretization of Eqs. (3.14-3.15) now allows us to integrate *analytically* over each time interval. In Appendix B we present the result of the time integration of each of the integrals in Eqs. (3.14-3.15), denoted by I_k and H_k, $k = 1,2,3,4$, respectively. The calculation of each integral requires several steps but the final result can be expressed in the following concise manner:

$$\Delta - \nu\mathcal{K}\{\zeta(\mathbf{r},t)\} = I_1 + I_2 + I_3 + I_4, \tag{3.16}$$

$$\nabla_{\mathbf{x}} T(\mathbf{x},t) = H_1 + H_2 + H_3 + H_4, \tag{3.17}$$

with the integrals $(I_1 - I_4)$ and $(H_1 - H_4)$ shown in Eqs. (B5-B12.)

Each of the expressions I_k (or, H_k) involves a two- or three-dimensional spatial integral (or, a N term sum thereof,) representing the non-local characteristics of the problem at the given time interval. Variables in each integral are denoted by a subscript which indicates the time at which the field variables are calculated. This is exemplified by the integral

$$\begin{aligned}
&\int d\mathbf{r}' \left[2 + \dot{\zeta}_n(\mathbf{r}')\right] \frac{\exp\{-\zeta_N(\mathbf{r}) + \zeta_n(\mathbf{r}')\}}{8\pi\,|\mathbf{x}_N - \mathbf{x}_n{}'|} \\
&\times \left\{ \exp|\mathbf{x}_N - \mathbf{x}_n{}'| \left(\operatorname{erf}\left[\frac{|\mathbf{x}_N - \mathbf{x}_n{}'|}{2\sqrt{(N-n)\Delta t}} + \sqrt{(N-n)\Delta t} \right] \right.\right. \\
&\qquad \left. - \operatorname{erf}\left[\frac{|\mathbf{x}_N - \mathbf{x}_n{}'|}{2\sqrt{(N-n+1)\Delta t}} + \sqrt{(N-n+1)\Delta t} \right] \right) \\
&+ \exp\{-|\mathbf{x}_N - \mathbf{x}_n{}'|\} \left(\operatorname{erf}\left[\frac{|\mathbf{x}_N - \mathbf{x}_n{}'|}{2\sqrt{(N-n)\Delta t}} - \sqrt{(N-n)\Delta t} \right] \right. \\
&\qquad \left.\left. - \operatorname{erf}\left[\frac{|\mathbf{x}_N - \mathbf{x}_n{}'|}{2\sqrt{(N-n+1)\Delta t}} - \sqrt{(N-n+1)\Delta t} \right] \right) \right\}
\end{aligned}$$

that belongs to the N term sum in Eq. (B6). Variables with the subscript $(_n)$ represent quantities previously calculated at time $t = t_n$ and are treated as constants during the spatial integration. Variables with the subscript $(_N)$ correspond to the unknown values at the present time, $t = t_N$, but are otherwise treated in exactly the same way.

Our analysis to this point can be applied to any solidification front that obeys the evolution equation (3.14) and the auxiliary equations (3.15) and (3.9). However, in order to derive an optimal *spatial* discretization, we need to define the basic state under investigation. From previous steady-state models, including the convective model presented in Chapter 2, it is well-established that there exist solutions to Eq. (3.14) that represent uniformly translating needle-crystals with a near-paraboloidal shape [3,4,8-10]. Although most of these solutions are unstable [11] or possess cusps at the tip of the needle [3,4], they do represent the only known shapes that satisfy the steady-state equivalent of Eq. (3.14). Since one of our objectives is to investigate the non-linear spatial and temporal evolution of such crystal forms, it follows that the asymptotic (spatial) characteristics of this system are determined by the far-field behavior of the temperature and flow fields that correspond to these steady-state needle crystals. The capillary term in Eq. (3.14) modifies the morphology of the interface in the vicinity of the needle tip, but otherwise the long-range behavior of the temperature field is determined solely by the heat transport mechanisms, i.e. heat diffusion and convection.

We will use the generalization of the Ivantsov family of steady-state needle crystals, derived in Chapter 2, to extract the asymptotic behavior of the integrands since, at large distances from the interface, the temperature and flow fields are

essentiallly unaffected by the interface perturbation. This generalized steady-state paraboloidal solution, denoted by the subscript $(_0)$, will also be used to define a new set of spatial variables that map the infinite integration domain onto a *unit cube.*

The calculation of the spatial integrals involves integration over the entire r, φ plane. In addition, the three dimensional "convective" integrals I_3, I_4, H_3, and H_4 require an extra z integration over the semi-infinite interval $[\zeta_n(\mathbf{r}), \infty)$. The immediate goal is to express these integrals in terms of selected values of the field variables in time and space. First, the two-dimensional integrals (I_1, I_2, H_1, and H_2) are examined by looking again at the representative example borrowed from Eq. (B6):

$$\int_0^{2\pi} d\varphi' \int_0^{\infty} r'\, dr' \left[2 + \dot{\zeta}_n(\mathbf{r}')\right] \frac{\exp\{-\zeta_N(\mathbf{r}) + \zeta_n(\mathbf{r}')\}}{8\pi\,|\mathbf{x}_N - \mathbf{x}_n{}'|}$$
$$\times \left\{ \exp|\mathbf{x}_N - \mathbf{x}_n{}'| \left(\operatorname{erf}\left[\frac{|\mathbf{x}_N - \mathbf{x}_n{}'|}{2\sqrt{(N-n)\Delta t}} + \sqrt{(N-n)\Delta t} \right] \right.\right.$$
$$\left. - \operatorname{erf}\left[\frac{|\mathbf{x}_N - \mathbf{x}_n{}'|}{2\sqrt{(N-n+1)\Delta t}} + \sqrt{(N-n+1)\Delta t} \right] \right)$$
$$+ \exp\{-|\mathbf{x}_N - \mathbf{x}_n{}'|\} \left(\operatorname{erf}\left[\frac{|\mathbf{x}_N - \mathbf{x}_n{}'|}{2\sqrt{(N-n)\Delta t}} - \sqrt{(N-n)\Delta t} \right] \right.$$
$$\left.\left. - \operatorname{erf}\left[\frac{|\mathbf{x}_N - \mathbf{x}_n{}'|}{2\sqrt{(N-n+1)\Delta t}} - \sqrt{(N-n+1)\Delta t} \right] \right) \right\},$$

where

$$|\mathbf{x}_N - \mathbf{x}_n{}'| = \sqrt{r^2 + (r')^2 - 2rr'\cos\varphi' + [\zeta_N(r) - \zeta_n(r')]^2}.$$

For axisymmetric interface perturbations, the φ' dependence comes solely from the cosine term in the expression for $|\mathbf{x}_N - \mathbf{x}_n{}'|$. It is obvious that the integrand becomes singular when $r = r'$ and $\varphi' = 0$, since the distance $|\mathbf{x}_N - \mathbf{x}_n{}'|$ between the points $\mathbf{x}_N$ and $\mathbf{x}_n{}'$ (which appears in the denominator) becomes zero. Nevertheless,

the integrals exist since this weak singularity ($1/|\mathbf{x}_N - \mathbf{x}_n{}'|$, as $|\mathbf{x}_N - \mathbf{x}_n{}'| \to 0$) is integrable. To demonstrate this we introduce the new variable

$$\eta = |\mathbf{x}_N - \mathbf{x}_n{}'| = \sqrt{\alpha(r,r') - \gamma(r,r')\cos\varphi'},$$

where

$$\alpha(r,r') = r^2 + (r')^2 + \left(\zeta_N(r) - \zeta_n(r')\right)^2$$

and

$$\gamma(r,r') = 2rr'.$$

The above integral, which can be written as

$$C \equiv \int_0^{2\pi} d\varphi \int_0^{\infty} dr' \frac{h(r,r',\varphi)}{|\mathbf{x}_N - \mathbf{x}_n{}'|},$$

where h is a non-singular function, becomes

$$C = \int_0^{\infty} dr' \int_{\sqrt{\alpha-\gamma}}^{\sqrt{\alpha+\gamma}} \frac{d\eta}{\sqrt{(\sqrt{\alpha+\gamma}-\eta)\,(\eta-\sqrt{\alpha-\gamma})}} \frac{4\,h(r,r',\eta)}{\sqrt{(\sqrt{\alpha+\gamma}+\eta)\,(\eta+\sqrt{\alpha-\gamma})}}.$$

The reader should note the similarity between the integral C and inverse elliptic functions. In fact, in the special case of a stationary coordinate system, C reduces to a non-singular inverse Jacobian elliptic function [13]. In the general case, the integrand in C is bounded by the integrand of the stationary case in the entire integration interval and thus its existence is guaranteed. To evaluate the integrals with respect to η, the orthogonal polynomial Gaussian quadrature (based on Chebyshev polynomials of the first kind) is applied [13], e.g.,

$$\int_a^b \frac{dy\,h(y)}{\sqrt{(y-a)(b-y)}} \approx \sum_{k=1}^{N_\varphi} \frac{\pi}{N_\varphi} h(y_k)$$
$$y_k = \frac{(b+a)}{2} + \frac{(b-a)}{2}\cos\left(\frac{2k-1}{N_\varphi}\frac{\pi}{2}\right).$$

For the η part of integral C we obtain

$$C = \frac{4\pi}{N_\varphi} \sum_{k=1}^{N_\varphi} \int_0^\infty dr' \frac{h(r, r', \eta_k)}{\sqrt{(\sqrt{\alpha+\gamma}+\eta_k)(\eta_k+\sqrt{\alpha-\gamma})}}, \tag{3.18}$$

where

$$\eta_k = \frac{\sqrt{\alpha+\gamma}+\sqrt{\alpha-\gamma}}{2} + \frac{\sqrt{\alpha+\gamma}-\sqrt{\alpha-\gamma}}{2} \cos\left(\frac{2k-1}{N_\varphi}\frac{\pi}{2}\right).$$

The two-dimensional integrals can now be written as sums of N_φ one-dimensional integrals in r'.

The interface shapes at time t_N (i.e., ζ_N) and at time t_n (i.e., ζ_n), both asymptote to the paraboloidal (unperturbed) interface shape $\zeta_0=(p/2)(1-r^2/p^2)$ as $r \to \infty$. As a result, $|\mathbf{x}_N - \mathbf{x}_n'|$ becomes

$$\lim_{r' \to \infty} |\mathbf{x}_N - \mathbf{x}_n'| = \frac{(r')^2}{2p}$$

and the asymptotic behavior (with respect to r') of the above integrand is determined by the exponentially decaying term

$$\exp\{\zeta_n(r')\} = \exp\left\{-\frac{(r')^2}{2p}\right\}.$$

The new variable

$$q = \exp\left\{-\frac{(r')^2}{2p}\right\}$$

maps the semi-infinite interval $[0, \infty)$ onto the finite interval $(0, 1]$, with $r \to \infty$ corresponding to $q \to 1$.

At this point we are faced with the choice of an optimal discretization for the q interval, so that the computation of the integrals is both *accurate* and ***flexible***. The satisfaction of both criteria is not a easy task. Most higher accuracy Gaussian quadrature formulae require a large number of "weights" and abscissas that

vary with the number of desired points, whereas equidistant, equal-weight formulae such as Simpson's rule suffer from poor accuracy. A quadrature formula based on Chebyshev polynomials of the first kind and of odd order was selected. It not only offers a high accuracy, but the weights and abscissas are simple functions of the number of points N_r, expressed in analytical form:

$$\int_0^1 f(y)\,dy = 2\pi \sum_{i=1}^{N_r} \frac{\sqrt{y_i(1-y_i)}}{2N_r+1} f(y_i), \tag{3.19}$$

where

$$y_i = \cos^2\left(\frac{2i-1}{2N_r+1}\frac{\pi}{2}\right).$$

The implementation of Eqs. (3.18-3.19) transforms the two-dimensional integral to a finite double sum in terms of the values of the integrands at selected points i, k in the q, η unit square (which is equivalent to the semi-infinite r, φ domain.)

The three-dimensional "convective" integrals I_3, I_4, H_3, and H_4 involve an additional integration in the z' direction. Again we examine a representative integral such as

$$\begin{aligned}
&\int d\mathbf{r}' \int_{\zeta_n(\mathbf{r}')}^{\infty} dz' \, \frac{\exp\{-\zeta_N(\mathbf{r}) + z'\}}{4\pi\,|\mathbf{x}_N - \mathbf{x}'|}\, \mathbf{v}_n(\mathbf{x}') \cdot \nabla_{\mathbf{x}'} T_n(\mathbf{x}') \\
&\times \left\{ \exp\{|\mathbf{x}_N - \mathbf{x}'|\} \left(\operatorname{erf}\left[\frac{|\mathbf{x}_N - \mathbf{x}'|}{2\sqrt{(N-n)\Delta t}} + \sqrt{(N-n)\Delta t} \right] \right.\right. \\
&\qquad \left. - \operatorname{erf}\left[\frac{|\mathbf{x}_N - \mathbf{x}'|}{2\sqrt{(N-n+1)\Delta t}} + \sqrt{(N-n+1)\Delta t} \right] \right) \\
&+ \exp\{-|\mathbf{x}_N - \mathbf{x}'|\} \left(\operatorname{erf}\left[\frac{|\mathbf{x}_N - \mathbf{x}'|}{2\sqrt{(N-n)\Delta t}} - \sqrt{(N-n)\Delta t} \right] \right. \\
&\qquad \left.\left. - \operatorname{erf}\left[\frac{|\mathbf{x}_N - \mathbf{x}'|}{2\sqrt{(N-n+1)\Delta t}} - \sqrt{(N-n+1)\Delta t} \right] \right) \right\},
\end{aligned}$$

found in Eq. (B8). The discretization of the $\int d\mathbf{r}'$ integral is identical to that of the two-dimensional integrals. For the z' integration the asymptotic behavior of

the integrand as $z' \to \infty$ is used to define a new variable transformation that maps the semi-infinite interval $[\zeta_n, \infty)$ onto the interval $(0, 1]$. It is easy to show that the integrand, excluding the dot product $\mathbf{v}_n(\mathbf{x}') \cdot \nabla_{\mathbf{x}'} T_n(\mathbf{x}')$, decays as $1/z'$ for $z' \to \infty$. As it was stated earlier, the behavior of the temperature and the velocity fields at large distances from the interface is determined by the corresponding "unperturbed" fields T_0 and $\mathbf{v}_0$. Although the flow velocity reaches a constant value, the temperature field decays exponentially as $z' \to \infty$ (see Chapter 2.) The integrand thus decays exponentially as $\exp\{-2(1+\lambda)z'\}$ for $z' \to \infty$, where λ represents the relative strength of the flow field. Define the variable

$$\xi = \exp\left\{-2(1+\lambda)\left[z' - \zeta_n(r')\right]\right\}$$

which is equal to unity on the interface $z' = \zeta_n(r')$ and approaches zero as $z' \to \infty$. Next use the quadrature scheme defined by Eq. (3.19) to discretize the transformed integral from $\xi = 0$ to $\xi = 1$ at the points ξ_m, $m = 1, 2, \ldots, N_z$, where

$$\xi_m = \cos^2\left(\frac{2m-1}{2N_z+1}\frac{\pi}{2}\right).$$

At this point we have a set of variable transformations and quadrature rules that transform the spatial integrals into weighted finite sums. Each term in the sums corresponds to a point $(q_i, \eta_{ik}, \xi_{im})^\star$, or

$$r_i = \sqrt{p \ln\left(\frac{1}{q_i}\right)},$$

$$\varphi_{ik} = \arccos\left(\frac{\alpha_i - \eta_{ik}^2}{\beta_i}\right),$$

$$z_{im} = \zeta(r_i) - \frac{1}{2(1+\lambda)}\ln(\xi_m),$$

---

* The double indices indicate the dependence of η_{ik} and ξ_{im} on q_i.

where $\alpha(r_i)$ and $\beta(r_i)$ were defined in Eq. (3.18). The discretized equivalent of each spatial integral is presented in Appendix C.

The integral equations (3.14) and (3.15) have now been transformed to a set of *non-linear* algebraic equations in terms of the interface shape $\zeta_n(r_i)$ and the temperature gradient $\nabla_{\mathbf{x}} T_n(r_i, z_m)$ at selected times t_n and locations (r_i, z_m). The non-linearity can be traced back to the evaluation of the Green's function along the interface. In contrast to the classical one-dimensional Stefan problem, the (generally unknown) curved shape of the interface cannot be represented by a constant coordinate surface. This, in turn, results in the explicit appearance of ζ (or, $\mathbf{x}_\Gamma$) as the argument of the Green's function in Eqs. (3.14-3.15). The discretized equations (3.14-3.15) can be written in the following concise manner*:

$$\Delta - \nu\mathcal{K}\{\zeta(r_j, t_N)\} = \sum_{n=1}^{N}\sum_{i=1}^{N_r}\sum_{k=1}^{N_\varphi} \mathcal{I}^D_{n,i,k;j,N}\{\zeta(r_i, t_n)\}$$
$$+ \sum_{n=1}^{N}\sum_{i=1}^{N_r}\sum_{k=1}^{N_\varphi}\sum_{m=1}^{N_z} \mathcal{I}^C_{n,i,k,m;j,N}\{\zeta(r_i, t_n), \mathbf{v}(r_i, z_m, t_{n-1})\cdot\nabla_{\mathbf{x}} T(r_i, z_m, t_{n-1})\}, \quad (3.20)$$

and the auxiliary equation

$$\mathbf{v}(r_i, z_m, t_{n-1})\cdot\nabla_{\mathbf{x}} T(r_i, z_m, t_{n-1})\} = \sum_{\sigma=0}^{n-1}\sum_{\mu=1}^{N_r}\sum_{\kappa=1}^{N_\varphi} \mathcal{H}^D_{\sigma,\mu,\kappa;i,n-1}\{\zeta(r_\mu, t_\sigma)\}$$
$$+ \sum_{\sigma=0}^{n-1}\sum_{\mu=1}^{N_r}\sum_{\kappa=1}^{N_\varphi}\sum_{l=1}^{N_z} \mathcal{H}^C_{\sigma,\mu,\kappa,l;i,n-1}\{\zeta(r_\mu, t_\sigma), \mathbf{v}(r_\mu, z_l, t_\sigma)\cdot\nabla_{\mathbf{x}} T(r_\mu, z_l, t_\sigma)\}, \quad (3.21)$$

where the interface is axisymmetric (ζ independent of k), $\mathcal{I}$ and $\mathcal{H}$ are the non-linear algebraic operators in Eqs. (C1-C8), and $\mathcal{K}$ is the curvature operator

$$\mathcal{K}\{\zeta(r,t)\} \equiv -\frac{r\zeta'' + (\zeta')^3 + \zeta'}{r\left[1 + (\zeta')^2\right]^{\frac{3}{2}}}. \quad (3.22)$$

---

* The superscripts $(^D)$ and $(^C)$ denote contributions from the "diffusive" and the "convective" integrals, respectively.

The velocity $\mathbf{v}_{n-1}(r_i, z_m)$ at time t_{n-1} is calculated from Eqs. (2.13), (D2), and (D12-D13). It represents the contribution of two terms: the "unperturbed" Oseen velocity, derived in Chapter 2, and a Stokes flow correction, calculated in Appendix D and representing the effect of the interface perturbation. Since the flow field is a solution of the quasistatic Oseen approximation to the Navier-Stokes equations, it satisfies the no-slip condition on the perturbed interface exactly and asymptotes to a constant velocity at infinity. The velocity is updated using the current interface position and is then used in Eqs. (3.20-3.21) to calculate the next interface position. It is worthy of note that in the case of pure diffusion, $\mathbf{v} = 0$. This simplifies Eq. (3.20) considerably since the spatial integration is eliminated, while Eq. (3.21) becomes obsolete since no interior values of the temperature gradient are required.

Eq. (3.20) represents the interface temperature at $r = r_j$ and at time $t = t_N$. By varying the index j from 1 to N_r, which corresponds to different radial distances from the z- axis, we can obtain N_r such equations for a given time $t = t_N$. If we assume that the all the variables at the times t_n, $n = 1, 2, \ldots, N-1$, are known, then the set of N_r non-linear algebraic equations

$$\begin{aligned}
&\Delta - \nu\mathcal{K}\{\zeta(r_j, t_N)\} - \sum_{i=1}^{N_r}\sum_{k=1}^{N_\varphi} \mathcal{I}^D_{N,i,k;j,N}\{\zeta(r_i, t_N)\} \\
&\qquad - \sum_{i=1}^{N_r}\sum_{k=1}^{N_\varphi}\sum_{m=1}^{N_z} \mathcal{I}^C_{N,i,k,m;j,N}\{\zeta(r_i, t_N), \mathbf{v}(r_i, z_m, t_{N-1}) \cdot \nabla_{\mathbf{x}} T(r_i, z_m, t_{N-1})\} \\
&= \sum_{n=1}^{N-1}\sum_{i=1}^{N_r}\sum_{k=1}^{N_\varphi} \mathcal{I}^D_{n,i,k;j,N}\{\zeta(r_i, t_n)\} + \sum_{n=1}^{N-1}\sum_{i=1}^{N_r}\sum_{k=1}^{N_\varphi}\sum_{m=1}^{N_z} \mathcal{I}^C_{n,i,k;j,N}\{\zeta(r_i, t_n), \\
&\qquad \mathbf{v}(r_i, z_m, t_{n-1}) \cdot \nabla_{\mathbf{x}} T(r_i, z_m, t_{n-1})\}, \; j = 1, 2, \ldots, N_r \quad (3.23)
\end{aligned}$$

can be solved to give the N_r unknowns, i.e. the interface shape at the points r_j, $j = 1, 2, \ldots, N_r$ (Note that the left-hand-side is expressed solely in terms of the unknown interface shape, whereas the right-hand-side contains only previously calculated quantities.)

Finally, by varying the value of N, we obtain a set of equations (3.23) representing the history of the interface position up to the corresponding time t_N. The sequential solution of these equations gives the interface position at $t = t_N$ as a function of previously calculated values at $t = t_n$, $n = 1, 2, \ldots, N-1$.

In the next section we will discuss the numerical characteristics of this methodology and present representative results.

3.2. DISCUSSION OF RESULTS

The non-linear set of Eqs. (3.23), the auxiliary Eq. (3.21) for the temperature gradient and Eqs. (2.13, D2, D12-D13) for the velocity represent the numerical approximation of the integral evolution equation for the interface shape. We will use these equations to examine the growth dynamics of the solid-liquid interface. The importance of quantities like surface tension and convective flow strength has already been established in the study of steady-state models. In this section we will first show that the interface tracking algorithm based on the above equations is numerically stable, convergent, and robust. We will then discuss our results which clearly demonstrate the significant role of surface tension and convection in the transient evolution of the dendritic interface.

The primary objective of this work was to develop an exact (i.e. without *ad hoc* approximations) mathematical scheme to represent the combined effects of interfacial tension and convective heat transport. This was achieved by transforming the governing set of equations into a tractable numerical scheme. In this section we present our current results and discuss several additions and generalizations that will extend the utility of our computational scheme. It will be shown that our algorithm is an effective tool for the study of spatial and temporal pattern formation.

The important input parameters are of two kinds. Numerical parameters, such as time step size and the number of quadrature points, determine the numerical characteristics of the algorithm. Their effect on the solutions is discussed in Sec. 3.2.a. The physical parameters (Péclet number, surface tension, flow strength, etc.) specify the characteristics of the physical system. The results from our calculations

at selected points of the parameter space are presented in Sec. 3.2.b. Finally, some concluding remarks and suggestions for future work are presented in Sec. 3.2.c.

3.2.a. Numerical Characteristics

This section describes the tests that were carried out to examine the robustness and accuracy of the numerical scheme. Representative results demonstrate the ability of the scheme to track known solutions such as Ivantsov's solution and the new "convective" steady-state solution. The convergence characteristics of the algorithm with respect to varying grid sizes and time steps were also studied. Fast convergence was achieved with a relatively small number of spatial and temporal discretization points.

The underlying basic state for the interface shape is determined by the Péclet number and the strength of the flow field. In the limiting case of no flow ($\lambda = 0$), the basic state is the Ivantsov steady-state paraboloid of revolution. As shown in Chapter 2, the paraboloidal shape of the interface is preserved for $\lambda \neq 0$ if the flow field satisfies certain conditions. Thus, the new "convective" steady-state solution, derived in Chapter 2, is used as the underlying basic state in the numerical calculations (since this solution reduces to Ivantsov's solution for $\lambda = 0$, there is no need to distinguish between the two). The test cases that were examined cover the range of moderate to high Péclet numbers (i.e., $p > 0.1$). Since the characteristic length is $2\alpha/V \equiv \rho/p$, smaller Péclet numbers decrease the resolution of the system and require a large number of spatial discretization points. A discussion of future improvements in the spatial discretization follows in Sec. 3.2.c.

The discretization of the integro-differential equations (3.14-15) combines the numerical approximation of derivatives and integrals by finite differences and finite

sums, respectively. The time derivative of the interface shape, $\dot{\zeta}$, in Eqs. (3.14-15) represents the perturbation on the interface velocity and can be approximated by a finite difference formula. An equivalent approach is to eliminate the time derivative altogether by integrating the corresponding time integrals in Eqs. (3-14-15) by parts. The first alternative was chosen since it provides one with the flexibility to start with either an initial perturbation on the interface shape or an initial perturbation on the interface velocity (the interface velocity is directly proportional to the gradient of the temperature field and is thus a good measure of thermal fluctuations in the temperature field around the crystal.)

The spatial integrals in the integral equation (3.14) are discretized using the coordinate transformations and the quadrature formulae presented in Section 3.1.b. The domain is mapped onto a unit cube and the number of the quadrature points in each of the three directions determines the spatial resolution of the system. As it was mentioned in the previous chapter, the interface shape, the temperature field, and the velocity field that correspond to a perturbed interface asymptote to the respective *unperturbed* quantities at large distances from the tip region. In the absence of flow, the Ivantsov paraboloid and the corresponding exponentially decaying temperature field represent the interface shape and the temperature field at infinite distances from the tip region. When flow is present, the Ivantsov solution is replaced by the "convective" steady-state solution presented in Chapter 2. The known asymptotic behavior can be incorporated into the integral formulation by replacing Δ in Eq. (3.14) with the steady-state integral expression Eq. (2.6). At large distances from the tip the integrands in the right-hand-side of Eq. (3.14) reduce to those of Eq. (2.6), since the interface shape approaches its unperturbed

state. As a result, the two sides of Eq. (3.14) cancel each other far from the tip and the integration need only be performed up to the point where there is no appreciable difference between the calculated interface shape and the corresponding unperturbed state. The minimum number of points required to adequately represent the interface shape is identified by examining the point furthest from the tip: if the calculated deviation from the unperturbed shape is small ($\mathcal{O}(10^{-3})$), then for $r > r_{N_r}$ the interface shape can be assumed to be that of the unperturbed steady-state paraboloid and no more points are required.

The first important test of the numerical scheme concerns *numerical noise*: in the absence of an externally imposed perturbation, the numerical solution should remain fixed onto the underlying basic state as time evolves. A wide range of flow strengths was studied ($0 \leq \lambda \leq 10$) and, in the absence of an *externally* imposed perturbation on the interface shape or velocity, no departure from the basic state was observed.* The calculations were carried out to arbitrarily large times, thus indicating that the accumulation of round-off error does not generate misleading numerical instabilities. This is an important result in itself since the corresponding basic states are often unstable to infinitesimal external perturbations, including random noise. The elimination of numerically driven instabilities enables us to concentrate on destabilizing mechanisms such as thermal fluctuations or interface shape perturbations. In addition, the amplification of random noise has been proposed as the triggering mechanism for sidebranch growth. Thus, the ability to distinguish

* Note that $\lambda = 1$ corresponds to a flow velocity that is equal to the freezing velocity of the crystal. For moderate to high supercoolings (or Péclet numbers), the freezing velocity of succinonitrile dendrites is of $\mathcal{O}$(cm/s), while comparable flow velocities were not observed [2].

between thermal and numerical noise (the latter being virtually uncontrolled) becomes important in the study of non-linear interaction of noise and sidebranching.

Several tests were carried out to examine the behavior of the solution as the number of points used to represent the interface shape and the field variables were changed. When a zero-surface-tension solution was used as an initial condition, the computed solution would stay on the initial condition as long as $\nu = 0$ and no external perturbation was imposed. However, once ν is changed, the system evolved to a new state to account for the effects of capillarity. The following procedure was used to test the convergence of the algorithm: The system was started with the zero-surface-tension solution in place, i.e. $\nu = 0$. Then ν was changed to a non-zero value and the system was allowed to evolve to a new state. Figures 7 and 8 show the behavior of the tip velocity for different numbers of discretization points in the $r-$ and φ-directions and for $p = 1$. The perturbation velocity at other points on the interface has a similar behavior. The results shown correspond to $\lambda = 0$ and $\nu = 0.001$. Similar results were obtained for $\lambda = 0.1$ and $\lambda = 1.0$, indicating that the convergence behavior of the algorithm is essentially independent of the strength of the convective flow in this range.

The point $r = 0$ is not a nodal point and thus one needs to extrapolate from the neighboring nodal points using a local Taylor series expansion for the interface shape. The 7 $r-$point result is fairly accurate and the 12 point result is almost indistinguishable from the 30 point case. (The maximum deviation from the 30 point result is 34% for the 7 point result and only 4% for the 12 point result.) The convergence is faster in the φ-direction and here less than 10 quadrature points give very accurate results: 23% and 2% maximum deviation from the 12 point result for

the 4 point and the 7 point case, respectively (see Fig. 8). The above results indicate that a small number of quadrature points is sufficient to accurately represent the growth velocity both in short and long times and over a variation of several orders of magnitude in the velocity.

While the number of quadrature points (N_r, N_φ, N_z) determines the spatial resolution of the model, the time step size determines the temporal resolution. The use of the time-dependent Green's function and the resulting time integration allows the choice of rather large time steps. As an alternative, one can use a time-differencing scheme, whereby the temporal derivative in the transient convective-diffusion equation (3.5) is approximated by a finite difference formula. However, the partial gain from the elimination of the time integration cannot compensate for the substantially smaller time steps required by time-differencing [14]. Figure 9 shows the tip velocity for different time steps and for $\lambda = 0.0$. Here again the zero surface tension solution was used as the initial condition and the system was allowed to evolve to a finite surface tension ($\nu = 0.001$) state. The results show that the algorithm is rather insensitive to variations of the time step size and, thus, large time steps give fairly accurate results. The time step $\Delta t = 0.1$ is quite large considering the fact that the system reaches a steady-state at times of order unity; however, the maximum deviation of the corresponding tip velocity from the $\Delta t = 0.002$ result is only 34%. (Similar results were obtained for $\lambda = 0.1$ and $\lambda = 1.0$). The larger time steps obviously cannot describe the evolution of the interface at very small times. Nevertheless, it is important to note that the final steady-state is predicted quite accurately by calculations with time steps varying over several orders of magnitude. This allows us to interchange large and small

time steps within a single run, thus accelerating the approach to the final state or increasing the resolution over a particular time interval.

At this point we reiterate that the global approach to a more-or-less identical steady-state, irrespective of time step size or number of quadrature points, implies that our solution scheme is both unusually robust and numerically stable. Considering the complexity of the mathematical problem and the transient, three-dimensional structure of the temperature field, this is a gratifying result.

3.2.b. Representative Results

The test cases that will be presented in this section demonstrate the effects of convection and capillarity on the evolution of the solid-liquid interface. The governing equations constitute an initial/boundary value problem in which the initial perturbation on the underlying basic state determines the short-time behavior of the system. The numerical approximation does not involve a linearization around the basic state and thus there is no limitation on the magnitude of the initial perturbation. At this point the algorithm is restricted to interface shapes $z = \zeta(r,t)$ that are single-valued functions of the radial coordinate r. (In simple terms, we are currently "counting" the surface elements that are located at the same radial coordinate r only once.) The formulation can be generalized by implementing a more general transformation of the surface integral in Eq. (A11) to account for multiple-valued functions of the radial coordinate. This loss of generality does not affect our results as long as the initial perturbations are sufficiently smooth functions of the radial coordinate. In testing the algorithm and in examining the effects

of surface tension and convection on the temporal and spatial evolution of the interface, we have chosen to use the zero-surface tension steady-state solutions as our initial conditions. These paraboloidal solutions (Ivantsov or "convective"), derived in Chapter 2, represent single-valued, long-wavelength perturbations on the underlying basic states with finite surface tension and can be used effectively in studying the role of surface tension.

The role of surface tension in the dynamics of the interface evolution is very important. In the zero surface tension limit and in the absence of flow, any perturbation, however weak, destabilizes the interface and in very short times *tip splitting* occurs with the tip region splitting into an increasing number of growing fingers. Tip splitting is characterized by the superposition of interface perturbations with an infinite spectrum of wavelengths. While the short end of the wavelength spectrum can only be represented by multiple-valued functions of the radial position, the long end of the spectrum is characterized by smoother, essentially single-valued, functions of the radial position. The quantitative validity of the calculations is currently restricted to single-valued interface shape functions and thus the growth of very short wavelength perturbations must be excluded. However, long-wavelength perturbations satisfy the single-valuedness requirement up to sufficiently long times and can be used effectively to study the dynamics of the interface. Isolated surface protrusions, smooth perturbations, and random noise were used to show that destabilization via tip splitting occurs invariably in the zero-surface-tension limit. Figure 10 demonstrates the effect of an interface perturbation on the stability of the interface. The initially smooth perturbation, centered at the tip, destabilized the interface into an increasing number of growing fingers. The qualitative features

of the interface destabilization were found to be independent of the amplitude or the structure of the externally imposed perturbation. Tip splitting was identified under a wide range of Péclet numbers (from 10^{-5} to 10) and flow strengths (from $\lambda = 0$ to $\lambda = 1$).

The fast convergence of the algorithm was demonstrated in the previous section. While the interface shape is generally independent of the number of interface discretization points for non-zero values of ν, it becomes strongly dependent at the limit of zero surface tension. This peculiar behavior stems from the special characteristics of the tip splitting mechanism and is backed by Langer's theoretical analysis of Ivantsov's solution [15]. Short wavelength perturbations grow faster and eventually dominate the interface shape. As a result, the wavelength of the fastest-growing mode is constrained by the spacing between adjacent points on the discretized interface. In the theoretical limit of the continuous interface, the fastest growing component of the spectrum corresponds to wavelength zero and the resulting interface shape resembles a growing "band". Although the calculated interface shapes are strongly dependent on the spatial discretization, is important to note that for a given grid spacing the resulting growth velocities are *independent* of the structure and magnitude of the initial perturbation.

The most striking result of the computations thus far has been the fact that small amounts of *isotropic* surface tension stabilize the interface. The forced perturbation on the interface shape at $t = 0$ does not lead to interface destabilization as in the zero-surface-tension case. As Figs. 11-12 indicate, finite surface tension stabilizes the perturbed interface when no flow is present. The perturbation growth velocity $\dot{\zeta}(\mathbf{r}, t)$, plotted *vs* the radial interface position for different times, finally

reaches a time-independent, spatially-uniform value, thus indicating that a steady-state has been reached. The *new* steady-state is characterized by a constant interface velocity $2 + \dot{\zeta}$ that is smaller than that of the corresponding zero-surface-tension state.*

In the initial stage of the interface evolution (i.e., approximately $t < 0.3$), the perturbation velocity $\dot{\zeta}$ increases with time and reaches a maximum value that varies along the interface. The stabilizing effect of capillarity is evident in Figs. 11-12. For $\nu = 0.020$, the perturbation velocity reaches a maximum value of about 20% of the corresponding zero-surface-tension value of 2 (see Eqs. (3.2) and (3.6) for the scaling of the freezing velocity). The growth of the perturbation is much slower in the case of a smaller surface-tension-parameter, i.e. $\nu = 0.001$. Figure 12 shows that the maximum value of the perturbation velocity $\dot{\zeta}$ is about 40 times smaller than that of the previous case. The magnitude of the capillary term in the evolution equation dictates the degree of interface rearrangement toward the new steady-state shape. As surface tension increases, the difference between the initial zero-surface-tension and the new finite-surface-tension states also increases and "faster" transition is required. This explains the strong dependence of the growth velocity on the surface-tension parameter ν during the early stage of evolution.

The zero-surface-tension case is characterized by interface instability via tip splitting. Irrespective of structure or magnitude, perturbations seem to focus on the tip and unstable fingers replace the paraboloidal tip. In the case of finite surface tension, however, tip splitting is absent and the maximum perturbation

* The underlying basic state for $t < 0$ is the zero-surface-tension steady-state solution, derived in Chapter 2. At $t = 0$, the surface tension becomes finite; this corresponds to imposing an interface perturbation, since the interface shape must conform to the new value of the surface-tension parameter.

velocity occurs at about one tip radius away from the tip (see Fig. 11). Given that interface instabilities concentrate on the tip, this result indicates that surface tension stabilizes the interface by "dissipating" the disturbance away from the tip.

As time elapses and the perturbation decays away from the tip, a slower phase of evolution sets in. The interface velocity becomes increasingly uniform and the velocity maximum moves close to the tip (see Figs. 11-12). At about $t = 1$ the perturbation growth velocity changes sign and finally approaches a constant negative value. The growth velocity $2 + \dot{\zeta}$ is thus smaller than that of the corresponding zero-surface-tension value of 2. The dependence of the total *steady-state* velocity on surface tension is rather weak (see Figs. 11-12), but the role of capillarity in the stabilization of the interface is important. There are two distict effects of surface tension on the growth velocity in Figs. 11-12:

(i) The initial perturbation is a function of surface tension and thus the initial stages of evolution *must* depend on surface tension. This dependence is evident for $t < 0.3$.

(ii) The stabilizing action of capillarity dictates the transition to the new steady-state and determines the value of the correction to the zero-surface-tension velocity of 2 as $t \to \infty$ (since $\nu \ll 1$ for most materials, the new steady-state interface shape and velocity are almost indistinguishable from those of the zero-surface-tension case).

Figure 15 shows that the dimensionless time required for the interface to reach its new steady state is about 5, thus indicating that the choice of the characteristic time $4\alpha/V^2$ in the scaling of the governing equations is appropriate (the final time recorded in each of the Figs. 11-14 represents a relative difference from the new

steady-state growth velocity of less than 10^{-3}). It is worthy of note that although the steady-state velocity differs only slightly from that of the zero-surface-tension case, the transition toward this new steady-state is rather complex and cannot be captured by a linearized evolution equation.

Only axisymmetric perturbations have been examined thus far. As a result, surface-tension anisotropy depends only on the angle θ between the interface normal and the z-axis. We can assume that the anisotropic correction to the surface tension, defined in Eq. (3.7), is equal to $\epsilon\nu\cos(4\theta)$, where ϵ represents a measure of the anistropy of the material and the factor 4 in the argument of the cosine corresponds to the fourfold symmetry of succinonitrile. Figure 15 indicates that in such a case, the anisotropic term in the interface evolution equation has a negligible effect on the interface dynamics for ϵ as large as unity. However, anisotropy has, by definition, a three-dimensional nature and the resulting interface shapes should, in general, be non-axisymmetric. A further discussion of anisotropy and three-dimensional calculations follows in the next section.

The combined effects of convection and capillarity on the interface velocity are shown in Figs. 13-14. For given supercooling Δ and flow strength λ, the zero-surface-tension solution, derived in Chapter 2, defines the underlying basic state for $t < 0$. At $t = 0$, ν changes value and thus a surface-tension dependent perturbation is imposed on the interface. The transient response of the interface varies with λ, but the interface invariably reaches a new steady-state. Figures 13 and 14 show the interface velocity as a function of the radial position at different times for $\lambda = 0.1$ and $\lambda = 1.0$, respectively. In comparing Figs. 13-14 with the corresponding Fig. 12 for $\lambda = 0.0$ ($\nu = 0.001$ and $Pe = 1$), it is important to note that each figure

corresponds to a different supercooling Δ, given by Eq. (2.20). Since the level of supercooling, and not the Péclet number, is controlled by the experimentalist, Fig. 6 can be used to obtain the correct Δ for given Pe and λ. However, for $\lambda \leq 1$ the differences are small and a constant Péclet number can be used. Furthermore, the flow strength $\lambda \equiv U_\infty/V$ depends on the scale factor for the freezing velocity, V. Since the actual velocity-tip radius relation is still unknown, V must be kept constant if one is to compare interface speeds corresponding to different levels of convection.

As in the $\lambda = 0$ case, the interface is quickly reshaped to conform to the new value of surface tension. The qualitative characteristics of interface evolution remain the same, but the coupling of capillarity and convection produces a more complex transition toward the new steady-state. Figures 13 (i.e. $\lambda = 0.1$) and 14 (i.e. $\lambda = 1.0$) show a perturbation-velocity maximum of about 1.6% and 13.0% of the corresponding zero-surface-tension value of 2, respectively (the $\lambda = 0.0$ value is 0.5%). In addition, a comparison of Figs. 12-14 suggests that the "dissipation" of the disturbance away from the tip becomes slower as λ increases (note the increasing number of local velocity maxima in the $t = 0.2$ curves). This non-linear interaction of the flow field and the interface disturbance seems to be linked to the orientational dependence of the interface morphology shown in Fig. 3 (the rigorous analysis of this phenomenon requires a φ-dependent flow field and is discussed in a later section).

After the initial reshaping, the interface slowly approaches its new steady-state, characterized by a negative correction to the zero-surface-tension interface velocity of 2. Figure 15 shows the decay of the perturbation velocity at the tip toward its steady-state value. For $\lambda = 1.0$, $\dot{\zeta}(0,t = 0.3)$ and $\dot{\zeta}(0,t \to \infty)$ are equal to 5.5%

and (7.5%) of the zero-surface-tension steady-state value of 2. For $\lambda = 0.1$, these values are about one order of magnitude smaller. As in the case of $\lambda = 0.0$, the time required for the interface to reach its new steady-state is approximately 5.

In conclusion, the total steady-state interface velocity decreases monotonically with respect to both increasing surface tension and flow strength. However, the calculations for $\nu = 0$ suggest that convection does not contribute to the stabilization of the interface. In the following section some conclusions are drawn and several ideas for future development are presented.

3.2.c. Conclusions and future work

1. Conclusions

The primary results of this chapter are the following:

(i) A non-linear tracking algorithm, based on the integral transformation of the transient convective-diffusion equation, has been developed for the study of complex growth forms. The ability to treat finite amplitude disturbances and the applicability to arbitrary geometries make this numerical scheme a valuable tool in the understanding of pattern formation. Analogous formulations have been used in the past for the study of dendritic growth and viscous fingering in Hele-Shaw flow cells [3,4]. The most important differences between this analysis and the ones preceeding it are:

1. The temporal derivative in the convective-diffusion equation has been neglected in previous quasistatic models. Howevr, scaling arguments show that at large supercoolings this term becomes imprortant and cannot be

ignored, at the expense of time integrals that are quite cumbersome to calculate.

2. The study of the convective effects on the interface evolution requires the calculation of spatial integrals over the entire liquid region, absent from similar work on diffusion-controlled growth. The algorithm employs a series of variable transformations and an *optimal* set of Gaussian quadrature points that evolves in time so that the temperature field is calculated at the *minimum* number of interior points.

3. The interface shape appears in the non-linear kernel of the integral equation. Previous efforts to linearize the evolution equation and carry out a linear stability analysis do not capture the non-linear features of dendritic growth. Sidebranching and tip splitting can be thought of as results of the non-linear interaction of interface perturbations and capillary forces. The algorithm presented here applies the Newton's iteration method to solve the non-linear evolution equation as a function of time and space. It can thus be used to address important issues such as the amplification of finite amplitude noise and the origination of sidebranches.

(ii) The numerical characteristics of the algorithm were tested as a function of the spatial and the temporal discretization of the interface. Fast convergence was achieved with a small number of quadrature points. In addition, the solutions are rather insensitive to the time step used for the discretization of the temporal integrals. Finally, in the absence of an externally imposed perturbation, the algorithm tracks the underlying basic state and numerical noise does not introduce artificial instabilities.

(iv) The tip was found unstable to *finite* amplitude perturbations if the effects of capillarity are ignored. The dominant destabilization mechanism is tip splitting. The tip region degenerates into a increasing number of unstable fingers and interface perturbations of arbitrary amplitude seem to invariably focus themselves on the tip region. This result, which is independent of the flow strength, represents the first evidence that tip splitting is not restricted to infinitesimal perturbations.

(v) Surface tension, however small, appears to stabilize the crystal interface for any flow strength by "dissipating" the disturbance away from the tip. A steady-state is always reached, irrespective of the structure or the magnitude of the initial perturbation on the interface shape. The growth velocity of the dendrite decreases with increasing surface tension but the difference from the zero-surface-tension case is small.

(vi) Anisotropy does not appear to have an important effect, qualitatively or quantitatively, on the dynamics of the interface. However, fully-three-dimensional (i.e., non-axisymmetric) perturbations will need to be tested before a complete understanding of the role of anisotropy can be gained.

(vii) Convection reduces the total growth velocity of the new steady-state, but does not seem to contribute to the stabilization of the interface. In the zero-surface-tension case, convection does not affect the qualitative features of tip splitting. However, the role of convection in the low supercooling regime needs further investigation and is discussed later in this section.

(viii) The operating point of the dendrite is not established from the non-linear analysis presented here. However, the results of the analysis call into question

all those obtained with the linearized theories now extant. Consider, first, the marginal stability hypothesis. Given the robust stability of shapes investigated here, it appears that the marginal stability hypothesis is wrong. The surface-tension adjusted shapes are found to be stable to finite amplitude perturbations. Thus, the central feature of marginal stability, a critical value of σ, simply does not exist when surface tension is considered in the context of finite amplitude effects. Second, microscopic solvability appears incomplete, at best. All the shapes investigated in this work are *stable* when finite amplitude effects were considered. Yet one feature of microscopic solvability is that only the fastest growing, smooth tip is stable. If this conclusion holds when finer resolution is considered at the tip, then the operating point selection mechanism is even more subtle than the microscopic solvability would suggest.

2. Future Work

The first extension of this work should be toward the study of three-dimensional (i.e. non-axisymmetric) interface perturbations. Since the formulation is applicable to fully three-dimensional systems and since the modification to anisotropic surface tension is straightforward, this numerical scheme can be used to test the microscopic solvability theory under the most general conditions of transient interface growth. The validity of the microscopic solvability theory at finite times can also be tested in a different way. Instead of prescribing the amount of surface tension and the corresponding anisotropy and then examining the slope at the tip, one can do the opposite: fix the tip slope to be zero and then calculate the time dependence of

the capillary parameters. The algorithm requires the solution of a set of non-linear equations with an equal number of unknowns. A logical choice for the set of unknown variables would be the interface shape function ζ calculated at the various quadrature points. However, there is no mathematical restriction applying to the replacement of one or more of these unknowns with an equivalent number of the physical parameters of the system. Therefore, by fixing the slope at the tip, one of the unknowns is effectively eliminated and a new degree of freedom is introduced in the physical parameter space. By allowing the amount of surface tension anisotropy (or, the amount of surface tension itself) to vary, one will be able to monitor the microscopic solvability condition through time and thus test its validity in transient dendritic growth.

The accurate calculation of the slope requires a fine discretization of the tip area. At the present time a high density of points close to the tip cannot be prescribed without introducing an unnecessarily large number of discretization points in the radial direction. This stems from the nature of the Gaussian quadrature formulae and the associated fixed distribution of points within a given interval. Future refinements of the algorithm should include a choice of "specialized" quadrature schemes in addition to the all-purpose Gaussian quadrature scheme presented here. Such flexibility would also speed up computations and reduce storage requirements in the case of an initial perturbation with a narrow range of wavelengths. Calculations for long wavelength perturbations require a "larger" domain but make no use of the increased resolution of the tip region, with the opposite being true for short-wavelength perturbations localized at the tip.

Experimental evidence indicates that the effects of convection become important at very low supercoolings ($\Delta \leq 0.05$) [2]. All the computations, however, were done at Péclet numbers greater than 0.1 which belong to the "diffusive" regime (see Chapter 2). The study of convection at lower Péclet numbers (or supercooling levels) requires a higher spatial resolution around the tip. In Sec. 3.1.a the length scale is defined as $2\alpha/V$. Using the definition of Péclet number ($p = V\rho/2\alpha$, where ρ is the tip radius of curvature), the above scale becomes ρ/p. For small Péclet numbers, it is obvious that this length scale is much larger than the tip radius and the spatial resolution in the tip region is severely decreased. Therefore, at low Péclet numbers, where convection is expected to play a stronger role, the tip radius ρ should be used as the more appropriate length scale near the tip. Also, values of λ greater than unity are possible in the low supercooling regime where the freezing velocities are quite small. It thus remains to be seen whether the use of a finer scale will show that convection qualitatively affects the stability of the freezing interface at low supercoolings.

Finally, the convective steady-state solution, derived in Chapter 2, applies only to axisymmetric flow fields, oriented along the z—axis. The study of the orientation-dependent elimination of sidebranches, shown in Fig. 3, requires the use of more general (i.e non-axisymmetric) flow fields. The integral formulation is not restricted to axisymmetric flow fields and can thus be used to examine growth subject to an arbitrary flow field (at the expense of an increase in the dimensionality of the equation and in the computation time).

REFERENCES

[1] J. S. Langer, Acta Metall. 25 (1977) 1121.

[2] M. E. Glicksman and S. C. Huang, Proc. 87th Natl. AIChE Meeting, Boston, August 1979; M. E. Glicksman and S. C. Huang, Proc. 3rd European Symp. on Material Sciences in Space, Grenoble, April 1979; S. C. Huang and M. E. Glicksman, Acta Metall. 29 (1981) 701.

[3] D. I. Meiron, Phys. Rev. A 33 (1986) 2704.

[4] D. A. Kessler, J. Koplik, and H. Levine, Phys. Rev. A 33 (1986) 3352.

[5] R. T. Delves, in: Crystal Growth (R. Pamplin, Ed., Pergamon Press, Oxford, 1975).

[6] C. W. Oseen, Neuere Methoden und Ergebnisse in der Hydrodynamik (Akademische Verlag, Leipzig, 1927).

[7] G. K. Youngren and A. Acrivos, J. Fluid Mech. 69 (1975) 377.

[8] B. Caroli, C. Caroli, B. Roulet, and J. S. Langer, Phys. Rev. A 33 (1986) 442.

[9] J. S. Langer, Phys. Rev. A 33 (1986) 435.

[10] P. Pelce and Y. Pomeau, Stud. Appl. Math. 74 (1986) 245.

[11] D. A. Kessler and H. Levine, Phys. Rev. Lett. 57 (1986) 3069.

[12] G. P. Ivantsov, Dokl. Akad. Nauk SSSR 58 (1947) 567.

[13] M. Abramowitz and I. A. Stegun, Eds., Handbook of Mathematical Functions, Applied Mathematics Series 55 (NBS, Washington, 1964).

[14] D. A. S. Curran, M. Cross, and B. A. Lewis, Appl. Math. Modelling 4 (1980) 398.

[15] J. S. Langer and H. Müller-Krumbhaar, Acta Metall. 26 (1978) 1681.

C-2

[16] B. Cantor and A. Vogel, J. Crystal Growth 41 (1977) 109.

APPENDIX A:

Derivation of the integral equation

In this appendix we derive the integro-differential equation that describes the evolution of the dendritic interface. The transient convective-diffusion equation is first written in differential form:

$$\frac{\partial \tilde{T}}{\partial \tilde{t}} + \tilde{\mathbf{v}} \cdot \nabla_{\tilde{\mathbf{x}}} \tilde{T} - \alpha \nabla^2_{\tilde{\mathbf{x}}} \tilde{T} - V \frac{\partial \tilde{T}}{\partial \tilde{z}} = 0, \qquad (A1a)$$

where $\tilde{\mathbf{x}} = (\tilde{x}, \tilde{y}, \tilde{z}) = (\tilde{\mathbf{r}}, \tilde{z}) = (\tilde{r}, \tilde{\varphi}, \tilde{z})$, α is the thermal diffusivity and $V\mathbf{i}_z$ is the constant velocity of the moving coordinate system. The hydrodynamic velocity field $\tilde{\mathbf{v}}$ satisfies the no-slip condition on the interface and is zero in the solid. Under the assumptions of the two-sided model proposed by Langer [1], the thermal diffusivities and the densities of the two phases are considered constant. We scale lengths with $2\alpha/V$ and times with $4\alpha/V^2$:

$$\frac{\partial T}{\partial t} + 2\lambda \mathbf{v} \cdot \nabla_{\mathbf{x}} T - \nabla^2_{\mathbf{x}} T - 2\frac{\partial T}{\partial z} = 0, \qquad (A1b)$$

where $\lambda \equiv U_\infty / V$ is the ratio of the characteristic fluid velocity scale to the velocity of the coordinate system and $T = (\tilde{T} - T_\infty) c_p / L$. The temperature field vanishes as $z \to \infty$ and is also constant as $z \to -\infty$:

$$\lim_{z \to \pm\infty} T(\mathbf{x}, t) \to \text{constant}. \qquad (A1c)$$

The temperature also satisfies the thermodynamic boundary condition

$$T_\Gamma = \Delta - \nu \mathcal{K}\{\zeta(\mathbf{r}, t)\} \qquad (A1d)$$

with $\Delta = (T_M - T_\infty)c_p/L$ and $\nu \equiv d_0 V/2\alpha$; $\mathcal{K}$ is the dimensionless curvature. Finally, heat conservation at the interface requires that

$$\hat{\mathbf{n}} \cdot \nabla_{\mathbf{x}} T_{(\text{liquid})} - \hat{\mathbf{n}} \cdot \nabla_{\mathbf{x}} T_{(\text{solid})} = -\left[2 + \dot{\zeta}(\mathbf{r}, t)\right] \hat{\mathbf{n}} \cdot \mathbf{i}_z. \qquad (A1e)$$

We now introduce the fundamental solution $G(\mathbf{x}, \mathbf{x}'; t - t')$ of the transient diffusion equation in an unbounded domain; in the moving coordinate system, it is defined by

$$\frac{\partial G}{\partial t'} - \nabla^2_{\mathbf{x}'} G - 2\frac{\partial G}{\partial z'} = -\delta(\mathbf{x} - \mathbf{x}')\,\delta(t - t'). \qquad (A2)$$

and $G(\mathbf{x}, \mathbf{x}'; t - t') \equiv 0$ for $t < t'$. The fundamental solution (or *Green's function*) is

$$G(\mathbf{x}, \mathbf{x}'; t - t') = \frac{H(t - t')}{[4\pi(t - t')]^{\frac{3}{2}}} \exp\left\{-\frac{|\mathbf{r} - \mathbf{r}'|^2 + [z - z' + 2(t - t')]^2}{4(t - t')}\right\}, \qquad (A3)$$

where $H(t - t')$ is Heaviside's step function [1]. By taking the Fourier transform of Eq. (A2), Langer [1] derived the following integral representation of $G(\mathbf{x}, \mathbf{x}'; t - t')$:

$$G(\mathbf{x}, \mathbf{x}'; t - t') = \int_{-\infty}^{\infty} \frac{d\omega}{2\pi} \int \frac{d\mathbf{k}}{(2\pi)^3} \frac{e^{i\omega(t-t') + i\mathbf{k}\cdot(\mathbf{x}-\mathbf{x}')}}{i\omega + k^2 - 2ik_z}. \qquad (A4)$$

Following the notation of Caroli *et al.* [2], we define: $t_- \equiv \lim_{c \to 0+} (t - c)$. Then

$$G(\mathbf{x}, \mathbf{x}'; t - t_-) = \delta(\mathbf{x} - \mathbf{x}'). \qquad (A5)$$

Let $\mathbf{k} = \mathbf{q} + k_z \mathbf{i}_z$. Eq. (A4) then becomes [2]

$$G(\mathbf{x}, \mathbf{x}'; t - t') = \int_{-\infty}^{\infty} \frac{d\omega}{2\pi} e^{i\omega(t-t')} \qquad (A6)$$
$$\int \frac{d\mathbf{q}}{(2\pi)^2} \frac{e^{i\mathbf{q}\cdot(\mathbf{r}-\mathbf{r}')}}{2[m(q,\omega) - 1]} \exp\left(-\{z - z' + |z - z'|[m(q,\omega) - 1]\}\right),$$

where

$$m(q,\omega) = 1 + (1 + i\omega + q^2)^{\frac{1}{2}} \tag{A7}$$

with $\mathrm{Re}(1 + i\omega + q^2)^{\frac{1}{2}} > 0$.

We now multiply Eqs. (A1b) and (A2) with $G(\mathbf{x},\mathbf{x}';t-t')$ and $T(\mathbf{x}',t')$, respectively, add and integrate in time and space:

$$\begin{aligned}
&\int_{-\infty}^{t-} dt' \int d\mathbf{r}' \int_{-\infty}^{\infty} dz' \left\{ G(\mathbf{x},\mathbf{x}';t-t') \frac{\partial T(\mathbf{x}',t')}{\partial t'} + T(\mathbf{x}',t') \frac{\partial G(\mathbf{x},\mathbf{x}';t-t')}{\partial t'} \right\} + \\
&\int_{-\infty}^{t-} dt' \int d\mathbf{r}' \int_{-\infty}^{\infty} dz' \left\{ -G(\mathbf{x},\mathbf{x}';t-t') \nabla^2_{\mathbf{x}'} T(\mathbf{x}',t') + T(\mathbf{x}',t') \nabla^2_{\mathbf{x}'} G(\mathbf{x},\mathbf{x}';t-t') \right\} + \\
&\int_{-\infty}^{t-} dt' \int d\mathbf{r}' \int_{-\infty}^{\infty} dz' \left\{ -2G(\mathbf{x},\mathbf{x}';t-t') \frac{\partial T(\mathbf{x}',t')}{\partial z'} - 2T(\mathbf{x}',t') \frac{\partial G(\mathbf{x},\mathbf{x}';t-t')}{\partial z'} \right\} + \\
&\int_{-\infty}^{t-} dt' \int d\mathbf{r}' \int_{\zeta(\mathbf{r}',t')}^{\infty} dz' 2\lambda\, G(\mathbf{x},\mathbf{x}';t-t') \mathbf{v}(\mathbf{x}',t') \cdot \nabla_{\mathbf{x}'} T(\mathbf{x}',t') \quad = 0,
\end{aligned} \tag{A8}$$

where the lower limit for the z' integration in the last term is $\zeta(\mathbf{r}',t')$ since the velocity $\mathbf{v}$ is zero for $z' < \zeta(\mathbf{r}',t')$.

By grouping similar derivatives together and applying Green's 2nd theorem to the second term in the left-hand-side of Eq. (A8) we get

$$\begin{aligned}
&\int_{-\infty}^{t-} dt' \int d\mathbf{r}' \int_{-\infty}^{\infty} dz' \frac{\partial}{\partial t'} \left[G(\mathbf{x},\mathbf{x}';t-t') T(\mathbf{x}',t') \right] + \\
&\int_{-\infty}^{t-} dt' \int d\Gamma' \hat{\mathbf{n}}' \cdot \Big[G(\mathbf{x},\mathbf{x}_\Gamma'(\mathbf{r}',t');t-t') \nabla_{\mathbf{x}'} T(\mathbf{x}',t') \\
&\qquad\qquad - T(\mathbf{x}',t') \nabla_{\mathbf{x}'} G(\mathbf{x},\mathbf{x}_\Gamma'(\mathbf{r}',t');t-t') \Big] - \\
&\int_{-\infty}^{t-} dt' \int d\mathbf{r}' \int_{-\infty}^{\infty} dz' 2 \frac{\partial}{\partial z'} \left[G(\mathbf{x},\mathbf{x}';t-t') T(\mathbf{x}',t') \right] + \\
&\int_{-\infty}^{t-} dt' \int d\mathbf{r}' \int_{\zeta(\mathbf{r}',t')}^{\infty} dz' 2\lambda\, G(\mathbf{x},\mathbf{x}';t-t')\, \mathbf{v}(\mathbf{x}',t') \cdot \nabla_{\mathbf{x}'} T(\mathbf{x}',t') \quad = 0.
\end{aligned} \tag{A9}$$

The second term represents integration over a surface *enclosing* the interface and placed at an infitesimal distance from it.

Next the z' integration in the third term of Eq. (A9) is performed so that the term becomes

$$-2\int_{-\infty}^{t_-} dt' \int d\mathbf{r}' \Big[\lim_{z_1\to\infty} G(\mathbf{x};\mathbf{r}',z_1;t-t')T(\mathbf{r}',z_1,t') - \lim_{z_1\to-\infty} G(\mathbf{x};\mathbf{r}',z_1;t-t')T(\mathbf{r}',z_1,t')\Big].$$

From Eq. (A1c) we know that the temperature as $z \to \infty$ is zero and thus the first term in the above expression vanishes. The temperature reaches a constant value at $z \to -\infty$ and can be taken out of the integral sign so the remaining integral is

$$\int_{-\infty}^{t_-} dt' \int d\mathbf{r}' \lim_{z_1\to\infty} G(\mathbf{x};\mathbf{r}',z_1;t-t').$$

Using Eq. (A7) and the fact that $\lim_{c\to 0+} G(\mathbf{x},\mathbf{x}';-c) = 0$, the integral can be written as

$$\lim_{z_1\to\infty} \int_{-\infty}^{\infty} dt' \int d\mathbf{r}' \int_{-\infty}^{\infty} \frac{d\omega}{2\pi} e^{i\omega(t-t')} \int \frac{d\vec{q}}{(2\pi)^2} \frac{e^{i\vec{q}\cdot(\mathbf{r}-\mathbf{r}')-(z-z_1)[2-m(q,\omega)]}}{2[m(q,\omega)-1]} = 0.$$

Thus, the third term in Eq. (A9) does not survive even if the the temperature at negative infinity is non-zero.

We can now perform the time integration in the first term of Eq. (A9):

$$\int d\mathbf{r}' \int_{-\infty}^{\infty} dz' \left[G(\mathbf{x},\mathbf{x}';t-t_-)T(\mathbf{x}',t_-) - \lim_{t'\to-\infty} \{G(\mathbf{x},\mathbf{x}';t-t')T(\mathbf{x}',t')\} \right].$$

With the help of Eq. (A5) and of the fact that $\lim_{t'\to-\infty} G(\mathbf{x},\mathbf{x}';t-t') = 0$, this integral becomes

$$\int d\mathbf{x}' \delta(\mathbf{x}-\mathbf{x}')T(\mathbf{x}',t_-) = T(\mathbf{x},t), \qquad (A10)$$

where t_- has been replaced by t since the temperature is a continuous function of time.

Returning to Eq. (A9), we find

$$T(\mathbf{x},t) =$$
$$\int_{-\infty}^{t-} dt' \int d\Gamma' \hat{\mathbf{n}}' \cdot \Big[G(\mathbf{x}, \mathbf{x}_\Gamma'(\mathbf{r}',t'); t-t') \nabla_{\mathbf{x}'} T(\mathbf{x}',t') - T(\mathbf{x}',t') \nabla_{\mathbf{x}'} G(\mathbf{x}, \mathbf{x}_\Gamma'(\mathbf{r}',t'); t-t') \Big] +$$
$$\int_{-\infty}^{t-} dt' \int d\mathbf{r}' \int_{\zeta(\mathbf{r}',t')}^{\infty} dz' 2\lambda\, G(\mathbf{x},\mathbf{x}'; t-t') \mathbf{v}(\mathbf{x}',t') \cdot \nabla_{\mathbf{x}'} T(\mathbf{x}',t'). \qquad (A11)$$

Since the domain Ω is infinite, we assume that it is bounded by a surface that has been removed to infinity. Langer [1] has shown that in the absence of external fluxes, the contribution of this outer surface to the second term of Eq. (A11) is zero. We thus restrict our attention to the crystal-melt interface Γ. The surface integral in Eq. (A11) contains the boundary values of the temperature and its normal derivative and the continuity of the temperature implies that the term proportional to the gradient of the Green's function cancels out. We can now evaluate the remaining term, proportional to the normal component of the temperature gradient, using Eq. (A1e):

$$T(\mathbf{x},t) = \int_{-\infty}^{t-} dt' \int d\mathbf{r}' \left[2 + \dot{\zeta}(\mathbf{r}',t') \right] G(\mathbf{x}, \mathbf{x}_\Gamma'(t'); t-t')$$
$$- 2\lambda \int_{-\infty}^{t-} dt' \int d\mathbf{r}' \int_{\zeta(\mathbf{r}',t')}^{\infty} dz' G(\mathbf{x},\mathbf{x}'; t-t')\, \mathbf{v}(\mathbf{x}',t') \cdot \nabla_{\mathbf{x}'} T(\mathbf{x}',t'), \quad (A12)$$

since for *single-valued* $z = \zeta(\mathbf{r},t)$ it is true that

$$\hat{\mathbf{n}} \cdot \mathbf{i}_z \, d\Gamma = d\mathbf{r} = r \, dr \, d\varphi.$$

Equation (A12) is the integral equivalent of the transient convective-diffusion equation in the moving coordinate system. In the case of a steadily propagating

interface, i.e. with a uniform velocity equal to that of the coordinate system, Eq. (A12) reduces to the *steady-state* equation

$$T(\mathbf{x}) = 2\int d\mathbf{r}' G_{ss}(\mathbf{x}, \mathbf{x}_\Gamma') - 2\lambda \int d\mathbf{r}' \int_{\zeta(\mathbf{r}')}^{\infty} dz' G_{ss}(\mathbf{x}, \mathbf{x}')\ \mathbf{v}(\mathbf{x}') \cdot \nabla_{\mathbf{x}'} T(\mathbf{x}'). \quad (A13)$$

Here $G_{ss}(\mathbf{x}, \mathbf{x}')$ represents the Green's function that corresponds to steady diffusion in the moving coordinate system and is given by

$$G_{ss}(\mathbf{x}, \mathbf{x}') = \int_{-\infty}^{t-} dt'\, G(\mathbf{x}, \mathbf{x}', t - t'). \quad (A14)$$

The integral equation that corresponds to the *one-sided* model is identical to Eq. (A12) at the limit of zero-surface-tension since there is no flux through the isothermal solid. In the presence of surface tension, the convective effects are represented by a term identical to that of Eq. (A13). On the other hand, the diffusive contribution is with the one sided model is different since heat cannot flow through the solid ($\alpha_S = 0$). The derivation of the corresponding "diffusion" term has been presented by Caroli *et al.* [2].

References:

[1] J. S. Langer, Acta Metall. 25 (1977) 1121.

[2] B. Caroli, C. Caroli, B. Roulet, and J. S. Langer, Phys. Rev. A 33 (1986) 442.

APPENDIX B: Temporal discretization

In this appendix the time discretization of the integral evolution equations (3.14-3.15) is described.

$$T_\Gamma = \Delta - \nu\mathcal{K}\{\zeta(\mathbf{r},t)\} = \int_{-\infty}^{t_-} dt' \int d\mathbf{r}' \left[2 + \dot{\zeta}(\mathbf{r}',t')\right] G(\mathbf{x}_\Gamma(t), \mathbf{x}_\Gamma{}'(t'); t-t')$$
$$- 2\lambda \int_{-\infty}^{t_-} dt' \int d\mathbf{r}' \int_{\zeta(\mathbf{r}',t')}^{\infty} dz' G(\mathbf{x}_\Gamma(t), \mathbf{x}'; t-t')\ \mathbf{v}(\mathbf{x}',t') \cdot \nabla'_x T(\mathbf{x}',t'), \quad (B1)$$

$$\nabla_x T(\mathbf{x},t) = \int_{-\infty}^{t_-} dt' \int d\mathbf{r}' \left[2 + \dot{\zeta}(\mathbf{r}',t')\right] \nabla_x G(\mathbf{x}, \mathbf{x}_\Gamma{}'(t'); t-t')$$
$$- 2\lambda \int_{-\infty}^{t_-} dt' \int d\mathbf{r}' \int_{\zeta(\mathbf{r}',t')}^{\infty} dz' \nabla_x G(\mathbf{x}, \mathbf{x}'; t-t')\ \mathbf{v}(\mathbf{x}',t') \cdot \nabla'_x T(\mathbf{x}',t'). \quad (B2)$$

From $t = -\infty$ to $t = t_0$, the interface shape, the temperature field, and the flow field are represented by steady-state solutions denoted by the subscript $(_0)$. At time $t = t_0$ a perturbation on either the interface shape, or the temperature field, or other boundary conditions causes deviation from the steady-state; the time integrals in Eqs. (B1-B2) can then be split in two parts:

$$T_\Gamma = \Delta - \nu\mathcal{K}\{\zeta(\mathbf{r},t)\} = \int_{-\infty}^{t_0} dt' \int d\mathbf{r}'\, 2\, G(\mathbf{x}_\Gamma(t), \mathbf{x}_{\Gamma 0}{}'(t'); t-t')$$
$$+ \int_{t_0}^{t_-} dt' \int d\mathbf{r}' \left[2 + \dot{\zeta}(\mathbf{r}',t')\right] G(\mathbf{x}_\Gamma(t), \mathbf{x}_\Gamma{}'(t'); t-t')$$
$$- 2\lambda \int_{-\infty}^{t_0} dt' \int d\mathbf{r}' \int_{\zeta_0(\mathbf{r}')}^{\infty} dz' G(\mathbf{x}_\Gamma(t), \mathbf{x}'; t-t')\ \mathbf{v}_0(\mathbf{x}') \cdot \nabla'_x T_0(\mathbf{x}')$$
$$- 2\lambda \int_{t_0}^{t_-} dt' \int d\mathbf{r}' \int_{\zeta(\mathbf{r}',t')}^{\infty} dz' G(\mathbf{x}_\Gamma(t), \mathbf{x}'; t-t')\ \mathbf{v}(\mathbf{x}',t') \cdot \nabla'_x T(\mathbf{x}',t'), \quad (B3)$$

$$\nabla_x T(\mathbf{x},t) = \int_{-\infty}^{t_0} dt' \int d\mathbf{r}'\, 2\, \nabla_x G(\mathbf{x}, \mathbf{x}_{\Gamma 0}{}'(t'); t-t')$$

$$+\int_{t_0}^{t-}dt'\int d\mathbf{r}'\left[2+\dot{\zeta}(\mathbf{r}',t')\right]\nabla_x G(\mathbf{x},\mathbf{x_\Gamma}'(t');t-t')$$
$$-2\lambda\int_{-\infty}^{t_0}dt'\int d\mathbf{r}'\int_{\zeta_0(\mathbf{r}')}^{\infty}dz'\nabla_x G(\mathbf{x},\mathbf{x}';t-t')\,\mathbf{v}_0(\mathbf{x}')\cdot\nabla_x' T_0(\mathbf{x}')$$
$$-2\lambda\int_{t_0}^{t-}dt'\int d\mathbf{r}'\int_{\zeta(\mathbf{r}',t')}^{\infty}dz'\nabla_x G(\mathbf{x},\mathbf{x}';t-t')\,\mathbf{v}(\mathbf{x}',t')\cdot\nabla_x' T(\mathbf{x}',t'). \quad (B4)$$

Let $\tau = t_N - t'$ and

$$\mathbf{x_\Gamma}(\mathbf{r},t_n) = \mathbf{x}\Big(\mathbf{r},\zeta(\mathbf{r},t_n)\Big) = \mathbf{x_n}(\mathbf{r}), \qquad n=0,1,\ldots,N.$$

The first integral in Eq. (B3) becomes

$$I_1 = \int_{t_N-t_0}^{\infty}d\tau\int d\mathbf{r}'\,2\,G(\mathbf{x_N},\mathbf{x_0}';\tau)$$
$$= \int_{t_N-t_0}^{\infty}d\tau\int d\mathbf{r}'\,\frac{1}{4(\pi\tau)^{\frac{3}{2}}}\exp\left\{\frac{-|\mathbf{x_N}-\mathbf{x_0}'|^2}{4\tau}-\tau-\zeta_N+\zeta'_0\right\},$$

where

$$|\mathbf{x_N}-\mathbf{x_n}'|^2 = |\mathbf{r}-\mathbf{r}'|^2+(\zeta_N-\zeta_n')^2, \qquad n=0,1,\ldots,N,$$

and

$$\zeta(\mathbf{r}',t_n)=\zeta_n'.$$

Let

$$\omega = \frac{|\mathbf{x_N}-\mathbf{x_0}'|}{2\sqrt{\tau}} \text{ and } \omega_N = \frac{|\mathbf{x_N}-\mathbf{x_0}'|}{2\sqrt{N\,\Delta t}}.$$

Then

$$I_1 = \int d\mathbf{r}'\frac{\exp\{-\zeta_N(\mathbf{r})+\zeta_0'(\mathbf{r}')\}}{\pi^{\frac{3}{2}}|\mathbf{x_N}-\mathbf{x_0}'|}\int_0^{\omega_N}d\omega\exp\left\{-\omega^2-\frac{|\mathbf{x_N}-\mathbf{x_0}'|^2}{4\omega^2}\right\}$$
$$= \int d\mathbf{r}'\frac{\exp\{-\zeta_N(\mathbf{r})+\zeta_0(\mathbf{r}')\}}{4\pi|\mathbf{x_N}-\mathbf{x_0}'|}\times$$
$$\times\left[\exp|\mathbf{x_N}-\mathbf{x_0}'|\,\mathrm{erf}\left(\omega+\frac{|\mathbf{x_N}-\mathbf{x_0}'|}{2\omega}\right)+\exp\{-|\mathbf{x_N}-\mathbf{x_0}'|\}\,\mathrm{erf}\left(\omega-\frac{|\mathbf{x_N}-\mathbf{x_0}'|}{2\omega}\right)\right]_0^{\omega_N}.$$

Finally

$$I_1 = \int d\mathbf{r}' \, \frac{\exp\{-\zeta_N(\mathbf{r}) + \zeta_0'(\mathbf{r}')\}}{4\pi\,|\mathbf{x_N} - \mathbf{x_0}'|} \left\{ -2\sinh|\mathbf{x_N} - \mathbf{x_0}'| + \exp|\mathbf{x_N} - \mathbf{x_0}'| \right. \qquad (B5)$$

$$\left. \times \operatorname{erf}\left[\frac{|\mathbf{x_N} - \mathbf{x_0}'|}{2\sqrt{t_N - t_0}} + \sqrt{t_N - t_0}\right] + \exp\{-|\mathbf{x_N} - \mathbf{x_0}'|\} \operatorname{erf}\left[\frac{|\mathbf{x_N} - \mathbf{x_0}'|}{2\sqrt{t_N - t_0}} - \sqrt{t_N - t_0}\right] \right\}.$$

The second integral in Eq. (B3) becomes:

$$I_2 = \int_0^{t_N - t_0} d\tau \int d\mathbf{r}' \left[2 + \dot{\zeta}'(\mathbf{r}', t')\right] G(\mathbf{x_N}, \mathbf{x_n}'; \tau)$$

$$= \int_0^{t_N - t_0} d\tau \int d\mathbf{r}' \, \frac{\left[2 + \dot{\zeta}'(\mathbf{r}', t_N - \tau)\right]}{(4\pi\tau)^{\frac{3}{2}}} \exp\left\{\frac{-|\mathbf{r} - \mathbf{r}'|^2 + [\zeta_N(\mathbf{r}) - \zeta'(\mathbf{r}', t_N - \tau) + 2\tau]^2}{4\tau}\right\}.$$

We now discretize the time domain $[0, t_N - t_0]$ in N intervals $[(N-n)\Delta t, (N-n+1)\Delta t]$, $n = 1, 2, \ldots, N$. The value $n = 0$ corresponds to $\tau = N\Delta t = t_N$, or, $t' = t_0$ (initial time), whereas n=N corresponds to $\tau = 0$, or, $t' = t_N$ (final time.) Quantities, such as the interface location $\zeta(\mathbf{r}, t)$, the temperature $T(\mathbf{x}, t)$, and the flow velocity $\mathbf{v}(\mathbf{x}, t)$, are considered constant over each interval and equal to the values corresponding to the *end* of the time interval. The integral now becomes a sum of N integrals and the time integration can be performed *analytically*:

$$I_2 = \sum_{n=1}^{N} \int_{(N-n)\Delta t}^{(N-n+1)\Delta t} d\tau \int d\mathbf{r}' \frac{2 + \dot{\zeta}_n(\mathbf{r}')}{(4\pi\tau)^{\frac{3}{2}}} \exp\left\{-\frac{|\mathbf{r} - \mathbf{r}'|^2 + [\zeta_N(\mathbf{r}) - \zeta_n(\mathbf{r}') + 2\tau]^2}{4\tau}\right\}$$

$$= \sum_{n=1}^{N} \int d\mathbf{r}' \left[2 + \dot{\zeta}_n(\mathbf{r}')\right] \exp\{-\zeta_N(\mathbf{r}) + \zeta_n(\mathbf{r}')\} \times$$

$$\times \int_{(N-n)\Delta t}^{(N-n+1)\Delta t} \frac{d\tau}{(4\pi\tau)^{\frac{3}{2}}} \exp\left\{-\frac{|\mathbf{x_N} - \mathbf{x_n}'|^2 + (\zeta_N - \zeta_n')^2}{4\tau} - \tau\right\}.$$

Again, let

$$\omega = \frac{|\mathbf{x_N} - \mathbf{x_n}'|}{2\sqrt{\tau}} \text{ and } \omega_{N-n} = \frac{|\mathbf{x_N} - \mathbf{x_n}'|}{2\sqrt{(N-n)\Delta t}}.$$

Then

$$I_2 = \sum_{n=1}^{N} \int d\mathbf{r}' \left[2 + \dot{\zeta}_n(\mathbf{r}')\right] \frac{\exp\{-\zeta_N(\mathbf{r}) + \zeta_n'(\mathbf{r}')\}}{2\pi^{\frac{3}{2}} |\mathbf{x_N} - \mathbf{x_n}'|} \times$$
$$\times \int_{\omega_{N-n}}^{\omega_{N-n+1}} d\omega \exp\left\{-\omega^2 - \frac{|\mathbf{x_N} - \mathbf{x_n}'|^2}{4\omega^2}\right\}.$$

The integration in ω finally yields

$$I_2 = \sum_{n=1}^{N} \int d\mathbf{r}' \left[2 + \dot{\zeta}_n(\mathbf{r}')\right] \frac{\exp\{-\zeta_N(\mathbf{r}) + \zeta_n(\mathbf{r}')\}}{8\pi |\mathbf{x_N} - \mathbf{x_n}'|}$$
$$\times \Bigg\{ \exp|\mathbf{x_N} - \mathbf{x_n}'| \left(\operatorname{erf}\left[\frac{|\mathbf{x_N} - \mathbf{x_n}'|}{2\sqrt{(N-n)\Delta t}} + \sqrt{(N-n)\Delta t}\right] \right.$$
$$\left. - \operatorname{erf}\left[\frac{|\mathbf{x_N} - \mathbf{x_n}'|}{2\sqrt{(N-n+1)\Delta t}} + \sqrt{(N-n+1)\Delta t}\right]\right) \qquad (B6)$$
$$+ \exp\{-|\mathbf{x_N} - \mathbf{x_n}'|\} \left(\operatorname{erf}\left[\frac{|\mathbf{x_N} - \mathbf{x_n}'|}{2\sqrt{(N-n)\Delta t}} - \sqrt{(N-n)\Delta t}\right] \right.$$
$$\left. - \operatorname{erf}\left[\frac{|\mathbf{x_N} - \mathbf{x_n}'|}{2\sqrt{(N-n+1)\Delta t}} - \sqrt{(N-n+1)\Delta t}\right]\right) \Bigg\}.$$

We now follow the same procedure for the evaluation of the domain integrals in Eq. (B3):

$$I_3 = -2\lambda \int_{t_N - t_0}^{\infty} d\tau \int d\mathbf{r}' \int_{\zeta_0(\mathbf{r}')}^{\infty} dz' G(\mathbf{x_\Gamma}(t), \mathbf{x}'; t - t')\, \mathbf{v}_0(\mathbf{x}') \cdot \nabla_x' T_0(\mathbf{x}')$$
$$= -\lambda \int_{t_N - t_0}^{\infty} d\tau \int d\mathbf{r}' \int_{\zeta_0(\mathbf{r}')}^{\infty} \frac{dz'}{4(\pi\tau)^{\frac{3}{2}}} \exp\left\{-\frac{|\mathbf{x_N} - \mathbf{x}'|^2}{4\tau} - \tau - \zeta_N + z'\right\} \mathbf{v}_0(\mathbf{x}') \cdot \nabla_x' T_0(\mathbf{x}').$$

Let

$$\omega = \frac{|\mathbf{x_N} - \mathbf{x}'|}{2\sqrt{\tau}} \text{ and } \omega_N = \frac{|\mathbf{x_N} - \mathbf{x}'|}{2\sqrt{N\,\Delta t}}.$$

Then

$$I_3 = -\lambda \int d\mathbf{r}' \int_{\zeta_0(\mathbf{r}')}^{\infty} dz' \frac{\exp\{-\zeta_N(\mathbf{r}) + z'\}}{\pi^{\frac{3}{2}} |\mathbf{x_N} - \mathbf{x}'|} \mathbf{v}_0(\mathbf{x}') \cdot \nabla_x' T_0(\mathbf{x}')$$
$$\times \int_0^{\omega_N} d\omega \exp\left\{-\omega^2 - \frac{|\mathbf{x_N} - \mathbf{x}'|^2}{4\omega^2}\right\}.$$

The integration in ω gives

$$I_3 = -\lambda \int d\mathbf{r}' \int_{\zeta_0(\mathbf{r}')}^{\infty} dz' \frac{\exp\{-\zeta_N(\mathbf{r}) + z'\}}{4\pi\,|\mathbf{x_N} - \mathbf{x}'|}\, \mathbf{v}_0(\mathbf{x}') \cdot \nabla'_x T_0(\mathbf{x}')$$
$$\times \quad \left\{ -2\sinh|\mathbf{x_N} - \mathbf{x}'| + \exp\{|\mathbf{x_N} - \mathbf{x}'|\}\,\mathrm{erf}\left[\frac{|\mathbf{x_N} - \mathbf{x}'|}{2\sqrt{t_N - t_0}} + \sqrt{t_N - t_0}\right]\right.$$
$$\left. + \exp\{-|\mathbf{x_N} - \mathbf{x}'|\}\,\mathrm{erf}\left[\frac{|\mathbf{x_N} - \mathbf{x}'|}{2\sqrt{t_N - t_0}} - \sqrt{t_N - t_0}\right]\right\}. \qquad (B7)$$

The second domain integral in Eq. (B3) becomes with $\tau = t_N - t'$:

$$I_4 = -2\lambda \int_0^{t_N - t_0} d\tau \int d\mathbf{r}' \int_{\zeta(\mathbf{r}',t')}^{\infty} dz' G(\mathbf{x_\Gamma}(t), \mathbf{x}'; t - t')\, \mathbf{v}(\mathbf{x}', t') \cdot \nabla'_x T(\mathbf{x}', t')$$
$$= -\lambda \int_0^{t_N - t_0} d\tau \int d\mathbf{r}' \int_{\zeta(\mathbf{r}',t')}^{\infty} \frac{dz'}{4(\pi\tau)^{\frac{3}{2}}} \exp\left\{-\frac{|\mathbf{x_N} - \mathbf{x}'|^2}{4\tau} - \tau - \zeta_N + z'\right\} \mathbf{v}(\mathbf{x}', t') \cdot \nabla'_x T(\mathbf{x}', t').$$

We now apply the time discretization (see Eq. (B6)) and we re-introduce the variable transformation

$$\omega = \frac{|\mathbf{x_N} - \mathbf{x}'|}{2\sqrt{\tau}} \text{ and } \omega_{N-n} = \frac{|\mathbf{x_N} - \mathbf{x}'|}{2\sqrt{(N-n)\Delta t}}.$$

Then

$$I_4 = -\lambda \sum_{n=1}^{N} \int d\mathbf{r}' \int_{\zeta_n(\mathbf{r}')}^{\infty} dz' \frac{\exp\{-\zeta_N(\mathbf{r}) + z'\}}{\pi^{\frac{3}{2}}\,|\mathbf{x_N} - \mathbf{x}'|}\, \mathbf{v}_n(\mathbf{x}') \cdot \nabla'_x T_n(\mathbf{x}')$$
$$\times \quad \int_{\omega_{N-n}}^{\omega_{N-n+1}} d\omega \exp\left\{-\omega^2 - \frac{|\mathbf{x_N} - \mathbf{x}'|^2}{4\omega^2}\right\}.$$

The integration in ω gives:

$$I_4 = -\lambda \sum_{n=1}^{N} \int d\mathbf{r}' \int_{\zeta_n(\mathbf{r}')}^{\infty} dz' \frac{\exp\{-\zeta_N(\mathbf{r}) + z'\}}{4\pi\,|\mathbf{x_N} - \mathbf{x}'|}\, \mathbf{v}_n(\mathbf{x}') \cdot \nabla'_x T_n(\mathbf{x}')$$
$$\times \left\{ \exp\{|\mathbf{x_N} - \mathbf{x}'|\} \left(\mathrm{erf}\left[\frac{|\mathbf{x_N} - \mathbf{x}'|}{2\sqrt{(N-n)\Delta t}} + \sqrt{(N-n)\Delta t}\right]\right.\right.$$
$$\left. - \mathrm{erf}\left[\frac{|\mathbf{x_N} - \mathbf{x}'|}{2\sqrt{(N-n+1)\Delta t}} + \sqrt{(N-n+1)\Delta t}\right]\right) \qquad (B8)$$
$$+ \exp\{-|\mathbf{x_N} - \mathbf{x}'|\} \left(\mathrm{erf}\left[\frac{|\mathbf{x_N} - \mathbf{x}'|}{2\sqrt{(N-n)\Delta t}} - \sqrt{(N-n)\Delta t}\right]\right.$$
$$\left.\left. - \mathrm{erf}\left[\frac{|\mathbf{x_N} - \mathbf{x}'|}{2\sqrt{(N-n+1)\Delta t}} - \sqrt{(N-n+1)\Delta t}\right]\right)\right\}.$$

The discretized (in time) equivalent of Eq. (B3) is now

$$T_\Gamma = \Delta - \nu\mathcal{K}\{\zeta(\mathbf{r},t)\} = I_1 + I_2 + I_3 + I_4 \qquad (B9)$$

where the integrals $(I_1 - I_4)$ are shown in Eqs. (B5-B8). The calculation of the interface shape at time $t = t_N$, as represented by $\zeta_N(\mathbf{r})$ (or, $\mathbf{x_N}$,) requires the prior knowledge of the temperature gradient field in the interior of the domain, $\nabla_x T(\mathbf{x},t)$. We shall use Eq. (B4) to evaluate the temperature gradient; our methodology will be similar to that applied to Eq. (B3).

We again discretize the time domain in N intervals and the interface location $\zeta(\mathbf{r},t)$, the temperature $T(\mathbf{x},t)$, and the flow velocity $\mathbf{v}(\mathbf{x},t)$ are considered constant over each interval. However, now these are considered equal to the values corresponding to the *beginning* of the time interval. This allows us to calculate the temperature gradient at time t_N (LHS) from quantities already calculated in previous time steps (RHS).

The first integral in Eq. (B4) becomes, after the transformation $\tau = t_N - t'$:

$$\begin{aligned} H_1 &= \int_{t_N - t_0}^{\infty} d\tau \int d\mathbf{r}'\, 2\,\nabla_x G(\mathbf{x},\mathbf{x_0}';\tau) \\ &= \int_{t_N - t_0}^{\infty} d\tau \int d\mathbf{r}'\, \frac{1}{4(\pi\tau)^{\frac{3}{2}}} \nabla_x \left[\exp\left\{ \frac{-|\mathbf{x}-\mathbf{x_0}'|^2}{4\tau} - \tau - z + \zeta_0' \right\} \right]. \end{aligned}$$

Instead of performing the differentiation in the spatial variables first and then integrating in time, we use the result of the time integration in I_1 (see Eq. (B5)) and then differentiate (we first have to replace $\mathbf{x_N}$ with $\mathbf{x}$ since the (H) integrals refer to interior points):

$$H_1 = \int d\mathbf{r}' \left\{ \left[-A + (B-A)\left(\frac{z - \zeta_0'}{|\mathbf{x}-\mathbf{x_0}'|^2} \right) \right] \mathbf{i}_z + (B-A)\left(\frac{r - r'\cos\varphi}{|\mathbf{x}-\mathbf{x_0}'|^2} \right) \mathbf{i}_r \right\}. \qquad (B10)$$

where

$$A = \frac{\exp\{-z+\zeta_0'(\mathbf{r}')\}}{4\pi\,|\mathbf{x}-\mathbf{x_0}'|}\left\{\exp|\mathbf{x}-\mathbf{x_0}'|\,\mathrm{erf}\left[\frac{|\mathbf{x}-\mathbf{x_0}'|}{2\sqrt{t_N-t_0}}+\sqrt{t_N-t_0}\right]\right.$$
$$\left.+\exp\{-|\mathbf{x}-\mathbf{x_0}'|\}\,\mathrm{erf}\left[\frac{|\mathbf{x}-\mathbf{x_0}'|}{2\sqrt{t_N-t_0}}-\sqrt{t_N-t_0}\right]-2\sinh|\mathbf{x}-\mathbf{x_0}'|\right\}$$

and

$$B = \frac{1}{4\pi}\exp\{-z+\zeta_0'(\mathbf{r}')\}\left[-2\cosh|\mathbf{x}-\mathbf{x_0}'|\right.$$
$$+\exp|\mathbf{x}-\mathbf{x_0}'|\,\mathrm{erf}\left[\frac{|\mathbf{x}-\mathbf{x_0}'|}{2\sqrt{t_N-t_0}}+\sqrt{t_N-t_0}\right]-\exp\{-|\mathbf{x}-\mathbf{x_0}'|\}$$
$$\left.\times\mathrm{erf}\left[\frac{|\mathbf{x}-\mathbf{x_0}'|}{2\sqrt{t_N-t_0}}-\sqrt{t_N-t_0}\right]+\frac{2}{\sqrt{\pi(t_N-t_0)}}\exp\left\{-\frac{|\mathbf{x}-\mathbf{x_0}'|^2}{4(t_N-t_0)}-t_N+t_0\right\}\right].$$

The second integral in Eq. (B4) is:

$$H_2 = \int_0^{t_N-t_0} d\tau\int d\mathbf{r}'\left[2+\dot\zeta(\mathbf{r}',t')\right]\nabla_x G(\mathbf{x},\mathbf{x_n}';\tau)$$
$$= \int_0^{t_N-t_0} d\tau\int d\mathbf{r}'\,\frac{\left[2+\dot\zeta(\mathbf{r}',t_N-\tau)\right]}{(4\pi\tau)^{\frac{3}{2}}}$$
$$\times\nabla_x\left[\exp\left\{\frac{-|\mathbf{r}-\mathbf{r}'|^2+[z-\zeta(\mathbf{r}',t_N-\tau)+2\tau]^2}{4\tau}\right\}\right].$$

We now discretize in time and use Eq. (B6); again, we change $\mathbf{x_N}$ to $\mathbf{x}$ since $\mathbf{x}\in\Omega$. The crucial difference from I_2 is that here the quantities in the RHS are all known from previous steps:

$$H_2 = \sum_{n=1}^{N}\int d\mathbf{r}'\left[2+\dot\zeta_{n-1}(\mathbf{r}')\right]\left\{\left[-C_{n-1}+\right.\right.$$
$$\left.\left.(D_{n-1}-C_{n-1})\left(\frac{z-\zeta_{n-1}}{|\mathbf{x}-\mathbf{x_{n-1}}'|^2}\right)\right]\mathbf{i}_z+(D_{n-1}-C_{n-1})\left(\frac{r-r'\cos\varphi}{|\mathbf{x}-\mathbf{x_{n-1}}'|^2}\right)\mathbf{i}_r\right\}. \quad (B11)$$

where

$$C_{n-1} = \frac{\exp\{-z + \zeta_{n-1}(\mathbf{r}')\}}{8\pi\,|\mathbf{x} - \mathbf{x_{n-1}}'|} \times$$
$$\times \left\{ \exp|\mathbf{x} - \mathbf{x_{n-1}}'| \left(\operatorname{erf}\left[\frac{|\mathbf{x} - \mathbf{x_{n-1}}'|}{2\sqrt{(N-n)\Delta t}} + \sqrt{(N-n)\Delta t} \right] \right.\right.$$
$$\left.\left. - \operatorname{erf}\left[\frac{|\mathbf{x} - \mathbf{x_{n-1}}'|}{2\sqrt{(N-n+1)\Delta t}} + \sqrt{(N-n+1)\Delta t} \right] \right)$$
$$+ \exp\{-|\mathbf{x} - \mathbf{x_{n-1}}'|\} \left(\operatorname{erf}\left[\frac{|\mathbf{x} - \mathbf{x_{n-1}}'|}{2\sqrt{(N-n)\Delta t}} - \sqrt{(N-n)\Delta t} \right] \right.$$
$$\left. \left. - \operatorname{erf}\left[\frac{|\mathbf{x} - \mathbf{x_{n-1}}'|}{2\sqrt{(N-n+1)\Delta t}} - \sqrt{(N-n+1)\Delta t} \right] \right) \right\}$$

and

$$D_{n-1} = \frac{1}{8\pi} \exp\{-z + \zeta_{n-1}(\mathbf{r}')\} \times$$
$$\times \left\{ \exp|\mathbf{x} - \mathbf{x_{n-1}}'| \left(\operatorname{erf}\left[\frac{|\mathbf{x} - \mathbf{x_{n-1}}'|}{2\sqrt{(N-n)\Delta t}} + \sqrt{(N-n)\Delta t} \right] \right.\right.$$
$$\left.\left. - \operatorname{erf}\left[\frac{|\mathbf{x} - \mathbf{x_{n-1}}'|}{2\sqrt{(N-n+1)\Delta t}} + \sqrt{(N-n+1)\Delta t} \right] \right)$$
$$- \exp\{-|\mathbf{x} - \mathbf{x_{n-1}}'|\} \left(\operatorname{erf}\left[\frac{|\mathbf{x} - \mathbf{x_{n-1}}'|}{2\sqrt{(N-n)\Delta t}} - \sqrt{(N-n)\Delta t} \right] \right.$$
$$\left. - \operatorname{erf}\left[\frac{|\mathbf{x} - \mathbf{x_{n-1}}'|}{2\sqrt{(N-n+1)\Delta t}} - \sqrt{(N-n+1)\Delta t} \right] \right)$$
$$+ \frac{2}{\sqrt{\pi(N-n)\Delta t}} \exp\left\{ -\frac{|\mathbf{x} - \mathbf{x_{n-1}}'|^2}{4(N-n)\Delta t} - (N-n)\Delta t \right\}$$
$$\left. - \frac{2}{\sqrt{\pi(N-n+1)\Delta t}} \exp\left\{ -\frac{|\mathbf{x} - \mathbf{x_{n-1}}'|^2}{4(N-n+1)\Delta t} - (N-n+1)\Delta t \right\} \right\}.$$

The same procedure is followed for the domain integrals in Eq. (B4). The first domain integral becomes for $\tau = t_N - t'$:

$$H_3 = -2\lambda \int_{t_N - t_0}^{\infty} d\tau \int d\mathbf{r}' \int_{\zeta_0(\mathbf{r}')}^{\infty} dz' \nabla_x G(\mathbf{x}, \mathbf{x}'; t - t')\, \mathbf{v}_0(\mathbf{x}') \cdot \nabla_x' T_0(\mathbf{x}')$$

$$= -\lambda \int_{t_N - t_0}^{\infty} d\tau \int d\mathbf{r}' \int_{\zeta_0(\mathbf{r}')}^{\infty} dz' \, \frac{1}{4(\pi\tau)^{\frac{3}{2}}} \mathbf{v}_0(\mathbf{x}') \cdot \nabla'_x T_0(\mathbf{x}') \times \nabla_x \left[\exp\left\{ -\frac{|\mathbf{x} - \mathbf{x}'|^2}{4\tau} - \tau - z + z' \right\} \right].$$

We now use the result of the time integration in I_3 (see Eq. (B7)), after we replace $\mathbf{x_N}$ with $\mathbf{x}$, since $\mathbf{x} \in \Omega$:

$$H_3 = -\lambda \int d\mathbf{r}' \int_{\zeta_0(\mathbf{r}')}^{\infty} dz' \mathbf{v}_0(\mathbf{x}') \cdot \nabla'_x T_0(\mathbf{x}') \qquad (B12)$$
$$\left\{ \left[-E + (F - E) \left(\frac{z - z'}{|\mathbf{x} - \mathbf{x}'|^2} \right) \right] \mathbf{i}_z + (F - E) \left(\frac{r - r' \cos\varphi}{|\mathbf{x} - \mathbf{x}'|^2} \right) \mathbf{i}_r \right\}.$$

where

$$E = \frac{\exp\{-z + z'\}}{4\pi |\mathbf{x} - \mathbf{x}'|} \left\{ \exp|\mathbf{x} - \mathbf{x}'| \operatorname{erf}\left[\frac{|\mathbf{x} - \mathbf{x}'|}{2\sqrt{t_N - t_0}} + \sqrt{t_N - t_0} \right] \right.$$
$$\left. + \exp\{-|\mathbf{x} - \mathbf{x}'|\} \operatorname{erf}\left[\frac{|\mathbf{x} - \mathbf{x}'|}{2\sqrt{t_N - t_0}} - \sqrt{t_N - t_0} \right] - 2\sinh|\mathbf{x} - \mathbf{x}'| \right\}$$

and

$$F = \frac{1}{4\pi} \exp\{-z + z'\} \left[-2\cosh|\mathbf{x} - \mathbf{x}'| \right.$$
$$+ \exp|\mathbf{x} - \mathbf{x}'| \operatorname{erf}\left[\frac{|\mathbf{x} - \mathbf{x}'|}{2\sqrt{t_N - t_0}} + \sqrt{t_N - t_0} \right] - \exp\{-|\mathbf{x} - \mathbf{x}'|\}$$
$$\left. \times \operatorname{erf}\left[\frac{|\mathbf{x} - \mathbf{x}'|}{2\sqrt{t_N - t_0}} - \sqrt{t_N - t_0} \right] + \frac{2}{\sqrt{\pi(t_N - t_0)}} \exp\left\{ -\frac{|\mathbf{x} - \mathbf{x}'|^2}{4(t_N - t_0)} - t_N + t_0 \right\} \right].$$

The second domain integral in Eq. (B3) becomes for $\tau = t_N - t'$:

$$H_4 = -2\lambda \int_0^{t_N - t_0} d\tau \int d\mathbf{r}' \int_{\zeta(\mathbf{r}', t')}^{\infty} dz' \nabla_x G(\mathbf{x}, \mathbf{x}'; t - t') \, \mathbf{v}(\mathbf{x}', t') \cdot \nabla'_x T(\mathbf{x}', t')$$
$$= -\lambda \int_0^{t_N - t_0} d\tau \int d\mathbf{r}' \int_{\zeta(\mathbf{r}', t')}^{\infty} \frac{dz'}{\pi^{\frac{3}{2}} |\mathbf{x} - \mathbf{x}'|} \mathbf{v}(\mathbf{x}', t') \cdot \nabla'_x T(\mathbf{x}', t')$$
$$\times \nabla_x \left[\exp\left\{ -\frac{|\mathbf{x} - \mathbf{x}'|^2}{4\tau} - \tau - z + z' \right\} \right].$$

We now discretize in time and use Eq. (B8) (after we change $\mathbf{x_N}$ to $\mathbf{x}$, since $\mathbf{x} \in \Omega$). Once again, the basic difference from I_4 is that here the quantities in the RHS are all known from previous steps:

$$H_4 = -\lambda \sum_{n=1}^{N} \int d\mathbf{r}' \int_{\zeta_{n-1}(\mathbf{r}')}^{\infty} dz'\, \mathbf{v}_{n-1}(\mathbf{x}') \cdot \nabla'_x T_{n-1}(\mathbf{x}') \left\{ \left[-Q_{n-1} + \right.\right.$$
$$\left.\left. + (R_{n-1} - Q_{n-1}) \left(\frac{z - z'}{|\mathbf{x} - \mathbf{x}'|^2} \right) \right] \mathbf{i}_z + (R_{n-1} - Q_{n-1}) \left(\frac{r - r' \cos\varphi}{|\mathbf{x} - \mathbf{x}'|^2} \right) \mathbf{i}_r \right\}. \quad (B13)$$

where

$$Q_{n-1} = \frac{\exp\{-z + z'\}}{4\pi\,|\mathbf{x} - \mathbf{x}'|} \times$$
$$\times \left\{ \exp|\mathbf{x} - \mathbf{x}'| \left(\operatorname{erf}\left[\frac{|\mathbf{x} - \mathbf{x}'|}{2\sqrt{(N-n)\Delta t}} + \sqrt{(N-n)\Delta t} \right] \right.\right.$$
$$\left. - \operatorname{erf}\left[\frac{|\mathbf{x} - \mathbf{x}'|}{2\sqrt{(N-n+1)\Delta t}} + \sqrt{(N-n+1)\Delta t} \right] \right)$$
$$+ \exp\{-|\mathbf{x} - \mathbf{x}'|\} \left(\operatorname{erf}\left[\frac{|\mathbf{x} - \mathbf{x}'|}{2\sqrt{(N-n)\Delta t}} - \sqrt{(N-n)\Delta t} \right] \right.$$
$$\left.\left. - \operatorname{erf}\left[\frac{|\mathbf{x} - \mathbf{x}'|}{2\sqrt{(N-n+1)\Delta t}} - \sqrt{(N-n+1)\Delta t} \right] \right) \right\}$$

and

$$R_{n-1} = \frac{1}{4\pi} \exp\{-z + z'\} \times$$
$$\times \left\{ \exp\{|\mathbf{x} - \mathbf{x}'|\} \left(\operatorname{erf}\left[\frac{|\mathbf{x} - \mathbf{x}'|}{2\sqrt{(N-n)\Delta t}} + \sqrt{(N-n)\Delta t} \right] \right.\right.$$
$$\left. - \operatorname{erf}\left[\frac{|\mathbf{x} - \mathbf{x}'|}{2\sqrt{(N-n+1)\Delta t}} + \sqrt{(N-n+1)\Delta t} \right] \right)$$
$$- \exp\{-|\mathbf{x} - \mathbf{x}'|\} \left(\operatorname{erf}\left[\frac{|\mathbf{x} - \mathbf{x}'|}{2\sqrt{(N-n)\Delta t}} - \sqrt{(N-n)\Delta t} \right] \right.$$
$$\left. - \operatorname{erf}\left[\frac{|\mathbf{x} - \mathbf{x}'|}{2\sqrt{(N-n+1)\Delta t}} - \sqrt{(N-n+1)\Delta t} \right] \right)$$

$$+\frac{2}{\sqrt{\pi(N-n)\Delta t}}\exp\left\{-\frac{|\mathbf{x}-\mathbf{x}'|^2}{4(N-n)\Delta t}-(N-n)\Delta t\right\}$$
$$-\frac{2}{\sqrt{\pi(N-n+1)\Delta t}}\exp\left\{-\frac{|\mathbf{x}-\mathbf{x}'|^2}{4(N-n+1)\Delta t}-(N-n+1)\Delta t\right\}\Bigg\}.$$

So the discretized equivalent of Eq. (B4) is now:

$$\nabla_x T(\mathbf{x},t) = H_1 + H_2 + H_3 + H_4 \qquad (B14)$$

with the integrals $(H_1 - H_4)$ shown in Eqs. (B9-B12.)

APPENDIX C:

SPATIAL DISCRETIZATION

This appendix contains the discretized equivalent of the spatial integrals derived in Appendix B. The coordinate transformations and the quadrature formulae that were employed can be found in Sec. 3.1.b.

$$I_1 = \sum_{i=1}^{N_r} \sum_{k=1}^{N_\varphi} \frac{p\pi}{2N_r N_\varphi} \tan\left(\frac{2i-1}{2N_r}\frac{\pi}{2}\right) \times \frac{\exp\{-\zeta_N(r_j) + \zeta_0(r_i)\}}{\sqrt{\left(\sqrt{\alpha_{i,N}+\beta_i}+\psi_{ik,N}\right)\left(\sqrt{\alpha_{i,N}-\beta_i}+\psi_{ik,N}\right)}}$$
$$\left\{-2\sinh(\psi_{ik,N}) + \exp\{\psi_{ik,N}\}\,\mathrm{erf}\left[\frac{\psi_{ik,N}}{2\sqrt{N\,\Delta t}} + \sqrt{N\,\Delta t}\right] + \exp\{-\psi_{ik,N}\}\,\mathrm{erf}\left[\frac{-\psi_{ik,N}}{2\sqrt{N\,\Delta t}} - \sqrt{N\,\Delta t}\right]\right\}, \quad (C1)$$

where

$$\alpha_{i,N} = r_i^2 + r_j^2 + [\zeta_N(r_j) - \zeta_0(r_i)]^2 \quad \text{and } \beta_i = 2r_i r_j,$$
$$\psi_{ik,N} = \sqrt{\alpha_{i,N}-\beta_i} + \left[\sqrt{\alpha_{i,N}+\beta_i} - \sqrt{\alpha_{i,N}-\beta_i}\right]\cos^2\left(\frac{2k-1}{2N_\varphi}\frac{\pi}{2}\right).$$

$$I_2 = \sum_{n=1}^{N} \sum_{i=1}^{N_r} \sum_{k=1}^{N_\varphi} \frac{p\pi}{4N_r N_\varphi}\left[2 + \dot{\zeta}_n(r_i)\right] \tan\left(\frac{2i-1}{2N_r}\frac{\pi}{2}\right) \times \frac{\exp\{-\zeta_N(r_j) + \zeta_n(r_i)\}}{\sqrt{\left(\sqrt{\alpha_{i,N-n}+\beta_i}+\psi_{ik,N-n}\right)\left(\sqrt{\alpha_{i,N-n}-\beta_i}+\psi_{ik,N-n}\right)}}$$
$$\times \left\{\exp\{\psi_{ik,N-n}\}\left[\mathrm{erf}\left(\frac{\psi_{ik,N-n}}{2\sqrt{(N-n)\,\Delta t}} + \sqrt{(N-n)\,\Delta t}\right)\right.\right.$$

$$- \operatorname{erf}\left(\frac{\psi_{ik,N-n}}{2\sqrt{(N-n+1)\,\Delta t}} + \sqrt{(N-n+1)\,\Delta t}\right)\Bigg]$$

$$+ \exp\{\psi_{ik,N-n}\}\Bigg[\operatorname{erf}\left(\frac{\psi_{ik,N-n}}{2\sqrt{(N-n)\,\Delta t}} - \sqrt{(N-n)\,\Delta t}\right)$$

$$- \operatorname{erf}\left(\frac{\psi_{ik,N-n}}{2\sqrt{(N-n+1)\,\Delta t}} - \sqrt{(N-n+1)\,\Delta t}\right)\Bigg]\Bigg\}, \quad (C2)$$

where

$$\alpha_{i,N-n} = r_i^2 + r_j^2 + [\zeta_N(r_j) - \zeta_n(r_i)]^2 \quad \text{and } \beta_i = 2r_i r_j,$$

$$\psi_{ik,N-n} = \sqrt{\alpha_{i,N} - \beta_i} + \left[\sqrt{\alpha_{i,N-n} + \beta_i} - \sqrt{\alpha_{i,N-n} - \beta_i}\right]\cos^2\left(\frac{2k-1}{2N_\varphi}\frac{\pi}{2}\right).$$

$$I_3 = -\lambda \sum_{i=1}^{N_r}\sum_{k=1}^{N_\varphi}\sum_{m=1}^{N_z} \frac{p\pi^2}{4(1+\lambda)N_r N_\varphi N_z} \tan\left(\frac{2i-1}{2N_r}\frac{\pi}{2}\right)\tan\left(\frac{2m-1}{2N_z}\frac{\pi}{2}\right)$$

$$\times \frac{\exp\{-\zeta_N(r_j) + \zeta_0(r_i) - \frac{\ln(\xi_m)}{2(1+\lambda)}\}}{\sqrt{\left(\sqrt{\alpha_{im,N} + \beta_i} + \psi_{imk,N}\right)\left(\sqrt{\alpha_{im,N} - \beta_i} + \psi_{imk,N}\right)}}$$

$$\Bigg\{-2\sinh(\psi_{imk,N}) + \exp\{\psi_{imk,N}\}\operatorname{erf}\left[\frac{\psi_{imk,N}}{2\sqrt{N\,\Delta t}} + \sqrt{N\,\Delta t}\right] \quad (C3)$$

$$+ \exp\{-\psi_{imk,N}\}\operatorname{erf}\left[\frac{\psi_{imk,N}}{2\sqrt{N\,\Delta t}} - \sqrt{N\,\Delta t}\right]\Bigg\} \times$$

$$\left[\mathrm{v}_0\left(r' = r_i, z' = \zeta_0(r_i) - \frac{\ln(\xi_m)}{2(1+\lambda)}\right)\right] \cdot \left[\nabla'_x T_0\left(r' = r_i, z' = \zeta_0(r_i) - \frac{\ln(\xi_m)}{2(1+\lambda)}\right)\right].$$

where

$$\alpha_{im,N} = r_i^2 + r_j^2 + \left[\zeta_N(r_j) - \zeta_0(r_i) + \frac{\ln(\xi_m)}{2(1+\lambda)}\right]^2,$$

$$\beta_i = 2r_i r_j,$$

$$\psi_{imk,N} = \sqrt{\alpha_{im,N} - \beta_i} + \left[\sqrt{\alpha_{im,N} + \beta_i} - \sqrt{\alpha_{im,N} - \beta_i}\right]\cos^2\left(\frac{2k-1}{2N_\varphi}\frac{\pi}{2}\right).$$

$$I_4 = -\lambda \sum_{n=1}^{N} \sum_{i=1}^{N_r} \sum_{k=1}^{N_\varphi} \sum_{m=1}^{N_z} \frac{p\pi^2}{4(1+\lambda)N_r N_\varphi N_z} \tan\left(\frac{2i-1}{2N_r}\frac{\pi}{2}\right) \tan\left(\frac{2m-1}{2N_z}\frac{\pi}{2}\right)$$

$$\times \frac{\exp\{-\zeta_N(r_j) + \zeta_n(r_i) - \frac{\ln(\xi_m)}{2(1+\lambda)}\}}{\sqrt{\left(\sqrt{\alpha_{im,N-n}+\beta_i} + \psi_{imk,N-n}\right)\left(\sqrt{\alpha_{im,N-n}-\beta_i} + \psi_{imk,N-n}\right)}}$$

$$\times \left\{ \exp\{\psi_{imk,N-n}\} \left[\operatorname{erf}\left(\frac{\psi_{imk,N-n}}{2\sqrt{(N-n)\,\Delta t}} + \sqrt{(N-n)\,\Delta t} \right) \right.\right.$$

$$\left. - \operatorname{erf}\left(\frac{\psi_{imk,N-n}}{2\sqrt{(N-n+1)\,\Delta t}} + \sqrt{(N-n+1)\,\Delta t} \right) \right]$$

$$+ \exp\{\psi_{imk,N-n}\} \left[\operatorname{erf}\left(\frac{\psi_{imk,N-n}}{2\sqrt{(N-n)\,\Delta t}} - \sqrt{(N-n)\,\Delta t} \right) \right. \qquad (C4)$$

$$\left.\left. - \operatorname{erf}\left(\frac{\psi_{imk,N-n}}{2\sqrt{(N-n+1)\,\Delta t}} - \sqrt{(N-n+1)\,\Delta t} \right) \right] \right\} \times$$

$$\left[\mathbf{v}_n\left(r' = r_i, z' = \zeta_n(r_i) - \frac{\ln(\xi_m)}{2(1+\lambda)} \right) \right] \cdot \left[\nabla'_x T_n\left(r' = r_i, z' = \zeta_n(r_i) - \frac{\ln(\xi_m)}{2(1+\lambda)} \right) \right].$$

where

$$\alpha_{im,N-n} = r_i^2 + r_j^2 + \left[\zeta_N(r_j) - \zeta_n(r_i) + \frac{\ln(\xi_m)}{2(1+\lambda)} \right]^2,$$

$$\beta_i = 2 r_i r_j,$$

$$\psi_{imk,N-n} = \sqrt{\alpha_{im,N-n} - \beta_i} \quad +$$

$$\left[\sqrt{\alpha_{im,N-n}+\beta_i} - \sqrt{\alpha_{im,N-n}-\beta_i} \right] \cos^2\left(\frac{2k-1}{2N_\varphi}\frac{\pi}{2} \right).$$

The vector integrals $(H_1 - H_4)$, that correspond to the gradient of the temperature field in the interior of the domain, are dotted into the flow velocity $\mathbf{v}(\mathbf{x}', t')$ to give the following discretized equivalents:

$$\hat{H}_1 = \sum_{\mu=1}^{N_r} \sum_{\nu=1}^{N_\varphi} \frac{p\pi}{2N_r N_\varphi} \tan\left(\frac{2\mu-1}{2N_r}\frac{\pi}{2}\right)$$

$$\times \frac{\exp\{-\zeta_N(r_i)+\zeta_0(r_\mu)+\frac{\ln(\xi_m)}{2(1+\lambda)}\}}{\sqrt{\left(\sqrt{\gamma_{\mu,N}+\beta_\mu}+\theta_{\mu\nu,N}\right)\left(\sqrt{\gamma_{\mu,N}-\beta_\mu}+\theta_{\mu\nu,N}\right)}}$$

$$\times \left\{ v_z \left[-\tilde{A} + \frac{\hat{B}-\hat{A}}{\theta_{\mu\nu,N}} \left(\zeta_N(r_i) - \zeta_0(r_\mu) - \frac{\ln(\xi_m)}{2(1+\lambda)} \right) \right] + v_r \frac{\hat{B}-\hat{A}}{\theta_{\mu\nu,N}} \left[r_i - \frac{(\gamma_{\mu,N}-\theta^2_{\mu\nu,N})}{2r_i} \right] \right\}, \quad (C5)$$

where

$$\gamma_{\mu,N} = r_\mu^2 + r_i^2 + \left[\zeta_N(r_i) - \zeta_0(r_\mu) - \frac{\ln(\xi_m)}{2(1+\lambda)} \right]^2,$$

$$\beta_\mu = 2 r_\mu r_i,$$

$$\theta_{\mu\nu,N} = \sqrt{\gamma_{\mu,N}-\beta_\mu} + \left[\sqrt{\gamma_{\mu,N}+\beta_\mu} - \sqrt{\gamma_{\mu,N}-\beta_\mu} \right] \cos^2\left(\frac{2\nu-1}{2N_\varphi}\frac{\pi}{2} \right).$$

The quantities $\tilde{A}$, $\hat{A}$, and $\hat{B}$ are given by

$$\tilde{A} = \left\{ \exp\{\theta_{\mu\nu,N}\} \operatorname{erf}\left[\frac{\theta_{\mu\nu,N}}{2\sqrt{N\,\Delta t}} + \sqrt{N\,\Delta t} \right] + \exp\{-\theta_{\mu\nu,N}\} \operatorname{erf}\left[\frac{\theta_{\mu\nu,N}}{2\sqrt{N\,\Delta t}} - \sqrt{N\,\Delta t} \right] - 2\sinh(\theta_{\mu\nu,N}) \right\},$$

$$\hat{A} = \frac{1}{\theta_{\mu\nu,N}} \left\{ \exp\{\theta_{\mu\nu,N}\} \operatorname{erf}\left[\frac{\theta_{\mu\nu,N}}{2\sqrt{N\,\Delta t}} + \sqrt{N\,\Delta t} \right] + \exp\{-\theta_{\mu\nu,N}\} \operatorname{erf}\left[\frac{\theta_{\mu\nu,N}}{2\sqrt{N\,\Delta t}} - \sqrt{N\,\Delta t} \right] - 2\sinh(\theta_{\mu\nu,N}) \right\},$$

and

$$\hat{B} = \left[-2\cosh(\theta_{\mu\nu,N}) + \exp\{\theta_{\mu\nu,N}\} \operatorname{erf}\left[\frac{\theta_{\mu\nu,N}}{2\sqrt{N\,\Delta t}} + \sqrt{N\,\Delta t} \right] - \exp\{-\theta_{\mu\nu,N}\} \times \operatorname{erf}\left[\frac{\theta_{\mu\nu,N}}{2\sqrt{N\,\Delta t}} - \sqrt{N\,\Delta t} \right] + \frac{2}{\sqrt{\pi(N\,\Delta t)}} \exp\left\{ -\frac{\theta^2_{\mu\nu,N}}{4(N\,\Delta t)} - N\,\Delta t \right\} \right].$$

The velocity components v_r and v_z are evaluated at $r = r_i$ and $z = \zeta_N(r_i) - \frac{\ln(\xi_m)}{2(1+\lambda)}$.

$$\hat{H}_2 = \sum_{\sigma=1}^{N}\sum_{\mu=1}^{N_r}\sum_{\nu=1}^{N_\varphi} \frac{p\pi}{4N_rN_\varphi}\tan\left(\frac{2\mu-1}{2N_r}\frac{\pi}{2}\right)\left[2+\dot{\zeta}_{\sigma-1}(r_\mu)\right]$$

$$\times \frac{\exp\{-\zeta_N(r_i)+\zeta_{\sigma-1}(r_\mu)+\frac{\ln(\xi_m)}{2(1+\lambda)}\}}{\sqrt{\left(\sqrt{\gamma_{\mu,N-\sigma+1}+\beta_\mu}+\theta_{\mu\nu,N-\sigma+1}\right)\left(\sqrt{\gamma_{\mu,N-\sigma+1}-\beta_\mu}+\theta_{\mu\nu,N-\sigma+1}\right)}}$$

$$\times\left\{v_z\left[-\tilde{C}_{\sigma-1}+\frac{\hat{D}_{\sigma-1}-\hat{C}_{\sigma-1}}{\theta_{\mu\nu,N-\sigma+1}}\left(\zeta_N(r_i)-\zeta_{\sigma-1}(r_\mu)-\frac{\ln(\xi_m)}{2(1+\lambda)}\right)\right]\right.$$

$$\left.+\,v_r\frac{\hat{D}_{\sigma-1}-\hat{C}_{\sigma-1}}{\theta_{\mu\nu,N-\sigma+1}}\left[r_i-\frac{(\gamma_{\mu,N-\sigma+1}-\theta^2_{\mu\nu,N-\sigma+1})}{2r_i}\right]\right\}, \quad (C6)$$

where

$$\gamma_{\mu,N-\sigma+1} = r_\mu^2 + r_i^2 + \left[\zeta_N(r_i)-\zeta_{\sigma-1}(r_\mu)-\frac{\ln(\xi_m)}{2(1+\lambda)}\right]^2,$$

$$\beta_\mu = 2r_\mu r_i,$$

$$\theta_{\mu\nu,N-\sigma+1} = \sqrt{\gamma_{\mu,N-\sigma+1}-\beta_\mu} \;+$$

$$\left[\sqrt{\gamma_{\mu,N-\sigma+1}+\beta_\mu}-\sqrt{\gamma_{\mu,N-\sigma+1}-\beta_\mu}\right]\cos^2\left(\frac{2\nu-1}{2N_\varphi}\frac{\pi}{2}\right).$$

The quantities $\tilde{C}_{\sigma-1}$, $\hat{C}_{\sigma-1}$, and $\hat{D}_{\sigma-1}$ are given by

$$\tilde{C}_{\sigma-1} = \left\{\exp\{\theta_{\mu\nu,N-\sigma+1}\}\left(\mathrm{erf}\left[\frac{\theta_{\mu\nu,N-\sigma+1}}{2\sqrt{(N-\sigma)\Delta t}}+\sqrt{(N-\sigma)\Delta t}\right]\right.\right.$$

$$\left.-\,\mathrm{erf}\left[\frac{\theta_{\mu\nu,N-\sigma+1}}{2\sqrt{(N-\sigma+1)\Delta t}}+\sqrt{(N-\sigma+1)\Delta t}\right]\right)$$

$$+\,\exp\{-\theta_{\mu\nu,N-\sigma+1}\}\left(\mathrm{erf}\left[\frac{\theta_{\mu\nu,N-\sigma+1}}{2\sqrt{(N-\sigma)\Delta t}}-\sqrt{(N-\sigma)\Delta t}\right]\right.$$

$$\left.\left.-\,\mathrm{erf}\left[\frac{\theta_{\mu\nu,N-\sigma+1}}{2\sqrt{(N-\sigma+1)\Delta t}}-\sqrt{(N-\sigma+1)\Delta t}\right]\right)\right\},$$

$$\hat{C}_{\sigma-1} = \frac{1}{\theta_{\mu\nu,N-\sigma+1}}\left\{\exp\{\theta_{\mu\nu,N-\sigma+1}\}\left(\mathrm{erf}\left[\frac{\theta_{\mu\nu,N-\sigma+1}}{2\sqrt{(N-\sigma)\Delta t}}+\sqrt{(N-\sigma)\Delta t}\right]\right.\right.$$

$$\left.\left.-\,\mathrm{erf}\left[\frac{\theta_{\mu\nu,N-\sigma+1}}{2\sqrt{(N-\sigma+1)\Delta t}}+\sqrt{(N-\sigma+1)\Delta t}\right]\right)\right.$$

$$+ \exp\{-\theta_{\mu\nu,N-\sigma+1}\}\left(\operatorname{erf}\left[\frac{\theta_{\mu\nu,N-\sigma+1}}{2\sqrt{(N-\sigma)\Delta t}} - \sqrt{(N-\sigma)\Delta t}\right]\right.$$
$$\left. - \operatorname{erf}\left[\frac{\theta_{\mu\nu,N-\sigma+1}}{2\sqrt{(N-\sigma+1)\Delta t}} - \sqrt{(N-\sigma+1)\Delta t}\right]\right)\Bigg\},$$

and

$$\hat{D}_{\sigma-1} = \Bigg\{\exp\{\theta_{\mu\nu,N-\sigma+1}\}\left(\operatorname{erf}\left[\frac{\theta_{\mu\nu,N-\sigma+1}}{2\sqrt{(N-\sigma)\Delta t}} + \sqrt{(N-\sigma)\Delta t}\right]\right.$$
$$\left. - \operatorname{erf}\left[\frac{\theta_{\mu\nu,N-\sigma+1}}{2\sqrt{(N-\sigma+1)\Delta t}} + \sqrt{(N-\sigma+1)\Delta t}\right]\right)$$
$$- \exp\{-\theta_{\mu\nu,N-\sigma+1}\}\left(\operatorname{erf}\left[\frac{\theta_{\mu\nu,N-\sigma+1}}{2\sqrt{(N-\sigma)\Delta t}} - \sqrt{(N-\sigma)\Delta t}\right]\right.$$
$$\left. - \operatorname{erf}\left[\frac{\theta_{\mu\nu,N-\sigma+1}}{2\sqrt{(N-\sigma+1)\Delta t}} - \sqrt{(N-\sigma+1)\Delta t}\right]\right)$$
$$+ \frac{2}{\sqrt{\pi(N-\sigma)\Delta t}}\exp\left\{-\frac{\theta^2_{\mu\nu,N-\sigma+1}}{4(N-\sigma)\Delta t} - (N-\sigma)\Delta t\right\}$$
$$\left. - \frac{2}{\sqrt{\pi(N-\sigma+1)\Delta t}}\exp\left\{-\frac{\theta^2_{\mu\nu,N-\sigma+1}}{4(N-\sigma+1)\Delta t} - (N-\sigma+1)\Delta t\right\}\right\}.$$

The velocity components v_r and v_z are evaluated at $r = r_i$ and $z = \zeta_N(r_i) - \frac{\ln(\xi_m)}{2(1+\lambda)}$.

$$\hat{H}_3 = -\lambda\sum_{\mu=1}^{N_r}\sum_{\nu=1}^{N_\varphi}\sum_{l=1}^{N_z}\frac{p\pi^2}{4(1+\lambda)N_rN_\varphi N_z}\tan\left(\frac{2\mu-1}{2N_r}\frac{\pi}{2}\right)\tan\left(\frac{2l-1}{2N_z}\frac{\pi}{2}\right)$$
$$\times\frac{\exp\{-\zeta_N(r_i)+\zeta_0(r_\mu)+\frac{\ln(\xi_m/\xi_l)}{2(1+\lambda)}\}}{\sqrt{\left(\sqrt{\gamma_{\mu l,N}+\beta_\mu}+\theta_{\mu l\nu,N}\right)\left(\sqrt{\gamma_{\mu l,N}-\beta_\mu}+\theta_{\mu l\nu,N}\right)}}$$
$$\times\Bigg\{v_z\left[-\tilde{E}+\frac{\hat{F}-\hat{E}}{\theta_{\mu l\nu,N}}\left(\zeta_N(r_i)-\zeta_0(r_\mu)-\frac{\ln(\xi_m/\xi_l)}{2(1+\lambda)}\right)\right]$$
$$+ v_r\frac{\hat{F}-\hat{E}}{\theta_{\mu l\nu,N}}\left[r_i - \frac{\left(\gamma_{\mu l,N}-\theta^2_{\mu l\nu,N}\right)}{2r_i}\right]\Bigg\}, \quad (C7)$$

where

$$\gamma_{\mu l,N} = r_\mu^2 + r_i^2 + \left[\zeta_N(r_i) - \zeta_0(r_\mu) - \frac{\ln(\xi_m/\xi_l)}{2(1+\lambda)}\right]^2,$$

$$\beta_\mu = 2 r_\mu r_i,$$

$$\theta_{\mu l\nu,N} = \sqrt{\gamma_{\mu l,N} - \beta_\mu} + \left[\sqrt{\gamma_{\mu l,N} + \beta_\mu} - \sqrt{\gamma_{\mu l,N} - \beta_\mu}\right] \cos^2\left(\frac{2\nu - 1}{2N_\varphi}\frac{\pi}{2}\right).$$

The quantities $\tilde{E}$, $\hat{F}$, and $\hat{F}$ are given by

$$\tilde{E} = \left\{\exp\{\theta_{\mu l\nu,N}\}\,\mathrm{erf}\left[\frac{\theta_{\mu l\nu,N}}{2\sqrt{N\,\Delta t}} + \sqrt{N\,\Delta t}\right]\right.$$
$$\left. + \exp\{-\theta_{\mu l\nu,N}\}\,\mathrm{erf}\left[\frac{\theta_{\mu l\nu,N}}{2\sqrt{N\,\Delta t}} - \sqrt{N\,\Delta t}\right] - 2\sinh(\theta_{\mu l\nu,N})\right\},$$

$$\hat{E} = \frac{1}{\theta_{\mu l\nu,N}}\left\{\exp\{\theta_{\mu l\nu,N}\}\,\mathrm{erf}\left[\frac{\theta_{\mu l\nu,N}}{2\sqrt{N\,\Delta t}} + \sqrt{N\,\Delta t}\right]\right.$$
$$\left. + \exp\{-\theta_{\mu l\nu,N}\}\,\mathrm{erf}\left[\frac{\theta_{\mu l\nu,N}}{2\sqrt{N\,\Delta t}} - \sqrt{N\,\Delta t}\right] - 2\sinh(\theta_{\mu l\nu,N})\right\},$$

and

$$\hat{F} = \left[-2\cosh(\theta_{\mu l\nu,N}) + \exp\{\theta_{\mu l\nu,N}\}\mathrm{erf}\left[\frac{\theta_{\mu l\nu,N}}{2\sqrt{N\,\Delta t}} + \sqrt{N\,\Delta t}\right] - \exp\{-\theta_{\mu l\nu,N}\}\right.$$
$$\left. \times\ \mathrm{erf}\left[\frac{\theta_{\mu l\nu,N}}{2\sqrt{N\,\Delta t}} - \sqrt{N\,\Delta t}\right] + \frac{2}{\sqrt{\pi(N\,\Delta t)}}\exp\left\{-\frac{\theta_{\mu l\nu,N}^2}{4(N\,\Delta t)} - N\,\Delta t\right\}\right].$$

The velocity components v_r and v_z are evaluated at $r = r_i$ and $z = \zeta_N(r_i) - \frac{\ln(\xi_m)}{2(1+\lambda)}$.

$$\hat{H}_4 = -\lambda \sum_{\sigma=1}^{N}\sum_{\mu=1}^{N_r}\sum_{\nu=1}^{N_\varphi}\sum_{l=1}^{N_z} \frac{p\pi^2}{4(1+\lambda)N_r N_\varphi N_z}\tan\left(\frac{2\mu-1}{2N_r}\frac{\pi}{2}\right)\tan\left(\frac{2l-1}{2N_z}\frac{\pi}{2}\right)$$
$$\times\ \frac{\exp\{-\zeta_N(r_i) + \zeta_{\sigma-1}(r_\mu) + \frac{\ln(\xi_m/\xi_l)}{2(1+\lambda)}\}}{\sqrt{\left(\sqrt{\gamma_{\mu l,N-\sigma+1} + \beta_\mu} + \theta_{\mu l\nu,N-\sigma+1}\right)\left(\sqrt{\gamma_{\mu l,N-\sigma+1} - \beta_\mu} + \theta_{\mu l\nu,N-\sigma+1}\right)}}$$
$$\times \left\{v_z\left[-\tilde{Q}_{\sigma-1} + \frac{\hat{R}_{\sigma-1} - \hat{Q}_{\sigma-1}}{\theta_{\mu l\nu,N-\sigma+1}}\left(\zeta_N(r_i) - \zeta_{\sigma-1}(r_\mu) - \frac{\ln(\xi_m/\xi_l)}{2(1+\lambda)}\right)\right]\right.$$
$$\left. + v_r\,\frac{\hat{Q}_{\sigma-1} - \hat{R}_{\sigma-1}}{\theta_{\mu l\nu,N-\sigma+1}}\left[r_i - \frac{\left(\gamma_{\mu l,N-\sigma+1} - \theta_{\mu l\nu,N-\sigma+1}^2\right)}{2r_i}\right]\right\}, \quad (C8)$$

where

$$\gamma_{\mu l,N-\sigma+1} = r_\mu^2 + r_i^2 + \left[\zeta_N(r_i) - \zeta_{\sigma-1}(r_\mu) - \frac{\ln(\xi_m/\xi_l)}{2(1+\lambda)}\right]^2,$$

$$\beta_\mu = 2r_\mu r_i,$$

$$\theta_{\mu l\nu,N-\sigma+1} =$$

$$\sqrt{\gamma_{\mu l,N-\sigma+1} - \beta_\mu} + \left[\sqrt{\gamma_{\mu l,N-\sigma+1} + \beta_\mu} - \sqrt{\gamma_{\mu l,N-\sigma+1} - \beta_\mu}\right] \cos^2\left(\frac{2\nu-1}{2N_\varphi}\frac{\pi}{2}\right).$$

The quantities $\tilde{Q}_{\sigma-1}$, $\hat{Q}_{\sigma-1}$, and $\hat{R}_{\sigma-1}$ are given by

$$\tilde{Q}_{\sigma-1} = \left\{\exp\{\theta_{\mu l\nu,N-\sigma+1}\}\left(\operatorname{erf}\left[\frac{\theta_{\mu l\nu,N-\sigma+1}}{2\sqrt{(N-\sigma)\Delta t}} + \sqrt{(N-\sigma)\Delta t}\right]\right.\right.$$
$$\left. - \operatorname{erf}\left[\frac{\theta_{\mu l\nu,N-\sigma+1}}{2\sqrt{(N-\sigma+1)\Delta t}} + \sqrt{(N-\sigma+1)\Delta t}\right]\right)$$
$$+ \exp\{-\theta_{\mu l\nu,N-\sigma+1}\}\left(\operatorname{erf}\left[\frac{\theta_{\mu l\nu,N-\sigma+1}}{2\sqrt{(N-\sigma)\Delta t}} - \sqrt{(N-\sigma)\Delta t}\right]\right.$$
$$\left.\left. - \operatorname{erf}\left[\frac{\theta_{\mu l\nu,N-\sigma+1}}{2\sqrt{(N-\sigma+1)\Delta t}} - \sqrt{(N-\sigma+1)\Delta t}\right]\right)\right\},$$

$$\hat{Q}_{\sigma-1} = \frac{1}{\theta_{\mu l\nu,N-\sigma+1}}\left\{\exp\{\theta_{\mu l\nu,N-\sigma+1}\}\left(\operatorname{erf}\left[\frac{\theta_{\mu l\nu,N-\sigma+1}}{2\sqrt{(N-\sigma)\Delta t}} + \sqrt{(N-\sigma)\Delta t}\right]\right.\right.$$
$$\left. - \operatorname{erf}\left[\frac{\theta_{\mu l\nu,N-\sigma+1}}{2\sqrt{(N-\sigma+1)\Delta t}} + \sqrt{(N-\sigma+1)\Delta t}\right]\right)$$
$$+ \exp\{-\theta_{\mu l\nu,N-\sigma+1}\}\left(\operatorname{erf}\left[\frac{\theta_{\mu l\nu,N-\sigma+1}}{2\sqrt{(N-\sigma)\Delta t}} - \sqrt{(N-\sigma)\Delta t}\right]\right.$$
$$\left.\left. - \operatorname{erf}\left[\frac{\theta_{\mu l\nu,N-\sigma+1}}{2\sqrt{(N-\sigma+1)\Delta t}} - \sqrt{(N-\sigma+1)\Delta t}\right]\right)\right\},$$

and

$$\hat{R}_{\sigma-1} = \left\{\exp\{\theta_{\mu l\nu,N-\sigma+1}\}\left(\operatorname{erf}\left[\frac{\theta_{\mu l\nu,N-\sigma+1}}{2\sqrt{(N-\sigma)\Delta t}} + \sqrt{(N-\sigma)\Delta t}\right]\right.\right.$$

$$- \operatorname{erf}\left[\frac{\theta_{\mu l\nu,N-\sigma+1}}{2\sqrt{(N-\sigma+1)\Delta t}} + \sqrt{(N-\sigma+1)\Delta t}\right]\Bigg)$$

$$- \exp\left\{-\theta_{\mu l\nu,N-\sigma+1}\right\}\left(\operatorname{erf}\left[\frac{\theta_{\mu l\nu,N-\sigma+1}}{2\sqrt{(N-\sigma)\Delta t}} - \sqrt{(N-\sigma)\Delta t}\right]\right.$$

$$\left. - \operatorname{erf}\left[\frac{\theta_{\mu l\nu,N-\sigma+1}}{2\sqrt{(N-\sigma+1)\Delta t}} - \sqrt{(N-\sigma+1)\Delta t}\right]\right)$$

$$+ \frac{2}{\sqrt{\pi(N-\sigma)\Delta t}} \exp\left\{-\frac{\theta^2_{\mu l\nu,N-\sigma+1}}{4(N-\sigma)\Delta t} - (N-\sigma)\Delta t\right\}$$

$$\left. - \frac{2}{\sqrt{\pi(N-\sigma+1)\Delta t}} \exp\left\{-\frac{\theta^2_{\mu l\nu,N-\sigma+1}}{4(N-\sigma+1)\Delta t} - (N-\sigma+1)\Delta t\right\}\right\}.$$

The velocity components v_r and v_z are evaluated at $r = r_i$ and $z = \zeta_N(r_i) - \frac{\ln(\xi_m)}{2(1+\lambda)}$.

The expressions C_1 through C_8 can now be combined to represent the discretized equivalent of the integral evolution equations.

APPENDIX D

Boundary integral formulation for the fluid velocity

In this appendix we present the boundary integral formulation used to evaluate the velocity field $\mathbf{v}$ at each time step. The flow past the unperturbed paraboloid is represented in the entire fluid domain by the Oseen approximation to the Navier-Stokes equation. When the crystal-melt interface is perturbed from its paraboloidal shape, one has to correct the flow field so that the no-slip condition on the perturbed surface is satisfied. The flow velocity $\mathbf{v}$ can then be expressed as a sum of two contributions:

a) the Oseen velocity, $\mathbf{v}_o$, for the *unperturbed paraboloid*, which is known in analytical form but does not satisfy the no-slip condition on the perturbed surface, and

b) a "correction" that vanishes at infinity but is equal to the negative of the Oseen velocity on the surface.

The total flow velocity then becomes

$$\mathbf{v} = \mathbf{v}_o + \mathbf{u} \tag{D1}$$

with

$$\mathbf{u} = -\mathbf{v}_o, \qquad \text{on the interface} \tag{D2}$$

and

$$\mathbf{u} \to 0, \qquad \text{as } \mathbf{x} \to \infty. \tag{D3}$$

The velocity $\mathbf{u}$ is only a local correction to the Oseen flow field in the vicinity of the surface; the asymptotic behavior of the total flow field at large distances from

the solid is determined solely by the Oseen solution. Thus, for the case of very low Reynolds numbers present in dendritic growth, the flow field $\mathbf{u}$ is inertialess and can be described by the Stokes equation

$$-\nabla P + \nabla^2 \mathbf{u} = 0. \qquad (D4)$$

(As was discussed in Chapter 3, the temporal term of the transient Stokes equation can be neglected because, at very low Reynolds numbers, the velocity field responds instantaneously to changes in the interface shape).

We solve the Stokes equation using the boundary integral formulation first applied by Youngren and Acrivos [1]. The differential equation is transformed into a boundary integral equation that relates the local surface stresses $\mathbf{f}$ to the velocity $\mathbf{u}$:

$$c(\mathbf{x})\,\mathbf{u}(\mathbf{x}) = \frac{3}{4\pi}\int_\Gamma \frac{(\mathbf{x}-\mathbf{y})\,[(\mathbf{x}-\mathbf{y})(\mathbf{x}-\mathbf{y}) : \hat{\mathbf{n}}(\mathbf{y})\mathbf{u}(\mathbf{y})]}{d_{xy}^5}\,d\Gamma + \frac{1}{8\pi}\int_\Gamma \left[\frac{\mathbf{f}(\mathbf{y})}{d_{xy}} + \frac{(\mathbf{x}-\mathbf{y})\,[(\mathbf{x}-\mathbf{y})\cdot\mathbf{f}(\mathbf{y})]}{d_{xy}^3}\right] d\Gamma, \qquad \mathbf{y}\in\Gamma, \quad (D5)$$

where $\hat{\mathbf{n}}$ is the unit normal on the interface pointing toward the fluid domain Ω, $d_{xy} = |\mathbf{x}-\mathbf{y}|$, and

$$c(\mathbf{x}) = \begin{cases} \frac{1}{2}, & \text{if } \mathbf{x}\in\Gamma; \\ 1, & \text{if } \mathbf{x}\in\Omega-\Gamma. \end{cases}$$

The calculation of the interior velocity takes place in two steps. First, the surface stresses, $\mathbf{f}$ are calculated from Eq. (D5) with $\mathbf{x}\in\Gamma$ (the surface velocities $\mathbf{u}(\mathbf{x}_\Gamma)$ are known from the boundary conditions, i.e. the Oseen flow velocity). Then, Eq. (D5) is used to evaluate the interior velocities for selected points $\mathbf{x}\in\Omega-\Gamma$.

For axisymmetric flows, the vector equation Eq. (D5) reduces to two scalar equations. In a polar cylindrical coordinate system, where $\mathbf{x} = (r_x, \varphi_x, z_x)$ and $\mathbf{y} = (r_y, \varphi_y, z_y)$, Eq. (D5) can be decomposed to

$$c(\mathbf{x})\, u_r(\mathbf{x}) - \frac{3}{4\pi}\int_0^{2\pi} d\theta \int_0^{\infty} \frac{dr_y r_y}{d_{xy}^5}(r_x - r_y\cos\theta)\left[z_x - \zeta_y - \frac{d\zeta_y}{dr_y}(r_x\cos\theta - r_y)\right] \times \left[u_r(\mathbf{y})(r_x\cos\theta - r_y) + (z_x - \zeta_y)u_z(\mathbf{y})\right]$$
$$= \frac{1}{8\pi}\int_0^{2\pi} d\theta \int_0^{\infty} dr_y\, r_y \sqrt{1 + \left(\frac{d\zeta_y}{dr_y}\right)^2}\left\{\frac{f_r(\mathbf{y})\cos\theta}{d_{xy}} + \frac{r_x - r_y\cos\theta}{d_{xy}^3} \times \left[f_r(\mathbf{y})(r_x\cos\theta - r_y) + (z_x - \zeta_y)\, f_z(\mathbf{y})\right]\right\}, \quad (D6)$$

and

$$c(\mathbf{x})\, u_z(\mathbf{x}) - \frac{3}{4\pi}\int_0^{2\pi} d\theta \int_0^{\infty} \frac{dr_y r_y}{d_{xy}^5}(z_x - \zeta_y)\left[z_x - \zeta_y - \frac{d\zeta_y}{dr_y}(r_x\cos\theta - r_y)\right] \times \left[u_r(\mathbf{y})(r_x\cos\theta - r_y) + (z_x - \zeta_y)u_z(\mathbf{y})\right]$$
$$= \frac{1}{8\pi}\int_0^{2\pi} d\theta \int_0^{\infty} dr_y\, r_y \sqrt{1 + \left(\frac{d\zeta_y}{dr_y}\right)^2}\left\{\frac{f_z(\mathbf{y})}{d_{xy}} + \frac{z_x - \zeta_y}{d_{xy}^3} \times \left[f_r(\mathbf{y})(r_x\cos\theta - r_y) + (z_x - \zeta(\mathbf{y}))\, f_z(\mathbf{y})\right]\right\}, \quad (D7)$$

where $z_y = \zeta_y \equiv \zeta(r_y)$ represents the interface Γ, $\theta = \varphi_x - \varphi_y$, and

$$d_{xy} = \sqrt{r_x^2 + r_y^2 - 2r_x r_y\cos\theta + (z_x - \zeta_y)^2}.$$

We now discretize the interface Γ in N_r ring-type elements. Each element Γ_j is associated with a "node" at $r = r_j$. Over each such element the surface velocities and the surface stresses are considered constant and are represented by their values at the corresponding node. The surface integrals in Eqs. (D6-D7) can now be written as the sums of the integrals over each surface element Γ_j. For $\mathbf{x} \in \Gamma$, Eqs.

(D6-D7) become

$$u_r(r_i) - \frac{3}{2\pi}\int_0^{2\pi} d\theta \int_0^{\infty} \frac{dr\, r}{d_{xy}^5}(r_i - r\cos\theta)\left[\zeta_i - \zeta(r) - \zeta'(r)(r_i\cos\theta - r)\right]$$
$$\times \left[u_r(r)(r_i\cos\theta - r) + (\zeta_i - \zeta(r))\, u_z(r)\right]$$
$$= \sum_{j=1}^{N_r} f_r(r_j)\int_0^{2\pi} d\theta \int_{\Gamma_j} \frac{dr\, r}{4\pi d_{xy}}\sqrt{1+(\zeta'(r))^2}\left[\cos\theta + \frac{r_i - r\cos\theta}{d_{xy}^2}\right] \qquad (D8)$$
$$+ \sum_{j=1}^{N_r} f_z(r_j)\int_0^{2\pi} d\theta \int_{\Gamma_j} \frac{dr\, r}{4\pi d_{xy}^3}\sqrt{1+(\zeta'(r))^2}(r_i - r\cos\theta)\,(\zeta_i - \zeta(r))$$

and

$$u_z(r_i) - \frac{3}{2\pi}\int_0^{2\pi} d\theta \int_0^{\infty} \frac{dr\, r}{d_{xy}^5}(\zeta_i - \zeta(r))\left[\zeta_i - \zeta(r) - \zeta'(r)(r_i\cos\theta - r)\right]$$
$$\times \left[u_r(r)(r_i\cos\theta - r) + (\zeta_i - \zeta(r))\, u_z(r)\right]$$
$$= \sum_{j=1}^{N_r} f_r(r_j)\int_0^{2\pi} d\theta \int_{\Gamma_j} \frac{dr\, r}{4\pi d_{xy}^3}\sqrt{1+(\zeta'(r))^2}(r_i\cos\theta - r)\,(\zeta_i - \zeta(r)) \qquad (D9)$$
$$+ \sum_{j=1}^{N_r} f_z(r_j)\int_0^{2\pi} d\theta \int_{\Gamma_j} \frac{dr\, r}{4\pi d_{xy}}\sqrt{1+(\zeta'(r))^2}\left[1 + \frac{(\zeta_i - \zeta(r))^2}{d_{xy}^2}\right]$$

where $r_i \equiv r_x$, $r_y \equiv r$, $z_x = \zeta(r_i) = \zeta_i$, $\zeta'(r) = \frac{d\zeta}{dr}$, and

$$d_{xy} = \sqrt{r_i^2 + r^2 - 2r_i r\cos\theta + \left(\zeta_i - \zeta(r)\right)^2}.$$

To calculate the left-hand-side of Eqs. (D8-D9) one needs to obtain the boundary condition for the velocity $\mathbf{u}$. From Eq. (D2)

$$\mathbf{u}(\mathbf{x}_\Gamma) = -\mathbf{v}_o(\mathbf{x}_\Gamma)\,.$$

But $\mathbf{v}_o$ is by definition equal to the Oseen velocity that satisfies Eq. (2.13) and is presented in analytical form in Eq. (2.14). This velocity is non-zero on the perturbed interface $z = \zeta(r)$, since it satisfies the no-slip condition on the surface

of the *unperturbed* paraboloid $z = \zeta_0(r)$. Equations (2.14) and (D2) are thus used to calculate the boundary values of u as explicit functions of the interface shape $z = \zeta(r)$. (The Oseen velocity in Eq. (2.14) is expressed in paraboloidal coordinates and a simple transformation to the cylindrical coordinate system is required). The expressions in the left-hand-side of Eqs. (D8-D9) are then calculated using a simple Gauss-Legendre quadrature.

The components of the local surface stress vector, f_r and f_z, are considered constant over each element Γ_j and are represented by the nodal vectors

$$\mathbf{t_r} = [f_r(r_1), f_r(r_2), \ldots, f_r(r_{N_r})],$$

$$\mathbf{t_z} = [f_z(r_1), f_z(r_2), \ldots, f_z(r_{N_r})].$$

The choice of the nodal points (r_i) in this problem is dictated by the discretization of the boundary integrals in the integral evolution equation for the interface shape. Equations (D8-D9) form a $(2N_r \times 2N_r)$ system of linear algebraic equations for the local surface stresses (written in compact notation)

$$\begin{pmatrix} \mathbf{A_1} & \mathbf{A_2} \\ \mathbf{A_3} & \mathbf{A_4} \end{pmatrix} \begin{pmatrix} \mathbf{t_r} \\ \mathbf{t_z} \end{pmatrix} = \begin{pmatrix} \mathbf{k_1} \\ \mathbf{k_2} \end{pmatrix} \qquad (D10)$$

where the matrix element $[A_{k,ij}]$, $k = 1, 2, 3, 4$, represents the integral over the element Γ_j with $r_x = r_i$.

The integrals $A_{k,ij}$ can be easily calculated for $i \neq j$ using a simple Gauss-Legendre quadrature. For $i = j$, the integrals $A_{k,jj}$ are singular because the integration interval includes the field point r_i and thus d_{xy} in the denominator becomes zero as $r \to r_j$. Nevertheless, the improper integrals $A_{k,jj}$ do exist as long as the surface Γ satisfies the Lyapunov condition at each node $r = r_j$. It can be easily

shown that the integrands in each of the singular integrals behave as $1/d_{xy}$ in the vicinity of the singular point ($r = r_j$). This weak singularity is integrable and the integration is carried out using the coordinate transformation

$$\eta = \sqrt{\alpha(r, r_i) - \gamma(r, r_i)\cos\theta},$$

where

$$\alpha(r, r_i) = r_i^2 + r^2 + \left(\zeta_i - \zeta(r)\right)^2$$

and

$$\gamma(r, r_i) = 2r_i r.$$

The integral

$$I = \int_0^{2\pi} d\theta \int_{\Gamma_j} dr \frac{h(r,\theta)}{d_{xy}},$$

where h is a non-singular function, becomes

$$I = \int_{\sqrt{\alpha-\gamma}}^{\sqrt{\alpha+\gamma}} d\eta \int_{\Gamma_j} \frac{dr}{\sqrt{(\sqrt{\alpha+\gamma}-\eta)\,(\eta-\sqrt{\alpha-\gamma})}} \frac{4\,h(r,\eta)}{\sqrt{(\sqrt{\alpha+\gamma}+\eta)\,(\eta+\sqrt{\alpha-\gamma})}}$$

We can now apply following Gaussian quadrature formula (based on the orthogonal Chebyshev polynomials of the first kind) [2]

$$\int_a^b \frac{h(y)}{\sqrt{(y-a)(b-y)}} \approx \sum_{m=1}^{M} \frac{\pi}{M} h(y_m)$$
$$y_m = \frac{(b+a)}{2} + \frac{(b-a)}{2}\cos\left(\frac{2m-1}{M}\frac{\pi}{2}\right)$$

to the integral I to get

$$I = \frac{4\pi}{M} \sum_{m=1}^{M} \frac{h(r,\eta_m)}{\sqrt{(\sqrt{\alpha+\gamma}+\eta_m)\,(\eta_m+\sqrt{\alpha-\gamma})}}, \qquad (D11)$$

where

$$\eta_m = \frac{\sqrt{\alpha+\gamma}+\sqrt{\alpha-\gamma}}{2} + \frac{\sqrt{\alpha+\gamma}-\sqrt{\alpha-\gamma}}{2}\cos\left(\frac{2m-1}{M}\frac{\pi}{2}\right).$$

We now calculate all the integrals $A_{k,ij}$ and then invert the matrix Eq. (D10) to obtain the local surface stresses at each node.

In order to calculate the velocity at a point $\mathbf{x} = (r_i, z_l)$, in the interior of the domain, we use Eqs. (D6-D7) for $\mathbf{x} \in \Omega - \Gamma$:

$$u_r(r_i, z_l) =$$

$$\frac{3}{4\pi}\int_0^{2\pi} d\theta \int_0^{\infty} \frac{dr\, r}{d_{xy}^5}(r_i - r\cos\theta)\left[z_l - \zeta(r) - \zeta'(r)(r_i\cos\theta - r)\right]$$

$$\times \left[u_r(r)(r_i\cos\theta - r) + (z_l - \zeta(r))\, u_z(r)\right]$$

$$+\sum_{j=1}^{N_r} f_r(r_j)\int_0^{2\pi} d\theta \int_{\Gamma_j} \frac{dr\, r}{8\pi d_{xy}}\sqrt{1+(\zeta'(r))^2}\left[\cos\theta + \frac{r_i - r\cos\theta}{d_{xy}^2}\right]$$

$$+\sum_{j=1}^{N_r} f_z(r_j)\int_0^{2\pi} d\theta \int_{\Gamma_j} \frac{dr\, r}{8\pi d_{xy}^3}\sqrt{1+(\zeta'(r))^2}(r_i - r\cos\theta)\,(z_l - \zeta(r)) \quad (D12)$$

and

$$u_z(r_i, z_l) =$$

$$\frac{3}{4\pi}\int_0^{2\pi} d\theta \int_0^{\infty} \frac{dr\, r}{d_{xy}^5}(z_l - \zeta(r))\left[z_l - \zeta(r) - \zeta'(r)(r_i\cos\theta - r)\right]$$

$$\times \left[u_r(r)(r_i\cos\theta - r) + (z_l - \zeta(r))\, u_z(r)\right]$$

$$+\sum_{j=1}^{N_r} f_r(r_j)\int_0^{2\pi} d\theta \int_{\Gamma_j} \frac{dr\, r}{8\pi d_{xy}^3}\sqrt{1+(\zeta'(r))^2}(r_i\cos\theta - r)\,(z_l - \zeta(r))$$

$$+\sum_{j=1}^{N_r} f_z(r_j)\int_0^{2\pi} d\theta \int_{\Gamma_j} \frac{dr\, r}{8\pi d_{xy}}\sqrt{1+(\zeta'(r))^2}\left[1 + \frac{(z_l - \zeta(r))^2}{d_{xy}^2}\right] \quad (D13)$$

where

$$d_{xy} = \sqrt{r_i^2 + r^2 - 2r_i r\cos\theta + \left(z_l - \zeta(r)\right)^2}.$$

Equations (D12-13) do not contain any singular integrals ($\mathbf{x} \in \Omega - \Gamma$ whereas $\mathbf{y} \in \Gamma$) and the Stokes correction velocities can be easily calculated using a Gauss-Legendre quadrature. The total velocity $\mathbf{v}$, which appears in the interface evolution equations in Chapters 2 and 3, is then calculated by adding the unperturbed Oseen velocity $\mathbf{v}_o$, given by Eq. (2.14), to the Stokes correction $\mathbf{u}$ for the perturbed interface. The new velocity $\mathbf{v}$ satisfies the no-slip condition on the perturbed interface and reduces to the unperturbed Oseen velocity away from the interface.

References

[1] G. K. Youngren and A. Acrivos, J. Fluid Mech. 69 (1975) 377.

[2] M. Abramowitz and I. A. Stegun, Eds., Handbook of Mathematical Functions, Applied Mathematics Series 55 (NBS, Washington, 1964).

APPENDIX E:

Derivation of the Gibbs-Thompson relation

This appendix describes the derivation of the Gibbs-Thompson thermodynamic equation, which determines the effect of capillarity on the temperature of a crystal-melt interface. The derivation presented here is similar to that of Delves [1].

Consider a very small section of the interface, over which the curvature is constant, and with small adjacent regions of the solid and liquid phases which are uniform in temperature and composition. The total extensive thermodynamic variables (E, S, V, F = Helmholtz free energy) can be divided between solid, liquid, and interface. Assuming that the volume and number of particles allocated to the interface are both zero, the surface free energy is defined by

$$F(\text{total}) = F_S + F_L + \gamma \cdot \text{Area}, \qquad (E1)$$

where γ is the solid-liquid interfacial tension. The equilibrium conditions at the interface are obtained by minimizing the free energy with respect to changes of energy and of particles between the two phases. This leads to the equality of temperature and chemical potentials of each component (μ_{Si}, μ_{Li}, i labels component), which are defined per atom of component. A further minimization with respect to an infinitesimal change of volume of one phase, the total volume being constant, leads to the condition

$$P_S - P_L = \gamma \frac{\text{d surface area}}{\text{d}V_S} = \gamma \left(\frac{1}{r_1} + \frac{1}{r_2} \right). \qquad (E2)$$

P_S and P_L are the pressures at the curved interface; r_1 and r_2 are the principal radii of curvature and are positive if the interface is concave towards the solid. If the pressures P_S and P_L are nearly the same as the pressures at a flat interface,

$$\Delta P_S = P_S - P_S(\text{flat}); \qquad |\Delta P_S| \ll P_S, \tag{E3}$$

one may use an approximate formula (approximate because ΔP_S is a small but finite change) from the Gibbs-Duhem relations, which are thermodynamic identities for each phase,

$$\begin{aligned} \sum \Delta\mu_{Si}\, N_{Si} &= V_S\, \Delta P_S - S_S \Delta T, \\ \sum \Delta\mu_{Li}\, N_{Li} &= V_L\, \Delta P_L - S_L \Delta T. \end{aligned} \tag{E4}$$

At a flat interface $P_S(\text{flat}) = P_L(\text{flat})$, so from Eq. (E2)

$$\Delta P_S - \Delta P_L = \gamma \left(\frac{1}{r_1} + \frac{1}{r_2} \right). \tag{E5}$$

and $\Delta\mu_{Si} = \Delta\mu_{Li}$ because the phases are always in equilibrium, and $\Delta\mu_{Si}$ is the change in chemical potential if the interface changes from flat to curved.

If the system has one component only (i.e. solidification from a pure melt), only one variable, ΔP_L for example, needs to be specified to find the other three variables ΔT, $\Delta\mu_L$ and ΔP_S. Assuming that the liquid is under a constant pressure and that variations in P_L at the interface due to hydrostatic effects and convection are negligible compared to ΔP_L, then it is reasonable to set $\Delta P_L = 0$ and all the pressure difference is taken up by the solid phase. The elimination of $\Delta\mu$ from Eqs. (E3-E4) gives

$$-\Delta T \left(\frac{S_L}{N_L} - \frac{S_S}{N_S} \right) = \frac{\gamma V_S}{N_S} \left(\frac{1}{r_1} + \frac{1}{r_2} \right). \tag{E6}$$

$T_M(S_L/N_L - S_S/N_S)$ is the latent heat of solidification per atom, so if L is defined as the latent heat per unit volume of solid and ΔT is the temperature at a curved interface minus the value at a flat interface,

$$\tilde{T}_\Gamma = T_M + \Delta T = T_M \left(1 - \frac{\gamma}{L}\tilde{\mathcal{K}}\right), \qquad (E7)$$

where $\tilde{T}_\Gamma$ is the temperature at the interface Γ and $\tilde{\mathcal{K}} = (1/r_1 + 1/r_2)$ is the local interface curvature. By defining $T = (\tilde{T} - T_\infty)c_p/L$, $\Delta = (T_M - T_\infty)c_p/L$, and $\mathcal{K}$ $= \tilde{\mathcal{K}}/\rho$, Eq. (E7) becomes

$$T_\Gamma = \Delta - (d_0/\rho)\mathcal{K}, \qquad (E8)$$

where $d_0 = \gamma\, T_M c_p/L^2$ is a capillary length and ρ is the tip radius of the crystal dendrite. Equation (E8) represents the Gibbs-Thompson relation in the case of a pure melt and is used in Chapter 3 as the interface boundary condition for the temperature field.

REFERENCES

[1] R. T. Delves, Theory of Interface Stability, in Crystal Growth, Vol. 1, B. R. Pamplin, Ed. (Pergamon Press Ltd., New York, 1974).

APPENDIX F: LIST OF FIGURES

Fig. 8. The perturbation tip velocity $\dot{\zeta}(0,t)$ is plotted *vs* time for different numbers N_φ of discretization points in the φ-direction ($\nu = 0.001$, $\lambda = 0.0$, $Pe = 1.0$, $N_r = 12$, $\Delta t = 0.002$).

Fig. 9. The perturbation tip velocity $\dot{\zeta}(0,t)$ is plotted *vs* time for different time steps Δt ($\nu = 0.001$, $\lambda = 0.0$, $Pe = 1.0$, $N_r = 12$, $N_\varphi = 7$).

Fig. 10. Interface destabilization via tip splitting. The interface shape is plotted *vs* the radial coordinate r for different times ($\nu = \lambda = 0$, $Pe = 1$, $N_r = 12$, $N_\varphi = 7$, $\Delta t = 0.002$).

Fig. 11. The perturbation growth velocity $\dot{\zeta}(r,t)$ is plotted *vs* the radial coordinate for different times and for $\lambda = 0.0$, $\nu = 0.020$, and $Pe = 1$.

Fig. 12. The perturbation growth velocity $\dot{\zeta}(r,t)$ is plotted *vs* the radial coordinate for different times and for $\lambda = 0.0$, $\nu = 0.001$, and $Pe = 1$.

Fig. 13. The perturbation growth velocity $\dot{\zeta}(r,t)$ is plotted *vs* the radial coordinate for different times and for $\lambda = 0.1$, $\nu = 0.001$, and $Pe = 1$.

Fig. 14. The perturbation growth velocity $\dot{\zeta}(r,t)$ is plotted *vs* the radial coordinate for different times and for $\lambda = 1.0$, $\nu = 0.001$, and $Pe = 1$.

Fig. 15. The perturbation velocity at the tip, $\dot{\zeta}(0,t)$, is plotted *vs* time for different values of the surface tension parameter ν ($\lambda = 0.0$, $Pe = 1.0$). The inset, which is a blow-up of the $\nu = 0.001$ curve, shows that anisotropy has a negligible effect on the growth velocity.

Fig. 16. The perturbation velocity at the tip, $\dot{\zeta}(0,t)$, is plotted *vs* time for different flow strengths λ. Its absolute value increases with λ, causing a decrease in the ***total*** growth velocity, $[2 + \dot{\zeta}]$ ($\nu = 0.001$, $Pe = 1.0$).

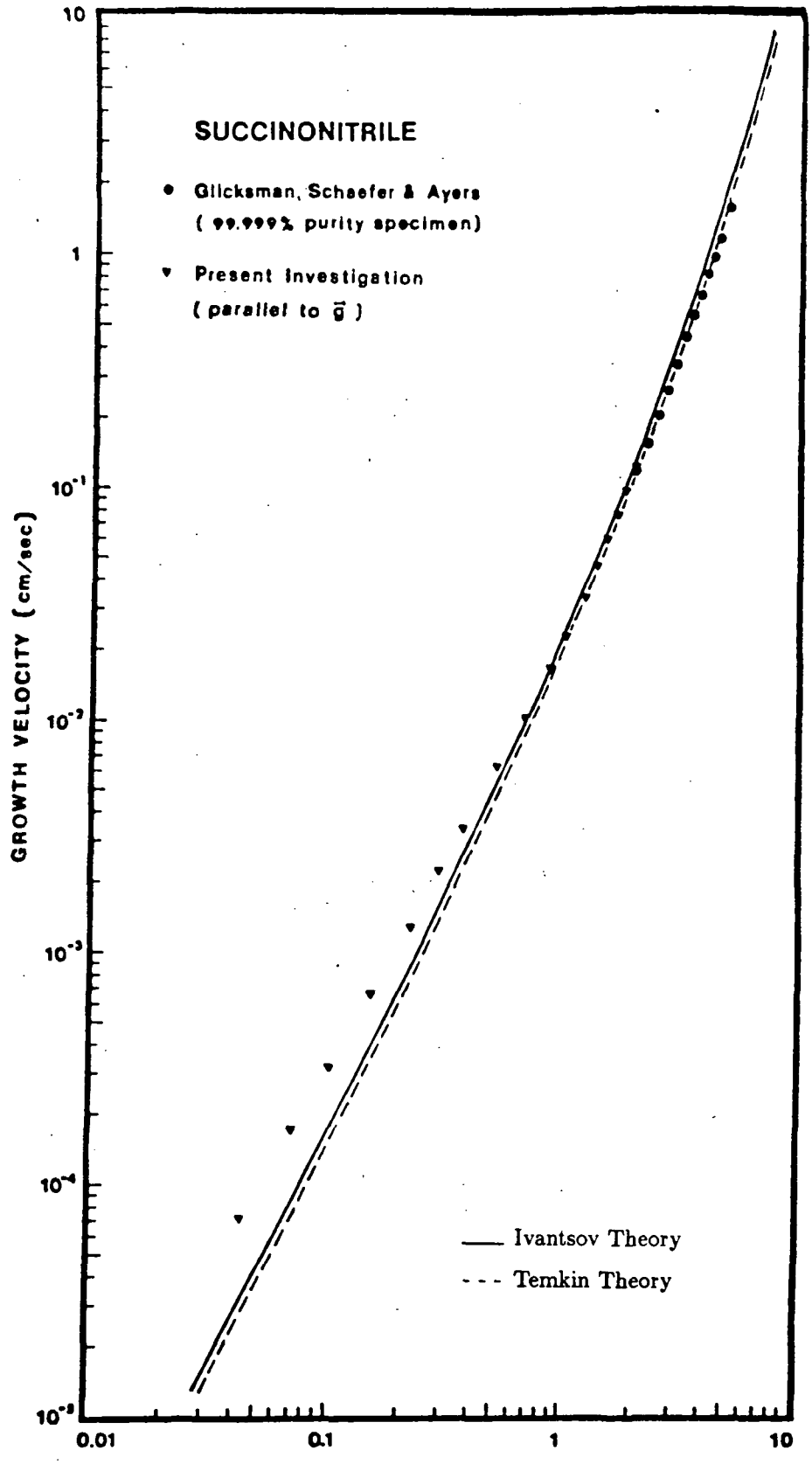

Fig 1. Measured tip velocity *vs* supercooling for succinonitrile. Note the deviation from the pure diffusion steady-state theories at low supercoolings. (Reprinted from Glicksman and Huang, Acta Metall. 29 (1981) 701).

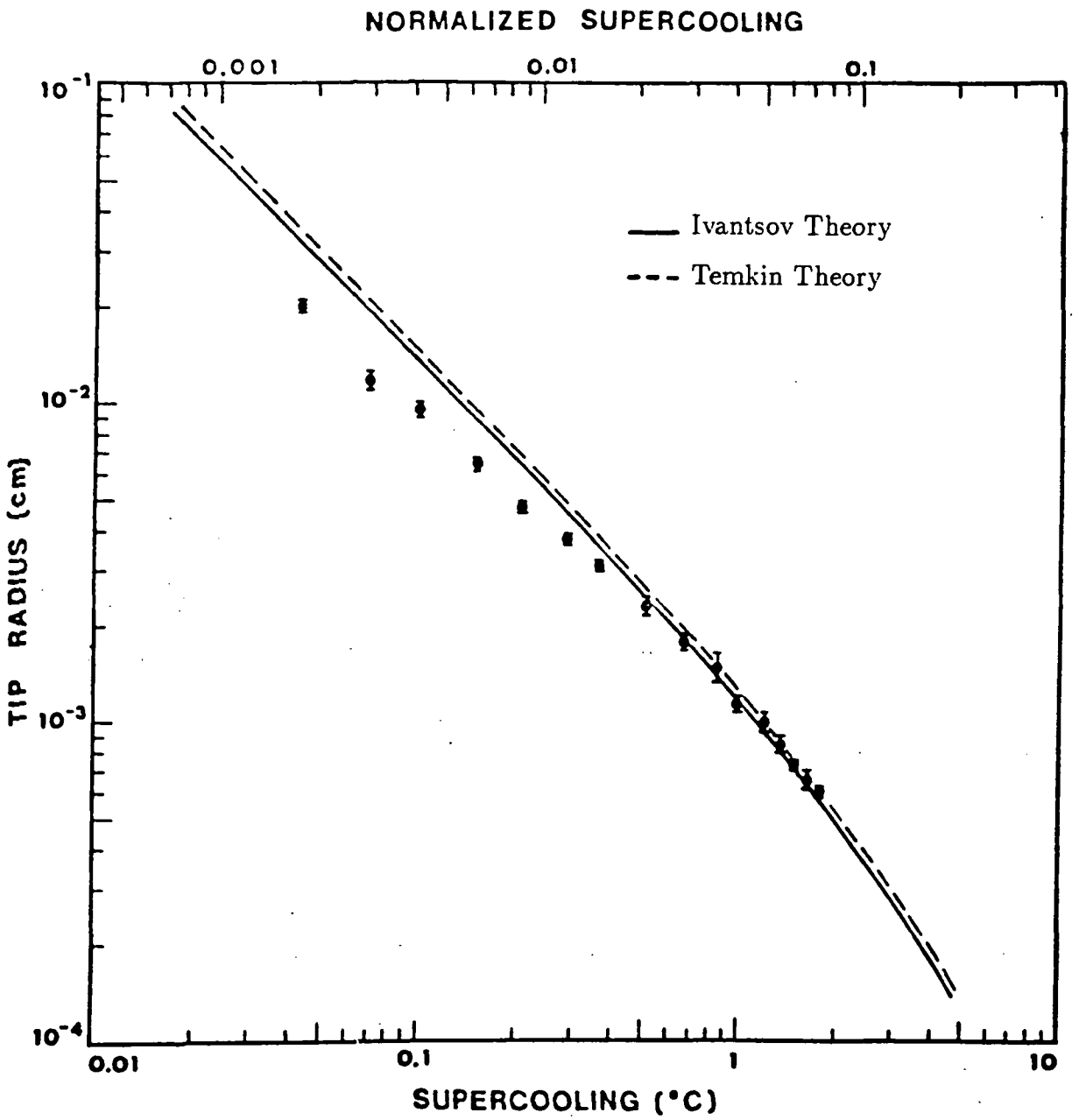

Fig.2. Measured tip radius *vs* supercooling for succinonitrile. Note the deviation from the pure diffusion steady-state theories at low supercoolings. (Reprinted from Glicksman and Huang, Acta Metall. 29 (1981) 701).

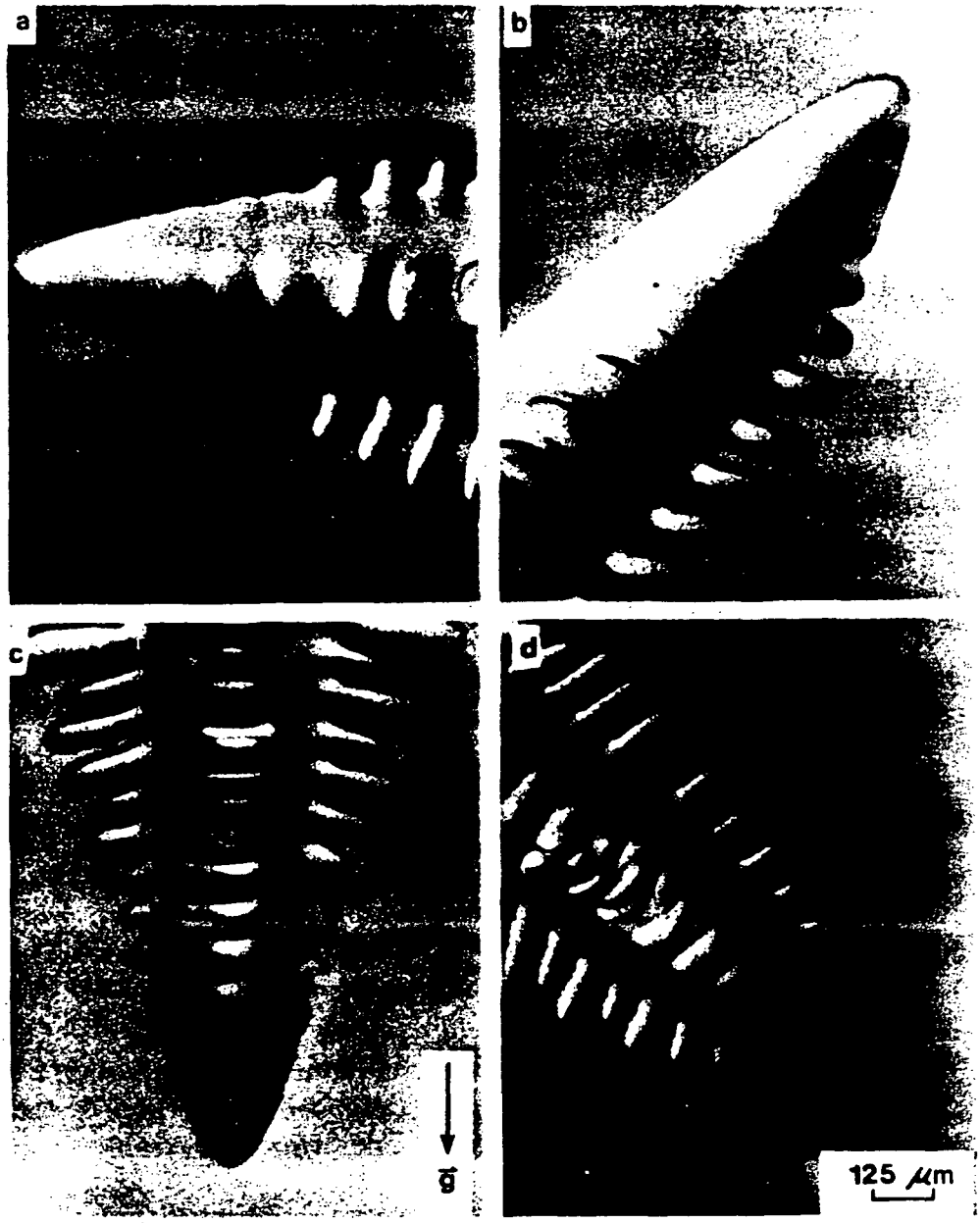

Fig 3. Effect of convection on the morphology of the interface. The distortion of the temperature field causes partial elimination of the sidebranches. (Reprinted from Glicksman and Huang, Proc. 3rd European Symp. on Material Sciences in Space, Grenoble, April 1979).

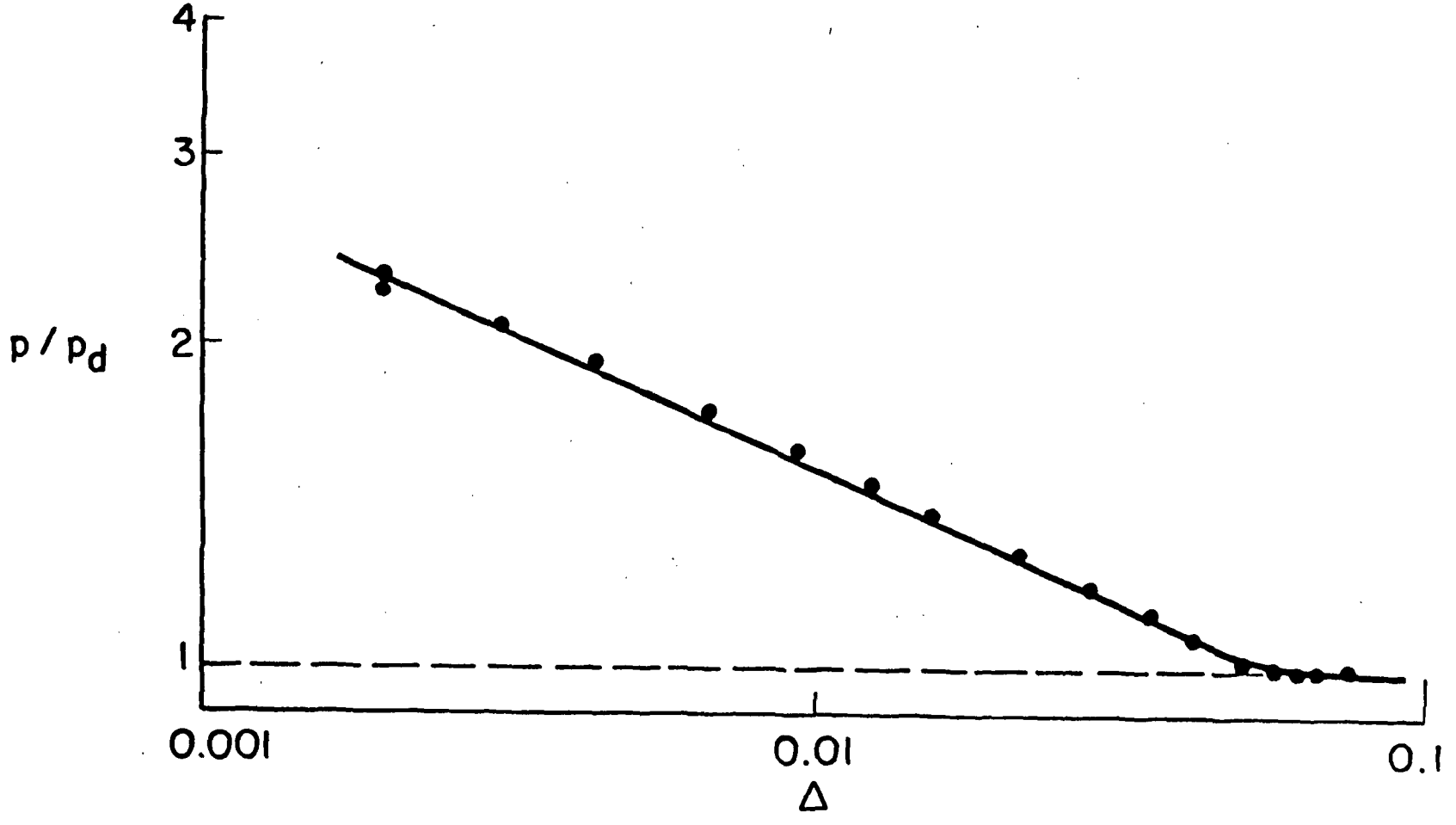

Fig.4. Ratio of measured Péclet number to Péclet number predicted by the Ivantsov theory. Convective effects cause a sharp transition to occur at $\Delta = 0.05$. (Reprinted from Glicksman and Huang, Proc. 3rd European Symp. on Material Sciences in Space, Grenoble, April 1979).

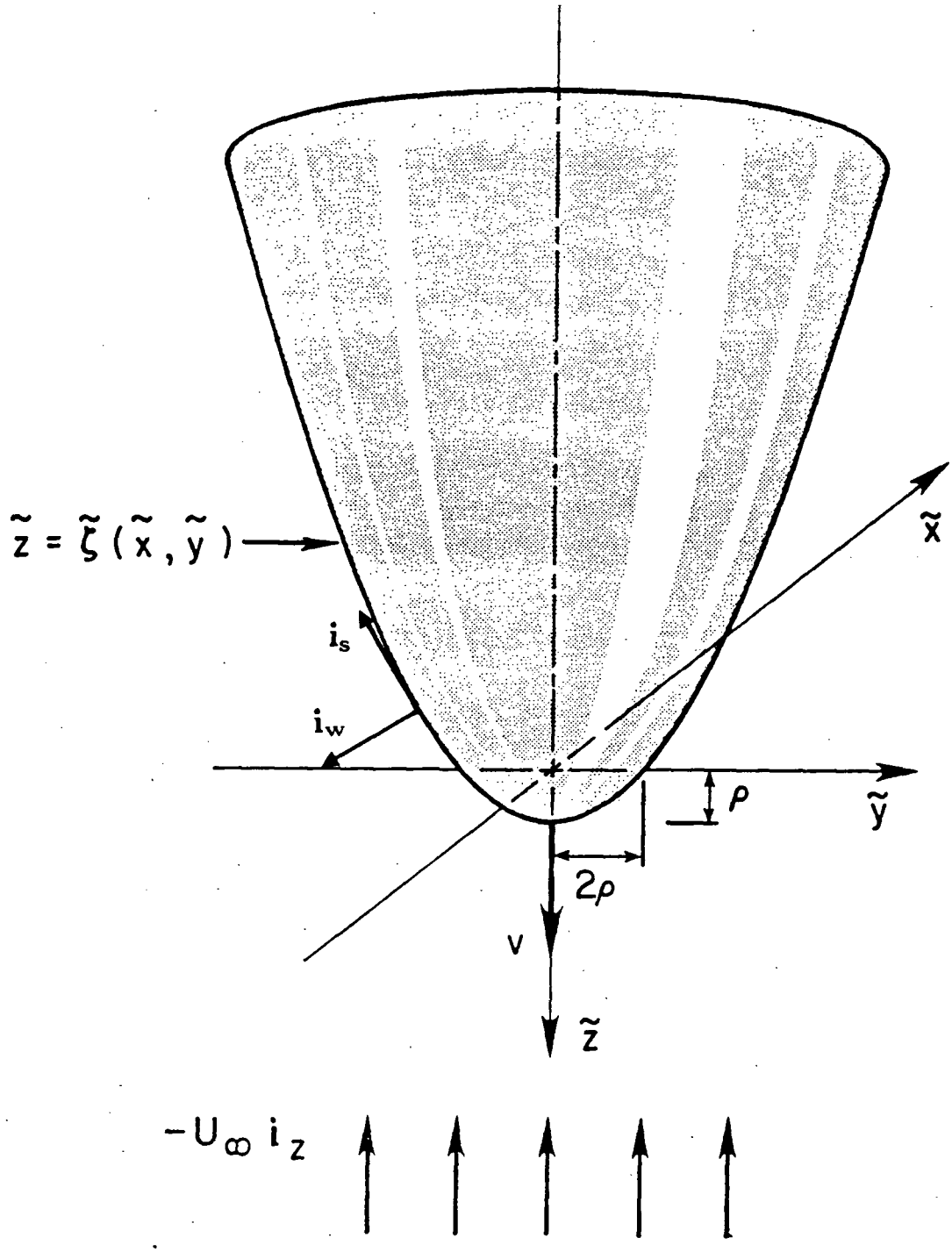

Fig. 5. Diagram of the coordinate system showing the orientation of the paraboloidal crystal and the flow.

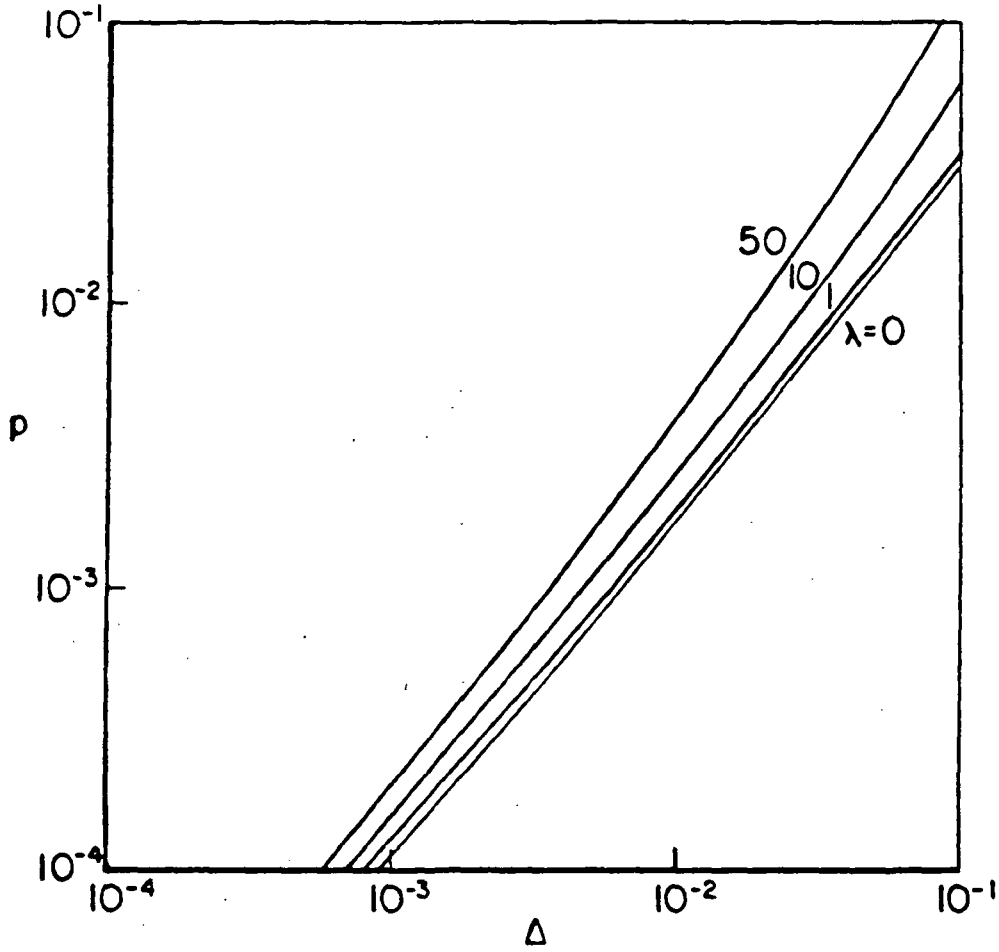

Fig. 6. The Péclet number as a function of supercooling for selected values of the velocity ratio. For these calculations the Prandtl number is 23.2 (succinonitrile). The Ivantsov solution corresponds to $\lambda = 0$.

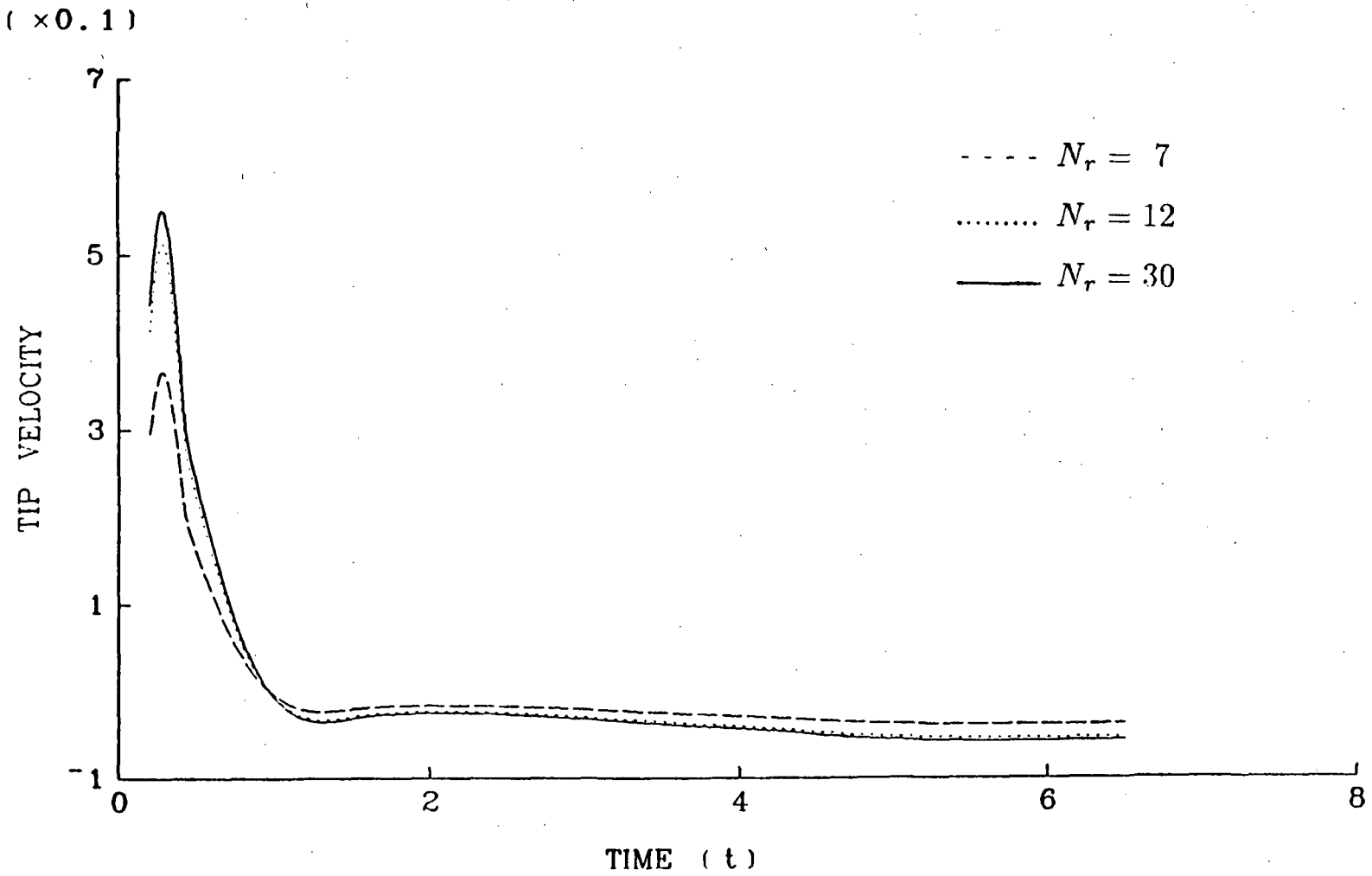

Fig. 7. The perturbation tip velocity $\dot{\zeta}(0,t)$ is plotted *vs* time for different numbers N_r of discretization points in the radial direction ($\nu = 0.001$, $\lambda = 0.0$, $Pe = 1.0$, $N_\varphi = 7$, $\Delta t = 0.002$).

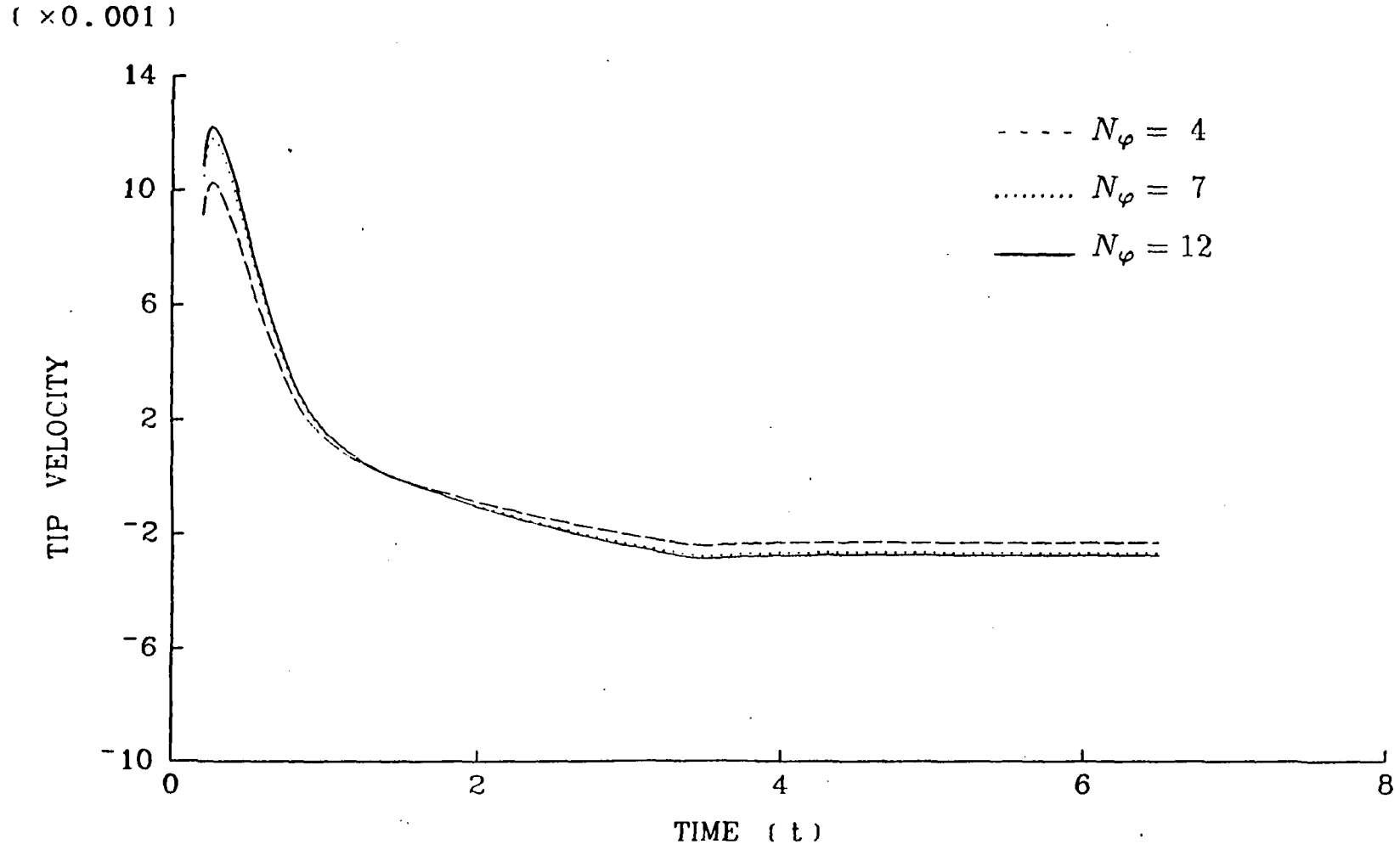

Fig. 8. The perturbation tip velocity $\dot{\zeta}(0,t)$ is plotted *vs* time for different numbers N_φ of discretization points in the φ-direction ($\nu = 0.001$, $\lambda = 0.0$, $Pe = 1.0$, $N_r = 12$, $\Delta t = 0.002$).

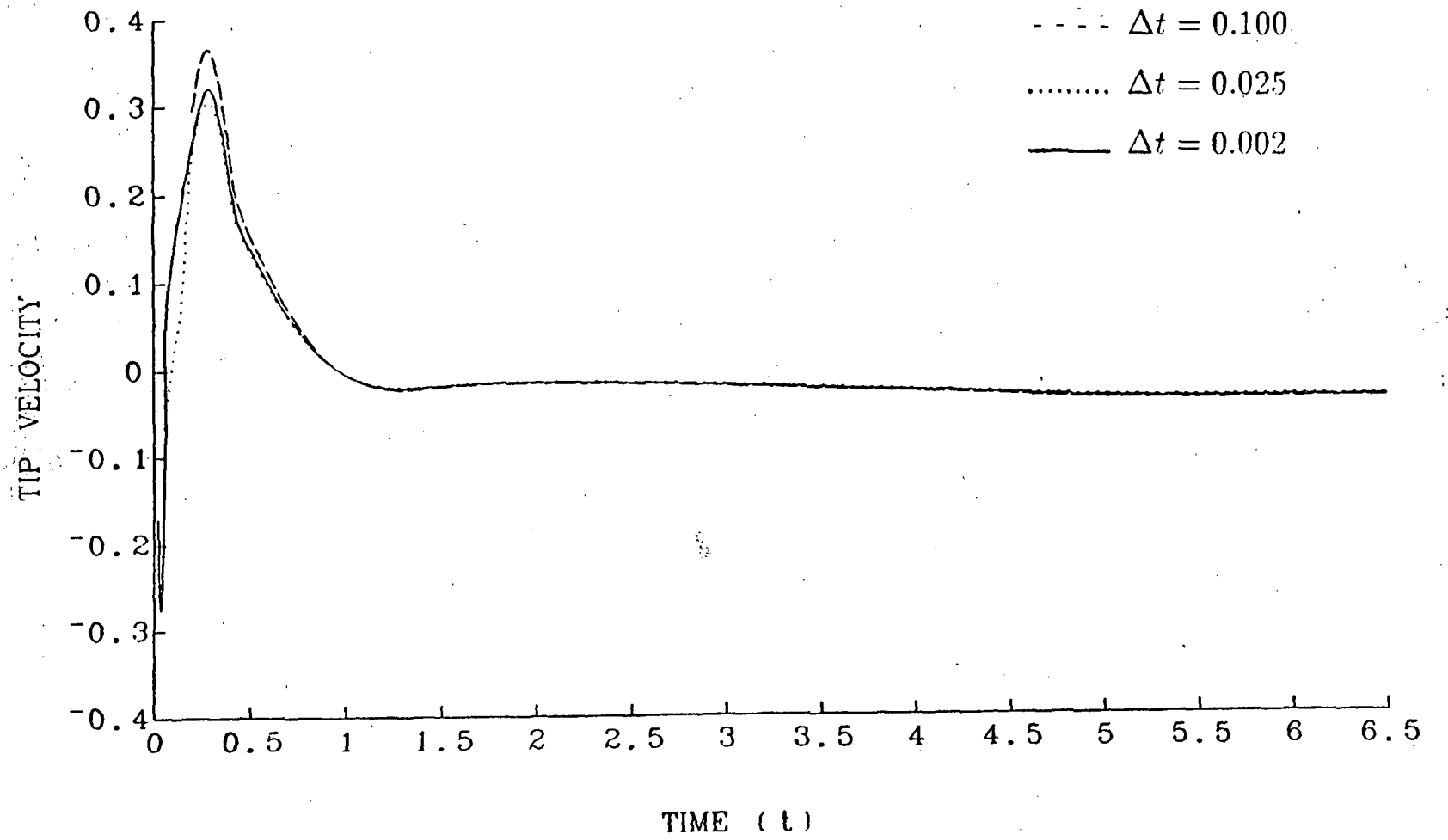

Fig. 9. The perturbation tip velocity $\dot{\zeta}(0,t)$ is plotted *vs* time for different time steps Δt ($\nu = 0.001$, $\lambda = 0.0$, $Pe = 1.0$, $N_r = 12$, $N_\varphi = 7$).

Fig. 10. Interface destabilization via tip splitting. The interface shape is plotted *vs* the radial coordinate r for different times ($\nu = \lambda = 0$, $Pe = 1$, $N_r = 12$, $N_\varphi = 7$, $\Delta t = 0.002$).

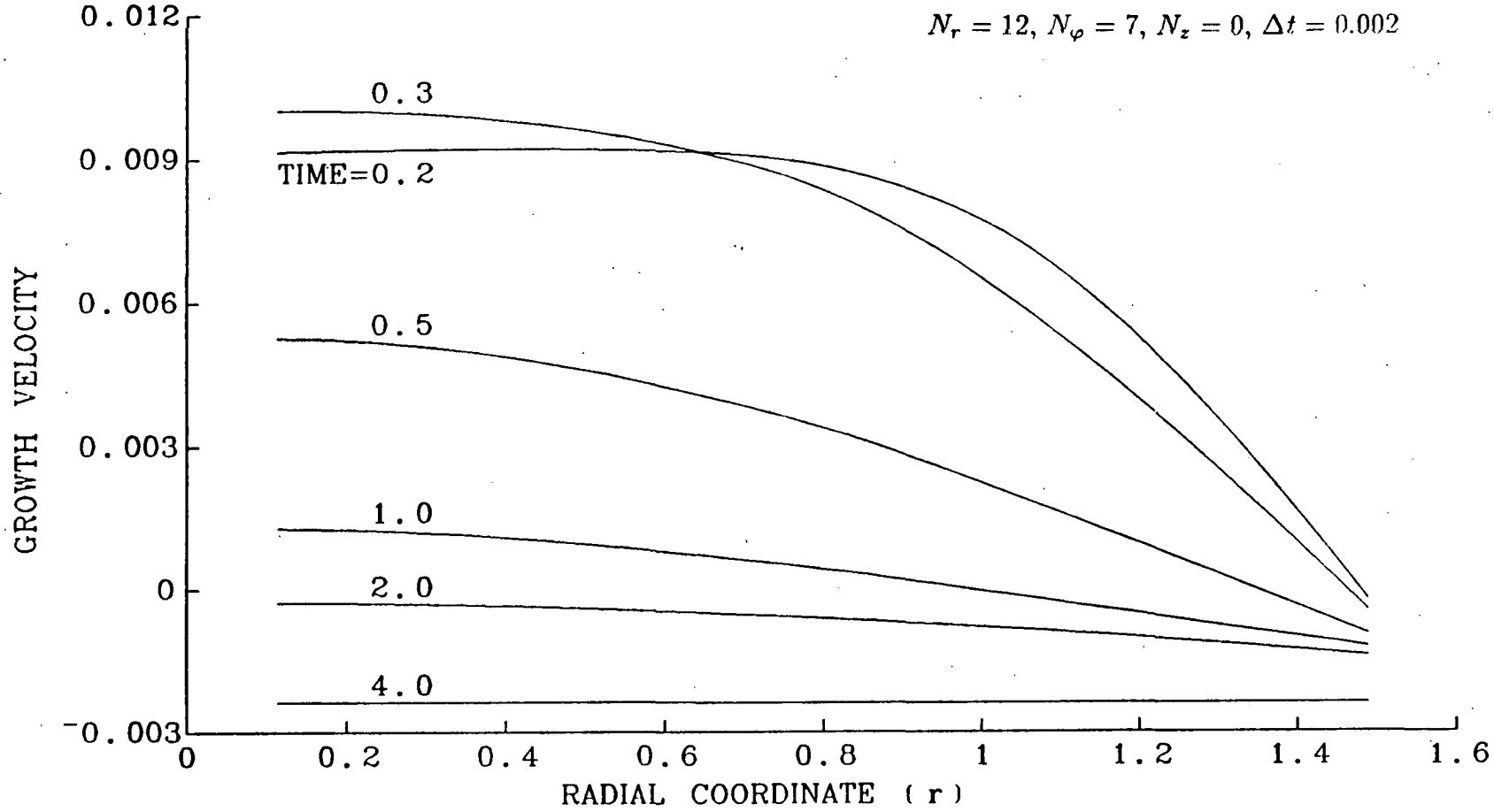

Fig. 11. The perturbation growth velocity $\dot{\zeta}(r,t)$ is plotted *vs* the radial coordinate for different times and for $\lambda = 0.0$, $\nu = 0.020$, and $Pe = 1$.

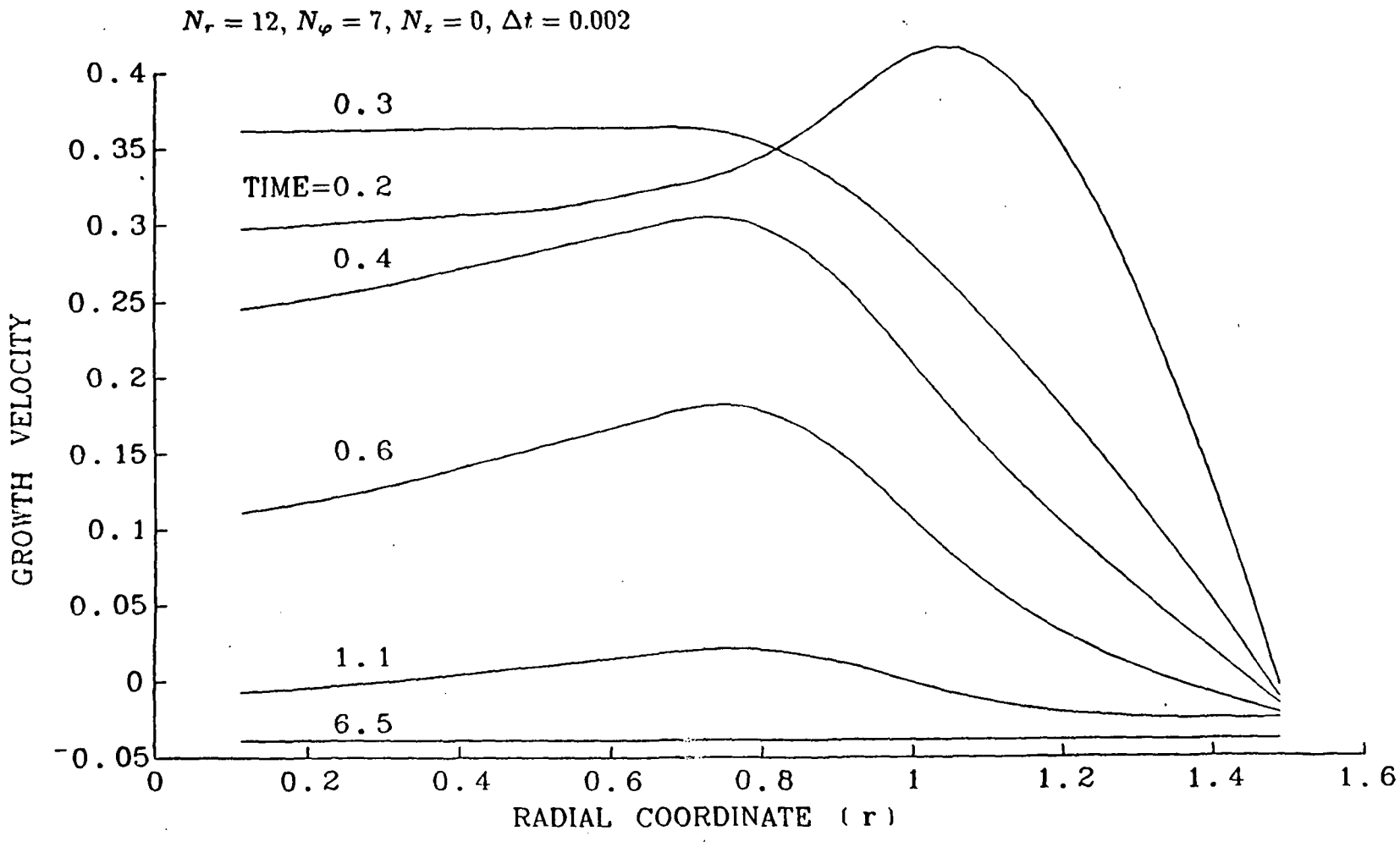

Fig. 12. The perturbation growth velocity $\dot{\zeta}(r,t)$ is plotted *vs* the radial coordinate for different times and for $\lambda = 0.0$, $\nu = 0.001$, and $Pe = 1$.

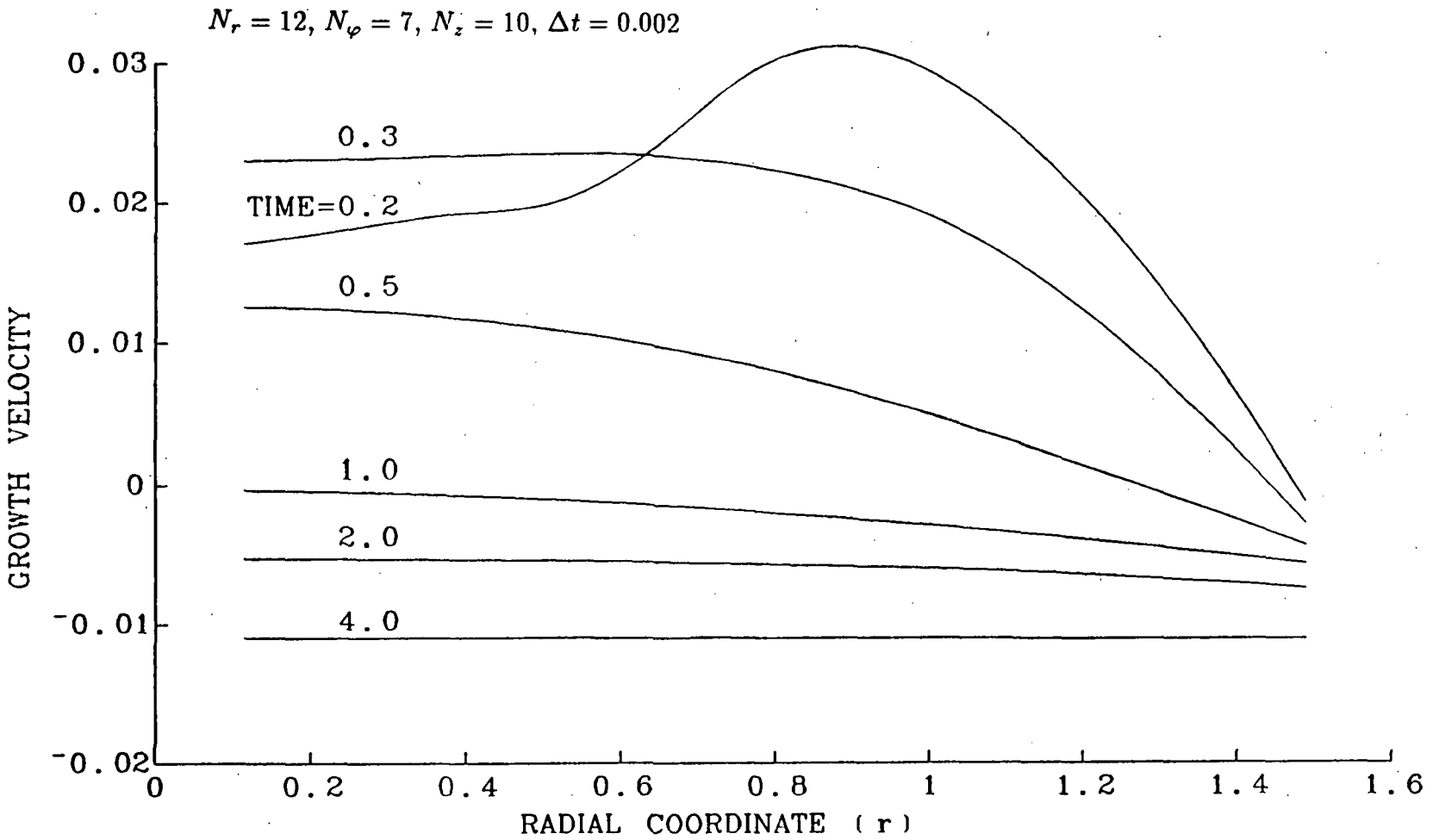

Fig. 13. The perturbation growth velocity $\dot{\zeta}(r,t)$ is plotted *vs* the radial coordinate for different times and for $\lambda = 0.1$, $\nu = 0.001$, and $Pe = 1$.

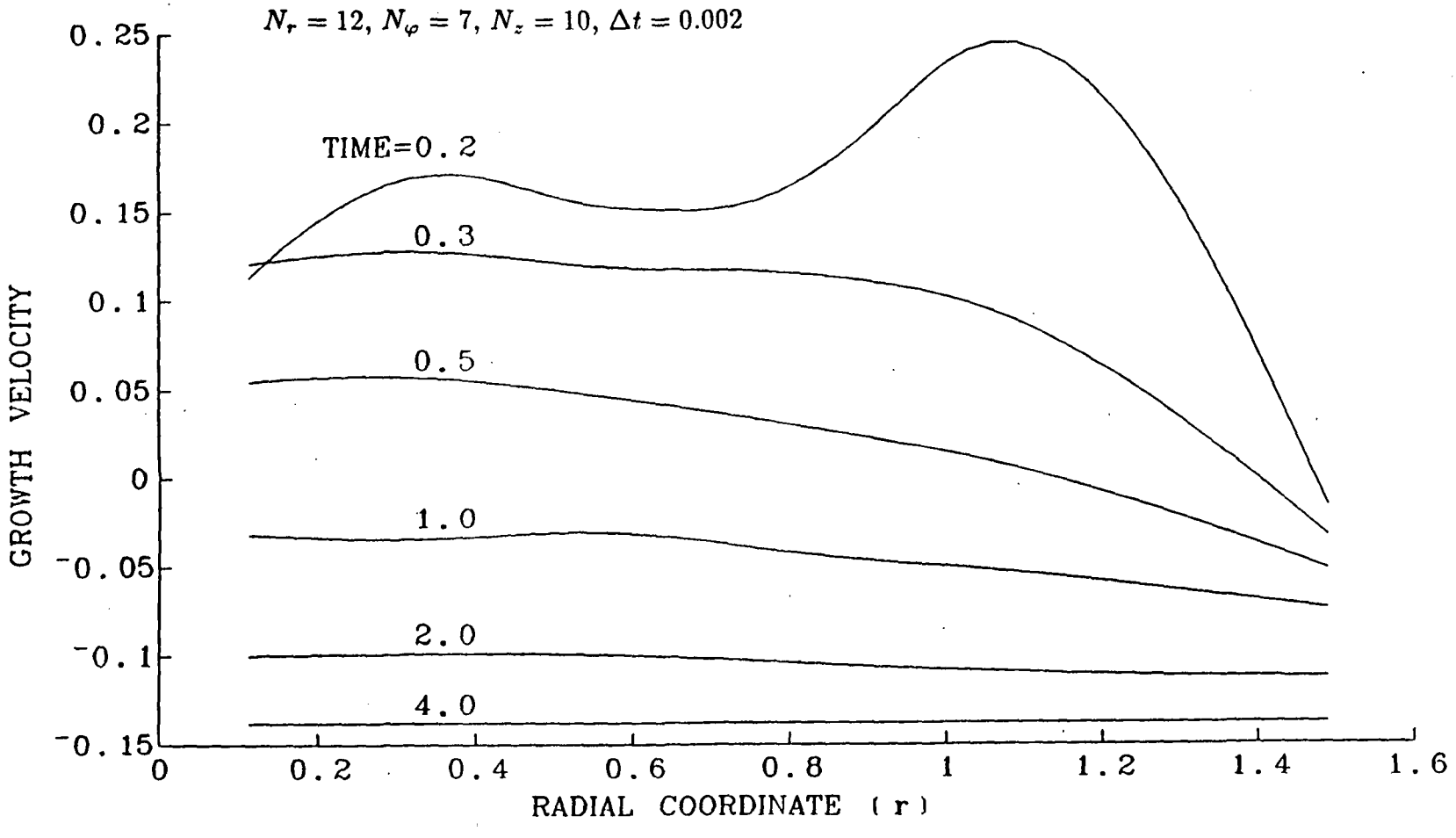

Fig. 14. The perturbation growth velocity $\dot{\zeta}(r,t)$ is plotted *vs* the radial coordinate for different times and for $\lambda = 1.0$, $\nu = 0.001$, and $Pe = 1$.

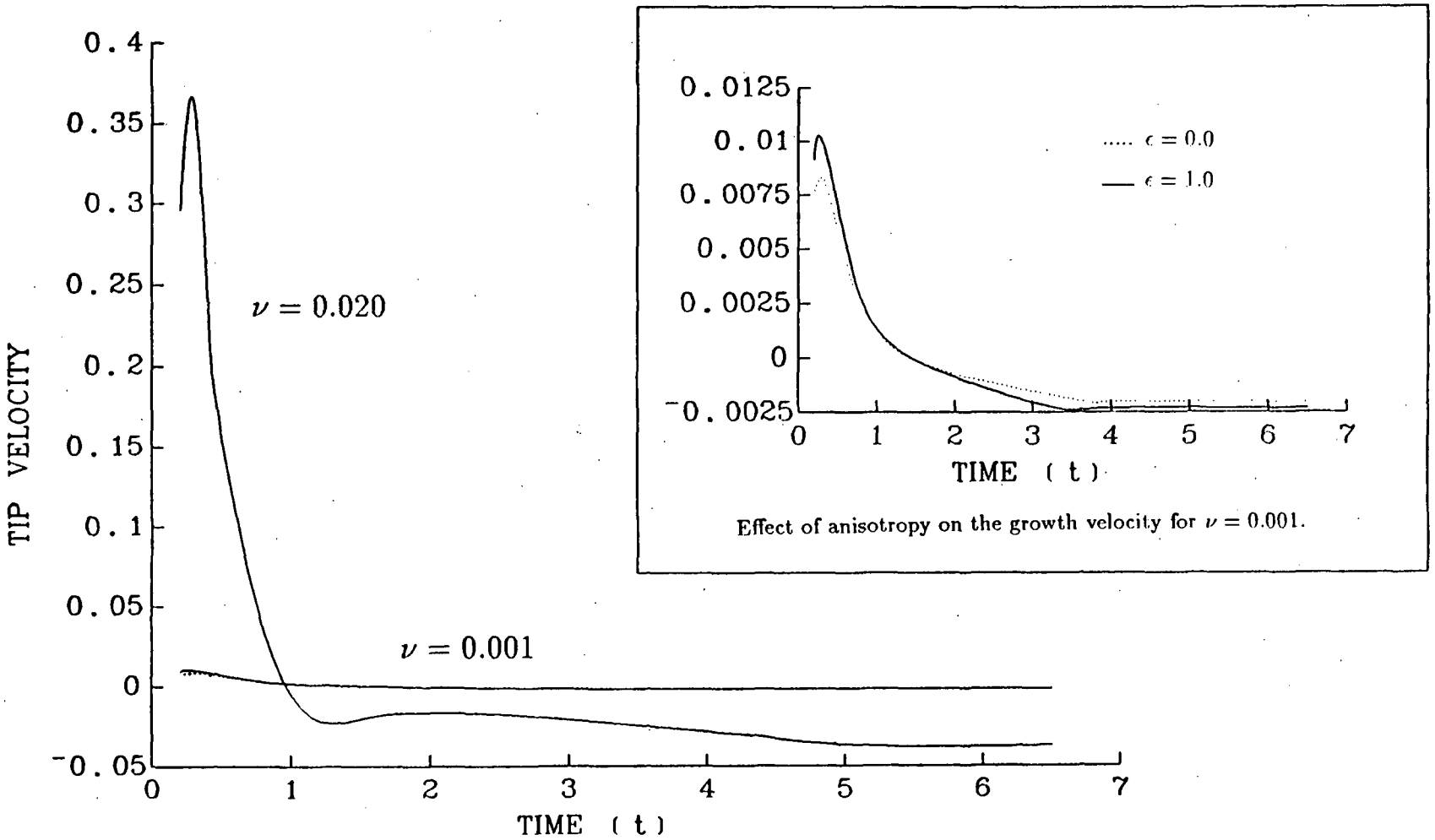

Fig. 15. The perturbation velocity at the tip, $\dot{\zeta}(0,t)$, is plotted *vs* time for different values of the surface tension parameter ν ($\lambda = 0.0$, $Pe = 1.0$). The inset, which is a blow-up of the $\nu = 0.001$ curve, shows that anisotropy has a negligible effect on the growth velocity. (see Eq. (3.3) for the definition of ϵ).

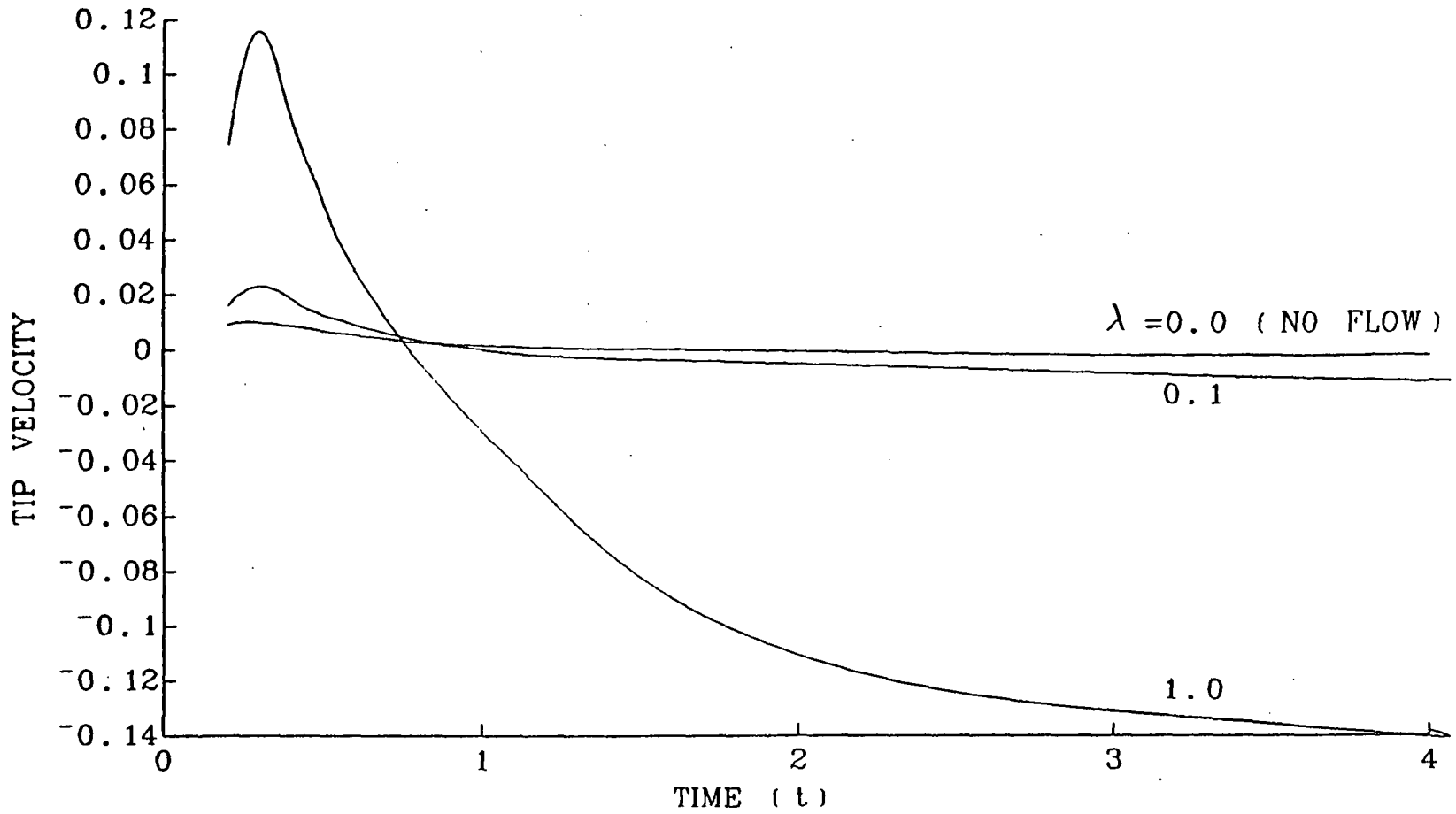

Fig. 16. The perturbation velocity at the tip, $\dot{\zeta}(0,t)$, is plotted *vs* time for different flow strengths λ ($\nu = 0.001$, $Pe = 1.0$). Its absolute value increases with λ, causing a decrease in the *total* growth velocity, $[2+\dot{\zeta}]$.

```
CCCCCCCCCCCCCCCCCCCCCCCCCCCCCCCCCCCCCCCCCCCCCCCCCCCCCCCCCCCCCCCCCCCCCCCCCCCCCCC
C            APPENDIX G: LISTING OF THE FORTRAN CODE                          C
C                                                                             C
C     THIS PROGRAM CALCULATES THE EVOLUTION OF THE DENDRITIC                  C
C     INTERFACE IN TIME AND SPACE UNDER THE INFLUENCE OF                      C
C     FLUID FLOW AND SURFACE TENSION.                                         C
C                                                                             C
CCCCCCCCCCCCCCCCCCCCCCCCCCCCCCCCCCCCCCCCCCCCCCCCCCCCCCCCCCCCCCCCCCCCCCCCCCCCCCC
      IMPLICIT REAL*8 (A-H,O-Z)
      REAL*8 WK(1700),UGT(30,30,1000),UGT0(30,30),Z(1000,30),
     .ZD(1000,30),X(30),Z0(30),R(30),CSI(30),CS2(30),FI(30),ZDINIT(30)
     .,ORD(30),C(30,3),VECRHO(3),ZETA(3),
     .BPAR(4),STRES(60),FLOW(60,60),QUAD(30),WKAREA(60),LAM,NU
      COMMON /A/UGT,UGT0,Z,ZD,ZDINIT,CSI,CS2,FI,Z0,LAM,PI,
     .DT,NU,ANIS,NF,NZ,N,INDEX,IVAN
     ./B/C,R,ORD,BPAR
     ./D/SMALL,P
     ./C/QUAD,RJ,ZJ,R2,MM,NR,UPFLOW
      EQUIVALENCE (WK,FLOW)
      INTEGER NPL(1000),NPERT(1000)
      LOGICAL IVAN,UPFLOW
      EXTERNAL DCADRE,FCN,FA,FB,FC,FD,RIGHT1,RIGHT2,EXPIN
      CALL XUFLOW(0)
      WRITE(6,*) 'NR,NF,NZ,MM,NTOTAL,DT,PECLET,LAMBDA,NU'
      READ (5,*) NR,NF,NZ,MM,NTOTAL,DT,P,LAM,NU
      READ (15,*) UPFLOW,PR,ANIS,(ZDINIT(I),I=1,NR)
      WRITE(6,*) 'THE TYPE OF FLOW (UPFLOW?), THE PRANDTL NUMBER,
     .THE DIM/LESS SURFACE TENSION, AND THE ANISOTROPY ARE:'
      WRITE(6,*) '*************************************************************'
      WRITE(6,*) UPFLOW,PR,NU,ANIS
      WRITE(6,*) '*************************************************************'
      WRITE(6,*) 'IF YOU WANT TO CHANGE SOMETHING, HALT EXECUTION
     . AND GO TO FILE 15 AS DEFINED IN YOUR EXEC FILE
     . (SOME DATA USEFUL TO THE COMPUTATION ARE STORED IN FILE 14)'
      READ (14,*) SMALL,ZEROPL,RMAX,NSIG,ITMAX,
     .(BPAR(N),N=1,4),(NPL(N),N=1,NTOTAL)
      READ (17,*) PRT,(NPERT(N),N=1,NTOTAL)
      IF (LAM.EQ.0.) IVAN=.TRUE.
CCCCCCCCCCCCCCCCCCCCCCCCCCCCCCCCCCCCCCCCCCCCCCCCCCCCCCCCCCCCCCCCCCCCCCCCCCCCCCC
C     CALCULATION OF DELTA(IVANTSOV)
CCCCCCCCCCCCCCCCCCCCCCCCCCCCCCCCCCCCCCCCCCCCCCCCCCCCCCCCCCCCCCCCCCCCCCCCCCCCCCC
      DELIVA=P*DEXP(P)*EXPIN(P)
      PI=3.14159265358979323
      RE=P*LAM/PR
      R2=RE/2.
CCCCCCCCCCCCCCCCCCCCCCCCCCCCCCCCCCCCCCCCCCCCCCCCCCCCCCCCCCCCCCCCCCCCCCCCCCCCCCC
C     GENERATION OF ARRAYS FOR VELOCITY, QUADRATURES, ETC
CCCCCCCCCCCCCCCCCCCCCCCCCCCCCCCCCCCCCCCCCCCCCCCCCCCCCCCCCCCCCCCCCCCCCCCCCCCCCCC
      DO 810 M=1,MM
  810 QUAD(M)=DCOS(DFLOAT(2*M-1)*PI/2./DFLOAT(MM))
      DO 5 I=1,NR
      R(I)=DSQRT(-2.*P*DLOG
     .(DCOS(DFLOAT(2*I-1)/DFLOAT(2*NR)*PI/2.)))
      Z0(I)=P/2.*(1.-R(I)**2/P**2)
```

```
      DO 5 M=1,NZ
      CSI(M)=DCOS(DFLOAT(2*M-1)/DFLOAT(2*NZ)*PI/2.)**2
      CS2(M)=DTAN(DFLOAT(2*M-1)/DFLOAT(2*NZ)*PI/2.)
      IF (IVAN) GO TO 5
      ZIM=Z0(I)-DLOG(CSI(M))/2./(1.+LAM)
      W=(ZIM+DSQRT(ZIM**2+R(I)**2))/P
      S=(-ZIM+DSQRT(ZIM**2+R(I)**2))/P
CCCCCCCCCCCCCCCCCCCCCCCCCCCCCCCCCCCCCCCCCCCCCCCCCCCCCCCCCCCCCCCCCCCCCCCCC
C     FLOW DOWN
CCCCCCCCCCCCCCCCCCCCCCCCCCCCCCCCCCCCCCCCCCCCCCCCCCCCCCCCCCCCCCCCCCCCCCCCC
      IF (UPFLOW) GO TO 51
      UGT0(I,M)=-2./(S+W)*
     .((DEXP(-R2)-DEXP(-R2*W))/R2/EXPIN(R2)+
     .W*(EXPIN(R2*W)/EXPIN(R2)-1.))
     .*W**(-1.+PR*DEXP(-R2)/EXPIN(R2))
     .*DEXP(P*(1.+LAM)*(1.-W)+
     .PR/EXPIN(R2)*(-EXPIN(R2)+EXPIN2(R2)+
     .EXPIN(R2*W)-EXPIN2(R2*W)))
      GO TO 5
CCCCCCCCCCCCCCCCCCCCCCCCCCCCCCCCCCCCCCCCCCCCCCCCCCCCCCCCCCCCCCCCCCCCCCCCC
C     FLOW UP
CCCCCCCCCCCCCCCCCCCCCCCCCCCCCCCCCCCCCCCCCCCCCCCCCCCCCCCCCCCCCCCCCCCCCCCCC
  51  UGT0(I,M)=2./(S+W)*
     .((DEXP(-R2)-DEXP(-R2*W))/R2/EXPIN(R2)+
     .W*(EXPIN(R2*W)/EXPIN(R2)-1.))
     .*W**(-1.-PR*DEXP(-R2)/EXPIN(R2))
     .*DEXP(P*(1.-LAM)*(1.-W)-
     .PR/EXPIN(R2)*(-EXPIN(R2)+EXPIN2(R2)+
     .EXPIN(R2*W)-EXPIN2(R2*W)))
  5   CONTINUE
      R(NR+1)=R(NR)+(RMAX-R(NR))/8.
      ORD(NR+1)=
     .P/2.*(1-R(NR+1)**2/P**2)
      R(NR+2)=R(NR)+(RMAX-R(NR))/3.
      ORD(NR+2)=
     .P/2.*(1-R(NR+2)**2/P**2)
      R(NR+3)=R(NR)+(RMAX-R(NR))/2.
      ORD(NR+3)=
     .P/2.*(1-R(NR+3)**2/P**2)
      WRITE (6,*) (R(I),I=1,NR+3)
      IF (RMAX.LE.R(NR)) WRITE (6,*) 'ERROR IN SELECTION OF RMAX'
      IF (RMAX.LE.R(NR)) GO TO 300
      DO 6 K=1,NF
  6   FI(K)=
     .DCOS(DFLOAT(2*K-1)/DFLOAT(2*NF)*PI/2.)**2
CCCCCCCCCCCCCCCCCCCCCCCCCCCCCCCCCCCCCCCCCCCCCCCCCCCCCCCCCCCCCCCCCCCCCCCCC
C     TIME LOOP
CCCCCCCCCCCCCCCCCCCCCCCCCCCCCCCCCCCCCCCCCCCCCCCCCCCCCCCCCCCCCCCCCCCCCCCCC
      WRITE (16,*) '************************************************'
      WRITE(16,*) 'NR,NF,NZ,NTOTAL,DT,P,LAM,NU,ANIS'
      WRITE (16,*) NR,NF,NZ,NTOTAL,DT,P,LAM,NU,ANIS
      WRITE (16,*) '************************************************'
      WRITE(76,*) 'NR,NF,NZ,MM,DT,P,LAM,NU,ANIS'
      WRITE (76,*) NR,NF,NZ,MM,DT,P,LAM,NU,ANIS
```

```
      WRITE(66,*) 'NR,NF,NZ,DT,P,LAM,NU,ANIS'
      WRITE (66,*) NR,NF,NZ,DT,P,LAM,NU,ANIS
      WRITE(56,*) 'NR,NF,NZ,DT,P,LAM,NU,ANIS'
      WRITE (56,*) NR,NF,NZ,DT,P,LAM,NU,ANIS
      WRITE(36,*) 'NR,NF,NZ,DT,P,LAM,NU,ANIS'
      WRITE (36,*) NR,NF,NZ,DT,P,LAM,NU,ANIS
      WRITE (76,*) '*************************************************************'
      WRITE (76,*) 'PERT ON (1),TIME,INT/FACE VEL. AT R1, AT 0, SLOPE AT
     . 0'
      WRITE (76,*) '*************************************************************'
      DO 100 N=1,NTOTAL
      INDEX=0
      IF (N.GT.1) WRITE (6,*) 'WMAX',WMAX
      IF (N.GT.1) WRITE (16,*) 'WMAX',WMAX
      IF (N.GT.1) WRITE (36,*) 'WMAX',WMAX
      DO 120 I=1,NR
      IF (N.EQ.1) X(I)=Z0(I)+ZDINIT(I)*DT
      IF (N.EQ.1) GO TO 120
      X(I)=Z(N-1,I)+ZD(N-1,I)*DT
  120 CONTINUE
      CALL ZSPOW(FCN,NSIG,NR,ITMAX,PAR,X,FNORM,WK,IER)
      WRITE (16,*) '***************************************'
      WRITE(16,*) 'TIME',N*DT
      WRITE (16,*) '***************************************'
      WRITE (6,*) '***************************************'
      WRITE(6,*) 'TIME',N*DT
      WRITE (6,*) '***************************************'
      WRITE (6,*) 'FNORM',FNORM,'INDEX',INDEX
      WRITE (6,*)'      Z0(I)                          X(I)'
      WRITE (16,*) 'FNORM',FNORM,'INDEX',INDEX
      WRITE (16,*)'      Z0(I)                          X(I)'
      WRITE (66,*) '***************************************'
      WRITE(66,*) 'TIME',N*DT,'PERT',NPERT(N)
      WRITE (66,*) '***************************************'
      DO 26 I=1,NR
      Z(N,I)=X(I)
      IF (N.GT.1)
     .ZD(N,I)=(X(I)-Z(N-1,I))/DT
      IF (N.EQ.1) ZD(N,I)=ZDINIT(I)
      WRITE (66,*) R(I),ZD(N,I)
      WRITE (16,*) Z0(I),X(I),X(I)-Z0(I)
      WRITE (6,*) Z0(I),X(I),X(I)-Z0(I)
   26 CONTINUE
      IF (NPERT(N).EQ.1) ZD(N,1)=ZD(N,1)+PRT
      DO 364 I=1,NR
      WRITE (6,*) R(I),ZD(N,I)
  364 ORD(I)=X(I)
      WRITE (6,*) '***************************************'
      ZTIPO=ZTIPN
      CALL ICSICU (R,ORD,NR+3,BPAR,C,30,IER)
      VECRHO(1)=R(1)
      VECRHO(2)=R(1)+SMALL
      VECRHO(3)=R(1)+2*SMALL
      CALL ICSEVU(R,ORD,NR+3,C,30,VECRHO,ZETA,3,IER)
```

```
      DZ1DR1=(ZETA(2)-ZETA(1))/SMALL
      DZ2DR2=(ZETA(3)+ZETA(1)-2*ZETA(2))/SMALL**2
      ZTIPN=ORD(1)-R(1)*DZ1DR1+R(1)**2/2.*DZ2DR2
      ZDO=(ZTIPN-ZTIPO)/DT
      IF (IER.GT.128) WRITE(76,*) 'ERROR',IER,'AT TIME',N*DT
      WRITE (76,760) NPERT(N),N*DT,ZD(N,1),ZDO,DZ1DR1-R(1)*DZ2DR2
 760  FORMAT (I3,1X,F6.4,1X,3(D16.8,2X))
      WRITE (36,*) 'TIME',N*DT
      WRITE(56,*) 'TIME',N*DT
      ZERO=0.
      DO 465 I=1,NR+3
      IF (I.GT.3)
     .WRITE (56,*) -R(NR+4-I),ORD(NR+4-I)-ZO(NR+4-I)
  465 WRITE (36,*) -R(NR+4-I),ORD(NR+4-I)
      WRITE (36,*) ZERO,ORD(1)-R(1)*DZ1DR1+R(1)**2/2.*DZ2DR2
      WRITE (56,*) ZERO,ORD(1)-R(1)*DZ1DR1+R(1)**2/2.*DZ2DR2-P/2.
      WRITE (6,*) ZERO,ORD(1)-R(1)*DZ1DR1+R(1)**2/2.*DZ2DR2
     .,ORD(1)-R(1)*DZ1DR1+R(1)**2/2.*DZ2DR2-P/2.
      DO 466 I=1,NR+3
  466 WRITE (36,*)  R(I),ORD(I)
      DO 467 I=1,NR
      WRITE (56,*) R(I),ORD(I)-ZO(I)
  467 WRITE (6,*)  R(I),ORD(I),ORD(I)-ZO(I)
CCCCCCCCCCCCCCCCCCCCCCCCCCCCCCCCCCCCCCCCCCCCCCCCCCCCCCCCCCCCCCCCCCCCCCCCCCCCCCC
C     INTERPOLATION IN CARTESIAN COORDINATES
CCCCCCCCCCCCCCCCCCCCCCCCCCCCCCCCCCCCCCCCCCCCCCCCCCCCCCCCCCCCCCCCCCCCCCCCCCCCCCC
 332  IF (N.EQ.NTOTAL) GO TO 300
CCCCCCCCCCCCCCCCCCCCCCCCCCCCCCCCCCCCCCCCCCCCCCCCCCCCCCCCCCCCCCCCCCCCCCCCCCCCCCC
C     CALCULATION OF U.GRAD(T) AT TIME N.DT AND AT
C     RHO=R(J), Z=Z(N,J)-DLOG(CSI(M))/2./(1.+LAM)
CCCCCCCCCCCCCCCCCCCCCCCCCCCCCCCCCCCCCCCCCCCCCCCCCCCCCCCCCCCCCCCCCCCCCCCCCCCCCCC
      IF (IVAN) GO TO 100
CCCCCCCCCCCCCCCCCCCCCCCCCCCCCCCCCCCCCCCCCCCCCCCCCCCCCCCCCCCCCCCCCCCCCCCCCCCCCCC
C             CALCULATE -(OSEEN VELOCITY) ON INTERFACE
C             (THE EXPRESSIONS FOR UR AND UZ HAVE A MINUS SIGN
C             TO SHOW THAT THEY ARE THE OPPOSITE OF THE OSEEN VEL.)
CCCCCCCCCCCCCCCCCCCCCCCCCCCCCCCCCCCCCCCCCCCCCCCCCCCCCCCCCCCCCCCCCCCCCCCCCCCCCCC
      DO 820 J=1,NR+2
      RJ=R(J)
      ZJ=ORD(J)
      W=(ZJ+DSQRT(ZJ**2+RJ**2))/P
      S=(-ZJ+DSQRT(ZJ**2+RJ**2))/P
      IF (S.LE.0) S=0.
CCCCCCCCCCCCCCCCCCCCCCCCCCCCCCCCCCCCCCCCCCCCCCCCCCCCCCCCCCCCCCCCCCCCCCCCCCCCCCC
C     FLOW DOWN
CCCCCCCCCCCCCCCCCCCCCCCCCCCCCCCCCCCCCCCCCCCCCCCCCCCCCCCCCCCCCCCCCCCCCCCCCCCCCCC
      IF (UPFLOW) GO TO 811
      UZ=-(-1.+EXPIN(R2*W)/EXPIN(R2)+
     .(DEXP(-R2)-DEXP(-R2*W))/EXPIN(R2)/R2/(W+S))
      UR=-((1.-EXPIN(R2*W)/EXPIN(R2))*DSQRT(S/(S+W)))
      GO TO 812
CCCCCCCCCCCCCCCCCCCCCCCCCCCCCCCCCCCCCCCCCCCCCCCCCCCCCCCCCCCCCCCCCCCCCCCCCCCCCCC
C     FLOW UP
CCCCCCCCCCCCCCCCCCCCCCCCCCCCCCCCCCCCCCCCCCCCCCCCCCCCCCCCCCCCCCCCCCCCCCCCCCCCCCC
```

```
 811  UZ=-(1.-EXPIN(R2*W)/EXPIN(R2)-
     .(DEXP(-R2)-DEXP(-R2*W))/EXPIN(R2)/R2/(W+S))
      UR=-(-(1.-EXPIN(R2*W)/EXPIN(R2))*DSQRT(S/(S+W)))
 812  STRES(J)=-UR
     .-DCADRE(RIGHT1,ZEROPL,R(NR+3)-SMALL,0.,1.D-7,ERROR,IER)
      STRES(J+NR+2)=-UZ
     .-DCADRE(RIGHT2,ZEROPL,R(NR+3)-SMALL,0.,1.D-7,ERROR,IER)
      DO 820 I=1,NR+2
      IF (I.GT.1) RD=(R(I)+R(I-1))*.5
      IF (I.EQ.1) RD=ZEROPL
      IF (I.LT.NR+2) RU=(R(I)+R(I+1))*.5
      IF (I.EQ.NR+2) RU=R(NR+3)-SMALL
      FLOW(J,I)=
     .DCADRE(FA,RD,RU,0.,1.D-7,ERROR,IER)
      FLOW(J,I+NR+2)=
     .DCADRE(FB,RD,RU,0.,1.D-7,ERROR,IER)
      FLOW(J+NR+2,I)=
     .DCADRE(FC,RD,RU,0.,1.D-7,ERROR,IER)
      FLOW(J+NR+2,I+NR+2)=
     .DCADRE(FD,RD,RU,0.,1.D-7,ERROR,IER)
 820  CONTINUE
      CALL LEQT1F (FLOW,1,2*NR+4,60,STRES,5,WKAREA,IER)
CCCCCCCCCCCCCCCCCCCCCCCCCCCCCCCCCCCCCCCCCCCCCCCCCCCCCCCCCCCCCCCCCCCCCCCCCCCCCCC
C            CALCULATION OF INTERIOR CORRECTION TO OSEEN SOLUTION
C            (WE ADD THIS SOLUTION TO THE OSEEN SOLUTION)
CCCCCCCCCCCCCCCCCCCCCCCCCCCCCCCCCCCCCCCCCCCCCCCCCCCCCCCCCCCCCCCCCCCCCCCCCCCCCCC
      WMAX=0.
      DO 7 J=1,NR
      DO 7 L=1,NZ
      RJ=R(J)
      ZJL=Z(N,J)-DLOG(CSI(L))/2./(1.+LAM)
      ZJ=ZJL
      W=(ZJL+DSQRT(ZJL**2+RJ**2))/P
      WMAX=DMAX1(W,WMAX)
      S=(-ZJL+DSQRT(ZJL**2+RJ**2))/P
      IF (S.LE.0) S=0.
      UR=.5*
     .DCADRE(RIGHT1,ZEROPL,R(NR+3)-SMALL,0.,1.D-7,ERROR,IER)
      UZ=.5*
     .DCADRE(RIGHT2,ZEROPL,R(NR+3)-SMALL,0.,1.D-7,ERROR,IER)
      DO 830 I=1,NR+2
      IF (I.GT.1) RD=(R(I)+R(I-1))*.5
      IF (I.EQ.1) RD=ZEROPL
      IF (I.LT.NR+2) RU=(R(I)+R(I+1))*.5
      IF (I.EQ.NR+2) RU=R(NR+3)-SMALL
      UR=UR+.5*STRES(I)*
     .DCADRE(FA,RD,RU,0.,1.D-7,ERROR,IER)
     .+.5*STRES(I+NR+2)*
     .DCADRE(FB,RD,RU,0.,1.D-7,ERROR,IER)
      UZ=UZ+.5*STRES(I)*
     .DCADRE(FC,RD,RU,0.,1.D-7,ERROR,IER)
     .+.5*STRES(I+NR+2)*
     .DCADRE(FD,RD,RU,0.,1.D-7,ERROR,IER)
 830  CONTINUE
```

```
CCCCCCCCCCCCCCCCCCCCCCCCCCCCCCCCCCCCCCCCCCCCCCCCCCCCCCCCCCCCCCCCCCCCCCCCCCC
C     FLOW DOWN
CCCCCCCCCCCCCCCCCCCCCCCCCCCCCCCCCCCCCCCCCCCCCCCCCCCCCCCCCCCCCCCCCCCCCCCCCCC
      IF (UPFLOW) GO TO 511
      WRITE (18,*) 'N=',N,'Z=',ZJL,'R=',RJ
      WRITE (18,*) 'CORRECTION',UR,UZ
      UZ=UZ-1.+EXPIN(R2*W)/EXPIN(R2)+
     .(DEXP(-R2)-DEXP(-R2*W))/EXPIN(R2)/R2/(W+S)
      UR=UR+(1.-EXPIN(R2*W)/EXPIN(R2))*DSQRT(S/(S+W))
      WRITE (18,*) 'TOTAL',UR,UZ
      GO TO 512
CCCCCCCCCCCCCCCCCCCCCCCCCCCCCCCCCCCCCCCCCCCCCCCCCCCCCCCCCCCCCCCCCCCCCCCCCCC
C     FLOW UP
CCCCCCCCCCCCCCCCCCCCCCCCCCCCCCCCCCCCCCCCCCCCCCCCCCCCCCCCCCCCCCCCCCCCCCCCCCC
 511  WRITE (18,*) 'N=',N,'Z=',ZJL,'R=',RJ
      WRITE (18,*) 'CORRECTION',UR,UZ
      UZ=UZ+1.-EXPIN(R2*W)/EXPIN(R2)-
     .(DEXP(-R2)-DEXP(-R2*W))/EXPIN(R2)/R2/(W+S)
      UR=UR-(1.-EXPIN(R2*W)/EXPIN(R2))*DSQRT(S/(S+W))
      WRITE (18,*) 'TOTAL',UR,UZ
 512  DO 20 I=1,NR
CCCCCCCCCCCCCCCCCCCCCCCCCCCCCCCCCCCCCCCCCCCCCCCCCCCCCCCCCCCCCCCCCCCCCCCCCCC
C     CONTRIBUTION FROM H1 & H3
CCCCCCCCCCCCCCCCCCCCCCCCCCCCCCCCCCCCCCCCCCCCCCCCCCCCCCCCCCCCCCCCCCCCCCCCCCC
      T0=P*PI/DFLOAT(2*NR*NF)*DTAN(DFLOAT(2*I-1)/DFLOAT(2*NR)*PI/2.)
      T1=T0
     .*DEXP(-Z(N,J)+Z0(I)+DLOG(CSI(L))/2./(1+LAM))
      ROOT1=DSQRT((R(I)+R(J))**2+(Z(N,J)-Z0(I)-DLOG(CSI(L))
     ./2./(1+LAM))**2)
      ROOT2=DSQRT((R(I)-R(J))**2+(Z(N,J)-Z0(I)-DLOG(CSI(L))
     ./2./(1+LAM))**2)
      DO 30 K=1,NF
      Y=ROOT2+(ROOT1-ROOT2)*FI(K)
      A1=
     .-2*DSINH(Y)+DEXP(Y)*DERF(Y/2./DSQRT(DFLOAT(N)*DT)
     .+DSQRT(DFLOAT(N)*DT))+
     .DEXP(-Y)*DERF(Y/2./DSQRT(DFLOAT(N)*DT)-
     .DSQRT(DFLOAT(N)*DT))
      A2=A1/Y
      B2=
     .-2*DCOSH(Y)+DEXP(Y)*DERF(Y/2./DSQRT(DFLOAT(N)*DT)
     .+DSQRT(DFLOAT(N)*DT))-
     .DEXP(-Y)*DERF(Y/2./DSQRT(DFLOAT(N)*DT)-
     .DSQRT(DFLOAT(N)*DT))
     .+2./DSQRT(DFLOAT(N)*DT*PI)*
     .DEXP(-Y**2/4./DFLOAT(N)/DT-N*DT)
      UGT(J,L,N)=UGT(J,L,N)+T1/DSQRT((ROOT1+Y)*(ROOT2+Y))*
     .(UZ*(-A1+(B2-A2)*
     .(Z(N,J)-Z0(I)-DLOG(CSI(L))/2./(1+LAM))/Y)
     .+UR*(B2-A2)*(R(J)-(0.5*(ROOT1**2+ROOT2**2)-Y**2)/2./R(J))/Y)
      DO 40 M=1,NZ
      ROOT3=DSQRT((R(I)+R(J))**2+(Z(N,J)-Z0(I)
     .-DLOG(CSI(L)/CSI(M))/2./(1+LAM))**2)
      ROOT4=DSQRT((R(I)-R(J))**2+(Z(N,J)-Z0(I)
```

```
     .-DLOG(CSI(L)/CSI(M))/2./(1+LAM))**2)
      OMEGA=ROOT4+(ROOT3-ROOT4)*FI(K)
      E1=
     .-2*DSINH(OMEGA)+DEXP(OMEGA)*DERF(OMEGA/2./DSQRT(DFLOAT(N)*DT)
     .+DSQRT(DFLOAT(N)*DT))+
     .DEXP(-OMEGA)*DERF(OMEGA/2./DSQRT(DFLOAT(N)*DT)-
     .DSQRT(DFLOAT(N)*DT))
      E2=E1/OMEGA
      F2=
     .-2*DCOSH(OMEGA)+DEXP(OMEGA)*DERF(OMEGA/2./DSQRT(DFLOAT(N)*DT)
     .+DSQRT(DFLOAT(N)*DT))-
     .DEXP(-OMEGA)*DERF(OMEGA/2./DSQRT(DFLOAT(N)*DT)-
     .DSQRT(DFLOAT(N)*DT))
     .+2./DSQRT(DFLOAT(N)*DT*PI)*
     .DEXP(-OMEGA**2/4./DFLOAT(N)/DT-N*DT)
      UGT(J,L,N)=UGT(J,L,N)-T0
     .*DEXP(-Z(N,J)+Z0(I)+DLOG(CSI(L)/CSI(M))/2./(1+LAM))
     .*PI*LAM/(1+LAM)/DFLOAT(2*NZ)
     .*CS2(M)
     ./DSQRT((ROOT3+OMEGA)*(ROOT4+OMEGA))*
     .(UZ*(-E1+(F2-E2)*
     .(Z(N,J)-Z0(I)-DLOG(CSI(L)/CSI(M))/2./(1+LAM))/OMEGA)
     .+UR*(F2-E2)*(R(J)-(0.5*(ROOT3**2+ROOT4**2)-
     .OMEGA**2)/2./R(J))/OMEGA)
     .*UGT0(I,M)
  40 CONTINUE
  30 CONTINUE
CCCCCCCCCCCCCCCCCCCCCCCCCCCCCCCCCCCCCCCCCCCCCCCCCCCCCCCCCCCCCCCCCCCCCCCCCCCCCCC
C     CONTRIBUTION FROM H2 & H4
CCCCCCCCCCCCCCCCCCCCCCCCCCCCCCCCCCCCCCCCCCCCCCCCCCCCCCCCCCCCCCCCCCCCCCCCCCCCCCC
      DO 50 NN=1,N
      IF (NN.GT.1) ZN=Z(NN-1,I)
      IF (NN.EQ.1) ZN=Z0(I)
      ROOT5=DSQRT((R(I)+R(J))**2+(Z(N,J)-ZN-DLOG(CSI(L))
     ./2./(1+LAM))**2)
      ROOT6=DSQRT((R(I)-R(J))**2+(Z(N,J)-ZN-DLOG(CSI(L))
     ./2./(1+LAM))**2)
      IF (NN.EQ.1) DZDT=ZDINIT(I)
      IF (NN.GT.1) DZDT=ZD(NN-1,I)
      T2=T0/2.*DEXP(-Z(N,J)+ZN+DLOG(CSI(L))/2./(1+LAM))
      DO 60 K=1,NF
      Y=ROOT6+(ROOT5-ROOT6)*FI(K)
      IF (NN.EQ.N) GO TO  68
      C1=
     .DEXP(Y)*(DERF(Y/2./DSQRT(DFLOAT(N-NN)*DT)
     .+DSQRT(DFLOAT(N-NN)*DT))-
     .DERF(Y/2./DSQRT(DFLOAT(N-NN+1)*DT)
     .+DSQRT(DFLOAT(N-NN+1)*DT)))+
     .DEXP(-Y)*(DERF(Y/2./DSQRT(DFLOAT(N-NN)*DT)
     .-DSQRT(DFLOAT(N-NN)*DT))-
     .DERF(Y/2./DSQRT(DFLOAT(N-NN+1)*DT)
     .-DSQRT(DFLOAT(N-NN+1)*DT)))
      C2=C1/Y
      D2=
```

```
     .DEXP(Y)*(DERF(Y/2./DSQRT(DFLOAT(N-NN)*DT)
     .+DSQRT(DFLOAT(N-NN)*DT))-
     .DERF(Y/2./DSQRT(DFLOAT(N-NN+1)*DT)
     .+DSQRT(DFLOAT(N-NN+1)*DT)))-
     .DEXP(-Y)*(DERF(Y/2./DSQRT(DFLOAT(N-NN)*DT)
     .-DSQRT(DFLOAT(N-NN)*DT))-
     .DERF(Y/2./DSQRT(DFLOAT(N-NN+1)*DT)
     .-DSQRT(DFLOAT(N-NN+1)*DT)))+
     .2./DSQRT(PI*DFLOAT(N-NN)*DT)
     .*DEXP(-Y**2/4./DFLOAT(N-NN)/DT-(N-NN)*DT)-
     .2./DSQRT(PI*DFLOAT(N-NN+1)*DT)
     .*DEXP(-Y**2/4./DFLOAT(N-NN+1)/DT-(N-NN+1)*DT)
      UGT(J,L,N)=UGT(J,L,N)+T2*(2.+DZDT)/
     .DSQRT((ROOT5+Y)*(ROOT6+Y))*
     .(UZ*(-C1+(D2-C2)*
     .(Z(N,J)-ZN-DLOG(CSI(L))/2./(1+LAM))/Y)
     .+UR*(D2-C2)*(R(J)-(0.5*(ROOT5**2+ROOT6**2)-Y**2)/2./R(J))/Y)
      GO TO  69
68    C1=
     .DEXP(Y)*
     .DERFC(Y/2./DSQRT(DT)
     .+DSQRT(DT))+
     .DEXP(-Y)*
     .DERFC(Y/2./DSQRT(DT)
     .-DSQRT(DT))
      C2=C1/Y
      D2=
     .DEXP(Y)*
     .DERFC(Y/2./DSQRT(DT)
     .+DSQRT(DT))-
     .DEXP(-Y)*
     .DERFC(Y/2./DSQRT(DT)
     .-DSQRT(DT))-
     .2./DSQRT(PI*DT)
     .*DEXP(-Y**2/4./DT-DT)
      UGT(J,L,N)=UGT(J,L,N)+T2*(2.+DZDT)/
     .DSQRT((ROOT5+Y)*(ROOT6+Y))*
     .(UZ*(-C1+(D2-C2)*
     .(Z(N,J)-ZN-DLOG(CSI(L))/2./(1+LAM))/Y)
     .+UR*(D2-C2)*(R(J)-(0.5*(ROOT5**2+ROOT6**2)-Y**2)/2./R(J))/Y)
69    DO 70 M=1,NZ
      IF (NN.EQ.1) UGTOLD=UGT0(I,M)
      IF (NN.GT.1) UGTOLD=UGT(I,M,NN-1)
      ROOT7=DSQRT((R(I)+R(J))**2+(Z(N,J)-ZN
     .+DLOG(CSI(M)/CSI(L))/2./(1+LAM))**2)
      ROOT8=DSQRT((R(I)-R(J))**2+(Z(N,J)-ZN
     .+DLOG(CSI(M)/CSI(L))/2./(1+LAM))**2)
      OMEGA=ROOT8+(ROOT7-ROOT8)*FI(K)
      IF (NN.EQ.N) GO TO 71
      Q1=
     .DEXP(OMEGA)*(DERF(OMEGA/2./DSQRT(DFLOAT(N-NN)*DT)
     .+DSQRT(DFLOAT(N-NN)*DT))-
     .DERF(OMEGA/2./DSQRT(DFLOAT(N-NN+1)*DT)
     .+DSQRT(DFLOAT(N-NN+1)*DT)))+
```

```
     .DEXP(-OMEGA)*(DERF(OMEGA/2./DSQRT(DFLOAT(N-NN)*DT)
     .-DSQRT(DFLOAT(N-NN)*DT))-
     .DERF(OMEGA/2./DSQRT(DFLOAT(N-NN+1)*DT)
     .-DSQRT(DFLOAT(N-NN+1)*DT)))
      Q2=Q1/OMEGA
      S2=
     .DEXP(OMEGA)*(DERF(OMEGA/2./DSQRT(DFLOAT(N-NN)*DT)
     .+DSQRT(DFLOAT(N-NN)*DT))-
     .DERF(OMEGA/2./DSQRT(DFLOAT(N-NN+1)*DT)
     .+DSQRT(DFLOAT(N-NN+1)*DT)))-
     .DEXP(-OMEGA)*(DERF(OMEGA/2./DSQRT(DFLOAT(N-NN)*DT)
     .-DSQRT(DFLOAT(N-NN)*DT))-
     .DERF(OMEGA/2./DSQRT(DFLOAT(N-NN+1)*DT)
     .-DSQRT(DFLOAT(N-NN+1)*DT)))+
     .2./DSQRT(PI*DFLOAT(N-NN)*DT)
     .*DEXP(-OMEGA**2/4./DFLOAT(N-NN)/DT-(N-NN)*DT)-
     .2./DSQRT(PI*DFLOAT(N-NN+1)*DT)
     .*DEXP(-OMEGA**2/4./DFLOAT(N-NN+1)/DT-(N-NN+1)*DT)
      UGT(J,L,N)=UGT(J,L,N)
     .-T2*PI*LAM/(1+LAM)/DFLOAT(NZ)*CSI(M)**(-.5/(1.+LAM))
     .*CS2(M)
     ./DSQRT((ROOT7+OMEGA)*(ROOT8+OMEGA))*
     .(UZ*(-Q1+(S2-Q2)*
     .(Z(N,J)-ZN-DLOG(CSI(L)/CSI(M))/2./(1+LAM))/OMEGA)
     .+UR*(S2-Q2)*
     .(R(J)-(0.5*(ROOT7**2+ROOT8**2)-OMEGA**2)/2./R(J))/OMEGA)
     .*UGTOLD
      GO TO 70
71    Q1=
     .DEXP(OMEGA)*
     .DERFC(OMEGA/2./DSQRT(DT)
     .+DSQRT(DT))+
     .DEXP(-OMEGA)*
     .DERFC(OMEGA/2./DSQRT(DT)
     .-DSQRT(DT))
      Q2=Q1/OMEGA
      S2=
     .DEXP(OMEGA)*
     .DERFC(OMEGA/2./DSQRT(DT)
     .+DSQRT(DT))-
     .DEXP(-OMEGA)*
     .DERFC(OMEGA/2./DSQRT(DT)
     .-DSQRT(DT))-
     .2./DSQRT(PI*DT)
     .*DEXP(-OMEGA**2/4./DT-DT)
      UGT(J,L,N)=UGT(J,L,N)
     .-T2*PI*LAM/(1+LAM)/DFLOAT(NZ)*CSI(M)**(-.5/(1.+LAM))
     .*CS2(M)
     ./DSQRT((ROOT7+OMEGA)*(ROOT8+OMEGA))*
     .(UZ*(-Q1+(S2-Q2)*
     .(Z(N,J)-ZN-DLOG(CSI(L)/CSI(M))/2./(1+LAM))/OMEGA)
     .+UR*(S2-Q2)*
     .(R(J)-(0.5*(ROOT7**2+ROOT8**2)-OMEGA**2)/2./R(J))/OMEGA)
     .*UGTOLD
```

```
 70   CONTINUE
 60   CONTINUE
 50   CONTINUE
 20   CONTINUE
  7   CONTINUE
100   CONTINUE
300   STOP
      END
      SUBROUTINE FCN(X,F,NR,PAR)
      IMPLICIT REAL*8 (A-H,O-Z)
      REAL*8 X(NR),F(NR),PAR(1),
     .UGT(30,30,1000 ),UGT0(30,30),Z(1000 ,30),
     .ZD(1000 ,30),Z0(30),R(30),CSI(30),CS2(30),FI(30),ZDINIT(30),
     .ORD(30),VECRHO(3),ZETA(3),BPAR(4),C(30,3),LAM,NU
      LOGICAL IVAN
      COMMON /A/UGT,UGT0,Z,ZD,ZDINIT,CSI,CS2,FI,Z0,LAM,PI,
     .DT,NU,ANIS,NF,NZ,NT,INDEX,IVAN
     ./B/C,R,ORD,BPAR
     ./D/SMALL,P
      F(NR)=X(NR)-Z0(NR)
      INDEX=INDEX+1
      IF (NU.EQ.0.) GO TO 999
CCCCCCCCCCCCCCCCCCCCCCCCCCCCCCCCCCCCCCCCCCCCCCCCCCCCCCCCCCCCCCCCCCCCCCCCCC
C     CONTRIBUTION FROM CURVATURE
CCCCCCCCCCCCCCCCCCCCCCCCCCCCCCCCCCCCCCCCCCCCCCCCCCCCCCCCCCCCCCCCCCCCCCCCCC
      ORD(NR+1)=
     .P/2.*(1-R(NR+1)**2/P**2)
      ORD(NR+2)=
     .P/2.*(1-R(NR+2)**2/P**2)
      ORD(NR+3)=
     .P/2.*(1-R(NR+3)**2/P**2)
      DO 4 I=1,NR
   4  ORD(I)=X(I)
      CALL ICSICU (R,ORD,NR+3,BPAR,C,30,IER)
      DO 992 J=1,NR-1
      RJ=R(J)
      IF (J.GT.1) GO TO 998
      VECRHO(1)=RJ
      VECRHO(2)=RJ+SMALL
      VECRHO(3)=RJ+SMALL*2
      CALL ICSEVU(R,ORD,NR+3,C,30,VECRHO,ZETA,3,IER)
      DZ1DR1=(ZETA(2)-ZETA(1))/SMALL
      DZ2DR2=(ZETA(3)+ZETA(1)-2*ZETA(2))/SMALL**2
      GO TO 997
 998  VECRHO(1)=RJ-SMALL
      VECRHO(2)=RJ
      VECRHO(3)=RJ+SMALL
      CALL ICSEVU(R,ORD,NR+3,C,30,VECRHO,ZETA,3,IER)
      DZ1DR1=(ZETA(3)-ZETA(1))/2./SMALL
      DZ2DR2=(ZETA(3)+ZETA(1)-2*ZETA(2))/SMALL**2
 997  F(J)=-NU*(RJ*DZ2DR2+DZ1DR1**3+DZ1DR1)/RJ
     ./(1+DZ1DR1**2)**1.5
CCCCCCCCCCCCCCCCCCCCCCCCCCCCCCCCCCCCCCCCCCCCCCCCCCCCCCCCCCCCCCCCCCCCCCCCCC
C     ANISOTROPY
```

```
CCCCCCCCCCCCCCCCCCCCCCCCCCCCCCCCCCCCCCCCCCCCCCCCCCCCCCCCCCCCCCCCCCCCCCC
     .*(1-ANIS*8*DZ1DR1**2/
     .(1+DZ1DR1**2)**2)
 992  CONTINUE
 999  DO 2 J=1,NR-1
      IF (NU.EQ.0.) F(J)=0.
      DO 20 I=1,NR
CCCCCCCCCCCCCCCCCCCCCCCCCCCCCCCCCCCCCCCCCCCCCCCCCCCCCCCCCCCCCCCCCCCCCCC
C     CONTRIBUTION FROM -DEL
CCCCCCCCCCCCCCCCCCCCCCCCCCCCCCCCCCCCCCCCCCCCCCCCCCCCCCCCCCCCCCCCCCCCCCC
      RPLUS=DSQRT(
     .(R(I)+RJ)**2+(Z0(J)-Z0(I))**2)
      RMIN=DSQRT(
     .(R(I)-RJ)**2+(Z0(J)-Z0(I))**2)
      DO 5 K=1,NF
      Y=RMIN+(RPLUS-RMIN)*FI(K)
      F(J)=F(J)-P*PI/DFLOAT(NR*NF)*DTAN
     .(DFLOAT(2*I-1)/DFLOAT(2*NR)*PI/2.)
     .*DEXP(Z0(I)-Z0(J)-Y)/
     .DSQRT((RMIN+Y)*(RPLUS+Y))
   5  CONTINUE
      DO 10 M=1,NZ
      RES1=PI**2*P/2./DFLOAT(NR*NF*NZ)*LAM/(1.+LAM)*
     .DTAN(DFLOAT(2*I-1)/DFLOAT(2*NR)*PI/2.)
     .*CS2(M)
     .*CSI(M)**(-1./2./(1.+LAM))
     .*DEXP(Z0(I)-Z0(J))
     .*UGT0(I,M)
      RPLUS=DSQRT((R(I)+RJ)**2+(Z0(J)-Z0(I)
     .+DLOG(CSI(M))/2./(1+LAM))**2)
      RMIN=DSQRT((R(I)-RJ)**2+(Z0(J)-Z0(I)
     .+DLOG(CSI(M))/2./(1+LAM))**2)
      DO 10 K=1,NF
      OMEGA=RMIN+(RPLUS-RMIN)*FI(K)
      F(J)=F(J)+RES1*DEXP(-OMEGA)/
     .DSQRT((RPLUS+OMEGA)*(RMIN+OMEGA))
  10  CONTINUE
CCCCCCCCCCCCCCCCCCCCCCCCCCCCCCCCCCCCCCCCCCCCCCCCCCCCCCCCCCCCCCCCCCCCCCC
C     CONTRIBUTION FROM I1 & I3
CCCCCCCCCCCCCCCCCCCCCCCCCCCCCCCCCCCCCCCCCCCCCCCCCCCCCCCCCCCCCCCCCCCCCCC
      T0=P*PI/DFLOAT(2*NR*NF)*DTAN(DFLOAT(2*I-1)/DFLOAT(2*NR)*PI/2.)
      T1=T0
     .*DEXP(-X(J)+Z0(I))
      ROOT1=DSQRT((R(I)+RJ)**2+(X(J)-Z0(I))**2)
      ROOT2=DSQRT((R(I)-RJ)**2+(X(J)-Z0(I))**2)
      DO 30 K=1,NF
      Y=ROOT2+(ROOT1-ROOT2)*FI(K)
      F(J)=F(J)+T1/DSQRT((ROOT1+Y)*(ROOT2+Y))*
     .(-2*DSINH(Y)+DEXP(Y)*DERF(Y/2./DSQRT(DFLOAT(NT)*DT)
     .+DSQRT(DFLOAT(NT)*DT))+
     .DEXP(-Y)*DERF(Y/2./DSQRT(DFLOAT(NT)*DT)-
     .DSQRT(DFLOAT(NT)*DT)))
      IF (IVAN) GO TO 30
      DO 40 M=1,NZ
```

```
      ROOT3=DSQRT((R(I)+RJ)**2+(X(J)-Z0(I)
     .+DLOG(CSI(M))/2./(1+LAM))**2)
      ROOT4=DSQRT((R(I)-RJ)**2+(X(J)-Z0(I)
     .+DLOG(CSI(M))/2./(1+LAM))**2)
      OMEGA=ROOT4+(ROOT3-ROOT4)*FI(K)
      F(J)=F(J)-T1*PI*LAM/(1+LAM)/DFLOAT(2*NZ)*CSI(M)**(-.5/(1.+LAM))
     .*CS2(M)
     ./DSQRT((ROOT3+OMEGA)*(ROOT4+OMEGA))*
     .(-2*DSINH(OMEGA)+DEXP(OMEGA)*DERF(OMEGA/2./DSQRT(DFLOAT(NT)*DT)
     .+DSQRT(DFLOAT(NT)*DT))+
     .DEXP(-OMEGA)*DERF(OMEGA/2./DSQRT(DFLOAT(NT)*DT)-
     .DSQRT(DFLOAT(NT)*DT)))
     .*UGT0(I,M)
  40  CONTINUE
  30  CONTINUE
CCCCCCCCCCCCCCCCCCCCCCCCCCCCCCCCCCCCCCCCCCCCCCCCCCCCCCCCCCCCCCCCCCCCCCCCCCC
C     CONTRIBUTION FROM I2 & I4
CCCCCCCCCCCCCCCCCCCCCCCCCCCCCCCCCCCCCCCCCCCCCCCCCCCCCCCCCCCCCCCCCCCCCCCCCCC
      DO 50 N=1,NT
      IF (N.EQ.NT) ZN=X(I)
      IF (N.LT.NT) ZN=Z(N,I)
      ROOT5=DSQRT((R(I)+RJ)**2+(X(J)-ZN)**2)
      ROOT6=DSQRT((R(I)-RJ)**2+(X(J)-ZN)**2)
      IF (N.EQ.NT.OR.NT.EQ.1) GO TO 57
      DZDT=ZD(N,I)
      GO TO 56
  57  IF (NT.EQ.1) DZDT=ZDINIT(I)
      IF (NT.GT.1) DZDT=(X(I)-Z(N-1,I))/DT
  56  T2=T0/2.*DEXP(-X(J)+ZN)
      DO 60 K=1,NF
      Y=ROOT6+(ROOT5-ROOT6)*FI(K)
      IF (N.NE.NT)
     .F(J)=F(J)+T2*(2.+DZDT)/
     .DSQRT((ROOT5+Y)*(ROOT6+Y))*
     .(DEXP(Y)*(DERF(Y/2./DSQRT(DFLOAT(NT-N)*DT)
     .+DSQRT(DFLOAT(NT-N)*DT))-
     .DERF(Y/2./DSQRT(DFLOAT(NT-N+1)*DT)
     .+DSQRT(DFLOAT(NT-N+1)*DT)))+
     .DEXP(-Y)*(DERF(Y/2./DSQRT(DFLOAT(NT-N)*DT)
     .-DSQRT(DFLOAT(NT-N)*DT))-
     .DERF(Y/2./DSQRT(DFLOAT(NT-N+1)*DT)
     .-DSQRT(DFLOAT(NT-N+1)*DT))))
      IF (N.EQ.NT)
     .F(J)=F(J)+T2*(2.+DZDT)/
     .DSQRT((ROOT5+Y)*(ROOT6+Y))*
     .(DEXP(Y)*
     .DERFC(Y/2./DSQRT(DT)
     .+DSQRT(DT))+
     .DEXP(-Y)*
     .DERFC(Y/2./DSQRT(DT)
     .-DSQRT(DT)))
      IF (IVAN) GO TO 60
      IF (N.EQ.1) ZOLD=Z0(I)
      IF (N.GT.1) ZOLD=Z(N-1,I)
```

```
      IF (N.EQ.NT) GO TO 78
      DO 70 M=1,NZ
      IF (N.EQ.1) UGTOLD=UGTO(I,M)
      IF (N.GT.1) UGTOLD=UGT(I,M,N-1)
      ROOT7=DSQRT((R(I)+RJ)**2+(X(J)-ZOLD
     .+DLOG(CSI(M))/2./(1+LAM))**2)
      ROOT8=DSQRT((R(I)-RJ)**2+(X(J)-ZOLD
     .+DLOG(CSI(M))/2./(1+LAM))**2)
      OMEGA=ROOT8+(ROOT7-ROOT8)*FI(K)
      F(J)=F(J)-
     .T0/2.*DEXP(-X(J)+ZOLD)
     .*PI*LAM/(1+LAM)/DFLOAT(NZ)*CSI(M)**(-.5/(1.+LAM))
     .*CS2(M)
     ./DSQRT((ROOT7+OMEGA)*(ROOT8+OMEGA))*
     .(DEXP(OMEGA)*(DERF(OMEGA/2./DSQRT(DFLOAT(NT-N)*DT)
     .+DSQRT(DFLOAT(NT-N)*DT))-
     .DERF(OMEGA/2./DSQRT(DFLOAT(NT-N+1)*DT)
     .+DSQRT(DFLOAT(NT-N+1)*DT)))+
     .DEXP(-OMEGA)*(DERF(OMEGA/2./DSQRT(DFLOAT(NT-N)*DT)
     .-DSQRT(DFLOAT(NT-N)*DT))-
     .DERF(OMEGA/2./DSQRT(DFLOAT(NT-N+1)*DT)
     .-DSQRT(DFLOAT(NT-N+1)*DT))))
     .*UGTOLD
   70 CONTINUE
      GO TO 60
   78 DO 75 M=1,NZ
      IF (N.EQ.1) UGTOLD=UGTO(I,M)
      IF (N.GT.1) UGTOLD=UGT(I,M,N-1)
      ROOT7=DSQRT((R(I)+RJ)**2+(X(J)-ZOLD
     .+DLOG(CSI(M))/2./(1+LAM))**2)
      ROOT8=DSQRT((R(I)-RJ)**2+(X(J)-ZOLD
     .+DLOG(CSI(M))/2./(1+LAM))**2)
      OMEGA=ROOT8+(ROOT7-ROOT8)*FI(K)
      F(J)=F(J)-
     .T0/2.*DEXP(-X(J)+ZOLD)
     .*PI*LAM/(1.+LAM)/DFLOAT(NZ)*CSI(M)**(-.5/(1.+LAM))
     .*CS2(M)
     ./DSQRT((ROOT7+OMEGA)*(ROOT8+OMEGA))*
     .(DEXP(OMEGA)*
     .DERFC(OMEGA/2./DSQRT(DT)
     .+DSQRT(DT))+
     .DEXP(-OMEGA)*
     .DERFC(OMEGA/2./DSQRT(DT)
     .-DSQRT(DT)))
     .*UGTOLD
   75 CONTINUE
   60 CONTINUE
   50 CONTINUE
   20 CONTINUE
    2 CONTINUE
      RETURN
      END
CCCCCCCCCCCCCCCCCCCCCCCCCCCCCCCCCCCCCCCCCCCCCCCCCCCCCCCCCCCCCCCCCCCCCCCC
      FUNCTION EXPIN(P)
```

```
      IMPLICIT REAL*8 (A-H,O-Z)
      IF (P.GT.14.) GO TO 30
      EXPIN=-0.57721566490245707 1-DLOG(P)
      DOE=-1.
      DO 20 I=1,1000000
      DOE=-DOE*P/DFLOAT(I)
      IF (DABS(DOE)/DFLOAT(I).LE.1.D-16)GO TO 40
   20 EXPIN=EXPIN+DOE/DFLOAT(I)
   30 EXPIN=DEXP(-P-DLOG(P))*(1-1./P+2/P**2-6/P**3
     .+24./P**4)
   40 RETURN
      END
CCCCCCCCCCCCCCCCCCCCCCCCCCCCCCCCCCCCCCCCCCCCCCCCCCCCCCCCCCCCCCCCCCCCCCCCCCCCCCC
      FUNCTION EXPIN2(P)
      IMPLICIT REAL*8 (A-H,O-Z)
      EXTERNAL EXPIN
      EXPIN2=DEXP(-P)-P*EXPIN(P)
      RETURN
      END
CCCCCCCCCCCCCCCCCCCCCCCCCCCCCCCCCCCCCCCCCCCCCCCCCCCCCCCCCCCCCCCCCCCCCCCCCCCCCCC
      FUNCTION FA(RHO)
      IMPLICIT REAL*8 (A-H,O-Z)
      REAL*8 QUAD(30),VECRHO(3),ZETA(3),C(30,3),R(30),ORD(30)
      COMMON
     ./B/C,R,ORD,BPAR
     ./D/SMALL,P
     ./C/QUAD,RJ,ZJ,R2,MM,NR
      IF (RHO.GT.(R(1)+SMALL)) GO TO 998
      VECRHO(1)=R(1)
      VECRHO(2)=R(1)+SMALL
      VECRHO(3)=R(1)+SMALL*2
      CALL ICSEVU(R,ORD,NR+3,C,30,VECRHO,ZETA,3,IER)
      DER1=(ZETA(2)-ZETA(1))/SMALL
      DER2=(ZETA(3)+ZETA(1)-2*ZETA(2))/SMALL**2
CCCCCCCCCCCCCCCCCCCCCCCCCCCCCCCCCCCCCCCCCCCCCCCCCCCCCCCCCCCCCCCCCCCCCCCCCCCCCCC
C     ZETA(2) WILL NOW REPRESENT ZETA IN [ZEROPL,R(1)]
C     DZ1DR1 WILL NOW REPRESENT DERIV IN [ZEROPL,R(1)]
CCCCCCCCCCCCCCCCCCCCCCCCCCCCCCCCCCCCCCCCCCCCCCCCCCCCCCCCCCCCCCCCCCCCCCCCCCCCCCC
      ZETA(2)=ZETA(1)+(RHO-R(1))*DER1+(RHO-R(1))**2/2.*DER2
      DZ1DR1=DER1+(RHO-R(1))*DER2
      GO TO 997
  998 VECRHO(1)=RHO-SMALL
      VECRHO(2)=RHO
      VECRHO(3)=RHO+SMALL
      CALL ICSEVU(R,ORD,NR+3,C,30,VECRHO,ZETA,3,IER)
      DZ1DR1=(ZETA(3)-ZETA(1))/2./SMALL
  997 B=2*RHO*RJ
      A=RHO**2+RJ**2+(ZETA(2)-ZJ)**2
      FA=0.
      DO 10 M=1,MM
      DIST=QUAD(M)*(DSQRT(A+B)-DSQRT(A-B))*.5
     .+(DSQRT(A+B)+DSQRT(A-B))*.5
      THCOS=(A-DIST**2)/B
   10 FA=FA+1./DFLOAT(MM)*RHO*DSQRT(1.+DZ1DR1**2)
```

```
     ./DSQRT((DSQRT(A-B)+DIST)*(DSQRT(B+A)+DIST))
     .*(THCOS+(RJ-RHO*THCOS)*(RJ*THCOS-RHO)/DIST**2)
      RETURN
      END
      FUNCTION FB(RHO)
      IMPLICIT REAL*8 (A-H,O-Z)
      REAL*8 QUAD(30),VECRHO(3),ZETA(3),C(30,3),R(30),ORD(30)
      COMMON
     ./B/C,R,ORD,BPAR
     ./D/SMALL,P
     ./C/QUAD,RJ,ZJ,R2,MM,NR
      IF (RHO.GT.(R(1)+SMALL)) GO TO 998
      VECRHO(1)=R(1)
      VECRHO(2)=R(1)+SMALL
      VECRHO(3)=R(1)+SMALL*2
      CALL ICSEVU(R,ORD,NR+3,C,30,VECRHO,ZETA,3,IER)
      DER1=(ZETA(2)-ZETA(1))/SMALL
      DER2=(ZETA(3)+ZETA(1)-2*ZETA(2))/SMALL**2
CCCCCCCCCCCCCCCCCCCCCCCCCCCCCCCCCCCCCCCCCCCCCCCCCCCCCCCCCCCCCCCCCCCC
C     ZETA(2) WILL NOW REPRESENT ZETA IN [ZEROPL,R(1)]
C     DZ1DR1 WILL NOW REPRESENT DERIV IN [ZEROPL,R(1)]
CCCCCCCCCCCCCCCCCCCCCCCCCCCCCCCCCCCCCCCCCCCCCCCCCCCCCCCCCCCCCCCCCCCC
      ZETA(2)=ZETA(1)+(RHO-R(1))*DER1+(RHO-R(1))**2/2.*DER2
      DZ1DR1=DER1+(RHO-R(1))*DER2
      GO TO 997
 998  VECRHO(1)=RHO-SMALL
      VECRHO(2)=RHO
      VECRHO(3)=RHO+SMALL
      CALL ICSEVU(R,ORD,NR+3,C,30,VECRHO,ZETA,3,IER)
      DZ1DR1=(ZETA(3)-ZETA(1))/2./SMALL
 997  B=2*RHO*RJ
      A=RHO**2+RJ**2+(ZETA(2)-ZJ)**2
      FB=0.
      DO 10 M=1,MM
      DIST=QUAD(M)
     .*(DSQRT(A+B)-DSQRT(A-B))*.5
     .+(DSQRT(A+B)+DSQRT(A-B))*.5
      THCOS=(A-DIST**2)/B
 10   FB=FB+1./DFLOAT(MM)*RHO*DSQRT(1.+DZ1DR1**2)
     ./DSQRT((DSQRT(A-B)+DIST)*(DSQRT(B+A)+DIST))
     .*(RJ-RHO*THCOS)/DIST*(ZJ-ZETA(2))/DIST
      RETURN
      END
      FUNCTION FC(RHO)
      IMPLICIT REAL*8 (A-H,O-Z)
      REAL*8 QUAD(30),VECRHO(3),ZETA(3),C(30,3),R(30),ORD(30)
      COMMON
     ./B/C,R,ORD,BPAR
     ./D/SMALL,P
     ./C/QUAD,RJ,ZJ,R2,MM,NR
      IF (RHO.GT.(R(1)+SMALL)) GO TO 998
      VECRHO(1)=R(1)
      VECRHO(2)=R(1)+SMALL
      VECRHO(3)=R(1)+SMALL*2
```

```
      CALL ICSEVU(R,ORD,NR+3,C,30,VECRHO,ZETA,3,IER)
      DER1=(ZETA(2)-ZETA(1))/SMALL
      DER2=(ZETA(3)+ZETA(1)-2*ZETA(2))/SMALL**2
CCCCCCCCCCCCCCCCCCCCCCCCCCCCCCCCCCCCCCCCCCCCCCCCCCCCCCCCCCCCCCCCCCCCCCCCCCC
C     ZETA(2) WILL NOW REPRESENT ZETA IN [ZEROPL,R(1)]
C     DZ1DR1 WILL NOW REPRESENT DERIV IN [ZEROPL,R(1)]
CCCCCCCCCCCCCCCCCCCCCCCCCCCCCCCCCCCCCCCCCCCCCCCCCCCCCCCCCCCCCCCCCCCCCCCCCCC
      ZETA(2)=ZETA(1)+(RHO-R(1))*DER1+(RHO-R(1))**2/2.*DER2
      DZ1DR1=DER1+(RHO-R(1))*DER2
      GO TO 997
 998  VECRHO(1)=RHO-SMALL
      VECRHO(2)=RHO
      VECRHO(3)=RHO+SMALL
      CALL ICSEVU(R,ORD,NR+3,C,30,VECRHO,ZETA,3,IER)
      DZ1DR1=(ZETA(3)-ZETA(1))/2./SMALL
 997  B=2*RHO*RJ
      A=RHO**2+RJ**2+(ZETA(2)-ZJ)**2
      FC=0.
      DO 10 M=1,MM
      DIST=QUAD(M)
     .*(DSQRT(A+B)-DSQRT(A-B))*.5
     .+(DSQRT(A+B)+DSQRT(A-B))*.5
      THCOS=(A-DIST**2)/B
  10  FC=FC+1./DFLOAT(MM)*RHO*DSQRT(1.+DZ1DR1**2)
     ./DSQRT((DSQRT(A-B)+DIST)*(DSQRT(B+A)+DIST))
     .*(RJ*THCOS-RHO)/DIST*(ZJ-ZETA(2))/DIST
      RETURN
      END
      FUNCTION FD(RHO)
      IMPLICIT REAL*8 (A-H,O-Z)
      REAL*8 QUAD(30),VECRHO(3),ZETA(3),C(30,3),R(30),ORD(30)
      COMMON
     ./B/C,R,ORD,BPAR
     ./D/SMALL,P
     ./C/QUAD,RJ,ZJ,R2,MM,NR
      IF (RHO.GT.(R(1)+SMALL)) GO TO 998
      VECRHO(1)=R(1)
      VECRHO(2)=R(1)+SMALL
      VECRHO(3)=R(1)+SMALL*2
      CALL ICSEVU(R,ORD,NR+3,C,30,VECRHO,ZETA,3,IER)
      DER1=(ZETA(2)-ZETA(1))/SMALL
      DER2=(ZETA(3)+ZETA(1)-2*ZETA(2))/SMALL**2
CCCCCCCCCCCCCCCCCCCCCCCCCCCCCCCCCCCCCCCCCCCCCCCCCCCCCCCCCCCCCCCCCCCCCCCCCCC
C     ZETA(2) WILL NOW REPRESENT ZETA IN [ZEROPL,R(1)]
C     DZ1DR1 WILL NOW REPRESENT DERIV IN [ZEROPL,R(1)]
CCCCCCCCCCCCCCCCCCCCCCCCCCCCCCCCCCCCCCCCCCCCCCCCCCCCCCCCCCCCCCCCCCCCCCCCCCC
      ZETA(2)=ZETA(1)+(RHO-R(1))*DER1+(RHO-R(1))**2/2.*DER2
      DZ1DR1=DER1+(RHO-R(1))*DER2
      GO TO 997
 998  VECRHO(1)=RHO-SMALL
      VECRHO(2)=RHO
      VECRHO(3)=RHO+SMALL
      CALL ICSEVU(R,ORD,NR+3,C,30,VECRHO,ZETA,3,IER)
      DZ1DR1=(ZETA(3)-ZETA(1))/2./SMALL
```

```
 997  B=2*RHO*RJ
      A=RHO**2+RJ**2+(ZETA(2)-ZJ)**2
      FD=0.
      DO 10 M=1,MM
      DIST=QUAD(M)
     .*(DSQRT(A+B)-DSQRT(A-B))*.5
     .+(DSQRT(A+B)+DSQRT(A-B))*.5
      THCOS=(A-DIST**2)/B
 10   FD=FD+1./DFLOAT(MM)*RHO*DSQRT(1.+DZ1DR1**2)
     ./DSQRT((DSQRT(A-B)+DIST)*(DSQRT(B+A)+DIST))
     .*(1+((ZETA(2)-ZJ)/DIST)**2)
      RETURN
      END
      FUNCTION RIGHT1(RHO)
      IMPLICIT REAL*8 (A-H,O-Z)
      REAL*8 QUAD(30),VECRHO(3),ZETA(3),C(30,3),R(30),ORD(30)
      LOGICAL UPFLOW
      COMMON
     ./B/C,R,ORD,BPAR
     ./D/SMALL,P
     ./C/QUAD,RJ,ZJ,R2,MM,NR,UPFLOW
      EXTERNAL EXPIN
      IF (RHO.GT.(R(1)+SMALL)) GO TO 998
      VECRHO(1)=R(1)
      VECRHO(2)=R(1)+SMALL
      VECRHO(3)=R(1)+SMALL*2
      CALL ICSEVU(R,ORD,NR+3,C,30,VECRHO,ZETA,3,IER)
      DER1=(ZETA(2)-ZETA(1))/SMALL
      DER2=(ZETA(3)+ZETA(1)-2*ZETA(2))/SMALL**2
CCCCCCCCCCCCCCCCCCCCCCCCCCCCCCCCCCCCCCCCCCCCCCCCCCCCCCCCCCCCCCCCCCCCCCCCCCC
C     ZETA(2) WILL NOW REPRESENT ZETA IN [ZEROPL,R(1)]
C     DZ1DR1 WILL NOW REPRESENT DERIV IN [ZEROPL,R(1)]
CCCCCCCCCCCCCCCCCCCCCCCCCCCCCCCCCCCCCCCCCCCCCCCCCCCCCCCCCCCCCCCCCCCCCCCCCCC
      ZETA(2)=ZETA(1)+(RHO-R(1))*DER1+(RHO-R(1))**2/2.*DER2
      DZ1DR1=DER1+(RHO-R(1))*DER2
      GO TO 997
 998  VECRHO(1)=RHO-SMALL
      VECRHO(2)=RHO
      VECRHO(3)=RHO+SMALL
      CALL ICSEVU(R,ORD,NR+3,C,30,VECRHO,ZETA,3,IER)
      DZ1DR1=(ZETA(3)-ZETA(1))/2./SMALL
 997  W=(ZETA(2)+DSQRT(ZETA(2)**2+RHO**2))/P
      S=(-ZETA(2)+DSQRT(ZETA(2)**2+RHO**2))/P
      IF (S.LE.0) S=0.
CCCCCCCCCCCCCCCCCCCCCCCCCCCCCCCCCCCCCCCCCCCCCCCCCCCCCCCCCCCCCCCCCCCCCCCCCCC
C     FLOW DOWN
CCCCCCCCCCCCCCCCCCCCCCCCCCCCCCCCCCCCCCCCCCCCCCCCCCCCCCCCCCCCCCCCCCCCCCCCCCC
      IF (UPFLOW) GO TO 811
      UZ=-(-1.+EXPIN(R2*W)/EXPIN(R2)+
     .(DEXP(-R2)-DEXP(-R2*W))/EXPIN(R2)/R2/(W+S))
      UR=-((1.-EXPIN(R2*W)/EXPIN(R2))*DSQRT(S/(S+W)))
      GO TO 812
CCCCCCCCCCCCCCCCCCCCCCCCCCCCCCCCCCCCCCCCCCCCCCCCCCCCCCCCCCCCCCCCCCCCCCCCCCC
C     FLOW UP
```

```
CCCCCCCCCCCCCCCCCCCCCCCCCCCCCCCCCCCCCCCCCCCCCCCCCCCCCCCCCCCCCCCCCCCCCCCCCCCCCCC
 811  UZ=-(1.-EXPIN(R2*W)/EXPIN(R2)-
     .(DEXP(-R2)-DEXP(-R2*W))/EXPIN(R2)/R2/(W+S))
      UR=-(-(1.-EXPIN(R2*W)/EXPIN(R2))*DSQRT(S/(S+W)))
 812  B=2*RHO*RJ
      A=RHO**2+RJ**2+(ZETA(2)-ZJ)**2
      RIGHT1=0.
      DO 10 M=1,MM
      DIST=QUAD(M)*(DSQRT(A+B)-DSQRT(A-B))*.5
     .+(DSQRT(A+B)+DSQRT(A-B))*.5
      THCOS=(A-DIST**2)/B
  10  RIGHT1=RIGHT1+6./DFLOAT(MM)*RHO
     ./DSQRT((DSQRT(A-B)+DIST)*(DSQRT(B+A)+DIST))
     .*(RJ-RHO*THCOS)/DIST
     .*(ZJ-ZETA(2)-DZ1DR1*(RJ*THCOS-RHO))/DIST
     .*(UR
     .*(RJ*THCOS-RHO)+(ZJ-ZETA(2))*UZ)
      RETURN
      END
      FUNCTION RIGHT2(RHO)
      IMPLICIT REAL*8 (A-H,O-Z)
      REAL*8 QUAD(30),VECRHO(3),ZETA(3),C(30,3),R(30),ORD(30)
      LOGICAL UPFLOW
      COMMON
     ./B/C,R,ORD,BPAR
     ./D/SMALL,P
     ./C/QUAD,RJ,ZJ,R2,MM,NR,UPFLOW
      EXTERNAL EXPIN
      IF (RHO.GT.(R(1)+SMALL)) GO TO 998
      VECRHO(1)=R(1)
      VECRHO(2)=R(1)+SMALL
      VECRHO(3)=R(1)+SMALL*2
      CALL ICSEVU(R,ORD,NR+3,C,30,VECRHO,ZETA,3,IER)
      DER1=(ZETA(2)-ZETA(1))/SMALL
      DER2=(ZETA(3)+ZETA(1)-2*ZETA(2))/SMALL**2
CCCCCCCCCCCCCCCCCCCCCCCCCCCCCCCCCCCCCCCCCCCCCCCCCCCCCCCCCCCCCCCCCCCCCCCCCCCCCCC
C     ZETA(2) WILL NOW REPRESENT ZETA IN [ZEROPL,R(1)]
C     DZ1DR1 WILL NOW REPRESENT DERIV IN [ZEROPL,R(1)]
CCCCCCCCCCCCCCCCCCCCCCCCCCCCCCCCCCCCCCCCCCCCCCCCCCCCCCCCCCCCCCCCCCCCCCCCCCCCCCC
      ZETA(2)=ZETA(1)+(RHO-R(1))*DER1+(RHO-R(1))**2/2.*DER2
      DZ1DR1=DER1+(RHO-R(1))*DER2
      GO TO 997
 998  VECRHO(1)=RHO-SMALL
      VECRHO(2)=RHO
      VECRHO(3)=RHO+SMALL
      CALL ICSEVU(R,ORD,NR+3,C,30,VECRHO,ZETA,3,IER)
      DZ1DR1=(ZETA(3)-ZETA(1))/2./SMALL
 997  W=(ZETA(2)+DSQRT(ZETA(2)**2+RHO**2))/P
      S=(-ZETA(2)+DSQRT(ZETA(2)**2+RHO**2))/P
      IF (S.LE.0) S=0.
CCCCCCCCCCCCCCCCCCCCCCCCCCCCCCCCCCCCCCCCCCCCCCCCCCCCCCCCCCCCCCCCCCCCCCCCCCCCCCC
C     FLOW DOWN
CCCCCCCCCCCCCCCCCCCCCCCCCCCCCCCCCCCCCCCCCCCCCCCCCCCCCCCCCCCCCCCCCCCCCCCCCCCCCCC
      IF (UPFLOW) GO TO 811
```

```
      UZ=-(-1.+EXPIN(R2*W)/EXPIN(R2)+
     .(DEXP(-R2)-DEXP(-R2*W))/EXPIN(R2)/R2/(W+S))
      UR=-((1.-EXPIN(R2*W)/EXPIN(R2))*DSQRT(S/(S+W)))
      GO TO 812
CCCCCCCCCCCCCCCCCCCCCCCCCCCCCCCCCCCCCCCCCCCCCCCCCCCCCCCCCCCCCCCCCCCCCCCCCCCCCC
C     FLOW UP
CCCCCCCCCCCCCCCCCCCCCCCCCCCCCCCCCCCCCCCCCCCCCCCCCCCCCCCCCCCCCCCCCCCCCCCCCCCCC
 811  UZ=-(1.-EXPIN(R2*W)/EXPIN(R2)-
     .(DEXP(-R2)-DEXP(-R2*W))/EXPIN(R2)/R2/(W+S))
      UR=-(-(1.-EXPIN(R2*W)/EXPIN(R2))*DSQRT(S/(S+W)))
 812  B=2*RHO*RJ
      A=RHO**2+RJ**2+(ZETA(2)-ZJ)**2
      RIGHT2=0.
      DO 10 M=1,MM
      DIST=QUAD(M)*(DSQRT(A+B)-DSQRT(A-B))*.5
     .+(DSQRT(A+B)+DSQRT(A-B))*.5
      THCOS=(A-DIST**2)/B
  10  RIGHT2=RIGHT2+6./DFLOAT(MM)*RHO
     ./DSQRT((DSQRT(A-B)+DIST)*(DSQRT(B+A)+DIST))
     .*(ZJ-ZETA(2))/DIST
     .*(ZJ-ZETA(2)-DZ1DR1*(RJ*THCOS-RHO))/DIST
     .*(UR
     .*(RJ*THCOS-RHO)+(ZJ-ZETA(2))*UZ)
      RETURN
      END
```

Two Puzzling Aspects of Protein Crystal Growth

M. L. Grant and D. A. Saville
Department of Chemical Engineering
Princeton University
Princeton, NJ 08544

Abstract

In order to determine a protein's tertiary structure, large, well ordered single crystals are required for x-ray analysis. Producing such crystals is often the rate-limiting step because many protein crystals grow slowly and they often reach a terminal size which is too small to be useful for x-ray diffraction studies. In this paper, we present our study of several mechanisms which may reduce crystal growth rates and/or terminate crystal growth entirely. On the basis of our analysis, we find that salt gradients which change the local chemical potential of the protein are insufficient to account for the slow crystal growth rates which have been reported. Contaminants which adsorb protein from solution may reduce the effective protein concentration, but the impurity's concentration and its affinity for protein are unknown. Association of protein molecules in bulk solution can reduce the monomer concentration significantly, but extant theory and experiment are not sensitive enough to determine the actual concentration of aggregates in solution. For systems of interest, shear-induced effects were found to be too weak to interfere with normal binding of incoming protein molecules. Although we found that most crystal growth occurs in a regime where both interfacial kinetics and diffusion influence crystal growth, the role of mass transfer rates on the terminal size of crystals is unknown, primarily because no data exist which cover the size range of interest (0.1mm - 1mm in length).

Experimental studies of growth of large protein crystals are essential if mechanisms by which crystals stop growing are to be elucidated. Growth rate measurements for a wide range of crystal sizes, coupled with measurements of system properties which vary with time, may reveal the factors responsible for this puzzling behavior. Several hypotheses have been advanced to explain growth cessation, but none have been verified by experiment. For example, if termination of

growth occurs by accumulation of defects, x-ray studies of the crystals at different stages in their growth should reveal some qualitative changes in the nature of the protein crystal which is related to its growth behavior.

Introduction

Protein crystals are useful for determining the tertiary structure of biological molecules but the task of preparing crystals is difficult because many proteins do not form crystals readily or form crystals which are unsuitable for x-ray analysis. Protein crystals differ from more familiar inorganic crystals in several ways. In many systems, crystals tend to grow at a constant rate, up to a point, and then stop growing. The molecules are held in the crystal lattice by weak hydrogen bonds (ΔH = -3 kcal/mole to -6 kcal/mole *in vacuo*) which are not well characterized [Creighton 1983] and each molecule has relatively few contacts with its neighbors [McPherson 1982]. Additionally, the bonding structure and the physical nature of the crystal are not well understood. Moreover, the crystallization process itself is complicated by small changes in temperature, pH, or the precipitating agent concentration. Although it has been shown that the precipitant concentration inside the crystal equilibrates with the external solvent [Wyckoff 1986], the concentration of precipitants in crystals has not been measured. Thus the mechanism by which precipitants act and their role inside the crystal are unsolved mysteries.

Some of the difficulty of understanding protein crystallization arises from the complexity of a system containing protein, precipitating agent, buffer, and solvent. Interactions between these components makes it nearly impossible to predict whether a given set of conditions is suitable for protein crystal growth. Thus, guidelines for producing protein crystals are largely rules of thumb. Results from groups working on the same model system under similar conditions can differ significantly, as evidenced by disparities in the solubility of lysozyme reported at 20°C in 5%(w/v) NaCl at pH 4. Values range from 1.7 mg/ml [Pusey *et al.* 1986] to 4.3 mg/ml [Kam *et al.* 1978, Feher and Kam 1985] with an intermediate value of 3.5 mg/ml [Fiddis *et al.* 1978].

When used to determine the concentration dependence of the crystal growth rate these solubilities lead to different kinetic expressions which makes it difficult to decide on the controlling mechanism(s).

As though studying crystal growth by diffusion of protein from the bulk were not complicated enough, fluid flow may also influence matters. It is known that forced convection in the form of stirring tends to produce large numbers of small crystals rather than the large single crystals desired. Recently it was suggested that natural convection engendered by the protein concentration gradient near the crystal surface disrupts the orderly deposition of protein molecules [Bugg *et al.* 1984]. This fluid motion might: (i) promote rapid transfer where incoming protein molecules are forced to bind at a random site rather than the specific sites that lead to well ordered crystals, or (ii) alter the state of the protein at or near the surface surface through fluid shear. In the first case the convective mass transfer rate is envisioned as being faster than the attachment rate so defects form due to improperly bound or misoriented molecules. Accordingly, growth ceases due to an accumulation of errors when the surface concentration of defects reaches the point where additional molecules cannot find a suitable attachment site [Kam *et al.* 1978, Feher and Kam 1985] . This implies that neighboring molecules on the surface are misaligned and the degree of local disorder is extremely high or that binding requires the cooperation of a large number of properly oriented molecules on the surface. Unless these defects arise suddenly, crystal disorder would increase gradually moving towards the crystal surface (with a corresponding decrease in the x-ray resolution). According to the second mechanism, shear stresses at the crystal surface strip the molecules from the crystal surface or align the protein molecules so that molecules near the surface cannot assume the proper orientation for binding to the crystal. The shear stress on the protein molecule would need to be strong enough to denature the protein molecule by breaking its internal hydrogen bonds and unfolding the molecule.

Finally, contaminants in the solution may accumulate at the surface of the crystal and either poison the surface so that no further addition is possible, or induce some change in the protein near

the crystal surface which prevents it from binding.

In this paper, two main questions are addressed: (i) Why do protein crystals grow so slowly? and (ii) Why do protein crystals reach a terminal size? To answer the first question, we have examined three mechanisms which might limit crystal growth rates: salt rejection at the crystal-fluid interface, contamination by impurities which adsorb protein, and the aggregation of protein monomer in the bulk (which would lower the effective concentration of protein available for crystal growth). Our analysis indicates that any salt gradients due to salt rejection are too small to produce the effects needed to reduce the diffusion-limited crystal growth rates to measured levels. The presence of dust or other contaminants may significantly reduce the effective protein concentration if the protein adsorbs strongly to the dust surface. Parameters which affect the importance of surface adsorption, such as the protein's affinity for the dust and the dust concentration found in typical protein solutions, are not currently known. Aggregation of protein may significantly reduce the amount of protein monomer in solution, but both the measurements and the current theory for determining size distributions are inadequate to determine the actual state of aggregation of the protein in solution. Further revisions of the theory and a more comprehensive set of experiments may provide enough information to determine whether protein aggregation plays a role in limiting crystal growth rates.

Several hypotheses concerning the effect of fluid flow on the terminal size of protein crystals were investigated by examining several mechanisms in which fluid shear at the crystal interface interferes with normal addition of protein molecules to the surface and by performing a quasi-steady analysis of the mass transfer to the crystal surface. The effects of shear due to fluid flow were found to be several orders of magnitude too weak to disrupt proper protein attachment to the crystal surface or to align the protein molecules in the vicinity of the surface. An analysis of mass transfer indicates that crystal growth occurs in a regime where diffusion and the attachment reaction both play roles in limiting the crystal growth rate.

Formulation of a a theory to explain the peculiarities of protein crystal growth is hindered by

the lack of reliable data on growth rates of large crystals. Extant results were obtained with crystals no larger than approximately 100 mm in length and size effects are not yet apparent in these crystals, so vital information about the slowing growth rate is missing. A thorough study should be performed wherein larger crystals are produced in order to relate growth rates to system properties which may change over the course of the crystal growth process.

Salt Rejection and Protein Crystal Growth

There are at least two possible ways in which the rejection of salt (precipitating agent) at the interface may influence protein crystal growth: (i) a "blowing" velocity away from the crystal surface which would slow the transport of protein to the crystal; and (ii) the alteration of the local protein solubility which would reduce the driving force for diffusion. In the first case, the blowing would appear in the "crystallization" flow which arises from the diffusion of protein to the crystal surface. This crystallization flow is related to the growth rate of the crystal, dR/dt, by

$$\underline{v}_f = \underline{n} \frac{dR}{dt} (1 - \rho_c/\rho_f) \qquad (1)$$

where $\underline{v}_f$ is the fluid velocity at the interface, $\underline{n}$ is the unit normal directed outward from the crystal surface, ρ_c is the crystal mass density and ρ_f is the fluid density at the interface. The crystallization flow is directed towards the crystal surface if $\rho_c > \rho_f$, and away from the crystal if $\rho_c < \rho_f$. A rising convective plume has been observed [Pusey 1986, personal conversation], indicating that the fluid at the interface is less dense than the bulk fluid. Because the crystal is denser than the bulk fluid, $\rho_c > \rho_f$ and the rejection of salt is insufficient to induce a blowing away from the crystal surface. Earlier calculations [Grant 1985] showed that the convective protein flux due to crystallization flow is approximately 1% of the diffusive flux for a spherical protein crystal. The effect of salt rejection is to reduce this small convective flux, and can be neglected without appreciable error.

The effect of variations in the local protein solubility can be examinied by considering the growth of a spherical protein crystal under diffusion control. At the crystal surface, salt is rejected

and must diffuse to the bulk solution so that a salt concentration gradient exists along with the resulting gradient in the local solubility of the protein. In the diffusion limit, protein in the liquid at the crystal interface is at the solubility concentration and is in equilibrium with the protein in the crystal. Since the crystal form is reported to be insensitive to the salt concentration, it may be reasonable to assume the chemical potential of the crystalline protein is independent of the salt concentration. In this case, the chemical potentials of the protein in solution and in the crystal are equal wherever the protein concentration equals the local protein solubility because we could, in principle, place a crystal in a saturated protein solution without producing a change in either the crystal size or the protein concentration of the solution. The chemical potential of the protein depends on the other species which are in solution, so the protein's chemical potential is no longer directly proportional to its concentration. The salt concentration gradients due to rejection at the crystal interface may alter the gradients in the protein's chemical potential with the result that the flux of protein to the crystal surface is less than the flux one would expect from examining only the protein concentration gradient.

To set this out in mathematical form, we first express the flux of protein (species 1) in terms of its chemical potential [Cussler 1982]

$$j = -\frac{D_0}{kT} C_1 \nabla \mu_1 \tag{2}$$

where μ_1 is the chemical potential of the protein, D_0 = thermodynamic diffusion coefficient, and C_1= molar concentration of protein. The chemical potential of the protein is given by

$$\mu_1 = \mu_1^{\circ} + kT \ln x_1 \gamma_1 \tag{3}$$

where μ_1° = standard state chemical potential, x_1= mole fraction of protein, and γ_1=activity coefficient of the protein. Since the chemical potential of the protein at the solubility concentration is constant, it follows that $\mu_1^{sol} = \mu_1^{\circ} + kT \ln x_1^{sol} \gamma_1^{sol}$ = constant. The flux relation given by Equation (2) is unchanged by adding the gradient of a constant, so the flux can also be expressed as

$$j = -\frac{D_0}{kT} C_1 \nabla (\mu_1 - \mu_1^{sol}) = -\frac{D_0}{kT} C_1 \nabla \ln \left[\frac{x_1 \gamma_1}{x_1^{sol} \gamma_1^{sol}} \right] \tag{4}$$

One form for the activity coefficient is [Debenedetti 1984]

$$\gamma_1 = \gamma_1^{\infty} e^{-Kx_1} \tag{5}$$

where γ_1^{∞} is the activity coefficient of protein when in the limit of an infinitely dilute solution. If K is a constant independent of salt concentration and γ_1^{∞} varies with salt concentration, then the chemical potential of the dissolved protein can always be written in terms of the local γ_1^{∞}:

$$\begin{aligned} \mu_1^o + kT \ln x_1 \gamma_1 &= \mu_1^o + kT \ln \left[x_1 \gamma_1^{\infty}(C_{salt})\, e^{-Kx_1} \right] \\ \mu_1^o + kT \ln x_1^{sol} \gamma_1^{sol} &= \mu_1^o + kT \ln \left[x_1^{sol} \gamma_1^{\infty}(C_{salt})\, e^{-Kx_1^{sol}} \right] \end{aligned} \tag{6}$$

Although this manner of adjusting γ_1^{∞} to satisfy the solubility constraints is *ad hoc*, it makes the mathematics somewhat simpler by absorbing the salt dependence into x_1^{sol} so that substitution of equations (5) and (6) into Equation (4) gives

$$j = -D_0 C_1 \nabla \ln \left[\frac{x_1}{x_1^{sol}} e^{-K(x_1 - x_1^{sol})} \right] \tag{7}$$

A quasi-steady mass balance around a growing spherical crystal is

$$\left(R \frac{dR}{dt}\right) C_X = r^2 D_0 C_1 \frac{d}{dr} \ln \left[\frac{x_1}{x_1^{sol}} e^{-K(x_1 - x_1^{sol})} \right] \tag{8}$$

where C_X is the molar concentration of protein in the crystal. If the following dimensionless variables are introduced:

$$\lambda = R / R_0$$
$$z = R / r = R_0 \lambda / r \qquad (9)$$
$$\tau = t D_0 / R_0^2$$

the mass balance becomes

$$x_1 \frac{d}{dz} \ln \left[\frac{x_1}{x_1^{sol}} e^{-K(x_1 - x_1^{sol})} \right] = - Pe (C_X / C_T) \qquad (10)$$

$$Pe = \lambda \frac{d\lambda}{d\tau} = \frac{R}{D_0} \frac{dR}{dt}$$

where the relation $C_1 = C_T x_1$ has been used and C_T will be taken as 55 molar. Transforming the equation from an expression for the activity into a differential equation for x_1 yields:

$$\frac{dx_1}{dz} = - \frac{Pe (C_X / C_T) + (K x_1 - x_1 / x_1^{sol}) \frac{dx_1^{sol}}{dz}}{1 - K x_1} \qquad (11)$$

The salt concentration was calculated from the quasi-steady diffusion profile

$$C_{salt} = C_{salt,\infty} + \Delta C_{salt} \, z \qquad (12)$$

where $C_{salt,\infty}$= 50 mg/ml, and $\Delta C_S = C_{salt,surf} - C_{salt,\infty}$. The solubility was assumed to obey the expression [Feher and Kam 1985]

$$x_1^{sol} = \alpha e^{-\beta C_{salt}} \qquad (13)$$

Combining equations (12) and (13) gives x_1^{sol} as a function of position:

$$x_1^{sol} = x_{1,\infty}^{sol} e^{-\beta \Delta C_{salt} z} \qquad (14)$$

Equation (14) was substituted into (11) to yield

$$\frac{dx_1}{dz} = -\frac{Pe\,(C_X / C_T) + \beta\Delta C_{salt}\, x_1 - \beta\Delta C_{salt}\, Kx_1\, x_{1,\infty}^{sol}\, e^{-\beta\Delta C_{salt} z}}{1 - Kx_1} \tag{15}$$

and the initial value problem could then be integrated numerically from the crystal surface (z=1, $x_1=x_{1,s}^{sol}$) to infinity (z=0, $x_1=x_{1,\infty}$). The resulting value of $x_{1,\infty}$ can in turn be used to calculate the nominal growth rate which would be predicted from the diffusion limit in a uniform salt concentration field, viz.

$$Pe_{nom} = \frac{C_T}{C_X}\left(x_{1,\infty} - x_{1,\infty}^{sol}\right) \tag{16}$$

and the ratio of the actual and nominal growth rates was determined as a function of system properties.

For a dilute protein solution, $Kx_1 << 1$ [Debenedetti 1984], and can be neglected in the denominator of Equation (15), while the Kx_1 term in the numerator will be neglected in order to obtain an upper bound on the effect of salt rejection on the diffusion rate. In this case, Equation (15) can be integrated analytically to yield

$$x_1 = x_{1,\infty}^{sol}\, e^{-\beta\Delta C_{salt} z} + \frac{Pe}{\beta\Delta C_{salt}} \frac{C_X}{C_T}\left[e^{-\beta\Delta C_{salt}(z-1)} - 1\right] \tag{17}$$

The value of $x_{1,\infty}$ obtained from Equation (17) can be substituted into (16) to obtain

$$Pe = \frac{\beta\Delta C_{salt}}{e^{\beta\Delta C_{salt}} - 1}\, Pe_{nom} \tag{18}$$

Although the form of the relation between the nominal Peclet number and the actual Peclet number has been established, the apparent reduction in diffusion rate depends on ΔC_{salt}, which has not yet been determined. Recall that the quasi-steady salt concentration profile, Equation (12), was used to obtain Equation (18), but the surface concentration was left unspecified. A mass

balance on the salt rejected at the crystal surface yields:

$$\frac{dR}{dt}(1-s)\,C_{salt,surf} = D_{salt}\left.\frac{\partial C_{salt}}{\partial r}\right|_R \tag{19}$$

where s = segregation coefficient of the salt ($C_{salt,crystal} / C_{salt,surface}$); $0 \le s \le 1$. In terms of the dimensionless variables introduced in Equation (9), Equation (19) is

$$Pe\,(D_0 / D_{salt})\,(1-s)\,C_{salt,surf} = C_{salt,surf} - C_{salt,\infty} \tag{20}$$

so that

$$\Delta C_{salt} = C_{salt,surf} - C_{salt,\infty} = C_{salt,\infty}\left[\frac{1}{1 - Pe\,(D_0 / D_{salt})\,(1-s)} - 1\right] \tag{21}$$

For proteins, $D_0 / D_{salt} \approx 10^{-1}$, and typical Peclet numbers for lysozyme crystals are less than 6×10^{-2}. The maximum concentration difference occurs when s = 0 (total segregation of the salt), in which case $\Delta C_{salt} \le 6 \times 10^{-3}\, C_{salt,\infty}$. At a bulk concentration of 50 mg/ml NaCl, this gives $\Delta C_{salt} \le 0.3$ mg/ml. For the actual growth rate to equal one tenth the nominal growth rate, β should be approximately 10, but reported values of lysozyme solubility put the value of β closer to 10^{-1} [Ataka and Tanaka 1986]. Thus, $Pe \approx 0.985\, Pe_{nom}$, and salt rejection cannot reduce the diffusion rate to the point where crystal growth is entirely diffusion controlled.

If the protein molecules are treated as large ions and the protein activity coefficient obeys the Debye-Hückel law, the chemical potential of the protein molecules decreases as the ionic strength increases. This leads to a greater driving force for diffusion and a corresponding increase in growth rate, a trend which would make diffusion less likely to limit the crystal growth process. The solutions from which protein crystals are usually grown, however, are too concentrated in salt for the limiting form of the Debye-Hückel law to hold and it is unreasonable to expect the protein molecules to behave like simple ions [Tanford 1961]. The actual form of the activity coefficient, then, may partially acount for the slow growth of protein crystals. Any mechanism which requires

large gradients in salt concentration due to salt rejection cannot account for the slow growth rate unless the protein is extremely sensitive to small changes in salt concentration.

Effect of Impurities on Protein Crystal Growth

The presence of dust or other impurities affects protein crystal growth in two different ways: 1) the dust surface acts as a nucleation site for the protein; and 2) the protein molecules may adsorb to the surface of the dust particle, thereby reducing the effective protein concentration in the solution. The nature of the dust surface is too ill-defined to determine quantitatively how the nucleation rate is affected, so we will address the effect of protein adsorption in this section.

Suppose that there are a certain number of sites, n_T, on the dust surface to which protein molecules will bind. Further, assume that the rate at which the protein adsorbs is proportional to the product of the protein concentration and the concentration of available sites, and that the desorption rate is proportional to the concentration of occupied sites:

$$\frac{dn^*}{dt} = - C_d [k_{ad} C_p n^* - k_d (n_T - n^*)] \tag{22}$$

where C_p=molar concentration of protein, C_d=molar concentration of dust, n*= number of available binding sites/dust particle, k_{ad}=adsorption rate constant, and k_d=desorption rate constant. At equilibrium, dn*/dt=0, and we have

$$K = \frac{k_{ad}}{k_d} = \frac{n_T - n^*}{n^* C_p} = \frac{\theta_{eq}}{(1 - \theta_{eq}) C_{P,eq}} \tag{23}$$

where θ is the fractional coverage of the particle surface.

A mass balance on the protein in solution yields:

$$C_p = C_{P,0} - n_T C_d \theta \tag{24}$$

where $C_{P,0}$ is the original protein concentration in solution. Equation (23) can be substituted into

(24) so that

$$C_{P,eq} = C_{P,0} - n_T C_d \frac{KC_{P,eq}}{1 + KC_{P,eq}} \tag{25}$$

which can be solved to yield:

$$C_{P,eq} = \frac{-(1 - KC_{P,0} + n_T C_d K) + \sqrt{(1 - KC_{P,0} + n_T C_d K)^2 + 4KC_{P,0}}}{2K} \tag{26}$$

We can take a typical dust particle to be approximately 0.5 μm in diameter, and if the particle is assumed to be completely covered by a monolayer of protein molecules (taken to be cubes with a length of twice the hydrodynamic radius of 20 Å), approximately 5×10^4 protein molecules can be adsorbed on each particle of dust. This indicates that a 5%(w/v) solution of lysozyme can be completely depleted by adsorption if $C_d > 6.9 \times 10^{-8}$ mol/liter, provided that $K >> 1$.

Contamination by dust, then, can serve to reduce the effective protein concentration by a large amount. As the protein is depleted by the growing crystals, the molecules on the dust can desorb and replenish the protein concentration in solution. This would maintain the protein level in the solution at a fairly constant level, which might explain the nearly constant rates of growth which have been observed.

Aggregation of Protein

The state of aggregation of protein in solution affects the crystal growth rate by changing the rate at which protein diffuses to the crystal surface and reduces the effective concentration of protein available for growth. The diffusion coefficient of a particle is inversely proportional to its hydrodynamic radius, so that the aggregates have smaller diffusion coefficients than monomers and will diffuse to the surface slower. Additionally, if crystal growth occurs by addition of aggregates of specific sizes (e.g. monomers, dimers, or trimers), then the formation of non-participating

aggregates acts as a protein sink,thereby reducing the growth rate. Kam *et al.* [1978] and Feher and Kam [1985] have proposed a method for determining a particle size distribution based on quasi-elastic light scattering measurements and a thermodynamic model of nucleation. The discussion below is in two parts: (i) an analysis of the experimental measurements, and (ii) a description of their model.

According to Kam *et al.* [1978] and Feher and Kam [1985], a solution illuminated with incident light of frequency ν_o will scatter light with a power spectrum given by:

$$S(\nu) \propto \sum_{j=1}^{\infty} j^2 C_j \frac{\Delta\nu_j}{(\nu_s - \nu_o)^2 + (\Delta\nu_j)^2} \tag{27}$$

where j = number of molecules in an aggregate, ν_s = frequency of scattered light, $\Delta\nu_j = (2D_jq^2/2\pi)$, q = scattering vector, D_j = diffusion coefficient of a j-mer, and C_j is proportional to the number density of the j-mers. The power spectrum obtained experimentally is usually approximated by a single Lorentzian:

$$S(\nu) \approx \frac{A}{(\nu_s - \nu_o)^2 + (\Delta\nu)^2} \tag{28}$$

where A is a constant and $\Delta\nu$ is the effective linewidth of the power spectrum. The parameters A and $\Delta\nu$ can be found from a non-linear least-squares fit of the spectrum to the form given by (28) or by transforming the data into the form

$$Y(\nu) = 1/S(\nu) = \frac{(\nu_s - \nu_o)^2}{A} + \frac{(\Delta\nu)^2}{A} = mx + b \tag{29}$$

where $m = A^{-1}$, $x = (\nu_s - \nu_o)^2$, and $b = (\Delta\nu)^2/A$. In these coordinates, $\Delta\nu = (b/m)^{1/2}$ and the parameters b and m can be obtained from a linear least-squares fit of $Y(\nu)$. The linewidth is a rough measure of the state of aggregation of the protein because it has a maximum value when the protein is entirely monomeric, and decreases as the fraction of aggregates in solution increases.

The amplitude, A, also contains information on the concentration of aggregates: as the number of aggregates increases, so does the amplitude of the power spectrum. Analysis of experimental data in this manner yields only an "average" degree of aggregation rather than information on the actual size distribution of the protein. Although some sort of average diffusion coefficient can be determined directly from the linewidth, more detailed information on the particle size distribution cannot be obtained from the scattering spectrum alone. For this reason, Kam *et al.* chose to measure how the normalized linewidth, $\Delta\nu^*=\Delta\nu/\Delta\nu_1$, changes with protein concentration and to fit the parameters of their model so that the agreement between theory and experiment is maximized. The resulting particle size distribution, which is consistent with both theory and experiment, may not accurately represent the true size distribution in solution. As we will show later, the proposed model is not sensitive enough to discern the true distribution unambiguously.

The model is based on the thermodynamics of aggregation of monomers to form nuclei of different sizes. The change in free energy required to form a nucleus from monomers is usually considered to consist of two contributions: a negative bulk contribution which acts to promote aggregation and a positive surface component which arises from the need to support the additional surface area of the aggregate. The formation of small nuclei is thermodynamically unfavorable because the free energy change is positive due to the large surface to volume ratio of the aggregates. As the nucleus grows, the addition of monomers becomes less unfavorable until the nucleus reaches a critical size beyond which further addition of monomers is favorable. Any nucleus which exceeds the critical size will grow spontaneously until it reaches macroscopic size. The critical size of the nucleus depends on how the surface area and volume of the nucleus varies with aggregate size. For a spherical nucleus, the volume (bulk) is proportional to the number of molecules, j, in the aggregate, while the surface area is proportional to $j^{2/3}$. The standard free energy change for the formation of an aggregate from j monomers is

$$\Delta G_j^\circ = (j - 1)\, G_B + \beta\, (j^{2/3} - 1)\, G_S \qquad (30)$$

where G_B = bulk free energy per molecule (assumed constant), G_S = surface free energy per

molecule (also constant), and β = geometrical factor which gives the surface area per molecule. The standard state conditions are 1 %(w/v) protein, at the temperature, pH, and salt concentration of the system. The actual change in Gibbs free energy is then

$$\Delta G_j = (j-1)\, G_B + \beta\,(j^{2/3} - 1)\, G_S - (j-1)\, kT \ln C_T \tag{31}$$

where C_T is the total protein concentration expressed in units of %(w/v). Differentiation of (31) shows that ΔG_j reaches a maximum at the critical size

$$j^* = \left[\frac{\frac{2}{3}\beta\, G_S/kT}{\ln C_T - G_B/kT} \right]^3 \tag{32}$$

The equilibrium constants for the aggregation reactions

$$A_j + A_1 \rightleftharpoons A_{j+1} \quad ; \quad K_j = \frac{C_{j+1}}{C_j\, C_1} \tag{33}$$

were obtained from the continuum approximation

$$\ln K_j = -\left[\frac{\Delta G^\circ_{j+1} - \Delta G^\circ_j}{kT} \right] \approx -\frac{d}{dj}\left[\frac{\Delta G^\circ_j}{kT} \right] \tag{34}$$

Although this approximation is reasonable for large clusters, it becomes less accurate for small aggregates such as those which may be present during the pre-nucleation stage. If the expression for ΔG_j° from Equation (30) is substituted into Equation (34), the result is

$$\ln K_j = -\left[\frac{G_B}{kT} + \frac{2}{3}\frac{G_S}{kT}\, j^{-1/3} \right] \tag{35}$$

Evaluating Equation (35) for j=1 and $j \to \infty$ shows that the equilibrium constants are related to the free energy terms as follows:

$$\ln K_\infty = -\frac{G_B}{kT}$$
$$\ln (K_\infty/K_1) = \frac{2}{3}\beta\frac{G_S}{kT} \qquad (36)$$

Substitution of (36) into (32) leads to

$$j^* = \left[\frac{\ln (K_\infty/K_1)}{\ln (K_\infty C_T)}\right]^3 \qquad (37)$$

and the free energy barrier for nucleation is

$$\frac{\Delta G_j^*}{kT} = \frac{1}{2}\frac{\ln^3 (K_\infty/K_1)}{\ln^2 (K_\infty C_T)} - \ln\left[\frac{(K_\infty/K_1)^{3/2}}{K_\infty C_T}\right] \qquad (38)$$

Kam *et al.* chose to use K_1 and K_∞/K_1 as the adjustable parameters in their model.

When $\Delta G_j^*/kT >> 1$, the formation of critical-sized nuclei is slow, and the system can reach a state of "quasi-equilibrium" in which particles smaller than j* are in equilibrium with each other and the concentration of larger particles is negligible. The concentration of aggregates during the pre-nucleation stage was calculated from the quasi-equilibrium approximation:

$$C_j = K_{j-1}\, C_{j-1}\, C_1 \quad ; \quad j \le j^*$$
$$C_j = 0 \quad ; \quad j \ge j^* \qquad (39)$$
$$\sum_{j=1}^{j^*} j\, C_j = C_T$$

In order to calculate the quasi-equilibrium distribution, all that is required is to select different values of K_1 and K_∞, calculate j* from Equation (37), and solve Equation (39) for the aggregate concentrations. The distributions obtained from the reported values of $K_1 = 0.065$ %(w/v)$^{-1}$ and $K_\infty/K_1 = 35$ are shown in Figure 1 for different protein concentrations.

Once the quasi-equilibrium distribution is known, the approximate power spectrum can be

calculated by substituting the C_j into Equation (27) and truncating the summation at j*. Kam *et al.* then plotted the normalized linewidth, $\Delta\nu^*$, against the normalized protein concentration, K_1C_T, for different values of K_∞/K_1 (solid curves in Figure 2). The normalized linewidths obtained from experiment were plotted against protein concentration on the same semilogarithmic scale, and then shifted until agreement between the experimental data and one of the theoretical curves was attained. The value of K_1 can be calculated from the shift required to align the experimental and theoretical curves, while the appropriate value of K_∞/K_1 is that corresponding to the theoretical curve. Unfortunately, imposing this model on the system can lead to erroneous interpretation of the data. To illustrate the problem, we have created a sample particle size distribution in which the aggregates cannot grow larger than j=4 and the equilibrium constants are K_1= 1%(w/v)$^{-1}$, K_2= 5%(w/v)$^{-1}$, and K_3= 3%(w/v)$^{-1}$. The power spectrum was calculated as a function of concentration according to Equation (27) and the linewidth was calculated from Equation (29). We then obtained an approximate fit according to Kam's method described above (Figure 2) and found that the best-fit parameters are K_1= 1%(w/v)$^{-1}$ and $K_\infty/K_1 \approx$ 130. The disparity between the trial distribution and the best-fit distribution is shown by comparing the fraction of monomer at 1%(w/v) protein concentration: the trial distribution contains approximately 26% monomer while the best-fit distribution contains essentially no monomer. This method of determining the size distribution is simply not sensitive enough to differentiate among all the possible distributions

This insensitivity to the actual particle size distribution is not the only problem with Kam's model; the quasi-equilibrium approximation breaks down at concentrations in the range of interest to crystallographers. The quasi-equilibrium approximation is valid only when the free energy barrier is large compared with kT. At higher concentrations, the free energy barrier is relatively low (Figure 3) and critical nuclei form rapidly enough that their concentration cannot be neglected. When the quasi-equilibrium approximation is applied in these circumstances, the protein is forced to distribute itself among an artificially small number of aggregate sizes with the result that the model predicts large "jumps" in the mass fraction of monomer due to small changes in total protein

concentration. At concentrations where small changes in protein concentration decrease j* by one, the fraction of monomer increases discontinuously (Figure 4a). The oscillations seen in the normalized linewidth (Figure 4b) are a consequence of these monomer jumps. The curves in Figure 2 do not show this behavior because they were terminated at concentrations below those at which Δv^* starts to increase.

The thermodynamic model of aggregation presented here is based on two assumptions that can have large effects on the predicted particel size distribution. The first is that the protein solutions behave as ideal solutions. Even though the solutions are dilute, they are highly supersaturated and could deviate significantly from ideal solution behavior. The second assumption is that both the bulk free energy and the surface free energy remain constant with crystal size. At least in the case of the surface energy, it would be reasonable to expect some size dependence because it makes little sense to speak of bulk and surface properties when the aggregates are as small as four or five molecules. The most likely possibility is that the surface energy is small for small aggregates and gradually increases until it reaches its macroscopic value. This would make the formation of small aggregates more favorable and reduce the monomer concentration.

On the basis of the analysis of Kam's work, aggregation of protein cannot yet be eliminated as a mechanism which slows protein crystal growth. There is enough ambiguity in the experimental results that the amount of protein in aggegates cannot be determined with any confidence. Definitive studies of particle size distributions or, at the least, average particle sizes under growth conditions may show whether or not protein aggregation plays an important role in controlling crystal growth. In addition, a refinement of the theory to include size dependent effects may show that the effective concentration of monomer is much lower than curently believed.

Effects of Fluid Flow on Protein Crystal Growth

Bugg *et al.* [1984] suggested that the terminal size of the crystals could result from the size dependence of the natural convection on crystal size. If the force required to break the crystal

bonds is comparable to that of the shear stress at the crystal surface due to natural convection, then the flow field may be strong enough to strip protein molecules from the surface. Because the shear stress at the surface increases with crystal size, this would act as a self-limiting process. We can determine if this is a likely explanation for the phenomenon by performing an order of magnitude estimate of the viscous stress based on the velocity profile for a vertical flat plate.

From the velocity profile presented by Schlichting [1979], the shear stress is given by

$$\tau = \mu\Gamma \sim \mu\left[\frac{g\Delta\rho}{\rho_\infty}\right]^{3/4}\left[\frac{R}{\nu^2}\right]^{1/4} \tag{40}$$

where: τ=shear stress, μ=fluid viscosity, Γ=shear rate, g=gravitational acceleration, $\Delta\rho$=density difference, ρ_∞=bulk fluid density, ν=kinematic viscosity, R=crystal radius. According to Equation (1.1), a 1mm diameter spherical crystal in a 5%(w/v) lysozyme solution under unit gravity would experience a shear rate on the order of 100 s^{-1}. This analysis ignores the effect of the Schmidt number, Sc=ν/D, on reducing the shear rate. At high values of Sc, such as Sc=10^4 for lysozyme, Γ would be much smaller than the value obtained above [Schlichting 1979]. Nevertheless, if we use Γ=100 s^{-1}, any effect of fluid flow on protein crystal growth will not be prematurely ruled out. The shear stress acting on the crystal surface in a solution where $\mu = 1 \times 10^{-3}$ Pa-s is approximately 0.1 Pa. If we take Fiddis' [1978] approximation of the lysozyme molecule being a cube 30.9 Å on a side, then the shear force acting on the molecule is approximately 10^{-18} N.

We can take Fiddis' [1978] value of the surface energy (7.5 kJ/mol) as representative of the strength of the crystal bond, but the form of the potential is still unknown. For want of a better estimate, we approximate the potential as a Lennard-Jones 6-12 potential with electrostatic interaction:

$$U = \frac{-A}{r^6} + \frac{B}{r^{12}} + \frac{q_1 q_2}{4\pi\varepsilon_0 r} \tag{41}$$

where A and B are constants for the particular bond of interest, q_1 and q_2 are the partial charges on the atoms in the bond, ε_0 is the permittivity of free space, and r is the separation between the atoms. Hagler *et al.* [1974] determined the values of A, B, $q_1$and q_2 for the bonds in amide crystals and found that the form of Equation (1.2) accounted adequately for the observed interactions. From the values of A, B, and q reported by Hagler *et al.*, the bond energies were calculated from the value of U at the equilibrium separation (where $F = -dU/dr = 0$) and the maximum attractive force was calculated by determining the force where $dF/dr = -d^2U/dr^2 = 0$. The bond energies ranged from -0.3 kJ/mole for the bond between the carbonyl carbon and the amino hydrogen, to -29.5 kJ/mole for the bond between the carbonyl carbon and carbonyl oxygen. The bond with an energy closest to the 7.5 kJ/mole reported by Fiddis is that between hydrogen and nitrogen, which has a strength of 5.6 kJ/mole and requires a maximum force of 2.2×10^{-11} N per bond to break. If the electrostatic potential is neglected, then the bond with the lowest breaking force is that between a non-carbonyl carbon and the amino hydrogen, which requires $F=8.3 \times 10^{-13}$ N/bond to break. The force generated by free convection is approximately six orders of magnitude too small to strip molecules from the crystal surface.

Even though the shear stess cannot remove molecules from the surface, it may impart some preferred orientation to the molecules near the surface so that they are unable to find the proper alignment for addition to the crystal. To test this hypothesis, we compare the characteristic rates of the processes: if the velocity gradient at the surface tends to align the protein molecules in a preferred orientation, it acts at a rate which is comparable to the shear rate, Γ; the characteristic rotational rate is given by the rotational diffusion coefficient, $D_{rot} = kT/8\pi\mu R^3$, where R is the hydrodynamic radius of the protein [Tanford 1961]. The hydrodynamic radius of lysozyme is approximately 20 Å [Tanford 1961], so $D_{rot} = 2 \times 10^7$ s^{-1} while the shear rate is certainly less than 100 s^{-1}, so the ratio of rotational and shear rates is 2×10^5. This indicates that randomization of the protein molecules occurs much faster than any orientation imposed by the shear flow. Once the molecule has reached the surface and formed some sort of bond, however, the situation is different

because the molecule is constrained at the binding site. If an improperly oriented protein molecule bonded to the surface, it would be possible for other protein molecules to orient themselves properly with respect to the first molecule. In this manner, the crystal would be made up of regions with the same local orientation and the average ordering for the crystal as a whole would be reduced. If the crystal does not consist of this ensemble of regions, it would indicate that some ordering takes place, possibly due to the electrostatic interactions between charged groups.

The effects of electrostatic interactions on the interatomic potential were mentioned only briefly above, but they exhibit a strong influence on the nature of the bonds. The electrostatic contribution is large compared with the other components of the hydrogen bond, so it is important to know the length scale over which it acts. The natural length scale for electrostatics is the Debye shielding length, κ^{-1}:

$$\kappa^{-1} = \left[\frac{\varepsilon \varepsilon_0 kT}{2000 N_A Z^2 e^2}\right]^{1/2} I^{-1/2} \qquad (42)$$

where ε=dielectric constant of water, k=Boltzmann's constant, T= absolute temperature, N_A=Avogadro's number, Z=charge on ion, e=electron charge, and I=ionic strength. The Debye length is approximately 3 Å for 50 mg/ml NaCl, which indicates that the effects of the electrostatic potential are substantially reduced when the atoms are separated by distances greater than the typical bond lengths reported by Hagler *et al.* Any orientation due to electrostatic interactions, therefore, would occur when the incoming protein molecule is practically bonded to the crystal surface.

The denaturation of proteins by the shear field was suggested by Marc Pusey in a conversation with M. L. Grant. The following model, suggested by W. B. Russel of Princeton University, was used to investigate the possibility of shear-induced denaturation. If the protein molecule must be in a particular conformation in order to bind to the crystal surface, crystal growth may be hindered if the shear stress due to fluid flow is sufficient to change the protein's conformation. For this analysis, consider a molecule of protein to be spherical as shown in Figure 5. The molecule is

maintained in this conformation by a single hydrogen bond placed at point A and is "hinged" at point B. If the shear forces on the molecule are sufficient to break the bond at A, the molecule will open up in the yz plane and the molecule will be unable to bond to the surface. The force on the bond at A can be determined by calculating the torque about B due to creeping flow past the sphere and determining the equivalent force to place at A.

Over any element area on the molecular surface, the magnitude of the torque is given by but only the component in the $\pm x$ direction contributes to opening the hinge in the y-z plane, so the appropriate expression for the x component of the torque is

$$dT_X = r\,(\tau_{r\theta} R^2 \sin\theta\, d\theta\, d\phi)\sin\alpha \sin\phi \tag{43}$$

From geometrical considerations, $\alpha = \theta/2$, and $r = R\{2(1 - \cos\theta)\}^{1/2}$, while $\tau_{r\theta} = (3\mu v_\infty/2R)\sin\theta$ [Bird, Stewart, and Lightfoot 1960]. If the integration of Equation (1.5) is carried out over half a sphere ($0 \le \phi \le \pi$, $0 \le \theta \le \pi$), then the x component of the torque is

$$\frac{1}{2} T_X = \frac{3R^2 \mu v_\infty}{\sqrt{2}} \int_0^\pi \int_0^\pi \sin^2\theta\,(1 - \cos\theta)^{1/2} \sin\frac{\theta}{2} \sin\phi\, d\phi\, d\theta = \frac{3\pi R^2 \mu v_\infty}{2} \tag{44}$$

and the corresponding force due to flow around half the sphere is $3\pi R\mu v_\infty/4$. The force, F, on the hydrogen bond is twice the force due to flow around half the sphere,

$$F = \frac{3\pi R \mu v_\infty}{2} \tag{45}$$

which must equal the breaking force of the hydrogen bond if the molecule is denatured.

From Hagler *et al.*, the weakest amide crystal bond (in the absence of the electrostatic contribution) has a breaking force of 8.3×10^{-13} N, which would require $v_\infty \approx 9$ cm/s to break the bond. This velocity is approximately two orders of magnitude greater than the free convection velocity one would estimate from the case of the vertical flat plate, and is certainly greater than the

velocity attained in the systems of interest. Furthermore, this is a worst case scenario since the weakest possible bond was chosen and only one hydrogen bond was permitted. In reality, the electrostatic contribution would strengthen the bond and there are many internal hydrogen bonds.

The analyses above indicate that viscous stresses due to natural convection are insufficient to disrupt crystal growth by stripping molecules from the surface, orienting molecules at the surface, or denaturing the protein as it approaches the surface. It is difficult to construct another mechanism by which the flow field can influence protein crystal growth except by altering the mass transfer rate to the crystal surface

Effect of Mass Transfer Rate on Protein Crystal Growth

The growth rate of tetragonal lysozyme crystals from solution (pH 4, salt concentration of 50 mg/ml NaCl, 22° C) was measured by Pusey *et al.* [1986]. For small crystals (less than 70 μm in length), the growth rate was found to obey the relation

$$\frac{dR}{dt} = k\left[\frac{C_i - C_S}{C_S}\right]^2 \tag{46}$$

where R is the crystal radius, C_i is the protein mass concentration at the interface, C_S=1.7 mg/ml is the solubility mass concentration under these conditions, and $k=1.46 \times 10^{-9}$ cm/s. No explanation of this unusual concentration dependence is given except that Schlichtkrull [1957] observed a similar behavior for insulin. The interfacial concentration calculated from their model of convective mass transfer was essentially the same as the bulk concentration. As we will show by means of a quasi-steady state analysis, the crystal sizes studied were too small for appreciable size effects to be evident and no reliable measurements have been made on larger crystals. Any discussion of growth rates of large crystals, then, is based on the extrapolation of small crystal measurements and should be considered speculative at best.

The crystal growth rate given by Equation (2.1) must also equal the volume flux to the crystal

surface:

$$\frac{dR}{dt} = \frac{D}{C_X} \left.\frac{\partial C}{\partial r}\right|_R \tag{47}$$

where C_X=725 mg/ml is the mass concentration of protein in the lysozyme crystal (corresponding to 50% solvent by volume [Matthews 1968, Bugg *et al.* 1984]). Note that the crystal shape has been approximated as spherical. The concentration gradient at the crystal surface can be expressed as

$$\left.\frac{\partial C}{\partial r}\right|_R = \left.\frac{\partial C}{\partial r}\right|_{R,\ diff'n} \cdot \frac{\partial C/\partial r|_R}{\partial C/\partial r|_{R,\ diff'n}} = \left.\frac{\partial C}{\partial r}\right|_{R,\ diff'n} Sh_R \tag{48}$$

where Sh_R is the Sherwood number based on the crystal radius and is given by the Ranz-Marshall correlation:

$$\begin{aligned} Sh_R &= 1 + 0.3\, Sc^{1/3} Gr^{1/4} \\ Sc &= \frac{\nu}{D} \\ Gr &= \frac{8R^3 g\, \Delta\rho}{\rho_\infty \nu^2} \end{aligned} \tag{49}$$

When the crystal grows by diffusion in a quasi-steady manner, the concentration gradient at the surface is given by

$$\left.\frac{\partial C}{\partial r}\right|_{R,\ diff'n} = \frac{C_\infty - C_i}{R} \tag{50}$$

Equating the two expressions for crystal growth given in equations (46) and (47) and making use of equations (48) through (50) yields

$$Da\left[\frac{C_i - C_S}{C_S}\right]^2 = \frac{C_\infty - C_i}{C_X}\left[1 + 0.3\,Sc^{1/3}Gr^{1/4}\right] \tag{51}$$

where Da=kR/D. Equation (51) can be solved for the interfacial concentration C_i as a function of size in order to determine the dependence of growth rate on crystal size. When g = 0 (no buoyancy driven flow), Equation (51) can be solved for C_i explicitly to yield

$$C_i = \frac{-1 + 2\,Da\,(C_X/C_S) + \sqrt{1 + 4\,Da\,(C_X/C_S)[(C_\infty - C_S)/C_S]}}{2\,Da\,(C_X/C_S^2)} \tag{52}$$

The results of these calculations are given in Figure 6a, while the corresponding growth rate calculated according to Equation (46) is shown in Figure 6b.

As shown in Figure 6a, the interfacial concentration is essentially equal to the bulk concentration over the entire size range studied by Pusey *et al.* whether or not natural convection is present. The surface concentration and growth rate for crystals larger than 70 μm are strictly extrapolations. If the crystal continues to grow at a nearly constant rate (broken lines), it would indicate that natural convection is sufficient to maintain the surface concentration at the bulk level so that crystal growth is entirely kinetically controlled. If convection is suppressed, a decrease in the growth rate from the small-size limit indicates that transport plays a role in controlling crystal growth as the crystal grows larger (solid lines). By the time a crystal growing from a 5%(w/v) solution of lysozyme has reached 1 mm in diameter, the growth rate has fallen to approximately 25% of its initial value. Similar results can be seen for growth from 1%(w/v) lysozyme solution. A rough indication of the relative importance of diffusion and kinetics can be obtained from the slope of the growth rate vs. crystal size curve (Figure 6b). The slope is zero when mass transfer is infinitely faster than interface kinetics, and the slope approaches -1 as diffusion begins to control the growth rate. From the curves in Figure 6b, it is clear that most crystal growth occurs in the transition region when both processes are important.

Quasi-steady models of this sort cannot predict the cessation of growth which has been reported [Kam *et al.* 1978, Feher and Kam 1985] because they do not include any mechanism which would reduce the ability of protein molecules to attach to the surface. The current data on the effect of mass transfer rate on crystal growth are not sufficient to determine if mass transfer plays a role in limiting crystal size. If crystal defects occur because natural convection maintains the interfacial concentration at excessive levels, the simplest remedy may be to grow crystals from less concentrated solutions, in which case, the growth of high quality crystals may depend on the trade-off between growing large crystals and growing them quickly.

Termination of Growth

Growing sufficiently large crystals is often the limiting step in protein crystallography. Generally, protein crystals reach some terminal size beyond which they do not grow, even when they are transferred to a fresh solution of protein [C. Schutt 1986, personal conversation]. Several growth-ending mechanisms involving the effects of fluid flow were examined in Section 1 of this work, but they hardly exhaust the list of possible explanations. For example, the solution conditions may change during the course of crystal growth so that a transformation of the dissolved protein occurs. Cole *et al.* [1964] measured the pH of lysozyme solutions and found that during the course of crystallization, the pH increases by approximately 0 - 0.4 pH units from original values between pH 2.5 and pH 4.6. Ataka and Tanaka [1986], on the other hand, report a slight decrease in pH from solutions of pH 5 or higher which they attributed to absorption of carbon dioxide from air. Association of lysozyme molecules which might account for the lack of growth in the original solution has been observed in the range of pH 4.5 - 6.5 [Sophianopoulos and Van Holde 1964, Bruzzesi *et al.* 1965]. This mechanism, however, cannot account for the lack of growth when the crystals are placed in a fresh bath of protein unless the pH change also makes an irreversible change in the state of the protein on the crystal surface.

The steady accumulation of errors suggested by Kam [Kam *et al.* 1978, Feher and Kam 1985]

would explain why crystals stop growing, but the theory has not been verified. Experiments which study the relation between crystal size and defect concentration are necessary to confirm the validity of Kam's hypothesis: if diffraction resolution does not increase with crystal size as expected, or if the resolution actually decreases, the accumulation of errors would be a suitable explanation. Finding a relation between defect concentration and crystal size, however, is not enough to explain how defects occur. To do this, a detailed study of the growing crystal is required so that local conditions such as interfacial concentrations of protein, precipitant, and hydrogen ion can be followed over the course of crystal growth. Such measurements, along with crystallographic studies of crystal ordering may provide some insight into the processes which terminate crystal growth.

The mechanisms by which defects accumulate have not been studied because previous researchers worked only with small crystals (less then 70 μm in length) [Fiddis 1978, Pusey *et al.* 1986]. Crystals this small would not produce strong size-dependent effects on the protein flux (see Ranz-Marshall correlation, Equation (2.4)) and probably have a low concentration of surface defects. It follows that the kinetic expressions for the growth rate obtained from these measurements are incomplete because the role of defects has been neglected. Growth rate measurements taken over the full range of crystal sizes would provide information on the accumulation of defects and possibly on the evolution of any buoyancy-driven convection. The results of these experiments could then be used to evaluate the effect of natural convection on protein crystal growth and to explain why defects inhibit crystal growth.

References

Ataka, M., and S. Tanaka. *Bioploymers* 25 (1986) 337-350.

Bird, R. B., W. E. Stewart, and E. N. Lightfoot. Transport Phenomena. Hohn Wiley and Sons (New York:1960).

Bruzzesi, M. R., E. Chiancone, and E. Antonini. *Biochemistry*. 4 (1965) 1796-1800.

Bugg, C. E. *et al.* Proposal: Protein Crystal Growth in a Microgravity Environment, submitted in response to Space Science and Applications Notice EN-1 (1982). Submited July, 1984.

Cole, J. B., M. L. Bryan, and W. P. Bryan. *Arch. Biochem. Biophys.* 130 (1969) 86-91.

Creighton, T. E. Proteins: Structure and Molecular Properties. W. H. Freeman and Company (New York:1983).

Cussler, E. L. Diffusion. Cambridge University Press (London:1984).

Debenedetti, P. G. *Doctoral Thesis Digest.* Department of Chemical Engineering, Massachusetts Inst. Tech. Cambridge, MA, December 1984.

Feher, G. and Z. Kam. *Meth. Enzym.* 114 (1985) 77-112.

Fiddis, R. W., R. A. Longman, and P. D. Calvert. *J. Chem. Soc. Faraday Trans.* 75 (1979) 2753-2761.

Grant, M. L. Unpublished results. (1985).

Hagler, A. T., E. Huler, and S. Lifson. *J. Amer. Chem. Soc.* 96 (1974) 5319-5327.

Kam. Z., H. B. Shore, and G. Feher. *J. Mol. Biol.* 123 (1978) 539-555.

Matthews, B. W. *J. Mol. Biol.* 33 (1968) 491-497.

McPherson, A. Preparation and Analysis of Protein Crystals. John Wiley and Sons (New York:1982).

Pusey, M. L., R. S. Snyder, and R. Naumann. *J. Biol. Chem.* 261 (1986) 6524-6529.

Schlichting, H. Boundary Layer Theory. 7 ed. McGraw-Hill (New York:1979).

Schlichtkrull, J. *Acta Chem. Scand.* 11 (1957) 439-460.

Sophianopoulos, A. J., and K. E. Van Holde. *J. Biol. Chem.* 239 (1964) 2516-2524.

Tanford, C. Physical Chemistry of Macromolecules. John Wiley and Sons (New York:1961).

Wyckoff, H. Conference: "New Directions in Protein Crystal Growth." Rogersville, AL, 12-15 May 1986.

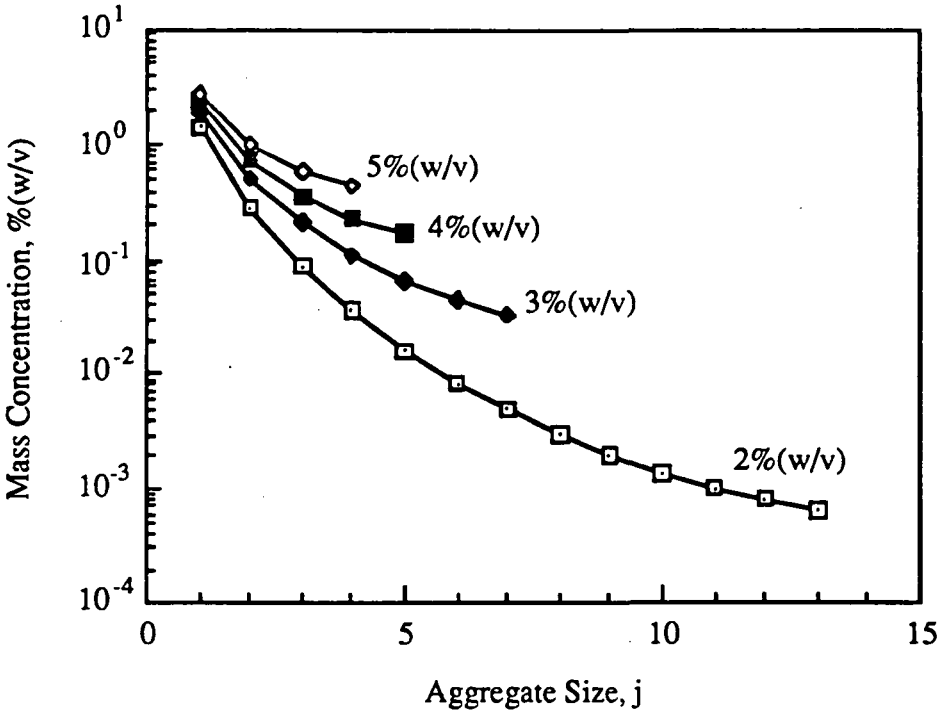

FIGURE 1 - Quasi-equilibrium size distributions
These distributions were calculated from the quasi-equilibrium approximation given by Equation (39) when the critical size is calculated from Equation (37) with $K_1 = 0.065/\%(w/v)$ and $K_\infty / K_1 = 35$.

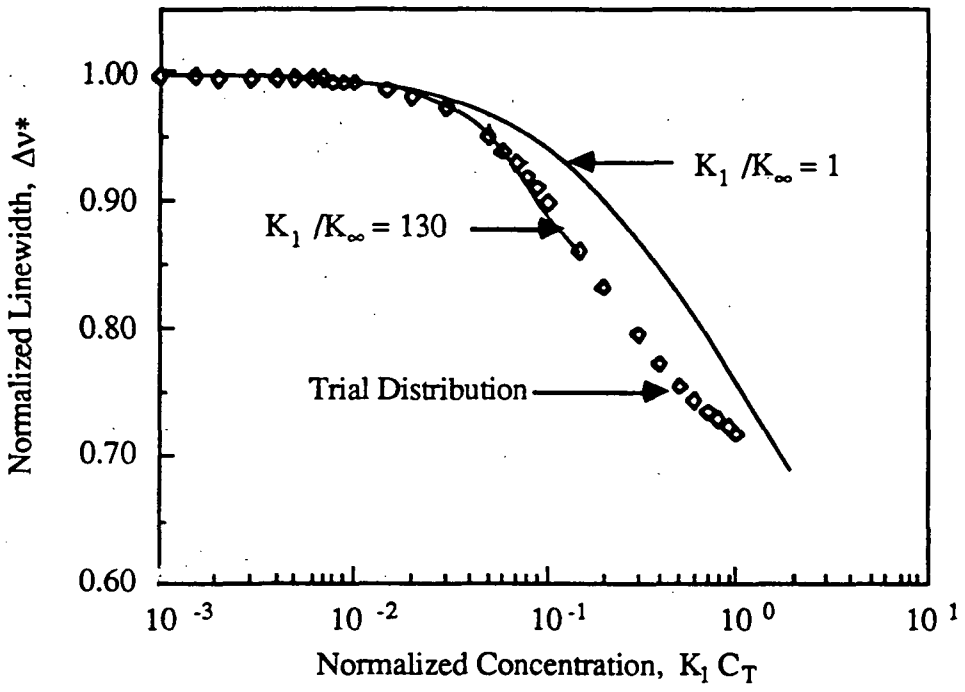

FIGURE 2 - Best-fit of trial size distribution
Figure shows approximate best-fit of trial distribution obtained in the manner of Kam et al. and Kam and Feher. Solid curves were obtained from the quasi-equilibrium distribution for the values of the parameters; the linewidth was calculated from Equation (29). The open diamonds were calculated for the trial distribution.

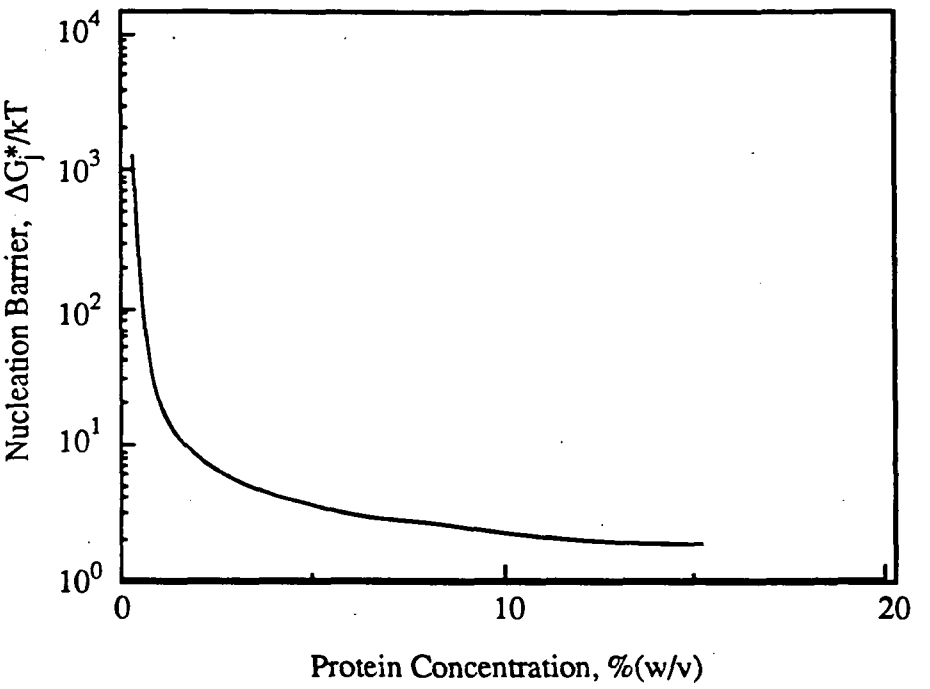

FIGURE 3 - Free energy barrier to nucleation
The maximum free energy required to form nuclei of critical size is calculated from Equation (38) for the reported values of $K_1 = 0.065/\%(w/v)$ and $K_\infty / K_1 = 35$.

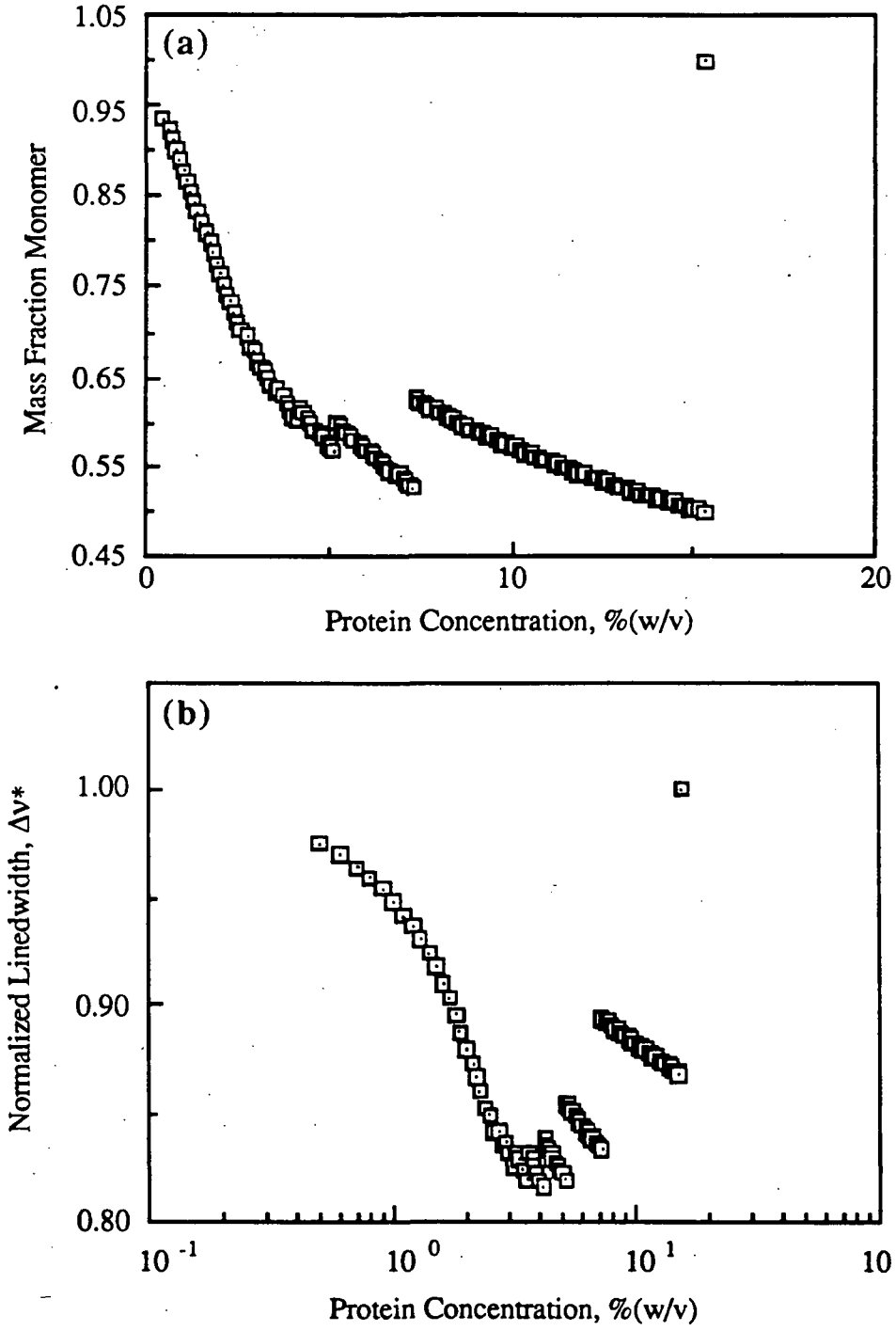

FIGURE 4 - Effects of quasi-equilibrium approximation at high concentration
(a) At concentrations where small changes in total protein concentration reduce j* by one, the amount of monomer in solution jumps discontinuously.
(b) The abrupt changes in monomer concentration affect the linewidth by making the system more monodisperse.
All calculations were based on j* calculated from Equation (37), quasi-equilibrium concentrations calculated from Equation (39), and linewidths calculated from Equation (29).

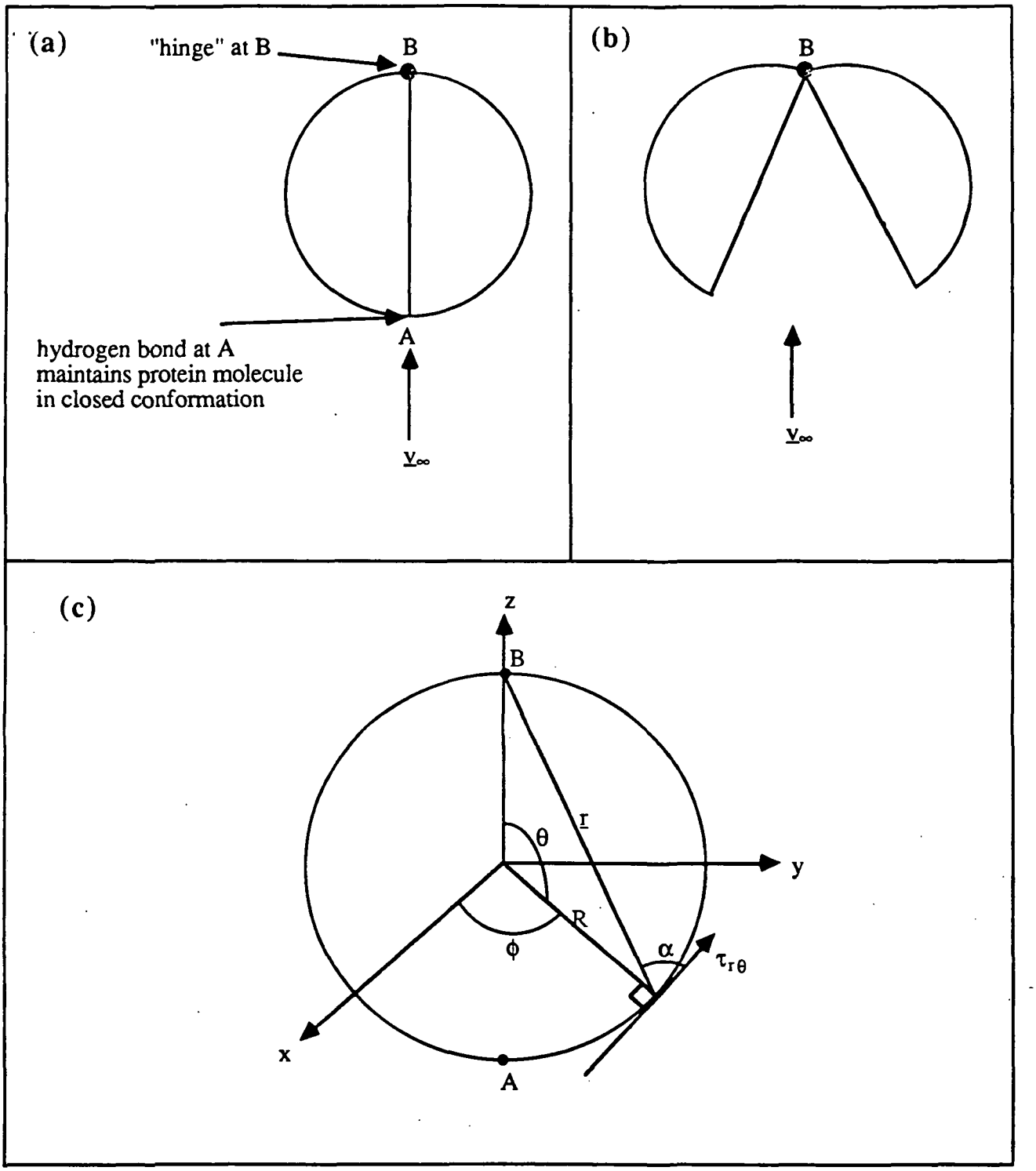

FIGURE 5 - Denaturation of protein molecules by fluid shear.
(a) Protein molecule in spherical (normal) conformation
(b) Protein swinging open under influence of shear
(c) Definition sketch showing coordinate system for calculations

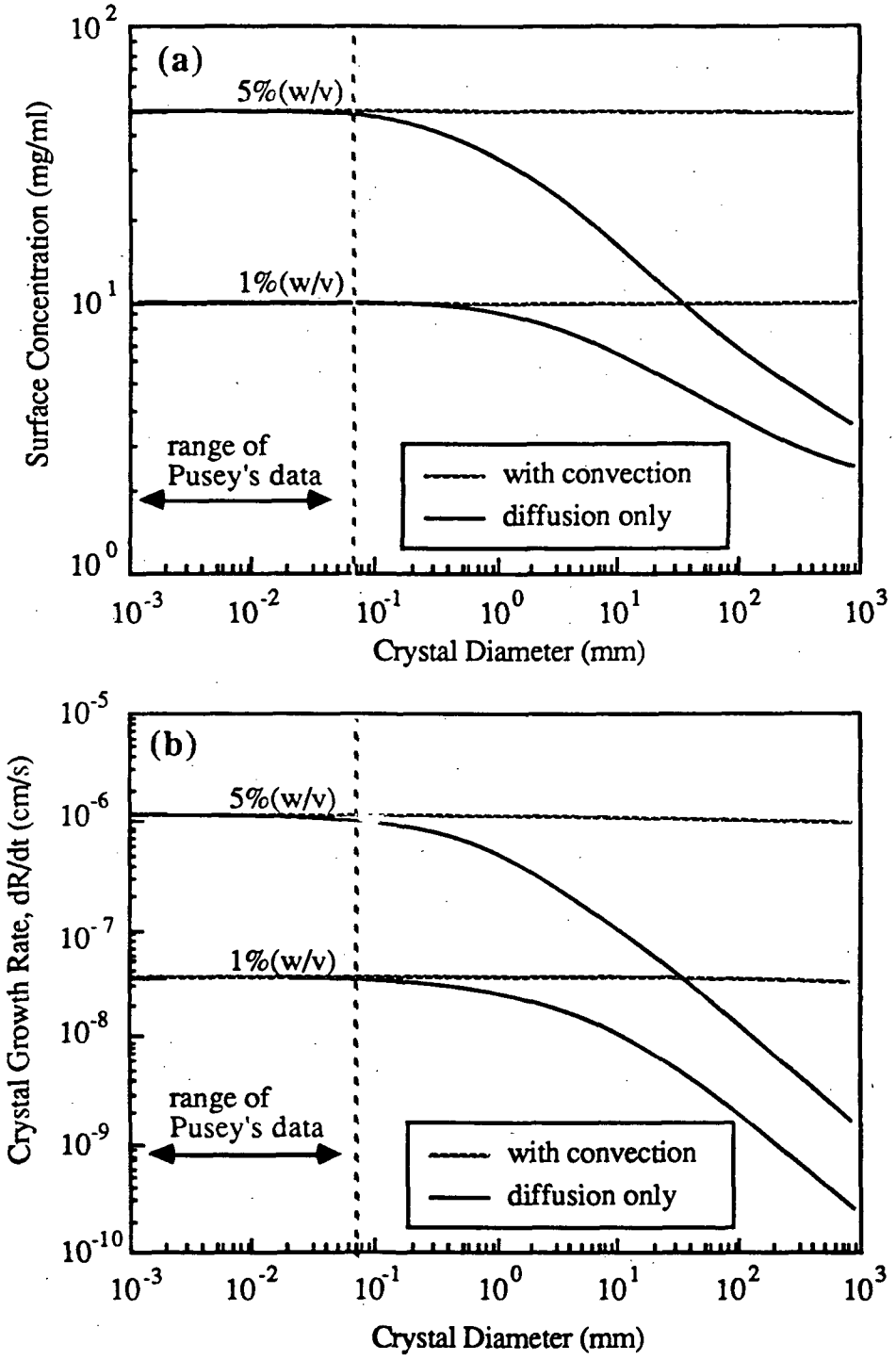

FIGURE 6 - Surface concentration and growth rates of lysozyme crystals
(a) Quasi-steady surface concentration of lysozyme when growth obeys the relation given by Equation (46).
(b) Quasi-steady growth rate when growth obeys relation given by Equation (46).
Growth rate constant reported by Pusey et al. to be $k = 1.46 \times 10^{-9}$ cm/s.